The Anharmonic Infrared Spectra of Polycyclic Aromatic Hydrocarbons

Proefschrift

ter verkrijging van
de graad van Doctor aan de Universiteit Leiden,
op gezag van de Rector Magnificus Prof. mr. C. J. J. M. Stolker,
volgens besluit van het College voor Promoties
te verdedigen op woensdag 15 July 2017
klokke 13:23 uur

door
Cameron J Mackie
geboren te Toronto, Ontario, Canada
in 1984

Promotiecommissie

Promotor:	Prof. dr. A. G. G. M. Tielens
Promotor:	Dr. T. J. Lee
Co-promotor:	Dr. A. Candian
Overige leden:	Dr. B. Name (University)
	Dr.
	Prof. dr.
	Prof. dr.
	Prof. dr.

ISBN TBD
Cover: .

Designed by .

Created by .

To the fairest

“Quote ”
-Person

Table of Contents

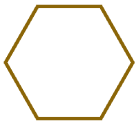

Introduction

Polycyclic aromatic hydrocarbons or "PAHs" are a family of related molecules. As with many labels in chemistry, the name is descriptive rather than catchy. This means however, everything that defines a PAH is fortunately right there in the name. We can work backwards through the name starting with "hydrocarbon", which simply refers to any molecule consisting solely of hydrogen and carbon. Next we have "aromatic". This word requires a more in depth knowledge of chemical bonding, but in brief it refers to the delocalization of bonding electrons over the surface of a planar molecule. So instead of each atom of a molecule holding tightly onto its and its neighbor's outer electrons, as in a non–aromatic molecule, these electrons are shared freely over the whole molecule. This particular arrangement lends extra stability, and unique chemical properties to these molecules. (In case the reader was wondering if the term "aromatic" has a connection to smell at all, it in fact does. When aromatic bond containing chemicals were first isolated they were found to have quite a strong smell.) Finally, we arrive at the last word "polycyclic". Again a simple term, referring to the fact that the carbon atoms of PAHs are arranged in rings or "cycles" and there are more than two adjoined rings. Figure 1.1 shows a few examples of various PAH structures.

We are actually very familiar with PAHs in our everyday life, perhaps without even knowing it. On Earth PAHs are one of the undesirable by–products of combustion[1, 2]. If you've ever seen black "smoke" pouring out of a car's exhaust, seen residue left behind by candles, or even ate a flame–broiled steak, then you've come into contact with PAHs (actually, that delicious smokey flavor of a charred steak is from those *aromatic* PAHs!). As can be guessed, all of that acrid smoke cannot be good for your health – PAHs have indeed been linked strongly to

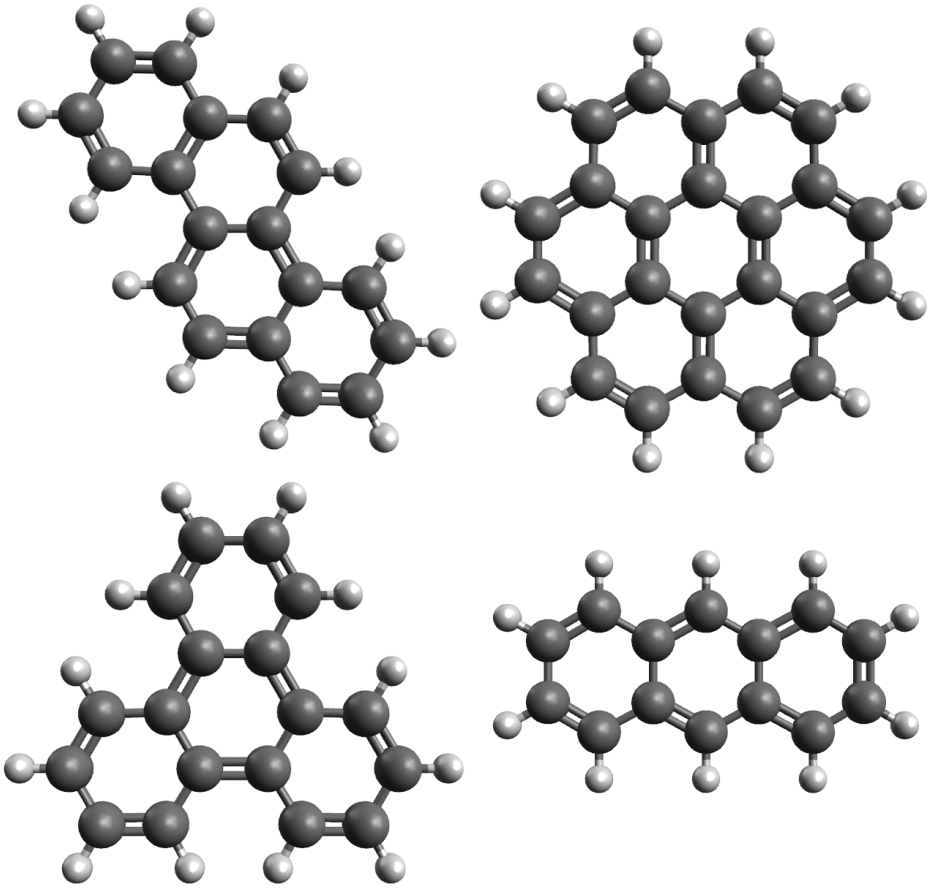

Figure 1.1 Examples of PAH species. Clockwise from top left: chrysene, coronene, anthracene, and triphenylene.

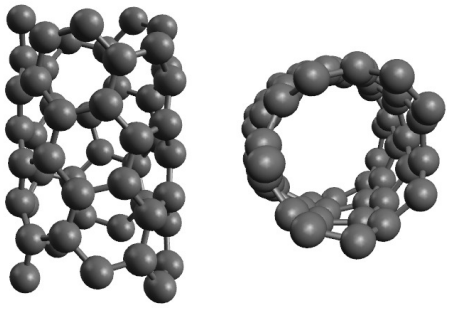

Figure 1.2 An example of PAH–like nano–structures. Side and top view of a piece of a nano–tube.

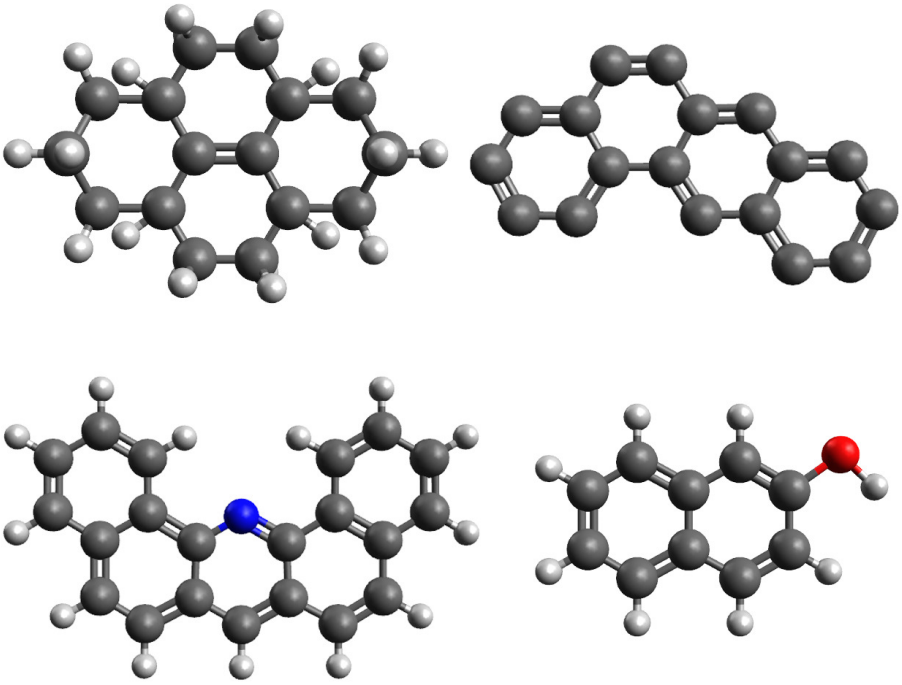

Figure 1.3 Examples of species that astronomers also consider PAHs. Clockwise from top left: super–hydrogenated pyrene, fully dehydrogenated benz[a]anthracene, 2OH–naphthalene, and dibenz[ch]acridine.

cancer[3]. Even the PAHs in that delicious steak have been shown to cause certain types of cancers[4]. While a terrible carcinogen and pollutant, PAHs can actually benefit society in the right context as well. PAHs have been used as stand–ins for the study of nano–materials such as graphene or nano–tubes (both polycyclic carbon containing structures, as shown in figure 1.2). These super strong, super light, wonder–materials may one day replace all of our conventional building materials[5, 6, 7]. These nano–materials also exhibit interesting electrical properties, and may someday be used to replace silicon transistors in our cell phones and computers[8]. While still a fairly new area of research, the study of the structural, physical and chemical properties of PAHs and nano–carbon materials will likely lead us into the next technological age.

Now that we have defined firmly what a PAH is from a chemistry standpoint, the reader should forget all of that, and focus on what astronomers think PAHs are. Why astronomers would be interested in PAHs in the first place will be explained later, but lets start by taking a look at the word “polycyclic aromatic

hydrocarbon" again. In order to explain their observations, astronomers have to relax the definition of PAHs. Sometimes it is necessary to assume a nitrogen atom has replaced a carbon and hydrogen atom[9], or that an oxygen or hydroxy group is inserted[9] into the PAH. But this breaks the strict "hydrocarbon" definition! Sometimes astronomers need to add additional hydrogens to the PAH[10] or strip all the hydrogens away[11]. But doing so however, completely disrupts the aromaticity of the molecule. They are no longer aromatic! Finally we arrive again at the last word, "polycyclic'. Surely astronomers can't touch that word, but they have... This last point is debatable, but some consider a PAH to be containing *more* than two rings. Astronomers however, happily accept naphthalene, a non–*poly* two ringed molecule to be a PAH without a second thought! Figure 1.3 shows a few examples of these "astronomer's PAHs".

Chemical arguments aside, these loose definitions of what constitutes a PAH is actually important for astronomers. Space is a very different environment from Earth. How PAHs form, how they interact with the abundance of hydrogen present[10, 12], how they interact chemically on the inside comets[13] or meteorites[14], how they survive high speed impacts from cosmic rays[15], how they chemically interact in the extreme environments around massive stars[16, 17], all of these considerations lead to PAHs that are less PAH–like than what is typical for a chemist on Earth. However, the behavior of these "PAHs" are similar enough in astrophysical environments, that from an astronomer's point of view calling them all PAHs is acceptable (even to a begrudging chemist) and leads to some outstanding science.

We have seen how PAHs can be paradoxically both a carcinogen, and a technological wonder here on Earth, but are they anything but a "pollutant" in space? In fact they are much more. PAHs are of interest to astronomers for a number of reasons. For example: they have been shown to control temperature and charge balance in large gaseous clouds of the interstellar medium (ISM)[18]. They act as catalysts for bringing hydrogen atoms together to form molecular hydrogen H_2[10]. They can act as nuclei for grain formation that could ultimately become planets. Even life itself could originate from the processing of interstellar PAHs! Evidence of the formation of nucleobases, the building blocks of DNA, have been found in comets and meteors[19]. These nucleobases possibly formed from the processing of PAH and PAH derivatives embedded in icy comets[20].

Unlike on Earth, in space we can't easily scoop up a sample and test it for PAHs. Instead all we have to work with is what we can see, or more technically what our "mechanical eyes", known as spectrographs, can see. Spectroscopy is a field of science that uses the unique frequencies of light (or "spectrum") emitted or absorbed by atoms and molecules to both detect the species present, and to examine their physical properties. In order to accomplish this we need an in depth understanding and high quality models of what frequencies of light we expect to be emitted from the molecules. In 2019, the James Webb Space Telescope will be launched. This will be the most powerful telescope ever sent into space, able to provide superior pictures to the Hubble Space Telescope. Attached to the telescope of JWST will be a set of spectrographs able to measure infrared light in higher detail than we havve ever been able to before. Amazingly, this is the exact

frequency of light in which PAHs emit. The wealth of knowledge we will gain from JWST about interstellar PAHs will dwarf all we know right now. However, our current spectra and models of the infrared light emitted from PAHs is not good enough for us to interpret all of the data we will soon receive from JWST.

Ideally if we could, we would measure in the lab all of the spectra of relevant PAHs here on Earth and use those to compare to what we observe in space. This however, is impossible for a number of reasons. The first being a matter of scale. There are a near infinite number of possible PAH species. For example, limiting ourselves to just ten rings or less still puts the number of possible species at over twenty thousand[11]! Add in the number of possible PAH derivatives and this set grows exponentially. Therefore, small sets of representative PAHs are selected for experimentation, and extrapolations to the larger family of PAHs are made based on them. The second issue is the low volatility of PAHs. As the size of PAH increases it becomes more and more difficult to vaporize the PAHs into the gas phase in order to measure their spectra accurately. This means that most of the experimental spectra taken to date is either at high temperatures[21] or "cooled" by embedding the PAHs in inert argon matrices using matrix isolation spectroscopic (MIS) techniques[77, 79, 80]. Unfortunately, this leaves PAHs in physical environments that are dissimilar to the interstellar medium of space. The high temperature and pressures lead to band shifts and broadenings, and the matrix of the MIS leads to unpredictable band shifts due to interactions with the matrix itself.

To circumvent these two issues, a heavy reliance is put on theoretical calculations of the IR spectra of PAHs. The experimental studies can then be used to validate and improve these theoretical methods, which in turn can be applied to a vastly wider variety of PAHs and PAH derivatives, under a variety of physical conditions that cannot be accomplished with experiment. Density functional theory (DFT) methods using the harmonic approximation (explained below) are often employed to achieve these goals. However, recent work[22] has shown that the harmonic approximation reproduces poorly the IR spectra of PAHs, especially in the C–H stretching region (see the red trace of figure 1.4 compared to the experimental trace in black). To truly model the interstellar IR spectra of PAHs, *anharmonic* calculations are necessary (see the blue trace of figure 1.4 compared to the experimental trace in black).

As noted, comparisons to experimental spectra are required to develop and validate theoretical techniques. The theoretical anharmonic IR spectra presented in this work requires comparisons to state–of–the–art spectra. To make this possible, Maltseva et al.[22, 23, 24] produced new high–resolution low–temperature gas–phase infrared spectra of a variety PAHs. As will be shown, the anharmonic calculations can not only produce spectra that are far superior to the harmonic spectra (Chapters 3 through 5), but can also be used calculate the spectra of a molecule at any desired temperature (Chapters 6 and 7); which is key to understanding the IR cascade process of interstellar PAHs (Chapter 7).

The aim of this thesis then becomes clear: Improve the theoretical infrared spectra of polycyclic aromatic hydrocarbons so that we are ready to fully understand what we are looking at when we see interstellar PAHs for the first time again

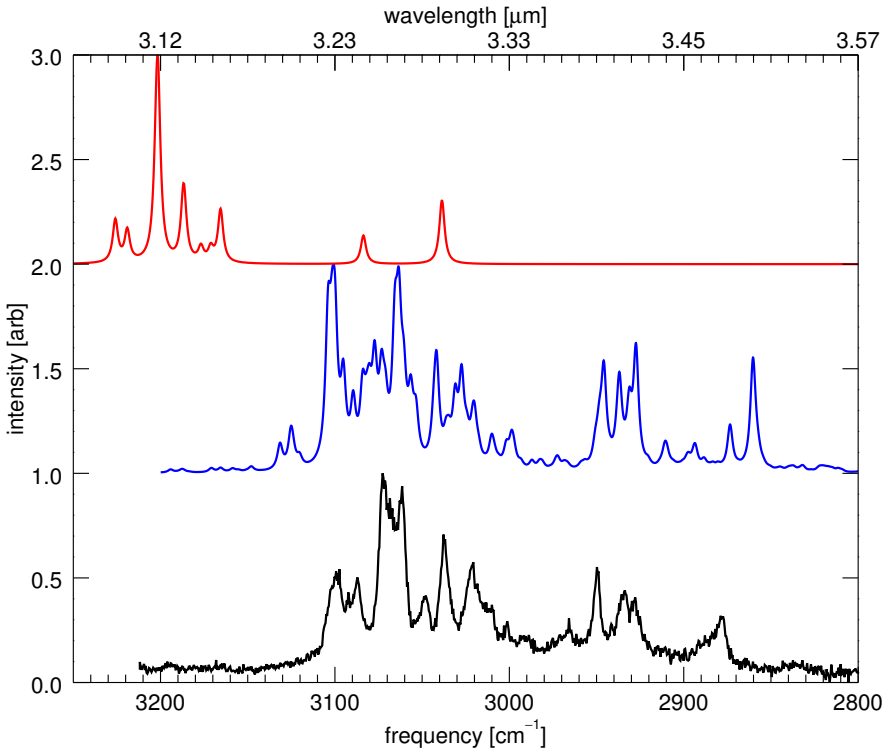

Figure 1.4 Three infrared spectra of the C–H stretching region of 9–methylanthracene: The harmonic spectrum (red, top), anharmonic spectrum (blue, middle), and the high–resolution experimental spectrum (black, bottom).

with the "new eyes" of JWST.

1.1 Interstellar PAH hypothesis

It may be surprising then to learn that these large, complex "pollutants" are found in space; and not just a trace here and there, they are found *everywhere*. Every object that astronomers have observed which contains dust and gas has been found to contain PAHs. As long as there is enough light (ultraviolet light from stars) to "excite" the PAHs, they see them. The amount we see is actually staggering; it has been estimated that 10 – 20% of *all* of the carbon in the interstellar medium (the vast space between stars) is locked up in PAHs. These PAHs aren't small either, current estimates say each PAH contains between 50 and 200 carbon atoms[25].

The presence of PAHs in space was first put forward in the 1980's to explain the series of IR features referred to at the time as the "unidentified infrared bands" (UIRs). In 1984, (coincidentally the birth year of the author of this thesis) Léger and Puget[26] proposed PAHs to be the carriers of the UIR bands based on physical arguments, such as the stability of PAHs in intense UV fields. Allamandola et. al[27] in 1985, showed that the observed UIR spectra in Orion Nebula matched the spectra of PAHs by comparing it to (of all things) car exhaust(!) as well as the IR fluorescence of a specific PAH called chrysene. However, it wasn't until the 1990's that the hypothesis that PAHs are responsible for the UIR bands began to take hold. As will be explained below in the section 1.2, an infrared spectrum is not the strongest evidence to prove the presence of a particular molecule. More concrete spectral evidence, such as an electronic spectrum (in the ultraviolet (UV) region), was needed. Léger et al.[28] then argued that the observed UV absorption bump in the interstellar spectra matched the general shape of the UV absorption of PAHs. Additionally, a set of distinct visible and UV features known as the "diffuse interstellar bands" (DIBs) were put forward to be the spectral fingerprints of PAHs[28]. Over the next decades, more evidence of the existence of PAHs in interstellar space began to accumulate: PAHs were found to be contained in meteorite samples[29], newly launched space telescopes provided better resolution of the UIR spectra than previously achieved with Earth–based telescopes[30, 31, 32], and theoretical models of the IR emission of PAHs were able to explain the variations seen in the UIRs from interstellar object to interstellar object[33]. Presently, the PAH hypothesis is the most widely accepted explanation for the appearance of the UIR bands. In fact these bands are now routinely referred to as the Aromatic Infrared Bands (AIBs), rather than UIRs.

So where do all of the interstellar PAHs come from? During the majority a star's lifetime it is constantly "burning" hydrogen into helium through nuclear fusion. As an inert helium core builds up eventually fusion of hydrogen in the core stops, and instead only takes place in a shell around the core. This causes the star's outer layers to cool and puff up in size (ten to hundreds of times their original radius) into what is called a red giant. Eventually enough helium is built up in the core, and with no hydrogen burning to provide outward pressure, the core collapses. This increase in pressure ignites the helium, which begins to fuse into

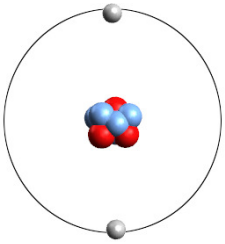

Figure 1.5 Electron "particles" (white) in orbit around around a nucleus (blue/red).

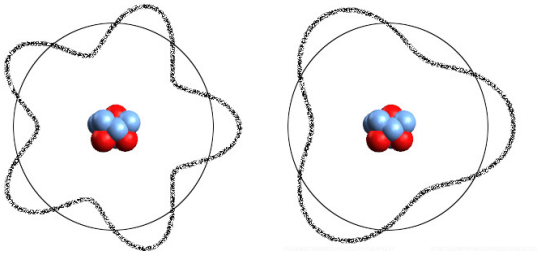

Figure 1.6 Electron "waves" (black dotted lines) around around nuclei (blue/red). The solid line represents the division between the mathematically positive and negative values of the wave.

carbon, nitrogen, and oxygen. Once again the star builds up an inert core, this time made up of a mixture of carbon, nitrogen, and oxygen. When the helium fuel in the core has been exhausted, fusion will only occur in shells of hydrogen and helium surrounding the core. This causes the star to swell once again into a asymptotic giant branch star or an "AGB star". During the last stages of this AGB phase, large convective currents dredge up the newly formed carbon, nitrogen, and oxygen. For a mid–sized star, at this point it is as good as dead. It is not massive enough to begin burning carbon, nitrogen, or oxygen, or to go supernova, or become a black hole. Instead it will begin rapidly losing mass as it can no longer hold onto its own gases. As this outflow of gas cools it can condense into molecules, mainly carbon monoxide (CO). If there is more oxygen than carbon left over after the formation of CO, then the remaining oxygen goes into forming water and oxides, and eventually silicate grains. If there is more carbon than oxygen left over after the formation of CO, then the remaining carbon goes into forming acetylene, hydrogen cyanide, other small organics, and eventually carbonaceous grains and of course PAHs.

1.2 Spectroscopy

As stated previously, spectroscopy is the study of the interaction of atoms and molecules with light. These interactions are dictated by quantum mechanics. Quantum mechanics itself is often seen as a mysterious entity which causes odd things to happen i.e., entanglement, teleportation, Schrödinger's cat, etc... but really at its core quantum mechanics is simple. Picture an atom. At its center are positively charged protons, and orbiting these protons some distance away are negatively charged electrons (figure 1.5). In our everyday macroscopic world we know that everything loses energy over time: wheels eventually stop turning, swings will stop swinging, even the orbits of planets and stars decay over time[34]. The same should hold true for electrons orbiting protons. Any accelerating (orbiting) charge, like an electron, should emit a continuous stream of energy in the form of light. Their orbits should then decay over time and they should eventually crash into the protons. However, this is not what we see. In fact, if that were true we would not exist. Our universe would not exist. The reason this does not happen is quantum mechanics. At the very small scale, all matter, even light, behaves both as a particle (like a billiard ball) and a wave (like a plucked guitar string). The so–called wave–particle duality. The most basic explanation of this duality is that the probability of finding the "particle" portion of matter at a particular point in space is equal to the square of the absolute value of the "wave" portion of the matter. You can never exactly pinpoint that location, but you can give probabilities that it will be in a particular location at a particular time. Since the particle *has* to be somewhere the total of this probability *has* to be equal to one. If we now picture the "wave" part of the electron in its orbit around the protons, we can see why it doesn't crash (figure 1.6). It can't. The wave itself can oscillate from positive to negative as many times as it wants as it travels around the protons, but the square of its absolute value must be equal to one. This means only certain energies of orbits are allowed. If the electron wants to switch to a higher or lower energy orbit (say from the left wave to the right wave in figure 1.6), it must emit *exactly* the amount of energy that separates those two allowed orbits. These allowed energies are limited to particular quantities, and are *quantized*. This simple principle that energy only comes in specific quantities gives quantum mechanics its name. While quantum mechanics can get quite complex and non–intuitive, all of it stems from this basic idea.

This quantization of energy is the key to spectroscopy. Since only certain energies are "allowed" for any given atom or molecule, this means that an atom or molecule can only interact with light of specific colors or "frequencies". If one were to separate the light being emitted or absorbed by the molecule using a prism, then it would produce a "rainbow" of colors with the spectral fingerprint, or *spectrum*, of the molecule clearly seen (see figure 1.7). Each spectra is unique to each type of atom or molecule. So by analyzing the light we see, we can tell exactly which atoms and molecules are present, just like fingerprints at the scene of a crime.

While the frequency of light emitted from these orbiting electrons tends to be in the ultraviolet down to the visible region of the spectrum, this notion of quantized energy also extends to all other behavior of molecules as well. The energies of

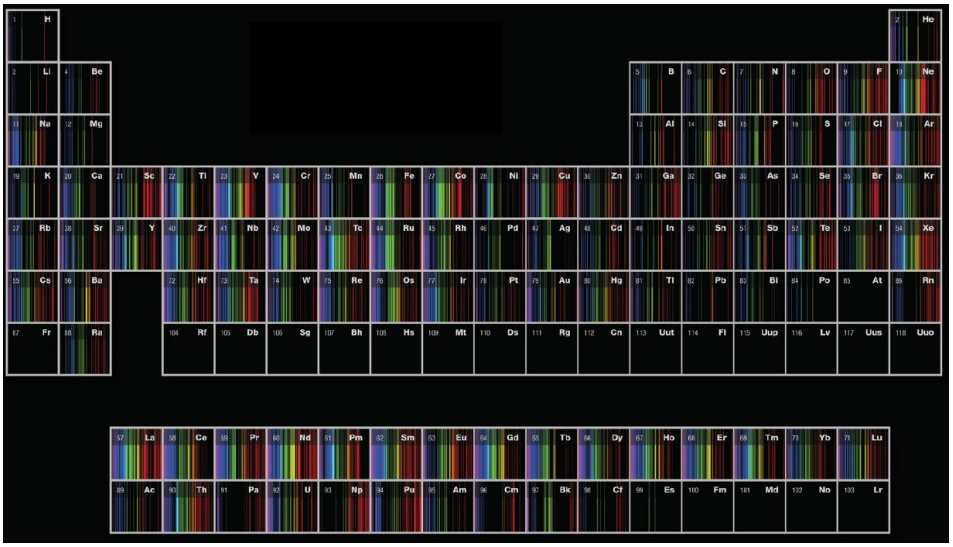

Figure 1.7 The visible light emission spectra of each element, arranged in the order of the periodic table of elements (available for purchase at http://www.fieldtestedsystems.com).

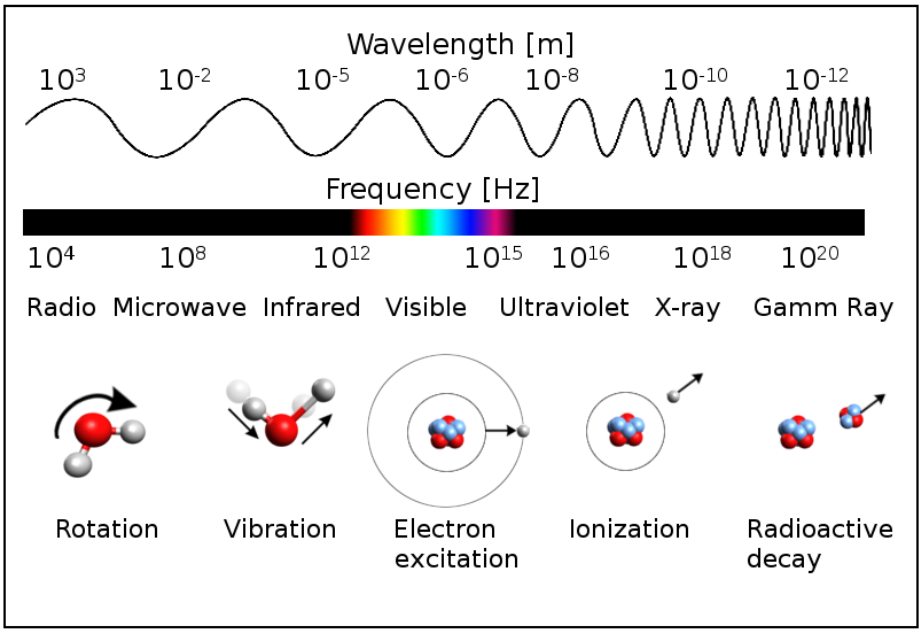

Figure 1.8 The regimes of molecular and atomic photon emissions.

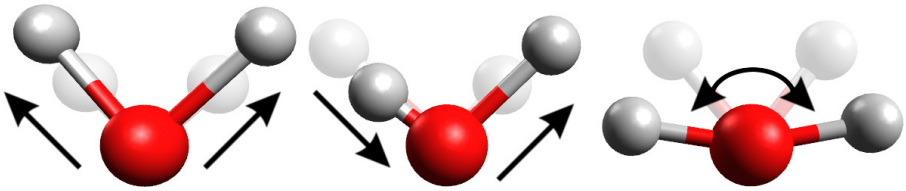

Figure 1.9 The three vibrational modes of water: symmetric stretching, asymmetric stretching, and bending.

allowed rotations are also quantized, meaning molecules can only rotate at specific rates specific to their structure. The frequency of light emitted from changes in rotation is in the microwave region of the spectrum. Vibrations of the atoms contained in molecules are also quantized, meaning the bonds between the atoms can only oscillate at specific rates, specific to the type of bonded atoms. The frequency of light emitted by these vibrations are in the infrared (IR) region of the spectrum. See figure 1.8.

Using the spectra of a molecule in all of these regions allows us to uncover many properties of molecules such as shape, size, bond lengths, bond strengths, chemical reactivity, ionization energy, etc., as well as uniquely identify the molecules themselves.

1.2.1 Infrared spectroscopy

The focus of this thesis is on the IR spectrum of PAHs. As stated above, the IR portion of a spectrum is linked to the vibrations of the atoms inside a molecule. The atoms in a molecule can oscillate back and forth as if they were attached together by springs, or groups of atoms can bend back and forth as if a spring loaded door hinge. These motions can be described in "normal coordinates", a set of orthogonal (independent) vibrations (see figure 1.9 for the three vibrational modes of water). Each normal coordinate motion, or *fundamental vibrational mode*, has a specific frequency at which it vibrates. For a vibrational mode to emit or absorb light its *electric dipole* must change through the course of the vibration. Simply put, light needs something to push against to get the molecule moving, without a changing electric dipole there is nothing to push against. These properties lead to an IR spectrum with spectral bands at specific frequencies (determined by the types of normal modes) and specific intensities (determined by how much the dipole changes through the course of the vibrational motion).

While the electronic spectrum (from the orbits of electrons) is unique for each and every molecule, the IR spectrum is not as unique. Since the IR spectrum is determined by the vibrations of bonds, molecules with similar bonds have similar IR spectra. For example, all molecules containing oxygen bonded to hydrogen will have a stretching mode that shows up in the spectrum between 3200 and 3400 cm^{-1} (3.125 and 2.941 μm) (see figure 1.10 for more examples).

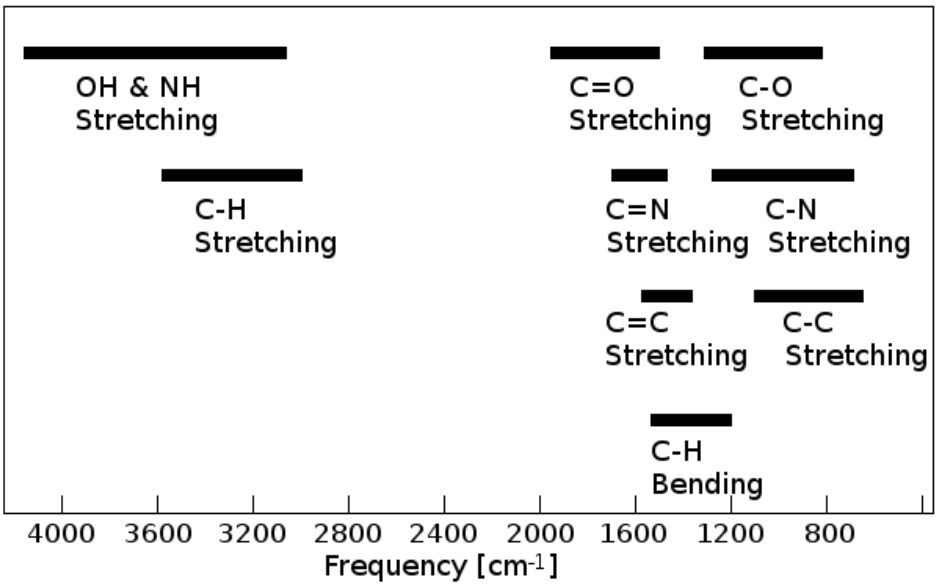

Figure 1.10 Typical infrared emission ranges for the vibrational modes of common function groups.

1.2.2 PAH IR signatures

The AIBs observed by astronomers shows great variation in the IR spectra, not only from interstellar object to interstellar object, but also spatially within an object itself[31]. The variation in the IR spectrum of PAHs is used to identify general properties of the population of PAHs, such as structure, shape, charge, temperature, and chemical make–up, as well as identify the physical conditions in which they are found, such as densities, overall charge balance, and temperature. Additionally, the variation in these observations can be used to explain the evolution of the objects in which they are found, and the evolution of carbon in the universe itself.

Since all PAHs contain similar bonds to one another their IR spectra are also

Band [cm^{-1}]	Band [μm]	Mode assignment
3030	3.3	aromatic C–H stretching
1920	5.2	combination bands: C–H bend + C–C stretch
1770	5.65	combination bands: C–H bend + C–C stretch
1610	6.2	aromatic C–C stretching
1320	7.6	C–C stretching and C–H in–plane bending
1280	7.8	C–C stretching and C–H in–plane bending
1160	8.6	C–H in–plane bending
940 – 700	10.6 – 14.2	C–H out–of–plane bending
610	16.4	C–C out–of–plane bending

Table 1.1 Typical band positions of PAH IR active vibrational modes

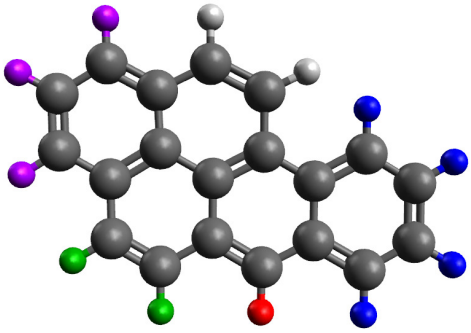

Figure 1.11 The possible variations in edge structure of a PAH. Hydrogens are classified by how many are attached to an individual ring: solo (red), duo (green), trio (purple), and quarto (blue).

Band range [cm^{-1}]	Band range [μm]	Mode assignment
940 – 880	10.6 – 11.4	C–H out–of–plane bending, solo
880 – 780	11.4 – 12.8	C–H out–of–plane bending, duo
800 – 750	12.5 – 13.3	C–H out–of–plane bending, trio
770 – 700	13.0 – 14.2	C–H out–of–plane bending, quarto

Table 1.2 The variation seen in the C–H out–of–plane bending modes due to the number of neighboring hydrogen atoms. (See figure 1.11 for definitions.)

similar. The approximate band positions of the IR features common to all PAHs are listed in Table 1.1. Although very similar overall, the IR spectra of PAHs do differ from one another in subtle ways. The edge structure (as shown in figure 1.11) can affect the position of the C–H out–of–plane bending modes[30] listed in table 1.2. The relative intensities of these sets of bands can be used to determine the edge structure of PAHs.

The charge of PAHs has also been correlated with changes in relative strengths of the 1660 – 1100 cm^{-1} (6.0 – 9.1 μm) region, with the intensity of the IR features of cations increasing ten–fold compared to their neutral counterparts[36]. The number of carbon atoms contained within a PAH has also been correlated with shifts and changes in the features[25].

In addition to structural changes, the addition of side groups can alter the IR spectrum of PAHs. The addition of extra hydrogens[37] or methyl groups[38] cause the appearance of aliphatic C–H stretching bands around 2940 cm^{-1} (3.4 μm), and aliphatic C–H bending modes around 1450 cm^{-1} (6.9 μm). If enough hydrogens are added it will cause the loss of the aromatic C–H stretching features completely. Hetero-atomic substitutions can also alter the spectrum. For example, the insertion of a nitrogen atom into a PAH causes a shift of the 1610 cm^{-1} (6.2 μm) feature to 1590 cm^{-1} (6.3 μm), with a possible correlation of how deep the nitrogen is inserted into the PAH[9].

1.2.3 Infrared cascade spectrum of PAHs

The process by which interstellar PAHs emit their IR spectrum differs greatly from PAHs on Earth. The key difference being due to densities. On Earth densities of any gas are high enough that collisions between neighboring molecules are inevitable. These collisions mean that the average energy of the system (i.e., temperature of the PAHs) is uniform. Additionally, on Earth energy flows in and out of any system from its surroundings. Meaning the temperature is stable and does not fluctuate wildly. For these reasons, measuring the spectra of PAHs in the lab produces a spectrum that is at one fixed temperature. Conversely, densities in space can be low enough that collisions between neighboring molecules are rare. This means that the PAHs are not in thermal equilibrium, and can therefore take on different temperatures from their neighbors. In interstellar space energy also flows in and out of the system stochastically, which is to say energy comes in short bursts. For PAHs this energy comes in the form of UV photons. A PAH will absorb a UV photon, become electronically excited, then return to the electronic ground state through non–adiabatic effects into highly excited (high temperature) vibrational states. Over the next few seconds the PAH will cool down by emitting IR photons, before eventually absorbing another UV photon and starting this process over again. This whole process known is known as an "infrared cascade"[39]. This stochastic process of absorbing a UV photon, becoming very hot suddenly, then slowly cooling means the IR spectrum is changing constantly. This process leads to a spectrum that is different from a spectrum recorded at a single temperature on Earth.

Attempts have been made to replicate the interstellar IR cascade emission spectrum of PAHs on Earth in the lab with some success[40, 41, 42]. However, due to the difficulty of reproducing interstellar conditions, a heavy reliance is put on theoretical models. Due to computational limits, most of these theoretical models[33, 43, 44] have relied on the harmonic approximation (explained below) to produce the IR spectrum at one temperature, after which statistical[44] and empirically[45] derived laws are applied to account for the constant change in temperature during the cascade process. These methods have also proven to be successful, but the laboratory data from which these empirical laws are derived is limited, and a large number of assumptions still need to be made in the models. What is truly required are full anharmonic calculations (as described throughout the chapters of this thesis).

1.3 Theoretical spectroscopy

In the previous section we discussed how quantum mechanics is at the heart of spectroscopy. The equation that describes quantum mechanical systems is simple. Known as Schrödinger's equation, it can be written as follows

$$\hat{H}\Psi = E\Psi \tag{1.1}$$

where Ψ is the wavefunction that describes your system, $\hat{H}$ is a Hamiltonian that corresponds to the how the energy of the system is described and E is the total

energy contained in the system. The equation simply describes the total energies contained in your system (i.e., molecule) depending on the specific state or wavefunction of the system (i.e., electron orbits). For a molecule, setting up the Hamiltonian itself can look rather complex

$$\begin{aligned}\hat{H} = &- \sum_i \frac{\hbar^2}{2M_i}\nabla^2_{\mathbf{R}_i} \\ &- \sum_i \frac{\hbar^2}{2m_e}\nabla^2_{\mathbf{r}_i} \\ &- \sum_i \sum_j \frac{Z_i e^2}{4\pi\epsilon_0|\mathbf{R}_i - \mathbf{r}_j|} \\ &+ \sum_i \sum_{j>i} \frac{e^2}{4\pi\epsilon_0|\mathbf{r}_i - \mathbf{r}_j|} \\ &+ \sum_i \sum_{j>i} \frac{Z_i Z_j e^2}{4\pi\epsilon_0|\mathbf{R}_i - \mathbf{R}_j|}\end{aligned} \tag{1.2}$$

where $\mathbf{R}$ are the coordinates of the nuclei, $\mathbf{r}$ are the coordinates of the electrons, M_i is the mass of nucleus i, m_e is the mass of an electron, but is rather simple when explained. It simply accounts for all of the interactions going on inside the molecule. The first term describes the kinetic energy of all of the nuclei, the second term describes the kinetic energy of all of the electrons, the third term describes the energy of attraction between each electron and each nucleus, the fourth term describes the energy of repulsion between different electrons, and finally the fifth term describes the energy of repulsion between different nuclei.

Applying this Hamiltonian to a molecule and solving it will yield absolutely everything you could want to know about the molecule. You could even reproduce every aspect of its spectrum in perfect reproduction of experiments. However, there is a caveat. As soon as there is more than one electron in your molecule, solving this equation mathematically exact becomes impossible. And not just hard. Literally impossible. It is only possible to solve mathematically exact for systems like the hydrogen atom or the helium$^+$ cation, or numerically exact for very small systems. All is not lost though, approximations to this equation can be made to make it much easier (possible) to solve. For example, the Born–Oppenheimer approximation assumes that the motions of the nuclei are independent from the motions of the electrons. A fair assumption, since the electrons are so much lighter than the nucleus and therefore react much faster to stimuli.

Under this assumption a potential energy surface (PES) from the solution of the electronic part of the Schrödinger equation can be constructed simply as a function of the position of the stationary nuclei. The nuclei are adjusted in position until a minimum in total energy is found, representing the equilibrium geometry (or shape) of the molecule. Although an approximation, these approximate methods can still predict the structure of molecules fairly accurately. The accuracy is often limited by how the electron interactions are modelled in the various electronic structure methods.

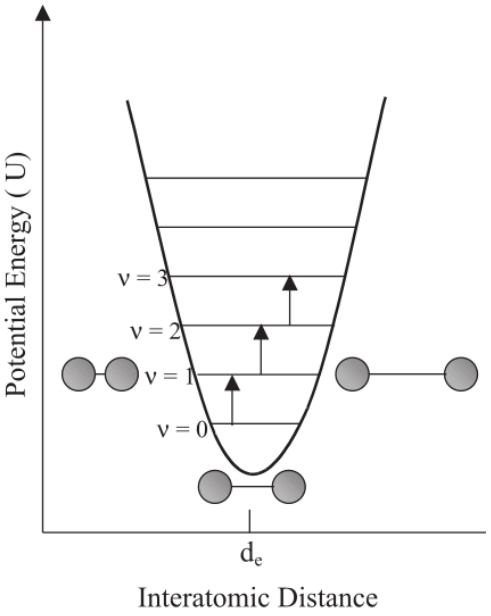

Figure 1.12 The harmonic potential of a diatomic molecule. (Adapted from reference 47.)

1.3.1 Density functional theory

Density functional theory (DFT) is perhaps the most widely used method for modeling the electronic structure of molecules due to it being relatively computationally inexpensive, while still remaining fairly accurate. The main assumption in DFT is that the electrons can be modeled as an electron density, which depends only on position ($\rho(\mathbf{r})$). With this electron density assumption, the second, third, and fourth terms of the Hamiltonian (equation 1.2) are replaced with functionals of $\rho(\mathbf{r})$, which are computationally much easier for a computer to handle. Errors do arise in this approximation from neglecting exchange correlation between electrons. Therefore, exchange interaction functionals must also be constructed to take into account the missing electron–electron interactions in the fourth term of equation 1.2. The choice of how these functionals are mathematically constructed impacts both the accuracy and speed of the computations. Since these functionals can be expressed in a vast number of ways, and no "universal" functional has been found, functional development is still a very active area of research in computational chemistry. For a more detail descriptions see reference 46.

1.3.2 Harmonic approximation

Once the electronic Schrödinger equation is solved (using methods such as DFT) and the equilibrium geometry is found, then the nuclear portion can be solved

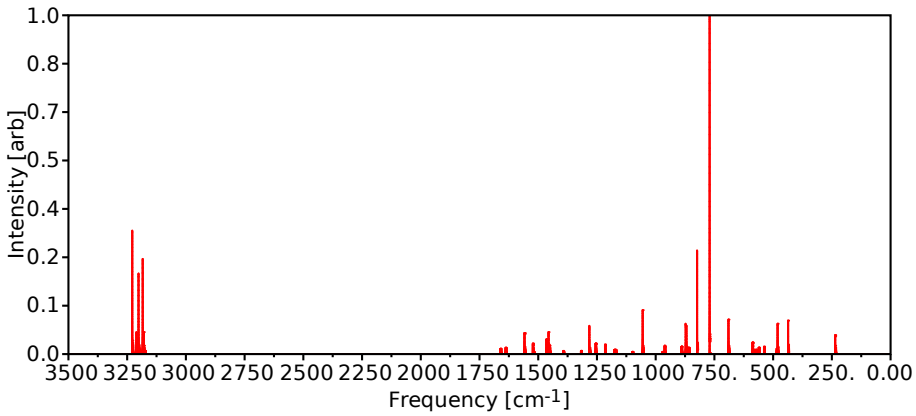

Figure 1.13 The harmonic infrared spectrum of chrysene.

independently. In molecules that contain three or more atoms the vibrations of the atoms are again too complex to handle in an exact manner. Therefore, approximations to solve the nuclear portion of Schrödinger's equation is again needed. The most common approximation to make is the harmonic approximation. In the harmonic approximation the potential energy (V) between each nuclei are approximated by a quadratic function given as

$$V = \frac{1}{2} \sum_{i} \sum_{i<j} F_{ij} X_i X_j \tag{1.3}$$

where $F_{ij} = \frac{\partial^2 V}{\partial X_i \partial X_j}$ are the quadratic force constants (strength of the bonds) between atoms i and j and X_i and X_j are the coordinates of atoms i and j. Figure 7.1 shows a visualization of a potential between two atoms. The quadratic force constants can be determined using numerical methods. Once these force constants are determined, they are mass weighted and put into a matrix. Diagonalizing this matrix gives the energies (frequencies of IR light) of the vibrational modes as the eigenvalues, and the descriptions of the vibrational motions (figure 1.9) as the eigenvectors. The intensities of these vibrational modes can then be determined by taking the derivative of the dipole moment along each of the vibrational modes.

The resulting harmonic IR spectrum for a typical PAH can be seen in figure 1.13. Databases containing the harmonic spectra of hundreds of PAHs are available online[33, 48].

1.3.3 Anharmonicities

While successful in getting the big picture correct, the harmonic approximation has many short comings. The main problem with the harmonic approximation is the potential itself. Figure 1.14 shows the harmonic potential of a diatomic molecule next to the true potential of a diatomic molecule. There are some noticeable

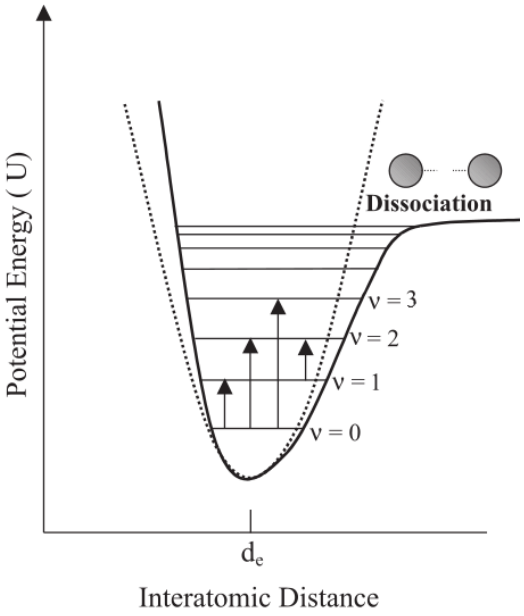

Figure 1.14 The anharmonic potential (solid black) of a diatomic molecule compared to the harmonic potential (dotted). (Adapted from reference 47.)

differences. Most importantly, the shape of the harmonic potential is incorrect. The harmonic potential is symmetric in shape, and continues to infinite energy on both sides, while the true, or "anharmonic" potential, is asymmetric in shape with a dissociation limit on the right side (long bond distances). Meaning, a molecule should break apart if it absorbs enough energy. This asymmetry of the anharmonic potential leads to many consequences. For one, it can be seen that the energy levels are no longer evenly spaced. This means that the photons emitted from these higher energy levels are also not evenly spaced in frequency. This uneven spacing leads to a shift in the spectrum at higher temperatures and excitations. In contrast to that, in the harmonic approximation all photons emitted from the excited vibrational levels would fall (incorrectly) at the exact same frequency as the lowest state.

In addition to the potential being incorrect, the harmonic approximation has made another fatal error. The mathematics of the eigenvalue/eigenvector solution to the potential result in a series of orthogonal vibrational modes. This means the vibrational modes do not interact with one another; exciting one vibrational mode would have no effect on the other vibrational modes. However, this is not true in nature due to anharmonicities. When a molecule is excited (such as at high temperatures) the modes interact with one another and cause thermal shifts in the band position frequencies, and broadenings of the features themselves, as shown in figure 1.15. Additionally, *resonances* can occur between the vibrational

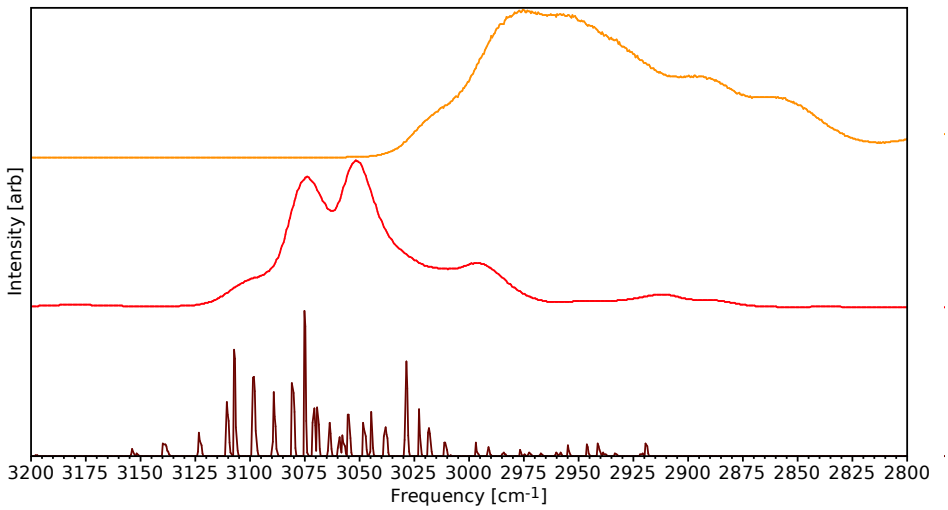

Figure 1.15 The anharmonic temperature dependent spectrum of the C–H stretching region of chrysene. Three temperatures are shown 100 K (brown), 1000 K (red), and 10,000 K (orange).

modes. If two vibrational modes are close to one another in frequency then they can begin to interact; much like how an opera singer can cause a wine glass to vibrate (resonate) with their voice making it shatter.

The exact nuclear potential of a molecule could be written as an infinite Taylor series around the equilibrium geometry

$$\begin{aligned} V = V_0 &+ \sum_i \left(\frac{\partial V}{\partial X_i}\right) X_i \\ &+ \frac{1}{2} \sum_i \sum_j \left(\frac{\partial^2 V}{\partial X_i \partial X_j}\right) X_i X_j \\ &+ \frac{1}{6} \sum_i \sum_j \sum_k \left(\frac{\partial^3 V}{\partial X_i \partial X_j \partial X_k}\right) X_i X_j X_k \\ &+ \frac{1}{24} \sum_i \sum_j \sum_k \sum_l \left(\frac{\partial^4 V}{\partial X_i \partial X_j \partial X_k \partial X_l}\right) X_i X_j X_k X_l \\ &+ \frac{1}{120} \sum_i \sum_j \sum_k \sum_l \sum_m \left(\frac{\partial^5 V}{\partial X_i \partial X_j \partial X_k \partial X_l \partial X_m}\right) X_i X_j X_k X_l X_m \\ &+ \ldots \end{aligned} \tag{1.4}$$

However, in order to account for the deficiencies of the harmonic approximation listed above, it is enough to retain only the first three non–zero terms of the equation. V_0 can be set to zero because it is arbitrary, and $\frac{\partial V}{\partial X_i}$ is zero because the Taylor

series is expanded about the minimum energy structure which is a stationary point on the PES. This leaves the terms with the second, third, and fourth partial derivatives. These partial derivatives are referred to as the quadratic, cubic, and quartic force constants respectively. These set of force constants together make up what is referred to as the quartic force field (QFF) of a molecule. To calculate the QFF, analytical 2^{nd} derivatives are computed along the normal coordinate displacements to numerically calculate the 3^{rd} and semi–diagonal 4^{th} derivatives.

Once calculated, the QFF can then be used to produce the anharmonic IR spectrum of a molecule. Unfortunately, this is not as easy as the harmonic case. A simple matrix cannot be constructed and diagonalized. Instead, a second order vibrational perturbation theory (VPT2) approach is necessary. In the VPT2 treatment, the potential is first solved using the quadratic force constants only, resulting in the harmonic solution. The harmonic solution is then altered with small corrections, or in other words is *perturbed*, using the cubic and quartic force constants.

The energies of the new perturbed states are then given as

$$E(\nu) = \sum_k \omega_k \left(n_k + \frac{1}{2}\right) + \sum_{k \le l} \chi_{kl} \left(n_k + \frac{1}{2}\right) \times \left(n_l + \frac{1}{2}\right) \tag{1.5}$$

where the ω_ks are the original harmonic frequencies, n_k are the number of quanta in the k^{th} vibrational mode (or the vibrational quantum numbers), and the χ_{kl}s are anharmonic constants.

The χ_{kl} values are calculated from the cubic and quartic force constant as follows

$$\chi_{kk} = \frac{1}{16}\phi_{kkkk} - \frac{1}{16}\sum_m (\phi_{kkm})^2 \times \left[\frac{8\omega_k^2 - 3\omega_m^2}{\omega_m\left(4\omega_k^2 - \omega_m^2\right)}\right] \tag{1.6}$$

and

$$\chi_{kl} = \frac{1}{4}\phi_{kkll} - \sum_m \frac{\phi_{kkm}\phi_{llm}}{4\omega_m} - \sum_m \frac{(\phi_{klm})^2\,\omega_m\left(\omega_k^2 + \omega_l^2 - \omega_m^2\right)}{2\Omega_{klm}} + \sum_\alpha B_\alpha^e \left(\zeta_{kl}^\alpha\right)^2 \times \left[\frac{\omega_k}{\omega_l} + \frac{\omega_l}{\omega_k}\right] \tag{1.7}$$

with

$$\Omega_{klm} = (\omega_k + \omega_l + \omega_m)(-\omega_k + \omega_l + \omega_m) \times (\omega_k - \omega_l + \omega_m)(\omega_k + \omega_l - \omega_m) \tag{1.8}$$

and

$$B_\alpha^e = \frac{h}{8\pi^2 c I_\alpha^e} \tag{1.9}$$

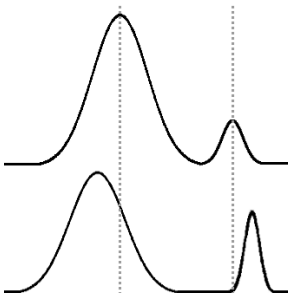

Figure 1.16 Two vibrational modes before resonance interactions (top), and after resonance interactions (bottom).

where ϕ_{xxx} and ϕ_{xxxx} are the cubic and quartic force constants respectively, ζ_{kl}^{α} are the Coriolis coupling constants, and I_{α}^{e} are the moments of inertia.

The energy difference for a given IR transition of mode k ($n_k \rightarrow n_k + 1$) is then given by

$$\Delta E^{(k)}(\{n\}) = \omega_k + 2\chi_{kk} + \frac{1}{2}\sum_{i\neq k}\chi_{ik} + 2\chi_{kk}n_k + \sum_{i\neq k}\chi_{ik}n_i \tag{1.10}$$

with the n_x values being the number of quanta in the x^{th} vibrational mode. It should be noted that these set of equations hold for asymmetric top molecules. However, since most PAHs do not have significant symmetry these equations suffice.

Looking closely at the equations for the χ values above it can be seen that many of the terms depend inversely on the difference between harmonic frequencies. If two harmonic frequencies, or the sum of two harmonic frequencies, are equal to another harmonic frequency then some of these denominators can end up close to zero. When this happens these terms become infinitely large. This occurrence is what is referred to as a resonance in the VPT2 treatment. Four types of resonance are possible: Coriolis, when two harmonic vibrational modes are approximately equal to one another; Darling–Dennison, when two harmonic overtones are approximately equal to one another; type one Fermi, when one harmonic frequency is approximately equal to a harmonic overtone; and type two Fermi, when one harmonic frequency is equal to the sum of two other harmonic frequencies. The VPT2 treatment as written is unable to handle these resonant terms, so the offending χ terms are removed completely, and a variational perturbation treatment is applied in order to account for these resonances.

In the variational treatment a resonance matrix is constructed, with the diagonal terms being the $E(v)$ terms of equation 7.3 with the offending χ terms removed, and the off–diagonal terms are the anharmonic coupling terms (given in reference 49). This matrix is diagonalized and the resulting eigenvalues are the new frequencies, and the square of the eigenvectors give the strength of the resonance between the modes and can be used to redistribute the intensity appropriately. Typically, the resonating IR features push each other apart in frequency, and the intensities are redistributed over both modes. (This will be discussed in more detail in the

following chapters.) Figure 1.16 shows a toy example of the effect that a resonance has on two spectral features.

Resonances do not usually occur in isolation, especially in large molecule like PAHs. A particular band may be involved simultaneously in many separate resonances (and in PAHs this can be hundreds). These simultaneous resonances cannot be treated separately, but instead must be treated in what is referred to as a *polyad*. The polyad is constructed similar to the variational matrix. Each frequency of the modes involved in the chain of resonances is again inserted into the diagonal of the matrix and the appropriate coupling terms of reference 49 again make up the off–diagonals. This polyad matrix is diagonalized, and the resulting eigenvalues and eigenvectors are handled in the same manner as before. Figure 1.4 shows the dramatic effect a polyad of resonances can have on an IR spectrum of a PAH. The appearance of the multitude of features in the blue trace compared to the red trace is directly due to resonances.

In addition to anharmonic corrections to the frequencies, anharmonic corrections to the intensities can also be made involving the QFF terms. The equations describing these anharmonic intensities are pages long, so for brevity are not shown here. See reference 50 for the full set of equations.

1.4 In this thesis

Linear transformation of anharmonic molecular force constants between normal and Cartesian coordinates (Chapter 2)

This particular chapter is a slight outlier from the rest of the thesis, but without it all of the following chapters would not be possible. As will be explained in the following chapters, resonances play a dominate role in the aromatic C–H stretching region of PAHs. The software available at the start of this research (Gaussian09[51]) was not adequately able to handle the large number of resonances that occur in PAHs in its VPT2 treatment. Therefore, it was necessary to bring in a second piece of software, called SPECTRO[52], which could handle these resonances. Unfortunately, the output of Gaussian09 and the input requirements of SPECTRO were not compatible. Gaussian09 outputted the QFF of the molecules in normal–coordinates, but SPECTRO required the QFF in Cartesian–coordinates.

A coordinate transformation method from normal–coordinates to Cartesian–coordinates does exist in the literature[53]. However, this transformation is non–linear and quite complex. While working through this transformation, we realized why it was so complex: it was missing the translation and rotation eigenvectors for the normal modes. If these eigenvectors were reconstructed, then the transformation is no longer non–linear, and all complex terms (i.e., Coriolis constants) drop to zero. This transformation then becomes as simple as inverting a matrix. The exact procedure for reconstructing these missing eigenvectors, and performing the transformation are described in detail in this chapter. Example applications are also given.

The anharmonic quartic force field infrared spectra of three Polycyclic Aromatic Hydrocarbons: naphthalene, anthracene, and tetracene (Chapter 3)

With the production of high–resolution gas–phase spectra of PAHs in the aromatic C–H stretching region, it was found that current theoretical methods (i.e., the harmonic approximation) could not reproduce the experimental results. Therefore, it was proposed that anharmonic corrections were necessary. Here we perform such theoretical corrections to a set of small linear PAHs: naphthalene, anthracene, and tetracene. We apply the QFF produced by Gaussian09 and VPT2 treatment of SPECTRO to test this hypothesis. This paper marks the first proper treatment of resonances incorporated into polyads for PAHs. Comparisons to experimental high–resolution gas–phase experimental spectra, low–resolution high–temperature spectra, and matrix isolation spectra were performed. It was found that anharmonicities, and resonances indeed play a major role especially in the C–H stretching region, particularly type–two Fermi resonances. Additionally, the features from 2000 – 1820 cm^{1-} (5.0 – 5.5 μm) (missing from harmonic calculations) were confirmed to be combination bands. Superior agreement between theory and experiment was achieved compared to previous harmonic calculations. All experimentally resolved IR bands are identified and characterized.

The anharmonic quartic force field infrared spectra of five non- linear Polycyclic Aromatic Hydrocarbons: benzanthracene, chrysene, phenanthrene, pyrene, and triphenylene (Chapter 4)

This chapter extends the methods applied in Chapter 3, to a larger set of non–linear PAHs. The effect anharmonicities and resonances have on the edge structure, symmetry and size are explored. Five PAHs were examined, benz[a]anthracene, chrysene, phenanthrene, pyrene, and triphenylene. Again, comparisons were made to experimental high–resolution gas–phase experimental spectra, low–resolution high–temperature spectra, and matrix isolation spectra. Agreement was found to within -0.13 ± 0.25%, 0.53 ±0.95%, and 0.41 ±0.63% respectively. A vast improvement over previous techniques. It was found again, that resonances dominate the C–H stretching region, especially for PAHs with low symmetry. This work solidifies the necessity of performing anharmonic calculations to reproduce accurately the IR spectra of PAHs. All experimentally resolved IR bands are identified and characterized.

The anharmonic quartic force field infrared spectra of hydrogenated and methylated PAHs (Chapter 5)

Aliphatic C–H stretching modes of functional–group additions to PAHs are thought to be responsible for the IR features observed at 3.40, 3.46, 3.51, and 3.56 μm (2941, 2890, 2850, and 2809 cm^{-1}) in interstellar PAH emissions. In our previous work, we showed how important anharmonic calculations, and proper treatment

of resonances are for the aromatic features in this region. This work explores the impact that anharmonic corrections have on these aliphatic features. Two methylated PAHs: 9–methylanthracene, and 9,10–dimethylanthracene; and four hydrogenated PAHs: 9,10–dihydroanthracene, 9,10–dihydrophenanthrene, 1,2,3,4–tetrahydronaphthalene, and 1,2,3,6,7,8–hexahydropyrene are examined. Comparisons to high–resolution gas–phase, and matrix isolation spectra are made. Changes to the basis/functional used are also made, showing great improvement in the agreement compared to our previous work. The agreement to the high–resolution data dropped to 0.00 ±0.17%, and the agreement to the matrix data dropped to -0.07 ±0.30%. Fermi resonances were found to continue to play a strong role in the C–H stretching region, even for the aliphatic modes. The changes to the spectra upon hydrogenation and methylation is also explored. All experimentally resolved IR bands are identified and characterized.

Accounting for large numbers of resonances in temperature dependent infrared spectra (Chapter 6)

The QFF used for the anharmonic IR spectra of molecules also allows for ab–initio calculations of temperature dependent band shifts, profiles, and broadenings. Proper resonance treatment has been shown to be crucial for reproducing the IR spectra of PAHs. Therefore, in order to reproduce the temperature dependent spectra of PAHs the incorporation of these resonances is necessary. In this chapter a new method of incorporating these resonances into a Wang–Landau biased Monte–Carlo walk is presented. It is shown that incorporating a resonance polyad at each step of the random walk can greatly affect the resulting spectrum, and is relatively simple. Additionally, an interesting temperature dependent resonance effect is shown for tetracene, whereby a combination band gains significant intensity through resonances at particular internal energies.

Fully anharmonic infrared cascade spectrum of polycyclic aromatic hydrocarbons (Chapter 7)

The processes involved in the IR emission spectrum of interstellar PAHs are complex. PAHs absorb a UV photon, then undergo an inter-conversion from an excited electronic state to their electronic ground state but with highly excited vibrational states, they then cool slowly through the emission of IR photons. To model accurately these IR cascade spectra, the temperature/energy dependent spectra must be calculated at each temperature visited by the PAHs as they cool. All methods and results of Chapters 2 through 6 are combined in this chapter to produce the full anharmonic theoretical IR cascade spectra of the PAHs. Anharmonic temperature dependence including the incorporation of polyads into the Wang–Landau method are used. The advantage of this random–walk method over more exact methods is shown and discussed. The effect that initial absorbed UV photon energies has on the cascade spectra is explored. It was found, contrary to previous studies, that the cascade features do not shift (as is expected for thermal equilibrium spectra). Rather, it is shown that the statistical nature of the cascade results

in cascade features that begin at their 0 Kelvin temperature, and only extend out along low energy wings whose length is determined by initial UV energies. The "pseudo-shifting" observed in the cascade features is found largely to be due to changes in intensities of lower frequency features as the long wings of their higher frequency neighbors slip underneath them. This misinterpretation of shifting from previous experimental and theoretical studies has led astronomers to incorrectly believe that *absorption* spectra of PAHs cannot be used to predict the cascade *emission* spectra of PAHs because of these shifts. Our results show this to be in error. Additionally, astronomers have applied shifts of 15 cm^{-1} to their interstellar PAH models to account for these non–existent shifts. Our study paves the way for a "simple" transformation from absorption spectra to emission spectra relevant for modeling observed interstellar PAH spectra.

1.5 Outlook

The James Webb Space Telescope will mark a new era for astronomy. Its predecessor, The Hubble Space Telescope, brought forth beauty and wonder never imagined before. JWST will continue this legacy with even higher spatial and spectral resolution. The amount of beauty and science JWST will produce will be truly astounding. This will also mark a new era for interstellar PAH research. JWST is specifically designed to peer into the infrared universe; coincidentally, the exact wavelength range which covers PAHs. The IR spectra returned to us will show such glorious details of the AIB (PAH) bands that we will be able to confirm (or refute) all of the previous fantastic science which relied on lower resolution instruments. JWST will also allow for new science too, and answer questions such as: What is the composition of the interstellar PAH family? Is there a wide variety of PAHs or just a handful of "grandPAHs"? What are the chemical processes that go into forming PAHs? Do fullerenes really form from PAHs? And perhaps most excitingly, first time we will be able to probe the chemical variations in regions of star and planet formation; and hence take the organic inventory of habitable zones. Truly, astronomers will be seeing the universe again through new rose (PAH) colored glasses.

Yet, without quality data here on Earth, the possibilities that these new observations would bring would indeed be overly optimistic. This thesis focused on improving the quality of the infrared spectrum of PAHs through the incorporation of anharmonicities. The comparisons to available experimental data show that we have indeed achieved this goal. Anharmonic calculations are shown to dramatically improve the theoretical IR spectra, as well as being crucial to understanding the 3.3, 3.4, and 5.5 μm astronomical IR features. In addition to this, this thesis has shown that the incorporation of resonances into temperature dependent spectra is both simple, and important. Lastly, we arrive at the anharmonic IR cascade models. Paradoxically, the results of this study both showed the complexity in producing fully anharmonic cascade spectrum, while at the same time hinted that it may be unnecessary for astrophysical purposes. However, these conclusions can be seen as complementary. Chemists and astrochemists who want to know the gritty

details, can apply these methods in full for a deeper understanding of PAHs, while the astronomers can happily apply the simplified conclusions to vastly improve their current models. With the results presented in this thesis, we can be confident that we ready for the deluge of IR data soon to be arriving from the James Webb Space Telescope.

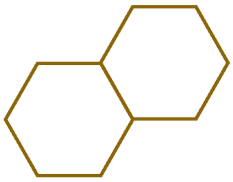

Linear transformation of anharmonic molecular force constants between normal and Cartesian coordinates

A full derivation of the analytic transformation of the quadratic, cubic, and quartic force constants from normal coordinates to Cartesian coordinates is given. Previous attempts at this transformation have resulted in non-linear transformations, however for the first time a simple linear transformation is presented here. Two different approaches have been formulated and implemented, one of which does not require prior knowledge of the translation-rotation eigenvectors from diagonalization of the Hessian matrix. The validity of this method is tested using two molecules H_2O and c-$C_3H_2D^+$.

Cameron J. Mackie, Alessandra Candian, Xinchuan Huang, Timothy J. Lee, Alexander G. G. M. Tielens

The Journal of Chemical Physics Volume 142, Issue 24, (2015)

2.1 Introduction

Over the past 25-30 years, quartic force fields (QFFs) have been used extensively to compute fundamental molecular vibrational frequencies, combination and overtone bands, and rovibrational spectroscopic constants (for example, see Refs. 54, 55, 56, 57, 58, 59, 60, 61 and references therein). QFFs have been used extensively in both second-order perturbation theory [62, 63, 64, 65] and variational treatments [66, 67, 68] to solve the bound-state nuclear Schrödinger equation. QFFs are usually computed in simple- or symmetry-internal coordinates and then transformed into either normal coordinates for perturbation theory analysis or some sort of Morse-cosine coordinate system for variational treatments. [69, 70] This allows one to compute the vibrational frequencies and rovibrational spectroscopic constants for all isotopologues. However, it was noted in a 1989 paper by Schneider and Thiel [71] that since the second-order perturbation theory formula only uses a subset of the quartic force constants in the normal coordinate basis, if one were to use central differences of analytical second derivative techniques, that many fewer displacements would be needed if displacements were made in normal coordinates, and only those quartic force constants needed were computed. One disadvantage to this approach is that since normal coordinates are mass-dependent, the resulting normal coordinate partial QFF will yield vibrational frequencies and rovibrational spectroscopic constants for only the isotopologue used to define the normal coordinates used to define the displacements.

Nonetheless, if one has the full or only a partial QFF in normal coordinates, there are good reasons to transform the QFF into Cartesian coordinates. For example, also in 1989, Thiel[53] showed how to transform the normal coordinate force constants into Cartesian coordinates in order to represent the QFF in simple internal or symmetry internal coordinates which may then be used in the spectroscopic analysis of an isotopologue or they may be transferred to molecular systems with a similar internal coordinate(s) in the approximate construction of a quadratic, cubic, or quartic force field of a larger molecule.

It has been shown in the literature that the transformation from Cartesian coordinate to normal coordinate force constants is a linear transformation [72]. However, the opposite transformation, from normal coordinate to Cartesian coordinate force constants, has until now only been dealt with in the literature as a non-linear transformation [53, 73]. The reason for the transformation to be thought as linear one way but non-linear the other way is due to the number of defined coordinates in the respective coordinate systems. The Cartesian coordinates that define the positions of the atoms in a molecule have 3N unique degrees of freedom (where N is the number of atoms) whereas normal coordinates that define the position of the atoms have 3N-6 coordinates (3N-5 in linear molecules). When moving from Cartesian coordinates to normal coordinates the loss of the six (five) degrees of freedom occurs because normal coordinates are defined in such a way that the origin of the coordinate system moves and rotates with the center of mass of the molecule, effectively eliminating the need for the six rotational and translational normal modes. This does not affect the transformation of the force constants from 3N Cartesian coordinates to 3N-6 normal coordinates since the loss

of the six extra degrees of freedom have no effect on the transformation. However, when transforming from normal coordinates to Cartesian coordinates the process involves going up from 3N-6 normal coordinates to 3N Cartesian coordinates. This increase in the number of coordinates was the reason for the need of the previous non-linear transformation.

The previously non-linear method, as mentioned above, involves the calculation of many terms including mixed partial derivatives of the second and third order (which themselves involve the calculation of another six additional sets of terms, including Coriolis constants). These terms arise precisely because the rotational and translational normal modes are not included in the transformation. This highly complicated non-linear transformation can be greatly simplified into a linear transformation if the rotational and translational normal modes are reintroduced. In this way all of the Coriolis terms and mixed partial derivatives become precisely zero, eliminating these non-linear terms in the previously derivation. This work outlines the method, effectively making the transformation from normal coordinate force constants to Cartesian coordinate force constants a simple linear 3N to 3N coordinate conversion. §2.2 shows the normal mode eigenvectors derivation as well as gives two methods to regenerate the missing translational and rotational normal mode eigenvectors. §2.3 derives the linear transformation equations for the conversion of the quadratic, cubic, and quartic force constants forwards and backwards between Cartesian and normal coordinates. §2.4 derives the partial derivatives needed in §2.3. §2.5 outlines two separate mathematical manipulations that can be implemented to speed up calculation time of the transformation. Finally §2.6 applies the transformation method described in this paper to two example molecules, H_2O and c-$C_3H_2D^+$, to show the validity of the method.

2.2 Derivation of the eigenvectors

The Hamiltonian for a molecule can be written using a Taylor expansion for the potential energy function as follows

$$\begin{aligned}\mathcal{H} = &-\frac{\hbar^2}{2}\sum_{a=1}^{3N}\frac{\partial^2}{\partial Y_a^2} + V_0 \\ &+ \sum_{a=1}^{3N}\left(\frac{\partial V}{\partial Y_a}\right)_0 Y_a \\ &+ \frac{1}{2}\sum_{a=1}^{3N}\sum_{b=1}^{3N}\left(\frac{\partial^2 V}{\partial Y_a \partial Y_b}\right)_0 Y_a Y_b + \cdots\end{aligned} \tag{2.1}$$

where the x,y,z coordinates of the atoms are numbered from 1 to 3N, and $Y_a = \sqrt{m_a}X_a$ is the mass-weighted Cartesian coordinate of a given atom

The harmonic approximation is made by retaining only the first non-vanishing term of its Taylor expansion (V_0 is arbitrary so it is set to zero and since the Taylor

expansion is taken at a stationary point any gradients are also zero).

$$\mathcal{H} = -\frac{\hbar^2}{2}\sum_{a=1}^{3N}\frac{\partial^2}{\partial Y_a^2} + \frac{1}{2}\sum_{a=1}^{3N}\sum_{b=1}^{3N}\left(\frac{\partial^2 V}{\partial Y_a \partial Y_b}\right)_0 Y_a Y_b \tag{2.2}$$

To solve for the normal mode eigenvalues (frequencies) of the molecule the mass-weighted Hessian is diagonalized by

$$\boldsymbol{\Omega}^T \boldsymbol{F} \boldsymbol{\Omega} = \boldsymbol{f} \tag{2.3}$$

where $\boldsymbol{F}_{(a,b)}$ is the mass-weighted Hessian that consists of the second order derivatives of the potential energy

$$F_{a,b} = \left(\frac{\partial^2 V}{\partial Y_a \partial Y_b}\right)_0 \tag{2.4}$$

and $\boldsymbol{f} = diag(f_1, f_2, ..., f_{3N-6}, 0, 0, 0, 0, 0, 0)$ are the frequencies of the normal modes.

The last six zero frequencies correspond to the rotational and translational modes of the non-linear molecule at its stationary point. The columns that make up the $\boldsymbol{\Omega}$ matrix are the normal mode eigenvectors $\boldsymbol{\omega}$ expressed in mass-weighted Cartesian coordinates. The last six columns correspond to the translational and rotational eigenvectors, but in reality can be linear combinations of these six eigenvectors and as such may not be easily visualized.

Generally only the non-zero frequency modes of the $\boldsymbol{\Omega}$ matrix and their corresponding eigenvectors $\boldsymbol{\omega}$ are reported in the literature or in the default output of computational packages. The rotational and translational eigenvectors are normally dropped, resulting in only the non-zero 3N-6 normal modes (3N-5 for linear molecules) being reported. However, these six (five) normal mode eigenvectors are needed to make the transformation from normal coordinate to Cartesian coordinate force constants linear. In such cases the translational and rotational eigenvectors can be regenerated by re-diagonalizing the mass-weighted Hessian as in equation 2.3, or by explicitly regenerating the missing mass-weighted eigenvectors as shown below. Note that when regenerating the six 'missing' eigenvectors as shown in this work, they will represent the pure rotational and translational eigenvectors and will be easily visualized as such, unlike the linearly combined eigenvectors that result from the numerical re-diagonalization method. It should be noted that the resulting individual Cartesian coordinate force constants obtained with these two methods may differ due to the degenerate nature of Cartesian coordinates, but will produce Cartesian coordinate force constants that are equivalent when taken as full sets. There are two sources of degeneracy when it comes to Cartesian force constants: One being the arbitrary orientation and position chosen for the molecule in the Cartesian plane, the other being the infinite number of linear combinations of the rotational and translational eigenvectors. One should also be cautious when re-diagonalizing the Hessian of a molecule with degenerate modes. The eigenvectors for degenerate vibrational modes can be arbitrarily rotated amongst each other which will give different self-consistent cubic and quartic force constants. Hence, if re-diagonalizing, one needs to ensure degenerate modes are aligned the

way they were when the normal coordinate force constants were generated. For this reason it would be advantageous to use the regeneration method for molecules with degenerate modes.

The missing eigenvectors can be regenerated using the methods extracted from Ref. 74. The translational eigenvectors can be written as follows

$$\boldsymbol{\omega}_{(3N-5)} = [\sqrt{m_1}, 0, 0, \sqrt{m_2}, 0, 0, \ \ldots\ , \sqrt{m_N}, 0, 0] \tag{2.5}$$

$$\boldsymbol{\omega}_{(3N-4)} = [0, \sqrt{m_1}, 0, 0, \sqrt{m_2}, 0, \ \ldots\ , 0, \sqrt{m_N}, 0] \tag{2.6}$$

$$\boldsymbol{\omega}_{(3N-3)} = [0, 0, \sqrt{m_1}, 0, 0, \sqrt{m_2}, \ \ldots\ , 0, 0, \sqrt{m_N}] \tag{2.7}$$

The rotation eigenvectors components can be written as follows

$$\omega_{(3N-2)_{j,i}} = \left[(P_y)_i D_{j,3} - (P_z)_i D_{j,2}\right] \times \sqrt{m_i} \tag{2.8}$$

$$\omega_{(3N-1)_{j,i}} = \left[(P_z)_i D_{j,1} - (P_x)_i D_{j,3}\right] \times \sqrt{m_i} \tag{2.9}$$

$$\omega_{(3N)_{j,i}} = \left[(P_x)_i D_{j,2} - (P_y)_i D_{j,1}\right] \times \sqrt{m_i} \tag{2.10}$$

where $\mathbf{D}$ is the matrix that diagonalizes the moment of inertial tensor and $\mathbf{P}_x$, $\mathbf{P}_y$, $\mathbf{P}_z$ are defined as

$$\mathbf{P}_x = [\mathbf{X}_1 \cdot \mathbf{D}_x, \mathbf{X}_2 \cdot \mathbf{D}_x, \ \ldots\ , \mathbf{X}_n \cdot \mathbf{D}_x] \tag{2.11}$$

$$\mathbf{P}_y = [\mathbf{X}_1 \cdot \mathbf{D}_y, \mathbf{X}_2 \cdot \mathbf{D}_y, \ \ldots\ , \mathbf{X}_n \cdot \mathbf{D}_y] \tag{2.12}$$

$$\mathbf{P}_z = [\mathbf{X}_1 \cdot \mathbf{D}_z, \mathbf{X}_2 \cdot \mathbf{D}_z, \ \ldots\ , \mathbf{X}_n \cdot \mathbf{D}_z] \tag{2.13}$$

where $\mathbf{X}_n$ is the Cartesian coordinate vector of the n^{th} atom, and $\mathbf{D}_\alpha$ is the α^{th} row of the $\mathbf{D}$ matrix.

All of the eigenvectors are then normalized to produce an orthonormal set of 3N eigenvectors $\boldsymbol{\Omega}$. Note that in the linear molecule case one of the rotational eigenvectors will come out as the zero vector, and should be dropped.

2.3 Derivation of the transformations equations

In the quartic force field approximation the potential energy of the Hamiltonian takes the form of the first three non-zero terms in its Taylor expansion

$$\begin{aligned}\mathcal{H} = &-\frac{\hbar^2}{2}\sum_{a=1}^{3N}\frac{\partial^2}{\partial Y_a^2} + \frac{1}{2}\sum_{a=1}^{3N}\sum_{b=1}^{3N}\left(\frac{\partial^2 V}{\partial Y_a \partial Y_b}\right)_0 Y_a Y_b \\ &+ \frac{1}{6}\sum_{a=1}^{3N}\sum_{b=1}^{3N}\sum_{c=1}^{3N}\left(\frac{\partial^3 V}{\partial Y_a \partial Y_b \partial Y_c}\right)_0 Y_a Y_b Y_c \\ &+ \frac{1}{24}\sum_{a=1}^{3N}\sum_{b=1}^{3N}\sum_{c=1}^{3N}\sum_{d=1}^{3N}\left(\frac{\partial^4 V}{\partial Y_a \partial Y_b \partial Y_c \partial Y_d}\right)_0 Y_a Y_b Y_c Y_d\end{aligned} \tag{2.14}$$

Instead of solving this Hamiltonian directly, second-order perturbation theory is often used. The quadratic force constants are used in the unperturbed harmonic terms, the cubic force constants are used in the first term of the perturbation, and the quartic force constants are used in the second term of the perturbation. Therefore it will be shown how to transform these three orders of force constants between normal and Cartesian coordinates. It will also be easy to see how the transformations can be extended to any number of orders. In order to convert the force constants between the two coordinate systems, the Taylor expansions of the potential in each coordinate system are considered. The potential energy function in Cartesian coordinates is given by

$$\begin{aligned}V_{cart} = &\frac{1}{2}\sum_{a=1}^{3N}\sum_{b=1}^{3N} F_{ab} X_a X_b \\ &+ \frac{1}{6}\sum_{a=1}^{3N}\sum_{b=1}^{3N}\sum_{c=1}^{3N} F_{abc} X_a X_b X_c \\ &+ \frac{1}{24}\sum_{a=1}^{3N}\sum_{b=1}^{3N}\sum_{c=1}^{3N}\sum_{d=1}^{3N} F_{abcd} X_a X_b X_c X_d\end{aligned} \tag{2.15}$$

where F_{ab}, F_{abc} and F_{abcd} the Cartesian quadratic, cubic, and quartic force constants respectively.

Likewise, the potential energy function in normal coordinates is given by

$$\begin{aligned}V_{norm} = &\frac{1}{2}\sum_{k=1}^{3N}\sum_{l=1}^{3N} \Phi_{kl} Q_k Q_l \\ &+ \frac{1}{6}\sum_{k=1}^{3N}\sum_{l=1}^{3N}\sum_{m=1}^{3N} \Phi_{klm} Q_k Q_l Q_m \\ &+ \frac{1}{24}\sum_{k=1}^{3N}\sum_{l=1}^{3N}\sum_{m=1}^{3N}\sum_{n=1}^{3N} \Phi_{klm} Q_k Q_l Q_m Q_n\end{aligned} \tag{2.16}$$

where Φ_{kl}, Φ_{klm} and Φ_{klmn} are the normal coordinate quadratic, cubic, and quartic force constants respectively.

Since the total potential energy of a molecule is independent of the coordinate system used, it can be written that

$$V_{cart} = V_{norm} \tag{2.17}$$

Subsequently, all derivatives of the total potential energy in any two different coordinate systems with respect to *same coordinate system* are also equal.

Taking the second derivatives of equations 2.15 and 2.16 with respect to X_a and X_b gives the following:

$$\begin{aligned}\left(\frac{\partial^2 V_{cart}}{\partial X_a \partial X_b}\right) &= \frac{1}{2}F_{ab} + \frac{1}{2}F_{ba} \\ &= F_{ab}\end{aligned} \tag{2.18}$$

and

$$\begin{aligned}\left(\frac{\partial^2 V_{norm}}{\partial X_a \partial X_b}\right) &= \frac{1}{2}\sum_{k=1}^{3N}\sum_{l=1}^{3N}\Phi_{kl}\left[\frac{\partial Q_k}{\partial X_a}\frac{\partial Q_l}{\partial X_b} + \frac{\partial Q_k}{\partial X_b}\frac{\partial Q_l}{\partial X_a}\right. \\ &\quad \left. + \frac{\partial^2 Q_k}{\partial X_a \partial X_b}Q_l + \frac{\partial^2 Q_l}{\partial X_a \partial X_b}Q_k\right] \\ &= \sum_{k=1}^{3N}\sum_{l=1}^{3N}\Phi_{kl}\left[\frac{\partial Q_k}{\partial X_a}\frac{\partial Q_l}{\partial X_b}\right]\end{aligned} \tag{2.19}$$

respectively.

When expressions 2.18 and 2.19 are equated it gives the transformation equation for going from normal coordinates to Cartesian coordinates for the quadratic force constant terms. A similar procedure is performed on equations 2.15, and 2.16, but with a third derivative with respect to X_c, and a third and forth derivative with respect to X_c and X_d respectively, to give the following set of transformations.

$$F_{ab} = \sum_{k=1}^{3N}\sum_{l=1}^{3N}\Phi_{kl}\left[\frac{\partial Q_k}{\partial X_a}\frac{\partial Q_l}{\partial X_b}\right] \tag{2.20}$$

$$F_{abc} = \sum_{k=1}^{3N}\sum_{l=1}^{3N}\sum_{m=1}^{3N}\Phi_{klm}\left[\frac{\partial Q_k}{\partial X_a}\frac{\partial Q_l}{\partial X_b}\frac{\partial Q_m}{\partial X_c}\right] \tag{2.21}$$

$$F_{abcd} = \sum_{k=1}^{3N}\sum_{l=1}^{3N}\sum_{m=1}^{3N}\sum_{n=1}^{3N}\Phi_{klmn}\left[\frac{\partial Q_k}{\partial X_a}\frac{\partial Q_l}{\partial X_b}\frac{\partial Q_m}{\partial X_c}\frac{\partial Q_n}{\partial X_d}\right] \tag{2.22}$$

Note that the summations are over all of the 3N normal modes, including translational and rotational modes. If the translational and rotational modes were neglected then the higher order mixed derivatives (not shown here) would be non-zero, resulting in the non-linear transformation mentioned above.

The derivation for the opposite transformation, going from Cartesian to normal coordinate force constants, is the same procedure as above except the derivatives are taken with respect to Q_k, Q_l, Q_m, and Q_n. This gives

$$\Phi_{kl} = \sum_{a=1}^{3N}\sum_{b=1}^{3N} F_{ab}\left[\frac{\partial X_a}{\partial Q_k}\frac{\partial X_b}{\partial Q_l}\right] \tag{2.23}$$

$$\Phi_{klm} = \sum_{a=1}^{3N}\sum_{b=1}^{3N}\sum_{c=1}^{3N} F_{abc}\left[\frac{\partial X_a}{\partial Q_k}\frac{\partial X_b}{\partial Q_l}\frac{\partial X_c}{\partial Q_m}\right] \tag{2.24}$$

$$\Phi_{klmn} = \sum_{a=1}^{3N}\sum_{b=1}^{3N}\sum_{c=1}^{3N}\sum_{d=1}^{3N} F_{abcd}\left[\frac{\partial X_a}{\partial Q_k}\frac{\partial X_b}{\partial Q_l}\frac{\partial X_c}{\partial Q_m}\frac{\partial X_d}{\partial Q_n}\right] \tag{2.25}$$

2.4 Deriving the partial derivatives

The derivatives in equations 2.20 through 2.25 are generated from the 3N normal mode eigenvectors. First the mass weighting of the eigenvector matrix, $\mathbf{\Omega}$, is removed and each column vector is re-normalized

$$\bar{\mathbf{\Omega}} = \left(\mathbf{M}^{-\frac{1}{2}}\mathbf{\Omega}\right)\mathbf{\Lambda} \tag{2.26}$$

where $\mathbf{M} = diag(m_1, m_2, ..., m_N)$ and $\mathbf{\Lambda}$ is a diagonal matrix containing the normalization factor for each respective mass-unweighted eigenvector.

Each normal mode vector $\boldsymbol{\omega}_N$ which are the components of $\bar{\mathbf{\Omega}}$ is then divided by the square root of its reduced mass μ_N

$$\tilde{\mathbf{\Omega}} = \bar{\mathbf{\Omega}}\boldsymbol{\mu}^{-\frac{1}{2}} \tag{2.27}$$

where $\boldsymbol{\mu} = diag(\mu_1, \mu_2, ..., \mu_N)$ with

$$\mu_N = \sum_i m_{N,i}\omega_{N,i}^2 \tag{2.28}$$

where $\omega_{N,i}$ is the i^{th} component of eigenvector $\boldsymbol{\omega}_N$ and $m_{N,i}$ is the corresponding mass of i^{th} component of eigenvector $\boldsymbol{\omega}_N$

This matrix $\tilde{\mathbf{\Omega}}$ is then a matrix of the values of the partial derivatives in equations 2.23 through 2.25 that are needed for the transformation from Cartesian to normal coordinate force constants.

$$\frac{\partial X_b}{\partial Q_l} = \tilde{\Omega}_{b,l} \tag{2.29}$$

The inverse of this matrix is then a matrix of the values of the partial derivatives in equations 2.20 through 2.22 that are needed for the transformation from normal coordinate to Cartesian coordinate force constants.

$$\frac{\partial Q_l}{\partial X_b} = \tilde{\Omega}^{-1}_{b,l} = \check{\Omega}_{l,b} \tag{2.30}$$

To reduce computational demand it is also possible to take advantage of the fact that the matrix $\bar{\mathbf{\Omega}}$ is orthonormal, which means $\bar{\mathbf{\Omega}}^{-1} = \bar{\mathbf{\Omega}}^T$. This can be used to avoid taking the inverse of the potentially large non-orthonormal $3N \times 3N$ matrix as is stated in equation 2.30. $\check{\mathbf{\Omega}}$ can instead be expressed as follows

$$\begin{aligned} \check{\mathbf{\Omega}} &= \tilde{\mathbf{\Omega}}^{-1} \\ &= \left(\bar{\mathbf{\Omega}}\boldsymbol{\mu}^{-\frac{1}{2}}\right)^{-1} \\ &= \boldsymbol{\mu}^{\frac{1}{2}}\bar{\mathbf{\Omega}}^{-1} \\ &= \boldsymbol{\mu}^{\frac{1}{2}}\bar{\mathbf{\Omega}}^{T} \end{aligned} \tag{2.31}$$

Both the inverse and transpose methods, equations 2.30 and 2.31 respectively, have been verified as numerically equivalent.

Furthermore, it can now be seen why the transformation from normal coordinate force constants to Cartesian coordinate force constants had previously been thought of as a non-linear transformation. Without the six additional rotational and translational normal modes added back into the $\mathbf{\Omega}$ matrix it is not possible to perform a standard inverse on the previously non-square $3N \times (3N - 6)$ normal mode matrix.

2.5 Implementation details

These transformations can be quite computationally demanding, especially with large molecules, since they are converting $(3N)^4$ values for the quartic force terms. To avoid nested summations the conversion equations can be broken up into a series of sequential summations. We thus have for the quadratic force constants:

$$F_{aj} = \sum_{i=1}^{3N} \check{\Omega}_{a,i} Q_{i,j} \tag{2.32}$$

$$F_{ab} = \sum_{j=1}^{3N} \check{\Omega}_{b,j} F_{a,j} \tag{2.33}$$

for the cubic force constants:

$$F_{ajk} = \sum_{i=1}^{3N} \check{\Omega}_{a,i} Q_{i,j,k} \tag{2.34}$$

$$F_{abk} = \sum_{j=1}^{3N} \check{\Omega}_{b,j} F_{a,j,k} \tag{2.35}$$

$$F_{abc} = \sum_{k=1}^{3N} \check{\Omega}_{c,k} F_{a,b,k} \tag{2.36}$$

and for the quartic force constants:

$$F_{ajkl} = \sum_{i=1}^{3N} \check{\Omega}_{a,i} Q_{i,j,k,l} \tag{2.37}$$

$$F_{abkl} = \sum_{j=1}^{3N} \check{\Omega}_{b,j} F_{a,j,k,l} \tag{2.38}$$

$$F_{abcl} = \sum_{k=1}^{3N} \check{\Omega}_{c,k} F_{a,b,k,l} \tag{2.39}$$

$$F_{abcd} = \sum_{l=1}^{3N} \check{\Omega}_{d,l} F_{a,b,c,l} \tag{2.40}$$

where $F_{a,\ldots,j,\ldots}$ are the intermediate mixed normal-Cartesian coordinate force constants calculated from the previous step.

2.6 Application to H_2O and c-$C_3H_2D^+$

In this section the linear transformation method described in this paper is tested on two molecules H_2O and c-$C_3H_2D^+$. Cartesian coordinate force constants are not unique for a given molecule (due to the infinite number of valid translational and rotational eigenvector sets) so direct comparison of the individual Cartesian force constants is not possible between different references. Instead two tests can be applied to check the validity of the transformation method. The first test is a forward transformation of the force constants from normal to Cartesian coordinates followed by a backwards transformation to obtain the same original values. The second test would use a set of reference force constants that were numerically calculated in both normal coordinates and Cartesian coordinates, transform the normal coordinate force constants to Cartesian coordinates, and then perform a second-order perturbation treatment using the original Cartesian force constants and finally comparing the results with a second-order perturbation treatment using the transformed Cartesian coordinates.

The first test was performed on the H_2O molecule. Table 2.1 lists the full non-zero set of the original normal coordinate force constants of H_2O as reported by Gaussian09[51] (B3LYP/4-31G) and the transformed values for each of the methods: the explicitly regeneration of the rotational and translational eigenvectors method (explicit), and the re-diagonalization of the Hessian method (re-diag). Six significant digits are available for the normal mode eigenvectors calculated by Gaussian09, and so are the limiting numerical factor in these transformations. It can therefore be seen that the resulting values from these tests all agree within the

Normal coordinate quadratic force constants			
I,J	Gaussian09	Explicit	Re-diag
1,1	0.588920	0.5889195204	0.5889195204
2,2	0.556360	0.5563597083	0.5563597083
3,3	0.103107	0.1031073853	0.1031073853
Normal coordinate cubic force constants			
I,J,K	Gaussian09	Explicit	Re-diag
2,1,1	-1.537841	-1.5378412008	-1.5378412008
2,2,2	-1.494314	-1.4943140745	-1.4943140745
3,1,1	0.147698	0.1476983577	0.1476983577
3,2,2	0.041158	0.0411582366	0.0411582366
3,3,2	0.109423	0.1094229743	0.1094229743
3,3,3	-0.061993	-0.0619934648	-0.0619934648
Normal coordinate quartic force constants			
I,J,K,L	Gaussian09	Explicit	Re-diag
1,1,1,1	3.743561	3.7435605526	3.7435605526
2,2,1,1	3.604032	3.6040318012	3.6040318012
2,2,2,2	3.484090	3.4840896130	3.4840896130
3,2,1,1	-0.366798	-0.3667977452	-0.3667977452
3,2,2,2	-0.191875	-0.1918745935	-0.1918745935
3,3,1,1	-0.755795	-0.7557945848	-0.7557945848
3,3,2,2	-0.611669	-0.6116693020	-0.6116693020
3,3,3,2	0.201451	0.2014514506	0.2014514506
3,3,3,3	-0.051939	-0.0519393906	-0.0519393906

Table 2.1 Non-zero normal coordinate force constants of H_2O before and after transformation from normal force constants and back to Cartesian coordinate force constants using the two methods for obtaining the missing eigenvectors, explicitly regenerating the rotational and translational eigenvectors, and re-diagonalizing the Hessian.

numerical accuracy available. The 'explicit' and 're-diag' values are reported to ten decimal places to show agreement between the two transformation methods.

For the second test the c-$C_3H_2D^+$ QFF, as described in reference 75, is used. They calculated both the Cartesian coordinate and normal coordinate force constants and supplied those values for this paper. Three sets of Cartesian force constants are used for this test: the original Cartesian force constants from reference 75 are used as reference, the 'explicit' transformation method of this work using the normal coordinate QFF of reference 75, and finally the Hessian 're-diag' transformation method of this work using the normal coordinate QFF of reference 75. Each of these sets of Cartesian coordinate force constants is used to perform a second-order perturbation theory (VPT2) analysis using SPECTRO[52]. All values should agree between the reference of reference 75 and the two VPT2 methods using the transformation here presented. Table 2.2 shows the resulting band positions and the resonances obtained by SPECTRO. Again, it can be seen that all values match within numerical accuracy. The position of the fundamental modes and spectroscopic constants obtained with the VPT2 implementation also agree, with numerical accuracy, between the reference and transformation method values.

These two tests show that the transformation has indeed been performed successfully from normal coordinate force constants to Cartesian coordinate force constants.

Mode	Ref.	Explicit	Re-diag
1	3170.36	3170.354	3170.354
4(2)	3137.34	3137.337	3137.337
2	3131.56	3131.562	3131.562
5(2)	2583.82	2583.820	2583.820
6(2)	2540.87	2540.869	2540.869
3	2388.12	2388.117	2388.117
5 + 7	2301.88	2301.874	2301.874
7 + 11	1734.36	1734.364	1734.364
4	1578.66	1578.660	1578.660
11(2)	1433.93	1433.928	1433.928
12(2)	1310.36	1310.360	1310.360
5	1293.31	1293.312	1293.312
6	1274.20	1274.198	1274.198
7	1015.48	1015.475	1015.475
8	1004.66	1004.658	1004.658
9	921.28	921.2834	921.2834
10	916.47	916.4719	916.4719
11	719.23	719.2262	719.2262
12	655.05	655.0473	655.0473

Table 2.2 The wavenumbers [cm^{-1}] of the bands and resonances resulting from the second-order perturbation theory treatment of c-$C_3H_2D^+$ calculated using three different Cartesian force constants: Originally calculated (Ref. 75), converted from normal coordinate force constants using explicit regeneration method (this work), and converted from normal coordinate force constants using re-diagonalization method (this work).

2.7 Conclusions

It has been shown that the transformation from normal coordinates to Cartesian coordinates (and vice versa) can be made linear through the re-introduction of the translational and rotational eigenvectors. This method eliminates the need to calculate mixed derivatives as in the non-linear procedure. Two methods for re-generating these eigenvectors are presented, one from the re-diagonalization of the mass-weighted Hessian and one from a series of equations to explicitly reconstruct the missing rotational and translational eigenvectors. These two methods avoid the complicated non-linear transformation that that arises if the rotational and translational normal mode eigenvectors are neglected. Application of the two new approaches to the H_2O and c-$C_3H_2D^+$ molecules has been performed to validate the equations and implementation.

Acknowledgments

Helpful discussions with David Schwenke, Joel Bowman, and Walter Thiel are gratefully acknowledged by the authors of this work. Studies of interstellar chemistry at Leiden Observatory that are supported through advanced European Research Council grant 246976 and a Spinoza award. XH and TJL gratefully acknowledge support from the NASA 12-APRA12-0107 grant. XH acknowledges the support from NASA/SETI Co-operative Agreement NNX12AG96A. The calculations were performed at the SARA supercomputer center in Almere (NL) under

project MP-270-13.

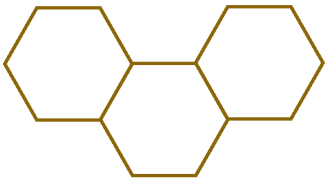

The anharmonic quartic force field infrared spectra of three Polycyclic Aromatic Hydrocarbons: naphthalene, anthracene, and tetracene

Current efforts to characterize and study interstellar polycyclic aromatic hydrocarbons (PAHs) rely heavily on theoretically predicted infrared (IR) spectra. Generally, such studies use the scaled harmonic frequencies for band positions and double harmonic approximation for intensities of species, and then compare these calculated spectra with experimental spectra obtained under matrix isolation conditions. High-resolution gas-phase experimental spectroscopic studies have recently revealed that the double harmonic approximation is not sufficient for reliable spectra prediction. In this paper, we present the anharmonic theoretical spectra of three PAHs: naphthalene, anthracene, and tetracene, computed with a locally modified version of the SPECTRO program using Cartesian derivatives transformed from Gaussian 09 normal coordinate force constants. Proper treatments of Fermi resonances lead to an impressive improvement on the agreement between the observed and theoretical spectra, especially in the C–H stretching region. All major IR absorption features in the full–scale matrix–isolated spectra, the high–temperature gas–phase spectra, and the most recent high–resolution gas–phase spectra obtained under supersonically-cooled molecular beam conditions in

the CH–stretching region, are assigned.

Cameron J. Mackie, Alessandra Candian, Xinchuan Huang, Elena Maltseva, Annemieke Petrignani, Jos Oomens, Wybren Jan Buma, Timothy J. Lee, Alexander G. G. M. Tielens
The Journal of Chemical Physics
Volume 143, Issue 22, (2015)

3.1 Introduction

Polycyclic aromatic hydrocarbon (PAH) molecules are a family of molecules consisting of two or more fused benzenoid rings with hydrogen atoms capped around the free edges. These molecules are very stable and participate in many reactions, which make them an attractive focus for various physics/chemistry research areas. For example, they serve as model compounds for innovative carbon-based materials, such as nanotubes and graphene[5, 6, 7]; their carcinogenic properties make them widely studied pollutants of water, air and even food[3]; and they are common by–products of both natural and anthropogenic pyrolysis and combustion [1, 2].

While ubiquitous and abundant on the Earth, PAHs are also of special interest to astronomers, as they are potentially responsible for the so–called Aromatic Infrared Bands (AIBs) [26, 27]. These bands have been observed in the IR spectrum of a variety of astrophysical environments: from young stellar objects, to planetary and reflection nebulae, to the diffuse interstellar medium, even in the emissions from entire galaxies[76]. PAHs may be formed in outflows of aging stars and their ubiquity and abundance lead to an estimate that PAH molecules lock up 10-20% of the cosmic carbon and are responsible for 30% of the IR emissions found in galactic observations [76]. Experimentalists and theoreticians have been working hand in hand to study the PAH IR spectroscopy as a means to identify relevant molecular structures and to use them as a tool to characterize the physical and chemical conditions in various astrophysical environments.

Experimental IR spectra have been reported for many PAHs[21, 77, 78, 79, 80, 81, 82, 83]. However due to the involatile nature of PAHs, low–temperature high–resolution spectra (as needed to understand the molecular physics involved in order to compare with astronomical observations) are difficult to produce. Most experimental spectra were acquired using low–temperature matrix–isolation techniques or high–temperature gas–phase spectroscopy. The matrix–isolation spectra suffer from the interaction with the matrix environment and are subject to hard to predict changes in line positions, intensities, band profiles, and even band splittings[84]. Likewise, for the high–temperature gas–phase spectra, temperature effects can mask underlying physics and make extrapolations to low temperatures difficult. For example, in a 2009 study by Pirali et al[85], the room temperature high-resolution rovibrational spectrum of naphthalene was presented, and most of the analysis in which was aimed at understanding the multiple bands in the low energy spectrum region, i.e., 400–900 cm^{-1}, due to temperature effects. Other issues, including contaminations originating from isotopologues and other PAH species, may further complicate the acquired spectra and analysis.

The difficulties in obtaining and understanding the IR spectrum of PAHs has led to an ever–increasing reliance on computational quantum chemistry. Computational chemistry approaches have been used to explain the IR spectrum of large ($N_C \geq 50$), astronomically–relevant PAHs. In this context it is important to note that databases of the theoretical PAH spectra have been created and available online [33, 48]. Previous computations were typically performed within the framework of Density Functional Theory (DFT), employing the B3LYP functional with

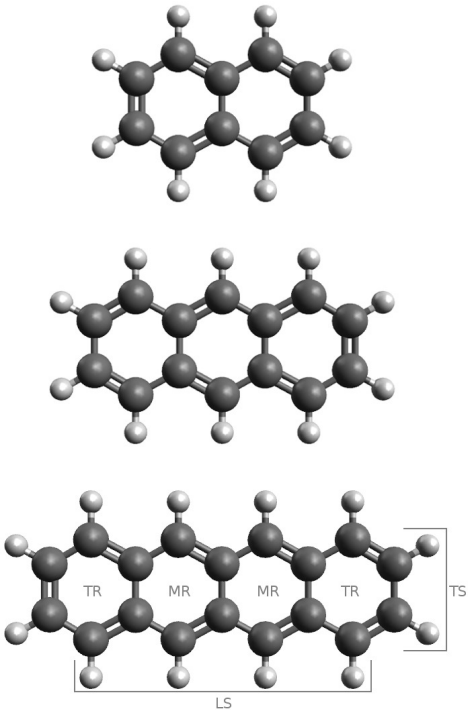

Figure 3.1 From top to bottom: naphthalene, anthracene, and tetracene. The rings are designated as either terminal ring (TR), or middle ring (MR). The side CH groups are designated as either terminal side CH groups (TS) or long side CH groups (LS). The designations are used for the vibrational mode descriptions in Appendix 3.6.

a small basis set (e.g. 4–31G). The double harmonic approximation is used for vibrational IR intensities. A scaling factor is used to down–scale the calculated harmonic frequencies to match with matrix–isolation experimental features [86]. As a first-order approximation, this approach has been successful enough in reproducing the overall IR spectrum of certain individual PAHs roughly, but serious problems persist when comparing it with high–resolution experiments. Specifically, the IR features in the C–H stretching region are poorly modeled using the harmonic level analysis, which include scaled harmonic frequencies and double harmonic intensities. This is most likely due to phenomena such as mode couplings and resonances that are not described at the harmonic level.

The most recent Gaussian 09 [51] release contains an improved module for second-order vibrational perturbations theory (VPT2) anharmonic analysis of molecules, thus enabling a VPT2-based IR spectrum simulation of PAHs. In this work

we make use of this module, and enhance its VPT2 analysis by additional treatments on vibrational state resonances, as will be described below. The anharmonic IR spectra of the three smallest linear PAHs, naphthalene ($C_{10}H_8$), anthracene ($C_{14}H_{10}$) and tetracene ($C_{18}H_{12}$) (see Fig. 5.1) are computed and compared with the currently available low resolution high–temperature gas–phase[21] (NIST), and argon matrix–isolation spectra[78] (MIS). Moreover, we present low–temperature high–resolution gas–phase experimental IR absorption spectra of the three PAHs (first presented in an astrophysical companion paper to this work[22]), which allows for the most direct comparison with theory possible and thus provides validation for our approach.

The article is built up in the following way. Section 7.2 briefly describes the theory behind the anharmonic calculations. Section 6.4 provides a description of the computational methods and programs that are used to perform the theoretical calculations. Section 3.3.2 describes the experimental methods for producing the gas–phase IR absorption spectra in the CH–stretching region. The results are arranged into two subsections: a comparison of the full anharmonic IR spectra with NIST and MIS data (Section 3.4.1), and an in–depth comparison of the calculated CH–stretching region with low–temperature high–resolution gas–phase experimental spectra (Section 3.4.2). Three subsections are presented in Discussion: Sections 3.5.1, 5.4.1, for 3.4.1 and 3.4.2, respectively, plus Section 5.4.5 for astrophysical implications. Conclusions follow at the end.

3.2 Theory

Theoretical predictions of the vibrational IR spectrum of molecules are most often performed at the harmonic level. If the geometry of a stationary point of a molecule is known, then the vibrational potential can be approximated as a simple pairwise interaction between atoms, akin to Hooke's law (see Ref. 72 for a complete description).

$$V = \frac{1}{2} \sum_{i=1}^{3N} \sum_{j=1}^{i} F_{ij} X_i X_j \tag{3.1}$$

where V is the total vibrational potential, $F_{ij} = \frac{\partial V}{\partial X_i \partial X_j}$ are the quadratic force constants (spring constant k_{ij} in Hooke's Law) between atoms i and j, and X_i and X_j are the Cartesian coordinates of atom i and j relative to the stationary point.

Ab-initio calculations can generate these force constants using various methods (see Ref. 87 for an overview). Once these force constants are known, a mass–weighed Hessian matrix $\mathbf{H}$, can be built where each $(i, j)^{th}$ entry of the matrix is generated by dividing the corresponding force constant F_{ij} by the square root of the product of the masses of atom i and j ($\sqrt{m_i m_j}$). This matrix is then diagonalized to produce a set of eigenvectors defining the vibrational normal modes at the stationary point; the corresponding eigenvalues give the harmonic frequencies (or energies) of the corresponding vibrational normal modes (see Ref. 72 for a full review). This method, while simple, is not a realistic model for the potential

energy surface and overlooks anything beyond harmonic level, e.g. vibrational anharmonicities, and mode couplings and resonances, which can significantly affect the spectra, especially true for those systems with many vibrational resonances such as PAH molecules.

To account for these effects, an improved expression for the vibrational potential energy surface is needed. The harmonic potential (Eq. 7.1) can then be thought of as the first non–zero term in a Taylor expansion of the vibrational potential energy function. The full vibrational potential surface would be the Taylor expansion to infinite order around the stationary point (equilibrium geometry) of the molecule. For the purpose of this work the first three non–zero terms of the Taylor expansion are considered relevant [87]

$$\begin{aligned} V = V_0 &+ \sum_{i=1}^{3N} \left(\frac{\partial V}{\partial X_i} \right)_{V_0} X_i \\ &+ \frac{1}{2} \sum_{i=1}^{3N} \sum_{j=1}^{i} \left(\frac{\partial^2 V}{\partial X_i \partial X_j} \right)_{V_0} X_i X_j \\ &+ \frac{1}{6} \sum_{i=1}^{3N} \sum_{j=1}^{i} \sum_{k=1}^{j} \left(\frac{\partial^3 V}{\partial X_i \partial X_j \partial X_k} \right)_{V_0} X_i X_j X_k \\ &+ \frac{1}{24} \sum_{i=1}^{3N} \sum_{j=1}^{i} \sum_{k=1}^{j} \sum_{l=1}^{k} \left(\frac{\partial^4 V}{\partial X_i \partial X_j \partial X_k \partial X_l} \right)_{V_0} X_i X_j X_k X_l \end{aligned} \tag{3.2}$$

Since V_0 is arbitrary and set to zero, and the first derivative terms are zero at a stationary point, this leaves the terms containing the second, third and fourth derivatives. These non–zero derivatives are referred to as the quadratic, cubic, and quartic force constants respectively. Collectively this group of force constants for a given molecule is referred to as the quartic force field (QFF). Given the equilibrium geometry, the QFF of a molecule can be calculated analytically or numerically through small displacements of the atoms along a defined set of coordinates. In the VPT2 anharmonic vibrational analysis, the quadratic force constants are used to obtain the harmonic solution (as described above) which is then corrected by a second–order perturbation using the cubic and quartic force constants. Following Ref. 88 the energy of the perturbed states (for an asymmetric top) are given by

$$\begin{aligned} E(v) = &\sum_{k} \omega_k \left(v_k + \frac{1}{2} \right) + \sum_{k \leq l} x_{kl} \left(v_k + \frac{1}{2} \right) \\ &\times \left(v_l + \frac{1}{2} \right) \end{aligned} \tag{3.3}$$

where the anharmonic constants are given by

$$x_{kk} = \frac{1}{16}\phi_{kkkk} - \frac{1}{16}\sum_{m}(\phi_{kkm})^2 \times \left[\frac{8\omega_k^2 - 3\omega_m^2}{\omega_m\left(4\omega_k^2 - \omega_m^2\right)}\right] \tag{3.4}$$

$$x_{kl} = \frac{1}{4}\phi_{kkll} - \sum_{m}\frac{\phi_{kkm}\phi_{llm}}{4\omega_m} - \sum_{m}\frac{(\phi_{klm})^2\,\omega_m\left(\omega_k^2 + \omega_l^2 - \omega_m^2\right)}{2\Omega_{klm}} + \sum_{\alpha}B_\alpha^e\left(\zeta_{kl}^\alpha\right)^2 \times \left[\frac{\omega_k}{\omega_l} + \frac{\omega_l}{\omega_k}\right] \tag{3.5}$$

$$\Omega_{klm} = (\omega_k + \omega_l + \omega_m)(-\omega_k + \omega_l + \omega_m) \times (\omega_k - \omega_l + \omega_m)(\omega_k + \omega_l - \omega_m) \tag{3.6}$$

$$B_\alpha^e = \frac{h}{8\pi^2 c I_\alpha^e} \tag{3.7}$$

where ϕ_{xxx} and ϕ_{xxxx} are the cubic and quartic force constants respectively, ω are the harmonic frequencies, ν are the fundamental vibrational states, ζ_{kl}^α are the Coriolis coupling constants, and I_α^e are the moments of inertia.

The VPT2 method still contains caveats such as the singularities, so–called *resonances*, that occur when a set of harmonic frequencies or their sums, differences, or combinations are accidentally nearly equal and of the same symmetry (see Ref.56 for a detailed explanation). Normally there are two main types of vibrational resonances considered in a VPT2 anharmonic analysis: a type–one Fermi resonance, where an overtone state is approximately equal to a vibrational fundamental state ($\nu_i \approx 2\nu_j$), and a type–two Fermi resonance, where a combination state is approximately equal to a fundamental ($\nu_i \approx \nu_j + \nu_k$). There also exists additional types of resonances that become important when considering ro–vibrational spectra, e.g. Darling–Dennison resonances, where two overtones are approximately equal ($2\nu_i \approx 2\nu_j$), and Coriolis resonances where two fundamentals are approximately equal ($\nu_i \approx \nu_j$) [49]. Typically, the effect of a resonance is that the higher energy state in the resonance pair tends to be pushed to even higher energies and the lower energy state to even lower energies, and also intensity can be transferred from on state to the other. These effects can significantly alter the band positions, the number of bands, and overall intensities in the IR spectrum. To properly treat such resonant states, related terms need to be removed from the VPT2 treatment and handled separately with a method akin to degenerate second–order perturbation theory as described in Ref. 49, 56. If a given mode is simultaneously involved in more than one resonance (as happens for PAH molecules), all the modes (and overtones and combination–bands) involved need to be treated together as a group referred to as a *polyad*. (see Ref. 56 for a complete

description). For a specific vibrational resonance polyad, a matrix is constructed using the appropriate anharmonic constants (as given in Ref. 49) and diagonalized. The resulting eigenvalues are then the new line positions of the involved states and the eigenvectors (squared) represent the complexity of state mixings. While we use a variational polyad approach to correct for resonant states in VPT2, an alternative approach is vibrational quasi-degenerate perturbation theory (VQDPT2)[89, 90] which has shown some success as well.

Vibrational IR intensities can also be either harmonically or anharmonically computed. So–called double harmonic intensities of vibrational modes are calculated using the derivative of the dipole moment with respect to a normal coordinate. By definition, at the harmonic level, combination–bands and overtones have zero IR intensity. However, when considered anharmonically these combination–bands and overtones can be IR–active and have significant intensity. The anharmonic treatment of these intensities has been described previously in Ref. 91, 92. Perhaps more importantly, IR intensity can be redistributed due to resonances between fundamentals and combination and overtone bands as well. Intensity redistribution due to Fermi resonances and anharmonicity has been addressed by Vazquez and Stanton within the context of VPT2 [93]. In the present work, we have adopted a similar but simpler approach. That is we have used the eigenvectors of the polyad matrix to distribute IR intensity across the polyad in conjunction with the double harmonic IR intensities of the fundamental vibrational frequencies.

In the present work, we have redistributed the IR intensity across a polyad by using the eigenvectors of the polyad matrix together with the double harmonic IR intensities of the fundamentals involved in the polyad. We used the double harmonic intensities, because it was found that the anharmonic IR intensities for a fundamental involved in a polyad resonance often blew up, which we surmise was due to resonant terms that need to be removed, as described by Vazquez and Stanton[93]. Table 3.1 gives an example for the IR–active b_{1u} polyad involving the naphthalene CH–stretching fundamentals to illustrate how the intensity borrowing is calculated. The first column list all the states in the polyad, while the remaining column headers are the eigenvalues (or state energies, in cm^{-1}) diagonalized from the polyad matrix. The elements of these columns are the squared eigenvectors, and represent the percentage contribution of each polyad state. Accordingly, the vibrational intensity of a diagonalized state can be estimated as the dot product of the related squared eigenvector and a vector of original contributing state intensities. For example: the state at 2946 cm^{-1} borrows 9.0% of the intensity of the original ν_3 vibrational state, 3.7% of the intensity of the original ν_7 vibrational state, 0.3% of the intensity of the original $\nu_{10} + \nu_{11}$ combination band, etc. See next section for more details of the intensities adopted for each original states.

3.3 Methods

3.3.1 Theoretical Methods

Quantum chemistry calculations were performed in two stages, with two separate software packages: Gaussian 09 [51] and SPECTRO [52]. Gaussian 09 was

Mode	2946	2956	2968	2979	3029	3066	3081	3142	3176
ν_3	9.0	0.7	1.6	2.4	0.1	81.3	2.8	0.0	2.2
ν_7	3.7	8.9	0.2	5.7	51.6	1.4	24.6	3.8	0.1
$\nu_{10} + \nu_{11}$	0.3	0.0	0.0	0.1	0.2	1.8	0.1	0.2	97.4
$\nu_{10} + \nu_{13}$	0.0	1.6	0.1	1.2	26.1	1.3	69.3	0.2	0.1
$\nu_{12} + \nu_{14}$	35.2	0.1	46.6	9.2	2.6	6.1	0.1	0.0	0.0
$\nu_{11} + \nu_{15}$	25.8	36.9	20.4	8.4	6.6	1.4	0.4	0.0	0.0
$\nu_{10} + \nu_{16}$	20.1	38.7	28.7	11.9	0.0	0.6	0.0	0.0	0.0
$\nu_9 + \nu_{17}$	5.8	13.0	2.3	61.0	11.2	6.0	0.6	0.0	0.0
$\nu_9 + \nu_{12}$	0.1	0.2	0.0	0.1	1.6	0.1	2.0	95.8	0.2

Table 3.1 Percentage of mixing between resonance–affected states in the b_{1u} symmetry polyad of naphthalene in the CH–stretching region, which was used to estimate the IR intensity sharing across the polyad. See text for details.

used to compute the optimized geometries, harmonic vibrational spectra, as well as the quadratic, cubic and quartic normal coordinate force constants within the DFT framework, using the B971 functional [94] and the T2ZP basis[95] for each molecule. In these calculations a tight convergence criterion was used for the geometry optimization and a very fine grid (Int=200974) for numerical integrations, following the suggestions in Ref.96, 97.

Although the latest release of Gaussian 09 (D.01) can also output the VPT2-based anharmonic spectrum of a molecule [51], we have found that these spectra can not reproduce the IR features observed in the CH–stretching region of PAHs [22]. We believe this is mainly due to polyads not being used to determine intensity sharing between resonant modes [91] though we do not know for sure since we do not have access to the source code. Actually, the resonance and intensity borrowing effect seems to be minor when the computational results are compared with low–resolution gas–phase spectra [50], but this is not the case for low–temperature high–resolution gas–phase spectra with significant resonances such as the PAHs C-H stretches. Therefore, the VPT2 treatment was carried out by the second program SPECTRO. SPECTRO allows for resonances to be handled in polyads which then are used to redistribute the intensities across the resonant modes (vide infra). This approach, while approximate, does avoid the difficulty of dealing directly with the singularities that occur in resonant calculations of intensities. If not involved in resonances or polyads, we have found the anharmonic combination or overtone band intensities computed by Gaussian G09 to be reliable and have used these.

The optimized molecular minimum structure and the force constants calculated by Gaussian 09 is used as input for SPECTRO. Since Gaussian evaluates the QFF along the normal modes of a molecule, the QFF force constants are represented in a normal coordinate basis. The current version of SPECTRO can take either Cartesian derivatives or internal coordinate force constants as input, but not a normal coordinate QFF. As such, a linear transformation method from a normal coordinate QFF to a Cartesian coordinate QFF was developed and implemented to mesh the two software packages together [98].

Two SPECTRO threshold parameters control the number of states to be included in a resonance: a) the maximum energy separation of the states (Δ) (i.e.,

the denominator in resonant terms), and b) the minimum magnitude of the interaction strength between states (W) (i.e., the numerator in resonant terms). In the present study, the SPECTRO default values of $\Delta = 200$ cm^{-1} and $W = 10$ cm^{-1} were used, respectively. Testing with larger/smaller thresholds showed no significant changes in the resulting spectra.

The final anharmonic spectrum of each target molecule is therefore constructed using: a) all line positions (fundamentals, overtones, combination–bands, resonances, and polyads) as determined using SPECTRO, and b) three types of intensities, i.e., one for vibrational fundamentals, one for combination–bands/overtones not involved in resonances, and one for those involved in resonances/polyads. It should be noted that for those states potentially affected by resonances, we found that the double harmonic intensities were more reliable than Gaussian's anharmonic intensities. Therefore, the anharmonic intensities from Gaussian 09 are only used for the combination–bands/overtones that have zero intensity in the double harmonic approximation and cannot borrow intensity from resonances/polyads. The double harmonic intensities are used for all other states, including non–resonant fundamentals. For the resonances/polyads the double harmonic intensities are used in the intensity sharing across the modes of the polyad using the squared eigenvectors from the polyad treatment as described earlier in Section 7.2.

3.3.2 Experimental Methods

A supersonic pulsed source similar to Ref. 99 was used to record the low–temperature high–resolution gas–phase spectra in the CH stretching region (see also the companion paper Ref. 22). The samples were heated in an oven and then supersonically cooled with a typical pulse duration of 190 μs and argon at a backing pressure of 2.2 bar as a buffer gas. The molecular beam was then introduced into the ionization chamber through a 2 mm diameter skimmer where they were ionized using a Resonance Enhanced MultiPhoton Ionization (REMPI) scheme. The ions created were accelerated into a reflector time–of–flight tube and detected with a dual microchannel plate detector (Jordan Co.), yielding mass spectra with a resolution of $M/\Delta M$ of about 2000.

IR absorption spectra have been recorded using an IR–UV depletion scheme. In these experiments, a constant ion signal was created using a two–color ionization scheme in which a frequency-doubled dye laser (Sirah Cobra Stretch) pumped by a 30 Hz Nd:Ya$_g$ laser (Spectra Physics Lab 190) excites molecules to the first excited state. From this state, the molecules were ionized by an ArF excimer laser (Neweks PSX–501), which is in temporal overlap with the dye laser output. To record the IR absorption, these two laser beams were preceded by an IR laser beam with a line width of 0.07 cm^{-1}, which produces a dip in the ion signal upon IR absorption of the molecules under investigation. The IR beam was generated by difference frequency mixing of the fundamental output of a LDS 798 dye laser (Sirah Precision Scan) pumped by a 30 Hz Nd:Ya$_g$ laser (Spectra Physics Lab 190) with the fundamental of the Nd:Ya$_g$ laser.

In these double–resonance experiments overlap of the two laser beams and matching their size is crucial for obtaining the optimal depletion of the ground

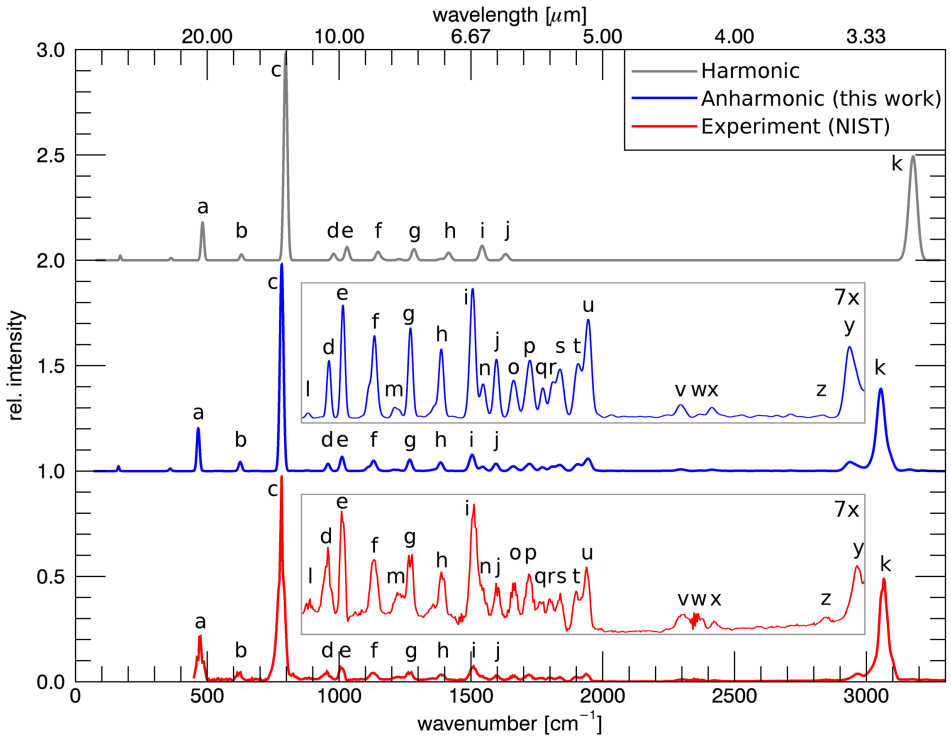

Figure 3.2 Full IR spectrum of naphthalene calculated using two methods, harmonic (top) and anharmonic (this work) (middle), compared with gas–phase spectra at 300 K[21] (bottom). A selected region is shown with the relative intensities increased by a factor of seven (see section 3.5.1 for details).

state. The IR beam has therefore been focused slightly with a long–focus lens beam with its focus after the molecular beam. Similarly, special care has been taken to record spectra under non–saturating conditions. Experimentally, it has been found that in these experiments depletion is optimal for a time delay between the two laser beams of 200 ns.

3.4 Results

3.4.1 Full infrared range

The full vibrational IR spectra of naphthalene, anthracene and tetracene are presented in Figures 3.2, 3.3, and 3.4. A comparison is given between the experimental spectra (NIST cq. MIS, bottom panel) and two theoretical spectra: anharmonic (this work, middle panel) and harmonic (this work, top panel). The harmonic spectra were calculated with Gaussian 09 using the same functional and basis set as in the anharmonic case. The experimental data for naphthalene

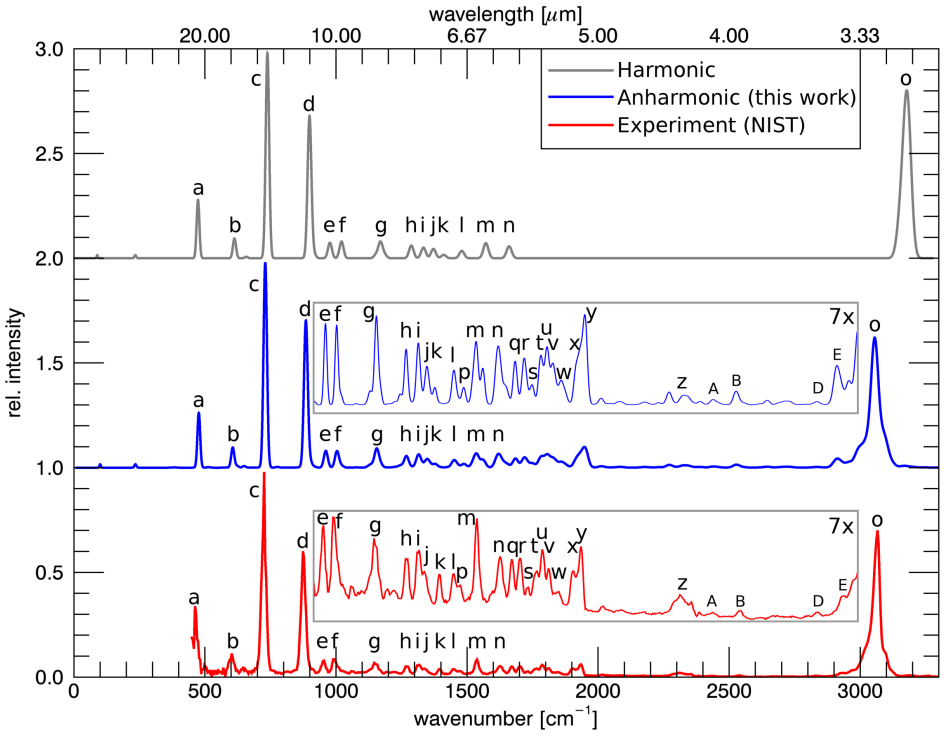

Figure 3.3 Full IR spectrum of anthracene calculated using two methods, harmonic (top) and anharmonic (this work) (middle), compared with gas–phase spectra at 300 K[21] (bottom). A selected region is shown with the relative intensities increased by a factor of five (see section 3.5.1 for details).

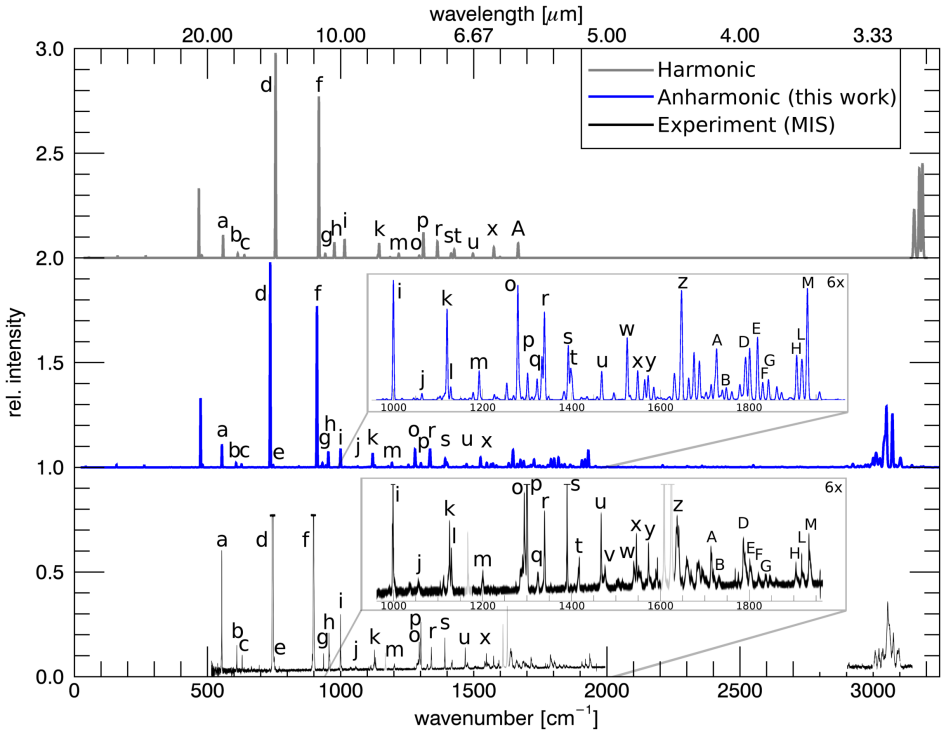

Figure 3.4 Full IR spectrum of tetracene calculated using two methods, harmonic (top) and anharmonic (this work) (middle), compared with Ar matrix–isolation spectrum[78] T≈10 K (bottom). A selected region is shown with the relative intensities increased by a factor of four (see section 3.5.1 for details). The greyed out lines in the matrix–isolation spectrum are water contamination.

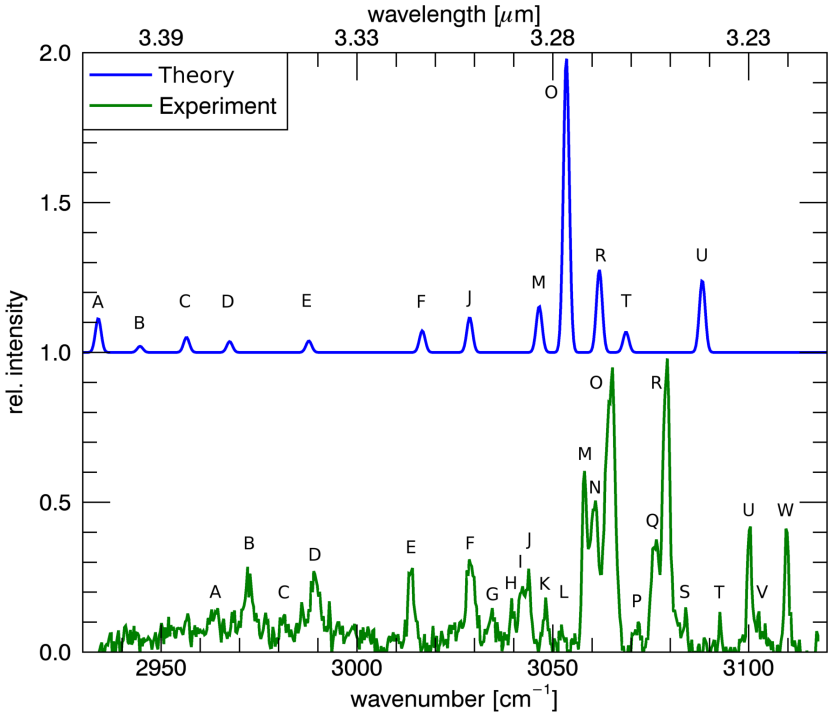

Figure 3.5 Anharmonic QFF IR spectrum of naphthalene (this work) compared to high–resolution gas–phase IR absorption spectra obtained in a molecular beam (this work).

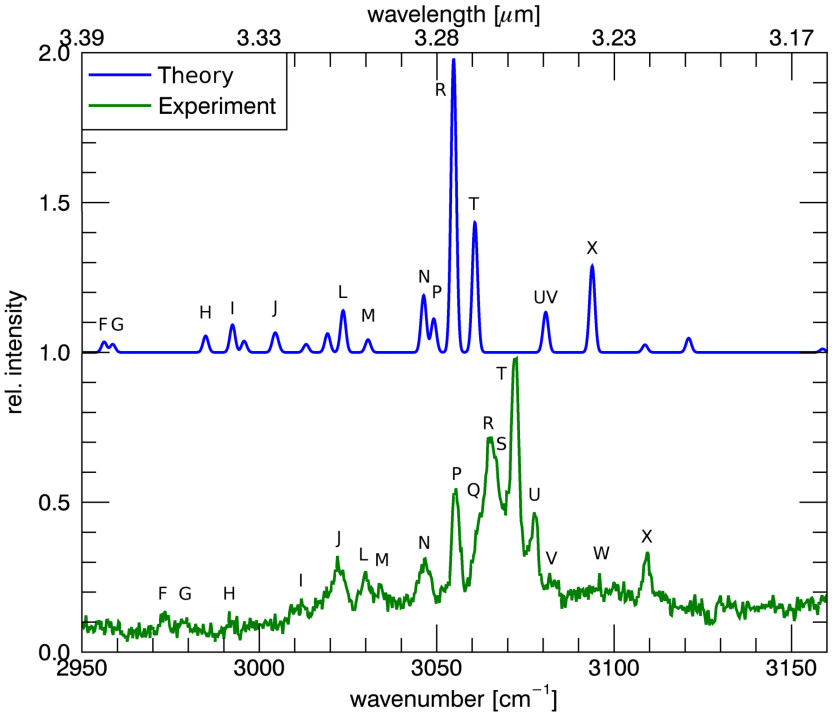

Figure 3.6 Anharmonic QFF IR spectrum of anthracene (this work) compared to high–resolution gas–phase IR absorption spectra obtained in a molecular beam (this work).

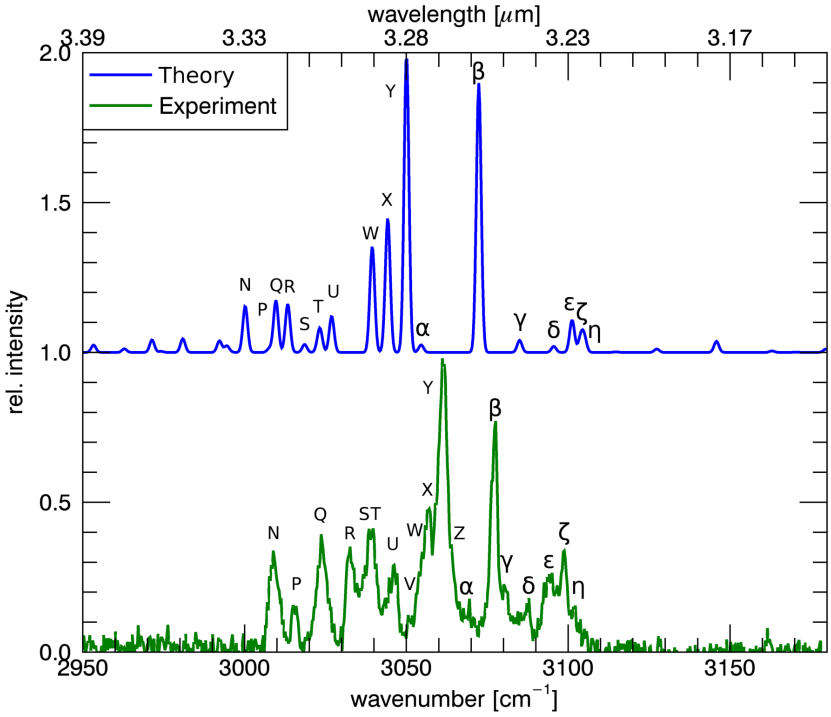

Figure 3.7 Anharmonic QFF IR spectrum of tetracene (this work) compared to high–resolution gas–phase IR absorption spectra obtained in a molecular beam (this work).

ID	modes	sym	exp	rel. I	harm	rel. I	anharm	rel. I
a	ν_{43}	b_{3u}	474	0.2	482	0.2	465.8	0.2
b	ν_{40}	b_{2u}	620	0.04	630	0.03	625.1	0.03
c	ν_{35}	b_{3u}	782	1	797	1	782.3	1
d	ν_{29}	b_{3u}	950	0.05	979	0.03	958.0	0.03
e	ν_{26}	b_{2u}	1011	0.07	1030	0.07	1011.3	0.07
f	ν_{24}	b_{1u}	1130	0.04	1147.1	0.04	1130.5	0.05
	$\nu_{47} + \nu_{30}$	b_{1u}						
g	ν_{18}	b_{1u}	1269	0.05	1284	0.06	1268.1	0.06
h	ν_{15}	b_{1u}	1388	0.04	1416	0.04	1385.3	0.04
i	ν_{12}	b_{2u}	1511	0.07	1542	0.07	1505.8	0.07
j	ν_{10}	b_{1u}	1599	0.03	1632	0.03	1594.9	0.03
k	See Tab. 3.5	-	3064	0.5	3176	0.51	3055	0.398
l	$\nu_{47} + \nu_{38}$	b_{1u}	880	0.02	-	-	877	0.003
m	ν_{20}	b_{2u}	1228	0.02	-	-	1212	0.007
	$\nu_{43} + \nu_{36}$	b_{1u}						
n	$\nu_{38} + \nu_{33}$	b_{1u}	1537	0.02	-	-	1544	0.02
o	$\nu_{35} + \nu_{32}$	b_{1u}	1662	0.03	-	-	1661	0.02
	$\nu_{38} + \nu_{29}$	b_{2u}						
p	$\nu_{33} + \nu_{32}$	b_{2u}	1719	0.03	-	-	1722	0.04
	$\nu_{35} + \nu_{30}$	b_{2u}						
	$\nu_{36} + \nu_{28}$	b_{2u}						
q	$\nu_{33} + \nu_{30}$	b_{1u}	1764	0.02	-	-	1772	0.02
r	$\nu_{33} + \nu_{27}$	b_{2u}	1801	0.02	-	-	1810	0.02
s	$\nu_{32} + \nu_{29}$	b_{1u}	1837	0.02	-	-	1836	0.03
	$\nu_{32} + \nu_{28}$	b_{2u}						
t	$\nu_{30} + \nu_{29}$	b_{2u}	1899	0.02	-	-	1905	0.03
	$\nu_{30} + \nu_{28}$	b_{1u}						
u	$\nu_{29} + \nu_{27}$	b_{1u}	1938	0.04	-	-	1944	0.06
	$\nu_{28} + \nu_{27}$	b_{2u}						
v	$\nu_{24} + \nu_{22}$	b_{2u}	2302	0.01	-	-	2295	0.009
	$\nu_{25} + \nu_{18}$	b_{1u}						
	$\nu_{23} + \nu_{22}$	b_{1u}						
	$\nu_{24} + \nu_{21}$	b_{1u}						
w	$\nu_{21} + \nu_{20}$	b_{2u}	2359	0.01	-	-	2368	0.003
x	$\nu_{25} + \nu_{15}$	b_{1u}	2422	0.007	-	-	2414	0.007
	$\nu_{34} + \nu_{9}$	b_{2u}						
	$\nu_{21} + \nu_{18}$	b_{1u}						
z	$\nu_{15} + \nu_{13}$	b_{1u}	2848	0.009	-	-	2835	0.002
	$\nu_{18} + \nu_{11}$	b_{1u}						
y	See Tab. 3.5	-	2966	0.04	-	-	2938	0.05

Table 3.2 Gas–phase experimental[21], theoretical harmonic, and theoretical anharmonic (this work) line positions [cm^{-1}], with the corresponding relative intensities and band assignments of the IR features of naphthalene taken from the data used to construct figure 3.2. Lines with more than one mode assigned are unresolved in experiment.

ID	modes	sym	exp	rel. I	harm	rel. I	anharm	rel. I
a	ν_{58}	b_{3u}	463	0.4	474	0.3	476	0.3
b	ν_{53}	b_{2u}	600	0.1	613	0.1	604	0.1
c	ν_{50}	b_{3u}	726	1	737	1	730	1
d	ν_{42}	b_{3u}	874	0.6	899	0.7	885	0.7
e	ν_{37}	b_{3u}	952	0.08	976	0.08	961	0.08
f	ν_{34}	b_{2u}	991	0.09	1021	0.08	1004	0.08
g	ν_{30}	b_{1u}	1150	0.07	1170	0.08	1154	0.08
h	ν_{25}	b_{1u}	1271	0.06	1287	0.06	1269	0.06
	$\nu_{58} + \nu_{46}$	b_{1u}						
i	ν_{23}	b_{1u}	1314	0.06	1334	0.05	1314	0.05
j	ν_{22}	b_{2u}	1338	0.04	1372	0.05	1347	0.05
	$\nu_{57} + \nu_{42}$	b_{2u}						
k	ν_{21}	b_{2u}	1394	0.04	1412	0.02	1379	0.02
	$\nu_{58} + \nu_{41}$	b_{1u}						
l	ν_{18}	b_{2u}	1448	0.05	1481	0.04	1451	0.040
	ν_{17}	b_{1u}						
m	ν_{15}	b_{2u}	1536	0.09	1572	0.08	1529	0.08
	$\nu_{49} + \nu_{46}$	b_{2u}						
	$\nu_{59} + \nu_{31}$	b_{2u}						
n	ν_{11}	b_{1u}	1626	0.06	1661	0.06	1619	0.07
	$\nu_{47} + \nu_{43}$	b_{1u}						
	$\nu_{47} + \nu_{42}$	b_{2u}						
o	See Tab. 3.6		3066	0.7	3176	0.8	3055	0.6
p	$\nu_{50} + \nu_{47}$	b_{2u}	1473	0.03	-	-	1486	0.02
q	$\nu_{44} + \nu_{43}$	b_{2u}	1670	0.05	-	-	1684	0.05
	$\nu_{50} + \nu_{38}$	b_{2u}						
r	$\nu_{44} + \nu_{42}$	b_{1u}	1702	0.06	-	-	1718	0.05
	$\nu_{47} + \nu_{37}$	b_{2u}						
	$\nu_{49} + \nu_{35}$	b_{2u}						
s	$\nu_{46} + \nu_{36}$	b_{2u}	1731	0.03	-	-	1747	0.02
	$\nu_{43} + \nu_{41}$	b_{2u}						
t	$\nu_{42} + \nu_{41}$	b_{1u}	1766	0.04	-	-	1783	0.06
	$\nu_{44} + \nu_{37}$	b_{1u}						
u	$\nu_{44} + \nu_{36}$	b_{2u}	1787	0.06	-	-	1805	0.07
	$\nu_{43} + \nu_{38}$	b_{1u}						
v	$\nu_{43} + \nu_{35}$	b_{2u}	1812	0.05	-	-	1828	0.05
	$\nu_{42} + \nu_{38}$	b_{2u}						
w	$\nu_{41} + \nu_{37}$	b_{1u}	1848	0.03	-	-	1861	0.03
	$\nu_{41} + \nu_{36}$	b_{2u}						
x	$\nu_{38} + \nu_{37}$	b_{2u}	1904	0.04	-	-	-	-
	$\nu_{38} + \nu_{36}$	b_{1u}						
	$\nu_{37} + \nu_{35}$	b_{1u}						
y	$\nu_{36} + \nu_{35}$	b_{2u}	1935	0.07	-	-	1949	0.1
z	$\nu_{51} + \nu_{12}$	b_{2u}	2310	0.02	-	-	2327	0.02
	$\nu_{31} + \nu_{28}$	b_{2u}						
	$\nu_{31} + \nu_{27}$	b_{1u}						
	$\nu_{30} + \nu_{28}$	b_{1u}						
A	$\nu_{29} + \nu_{24}$	b_{1u}	2438	0.008	-	-	2438	0.009
	$\nu_{28} + \nu_{25}$	b_{1u}						
B	$\nu_{40} + \nu_{12}$	b_{2u}	2537	0.01	-	-	2528	0.02
	$\nu_{39} + \nu_{11}$	b_{2u}						
D	$\nu_{19} + \nu_{18}$	b_{2u}	2833	0.01	-	-	2835	0.007
E	See Tab. 3.6	-	2932	0.02	-	-	2914	0.05

Table 3.3 Gas–phase experimental[21], theoretical harmonic, and theoretical anharmonic (this work) line positions [cm^{-1}], with the corresponding relative intensities and band assignments of the IR features of anthracene taken from data used to construct figure 3.3. Lines with more than one mode assigned are unresolved in experiment.

ID	modes	sym	exp	rel. I	harm	rel. I	anharm	rel. I
a	ν_{68}	b_{2u}	551.6	0.1	558.7	0.1	554	0.1
b	ν_{66}	b_{1u}	607.7	0.02	613.8	0.02	608	0.02
c	ν_{64}	b_{2u}	627.7	0.01	638.6	0.01	628	0.02
d	ν_{60}	b_{3u}	742.9	1	755.8	1	736	1
e	ν_{61}	b_{2u}	766.7	0.01	754.3	0.01	747	0.01
f	ν_{48}	b_{3u}	895.3	0.8	918.3	0.8	911	0.8
g	ν_{47}	b_{1u}	933.4	0.02	942.4	0.02	932	0.02
h	ν_{45}	b_{3u}	953.6	0.08	-	-	954	0.1
i	ν_{42}	b_{2u}	997.7	0.07	-	-	999	0.1
j	$\nu_{77} + \nu_{63}$	b_{2u}	1054.3	0.01			1064	0.005
k	ν_{39}	b_{1u}	1124.4	0.06	-	-	1120	0.07
l	ν_{40}	b_{2u}	1128.7	0.06	-	-	1129	0.01
m	ν_{34}	b_{1u}	1199.3	0.01	-	-	1193	0.02
o	ν_{29}	b_{1u}	1292.3	0.04	-	-	1279	0.09
p[a]	ν_{29}	b_{1u}	1298.8	0.08	-	-	1301	0.02
	$\nu_{71} + \nu_{57}$							
	$\nu_{73} + \nu_{57}$							
q	$\nu_{69} + \nu_{55}$	b_{2u}	1322.9	0.02	-	-	1323	0.02
r	ν_{27}	b_{2u}	1337.9	0.05	-	-	1339	0.07
s	ν_{23}	b_{2u}	1388.7	0.04	-	-	1393	0.04
t	ν_{25}	b_{1u}	1416.1	0.02	-	-	1399	0.03
u	ν_{20}	b_{2u}	1465.2	0.04	-	-	1469	0.03
v	-	-	1474.1	0.01	-	-	-	-
w	ν_{17}	b_{2u}	1540.1	0.01	-	-	1525	0.05
x	$\nu_{62} + \nu_{55}$	b_{1u}	1546.2	0.02	1575.6	0.05	1549	0.05
y	$\nu_{60} + \nu_{54}$	b_{1u}	1573.2	0.03	-	-	1572	0.02
z	ν_{13}	b_{1u}	1685.5	0.03	1666.7	0.07	1645.7	0.06
A	$\nu_{52} + \nu_{51}$	b_{1u}	1712.7	0.05	-	-	1726	0.04
B	$\nu_{54} + \nu_{48}$	b_{1u}	1730.9	0.01	-	-	1748	0.01
D	$\nu_{54} + \nu_{45}$	b_{1u}	1786.0	0.08	-	-	1791	0.03
E	$\nu_{49} + \nu_{48}$	b_{1u}	1800.3	0.03	-	-	1818	0.05
F	$\nu_{51} + \nu_{46}$	b_{1u}	1819.8	0.01	-	-	1830	0.02
G	$\nu_{51} + \nu_{43}$	b_{2u}	1836.3	0.01	-	-	1842	0.02
H	$\nu_{46} + \nu_{45}$	b_{2u}	1904.2	0.02	-	-	1906	0.04
L	$\nu_{46} + \nu_{44}$	b_{1u}	1917.1	0.02	-	-	1918	0.04
M	$\nu_{44} + \nu_{43}$	b_{2u}	1933.3	0.05	-	-	1931	0.09

Table 3.4 Matrix–isolation experimental[78], theoretical harmonic, and theoretical anharmonic (this work) line positions [cm^{-1}], with the corresponding relative intensities and band assignments of the IR features of tetracene taken from data used to construct figure 3.4. Lines with more than one mode assigned are unresolved in experiment.

[a]resonance

ID	sym	exp[22]	rel. I[22]	anharm	rel. I	components	I source
A	b_{1u}	2963.8	0.20	2934.0	0.12	$\nu_{15} + \nu_{11}$	ν_3
						$\nu_{14} + \nu_{12}$	
B	b_{1u}	2972.4	0.30	2944.6	0.021	ν_7	ν_3
						$\nu_{15} + \nu_{11}$	ν_7
						$\nu_{16} + \nu_{10}$	
C	b_{2u}	2981.3	0.20	2956.4	0.032	ν_2	ν_2
						ν_6	
						$\nu_{13} + \nu_{12}$	
C	b_{1u}	2981.3	0.20	2956.6	0.020	$\nu_{14} + \nu_{12}$	ν_3
						$\nu_{16} + \nu_{10}$	
D	b_{1u}	2989.0	0.28	2967.5	0.037	ν_3	ν_3
						ν_7	
						$\nu_{17} + \nu_9$	
E	b_{2u}	3014.0	0.30	2987.7	0.039	ν_6	ν_2
						$\nu_{15} + \nu_9$	
F	b_{1u}	3029.5	0.19	3016.6	0.074	ν_7	ν_7
						$\nu_{13} + \nu_{11}$	
G	-	3034.5	0.15	-	-	-	-
H	-	3039.5	0.19	-	-	-	-
I	-	3042.3	0.29	-	-	-	-
J	b_{2u}	3043.8	0.35	3028.8	0.12	ν_2	ν_2
						ν_6	
						$\nu_{14} + \nu_{10}$	
						$\nu_{15} + \nu_9$	
K	-	3048.2	0.19	-	-	-	-
L	-	3052.2	0.17	-	-	-	-
M	b_{2u}	3058.1	0.65	3046.5	0.16	ν_2	ν_2
						ν_6	
						$\nu_{14} + \nu_{10}$	
N	-	3060.5	0.54	-	-	-	-
O	b_{1u}	3065.2	0.99	3053.4	1	ν_3	ν_3
P	-	3071.4	0.10	-	-	-	-
Q	-	3076.2	0.37	-	-	-	-
R	b_{2u}	3079.2	1	3061.9	0.28	ν_2	ν_2
						$\nu_{12} + \nu_{11}$	
						$\nu_{14} + \nu_{10}$	
S	-	3092.6	0.21	-	-	-	-
T	b_{1u}	3083.9	0.16	3068.7	0.069	ν_7	ν_3
						$\nu_{13} + \nu_{10}$	ν_7
U	b_{2u}	3100.2	0.45	3088.1	0.24	ν_2	ν_2
						$\nu_{12} + \nu_{11}$	
V	-	3102.6	0.21	-	-	-	-
W	-	3109.4	0.45	-	-	-	-

Table 3.5 Line positions [cm^{-1}], relative intensities, dominant resonant components, and origin of intensities for the bands of the naphthalene in the high–resolution gas–phase IR absorption spectra obtained in a molecular beam (this work) and the theoretical anharmonic spectrum (this work) as shown in figure 3.5.

ID	sym	exp[22]	rel. I[22]	anharm	rel. I	components	I source
F	b_{1u}	2973.2	0.10	2956.2	0.036	$\nu_{21} + \nu_{13}$	ν_3
						$\nu_{22} + \nu_{12}$	
G	b_{1u}	2979.6	0.08	2958.6	0.028	$\nu_{21} + \nu_{13}$	ν_3
						$\nu_{22} + \nu_{12}$	ν_{10}
H	b_{2u}	2992.5	0.07	2984.8	0.056	ν_6	ν_2
						$\nu_{18} + \nu_{14}$	
						$\nu_{20} + \nu_{11}$	
I	b_{1u}	3011.8	0.15	2992.4	0.094	ν_3	ν_7
						$\nu_{17} + \nu_{14}$	
J	b_{1u}	3022.0	0.30	3004.2	0.050	$\nu_{17} + \nu_{14}$	ν_3
						$\nu_{19} + \nu_{11}$	
						$\nu_{21} + \nu_{12}$	
J	b_{2u}	3022.0	0.30	3005.0	0.027	$\nu_{17} + \nu_{14}$	ν_3
						$\nu_{19} + \nu_{11}$	
						$\nu_{21} + \nu_{12}$	
L	b_{1u}	3030.0	0.25	3023.6	0.14	ν_{10}	ν_{10}
						$\nu_{18} + \nu_{13}$	
M	b_{2u}	3033.7	0.20	3030.6	0.043	$\nu_{17} + \nu_{13}$	ν_2
N	b_{2u}	3046.7	0.30	3046.3	0.19	ν_2	ν_2
						ν_6	
P	b_{1u}	3055.4	0.54	3049.1	0.11	ν_7	ν_7
						$\nu_{18} + \nu_{13}$	
Q	-	3062.3	0.45	-	-	-	-
R	b_{1u}	3065.3	0.72	3054.7	1	ν_3	ν_3
S	-	3066.9	0.64	-	-	-	-
T	b_{2u}	3071.9	1	3060.7	0.44	ν_2	ν_2
						$\nu_{15} + \nu_{14}$	
						$\nu_{17} + \nu_{12}$	
						$\nu_{17} + \nu_{13}$	
U	b_{2u}	3077.8	0.40	3080.5	0.052	$\nu_{17} + \nu_{12}$	ν_2
V	b_{1u}	3081.8	0.24	3080.8	0.088	$\nu_{18} + \nu_{12}$	ν_3
W	-	3095.9	0.24	-	-	-	-
X	b_{2u}	3109.6	0.32	3093.8	0.29	ν_2	ν_2
						$\nu_{15} + \nu_{14}$	

Table 3.6 Line positions [cm^{-1}], relative intensities, dominant resonant components, and origin of intensities for the bands of anthracene in the high–resolution gas–phase IR absorption spectra obtained in a molecular beam (this work) and the theoretical anharmonic spectrum (this work) as shown in figure 3.6.

ID	sym	exp[22]	rel. I[22]	anharm	rel. I	components	I source
N	b_{1u}	3008.9	0.39	3000.0	0.16	ν_7	ν_3
						$\nu_{21} + \nu_{16}$	ν_7
						$\nu_{23} + \nu_{14}$	
P	b_{2u}	3015.3	0.20	3007.7	0.013	$\nu_{20} + \nu_{18}$	ν_2
						$\nu_{25} + \nu_{14}$	
Q	b_{1u}	3023.7	0.44	3009.6	0.17	ν_7	ν_3
						$\nu_{21} + \nu_{16}$	ν_7
						$\nu_{23} + \nu_{14}$	ν_{10}
R	b_{1u}	3032.6	0.40	3013.2	0.17	ν_{10}	ν_{10}
						$\nu_{23} + \nu_{14}$	
S	b_{2u}	3038.5	0.45	3018.6	0.034	$\nu_{22} + \nu_{16}$	ν_2
T	b_{1u}	3039.7	0.46	3022.8	0.023	$\nu_{19} + \nu_{17}$	ν_2
							ν_{11}
T	b_{1u}	3039.7	0.46	3023.4	0.063	$\nu_{26} + \nu_{13}$	ν_3
U	b_{1u}	3046.2	0.34	3026.9	0.12	$\nu_{24} + \nu_{13}$	ν_3
V	-	3050.6	0.18	-	-	-	-
W	b_{1u}	3054.8	0.38	3039.4	0.35	ν_7	ν_7
						ν_{10}	ν_{10}
						$\nu_{21} + \nu_{16}$	
X	b_{2u}	3056.8	0.51	3043.9	0.15	ν_{11}	ν_2
						$\nu_{19} + \nu_{17}$	
X	b_{2u}	3056.8	0.51	3044.3	0.31	ν_2	ν_2
						ν_6	
						$\nu_{18} + \nu_{17}$	
Y	b_{1u}	3061.1	1	3050.0	1	ν_3	ν_3
Z	-	3066.6	0.20	-	-	-	-
α	b_{2u}	3069.5	0.23	3054.6	0.025	ν_6	ν_6
						$\nu_{18} + \nu_{17}$	
β	b_{2u}	3077.6	0.80	3072.3	0.90	ν_2	ν_2
γ	b_{1u}	3080.4	0.27	3085.0	0.041	$\nu_{19} + \nu_{16}$	ν_3
							ν_{10}
δ	b_{1u}	3087.9	0.23	3095.5	0.020	$\nu_{20} + \nu_{14}$	ν_7
ϵ	b_{1u}	3094.1	0.31	3101.0	0.11	$\nu_{18} + \nu_{16}$	ν_3
ζ	b_{2u}	3098.8	0.38	3103.9	0.048	$\nu_{22} + \nu_{13}$	ν_2
η	b_{1u}	3101.5	0.19	3104.9	0.040	$\nu_{18} + \nu_{16}$	ν_7
						$\nu_{21} + \nu_{13}$	ν_{10}

Table 3.7 Line positions [cm^{-1}], relative intensities, dominant resonant components, and origin of intensities for the bands of tetracene in the high–resolution gas–phase IR absorption spectra obtained in a molecular beam (this work) and the theoretical anharmonic spectrum (this work) as shown in figure 3.7.

and anthracene in these plots are taken from the NIST database[21] (gas–phase, T=300 K). The experimental data for tetracene is an argon matrix–isolation spectrum taken from Ref. 78. Some water contamination is present in the tetracene experimental data, and it has been greyed out in the figure. Each of the three comparisons also includes an inset that shows the 1000–3000 cm^{-1} region magnified in order to show detail. The choice for these three experimental spectra was based on the availability of data for the widest vibrational IR range. Original gas–phase or uncontaminated matrix–isolation data are not available for tetracene, so the spectrum was produced by combining four figures from Ref. 78.

The theoretical overview spectra of naphthalene and anthracene are convolved with a Gaussian profile (FWHM = 18 cm^{-1}) to approximately match the resolution of the experimental gas–phase data. Likewise, the theoretical overview spectrum of tetracene is convolved with a Gaussian profile (FWHM = 3 cm^{-1}) to match the matrix–isolation data. Theoretical frequencies have not been scaled.

Three tables (3.2, 3.3, and 3.4) are presented along with these overview spectra. These tables contain the line positions and relative intensities of the experimental data, the harmonic theoretical data and the anharmonic theoretical data from this work. Since the full IR experimental spectra contain many unresolved features, assignments are based on the convolved theoretical spectrum. The underlying states and combination–bands of the experimental features are determined using the theoretical results. The symmetries of the corresponding bands are also given. The spectroscopic features identified for naphthalene and anthracene are based on the excellent correspondence between experiment and theory. The features identified for tetracene are based on the line positions given in Ref. 78. Each feature is identified by a letter that corresponds to the letters appearing in the corresponding figures 3.2, 3.3, and 3.4. The supplemental material contains the full IR line list, as well as the corresponding polyads for each of the three PAHs. Appendix 3.6 also provides vibrational mode descriptions for all the vibrational modes included in these tables.

3.4.2 CH–stretching region

We focus on the CH–stretching region since harmonic level analysis failed to explain the features in this region and significant anharmonic effects are expected. Figures 3.5, 3.6, and 3.7 compare the anharmonic theoretical lines (top panel) convolved with a FWHM = 1 cm^{-1} Gaussian profile for naphthalene, anthracene, and tetracene, respectively, with our low–temperature high–resolution gas–phase IR absorption experimental spectra (bottom panel). Theoretical frequencies have not been scaled.

Similar to the full IR range, three tables accompany these spectra (tables 3.5, 3.6, and 3.7). The assignments are based upon relative intensities, distance between neighbouring bands, and general trends in the shape of the spectrum. In the case of naphthalene, fits of the rotational contours of bands in the experimental spectrum allowed us to determine their symmetries (refer to companion paper Ref. 22), which provided us with additional means to assign them to specific bands as predicted by the calculations. For anthracene and tetracene the bands were not

resolved enough to determine reliably the symmetries. Line positions and relative intensities of the experimental and theoretical spectra are given as an indication between the best matches; also listed are the theoretically computed symmetries, major resonance components and intensity sources for each peak or feature. The major resonance components are determined as the fundamentals/combination–bands whose contributions dominate the polyad, as evaluated from the eigenvector component. The "sources" of IR intensities listed are the vibrational fundamentals that lend the most intensity through resonance to each band. Note that the major vibrational resonance components are not necessarily the major intensity sources and vice versa. In some cases there is more than one dominant resonance component, with nearly equal contributions of various fundamentals or combination modes. Labeling of a given band with a single fundamental or combination state can thus be ambiguous.

3.5 Discussion

3.5.1 Full infrared range

The theoretical anharmonic spectra of all three molecules for the full IR range (figures 3.2, 3.3, and 3.4) show good agreement, both in band position and relative intensities, with the NIST and matrix–isolation data. Inspection of tables 3.5, 3.6, and 3.7 shows that the bands in the theoretical anharmonic spectrum differ from experiment by an absolute average deviation for naphthalene of 6.5 cm^{-1} with a maximum deviation of 28 cm^{-1}, for anthracene by an absolute average deviation of 10.2 cm^{-1} with a maximum deviation of 18 cm^{-1}, and for tetracene by an absolute average deviation of 7.4 cm^{-1} with a maximum deviation of 39.8 cm^{-1}. These deviations are not frequency dependent, nor are there any trends present; there is near even split between being too high in frequency and too low in frequency for each band. This means that these deviations are most due to the level of electronic structure theory, and not physical effects i.e., temperature shifts, or emission versus absorption.

The anharmonic calculations of the CH–stretching region of the full IR spectra also show fairly good agreement with the NIST experiments. The shape of this region (the left and right wings of the main feature, as well as the prominent secondary bumps on the left) can be explained with resonances. However, the secondary bumps are too low in frequency when compared with the experimental data, and in fact these are the largest absolute deviations in the full IR comparison of naphthalene and anthracene. These secondary bumps consist of many lines and as such the position of the convolved feature is highly dependent on the individual features. A detailed analysis is therefore postponed until Section 5.4.1. Neglecting these secondary bumps, the absolute average deviation for the two molecules falls to 5.6 cm^{-1} for naphthalene with maximum deviation of 13 cm^{-1}, and 9.9 cm^{-1} for anthracene with a maximum deviation of 18 cm^{-1}

For tetracene, the maximum deviation is due to the line labeled 'z'. This line was identified in Ref. 78. However, it is right next to the water contamination so possibly the feature is overly intense causing confusion in the assignment with our

theoretical data. If this line is neglected, the absolute average deviation falls to 6.4 cm^{-1} with a maximum deviation of 20 cm^{-1}.

It is important to note that these deviations are significantly smaller than the large deviations for the harmonic approximation. Harmonic calculations led to PAH spectra with blue–shifts appearing as a function of state energies (i.e., there is a systematic percentage error). At lower frequencies the harmonic spectrum tends to differ by 10 cm^{-1} while at the higher frequencies, the spectrum tends to differ by 100 cm^{-1}. This trend in the harmonic spectra of the three PAHs studied is consistent with the frequency scaling factor of 0.958 that is typically used in the literature [86] to bring the harmonic spectra into closer agreement with matrix–isolation experiments.

The experimental and theoretical intensities are normalized to each of their strongest intensities in order to compare their relative intensities. The average relative intensity ratios for the theoretical spectra to the experimental spectra for naphthalene, anthracene and tetracene are 0.92, 1.01, and 1.41 respectively. These are in excellent agreement, but it is unclear if, in the case of tetracene, matrix interactions are the cause for some of the experimental lines to be lower in intensity when compared to theory.

The NIST/MIS experimental spectra of the three PAHs show a large number of bands in the 1200–2600 cm^{-1} range with intensities comparable to the fundamental bands in the same region. These have been previously attributed, both experimentally[100, 101] and theoretically[102], to combination–bands, although at that time it was only possible to calculate their frequencies and not their intensities. We now can confirm that these bands are indeed pure combination–bands possessing their own unborrowed (non-resonant) anharmonic intensities. These combination–bands show good enough agreement with experimental results that a more detailed set of line assignments would be possible if higher resolution experimental spectra were to be taken in this region. It was found that the VPT2 is capable of reliable predictions without the aid of polyad mixings for this wavelength range. These combination bands are found to be generated by modes of the same type, i.e., out–of–plane in combination with out–of–plane, and in–plane in combination with in–plane. The out-of-plane–out-of-plane combination bands range from 1200–1900 cm^{-1} and the in-plane–in-plane combination bands range from 2200–2600 cm^{-1}. The out-of-plane–out-of-plane combination bands are found to have more intensity than the in-plane–in-plane combination bands by approximately an order of magnitude. Bands originating between a combination of one in–plane mode and one out–of–plane mode were not found to have significant intensity, even in other frequency regions.

3.5.2 CH–stretching region

Our high–resolution gas–phase experiments allow for a closer look at the effect of resonances in the CH–stretching region of PAH spectra. Indeed the large number of CH–stretching bands in the experimental spectra shown in figures 3.5, 3.6, 3.7 (naphthalene, anthracene, and tetracene respectively) cannot be explained by the harmonic approximation.

Line positions for naphthalene, anthracene, and tetracene differ between our anharmonic calculations and our experimental spectra by absolute deviations of 19.3 cm^{-1}, 10.5 cm^{-1}, and 11.7 cm^{-1}, with maximum absolute deviations of 29.8 cm^{-1}, 21.0 cm^{-1}, and 19.9 cm^{-1} respectively. All theoretical frequencies were left unscaled.

The three molecules in this study belong to the D_{2h} point group for which only type–two Fermi resonances ($\nu_i \approx \nu_j + \nu_k$) are of importance for the analysis of the spectrum. Type–one Fermi resonances ($\nu_i \approx 2\nu_j$) have no effect since for this point group all overtones are totally symmetric and hence not IR active. The IR–active modes belong to b_{1u}, b_{2u}, and b_{3u} symmetries. However, the b_{3u} symmetry modes are out–of–plane modes and therefore the fundamental and combination bands do not occur in the CH–stretching region. This means that the CH–stretching region is mainly controlled by two large vibrational resonance polyads, one for the b_{1u} symmetry bands and the other one for the b_{2u} symmetry bands. These large polyads have a significant effect on the resulting spectrum, and completely change the band positions and intensities when moving from the harmonic to the non-polyad VPT2 to the polyad VPT2 anharmonic simulation [22].

It has been shown in this work that the anharmonic QFF treatment can reproduce the large number of bands seen in the CH–stretching region for anthracene and tetracene. Our experiment for naphthalene, however, shows many more lines than can be explained with the current "VPT2 + resonance polyad" approach. In previous experiments it could not be ruled out that some (or more) of these bands were actually due to isotopologues or other contaminations, or associated with excitation from vibrationally excited levels. The mass-resolved and conformer selectivity nature of our experiments, and the use of supersonically-cooled molecules ensures that in our experiments we can unambiguously conclude that all of the measured CH-stretching features concern excitations from the vibrational ground state of each PAH, even though our current theory cannot explain all of them adequately. One possible explanation for the presence of additional bands is that the resonance polyads should include second overtones or combination–bands of three (or more) vibrational quanta or modes to explain all the observed experimental lines.

Though subtle, there seems to be a slight effect in the spectral range over which features are observed in the CH–stretching region when comparing the three experimental spectra (Fig. 3.2, 3.3, and 3.4). The spectral range narrows when PAH length increases. This may be explained by the linear increase of the number of CH oscillators with increasing length of the PAH together with the vibrational state density increasing much more rapidly. Since one can reasonably assume that the anharmonic coupling strengths are not significantly influenced by the size of the PAH, the available oscillator strength, increasing roughly linearly with PAH size, will be distributed over many more background levels. Since the intensity borrowing is roughly inversely proportional with the distance to the fundamental band, this effectively leads to a narrowing of the CH–stretching band envelope. Such a conclusion is further supported by MIS studies on larger PAHs[78], which indeed show that the spectral band envelope becomes increasingly narrower for larger PAHs.

It can be seen that the frequencies of the major CH–stretching fundamental bands are about the same for all types of PAHs. The frequencies of the CC stretching modes that are potentially involved in combination–bands, on the other hand, are much more sensitive to the finer structure details and point group of the individual PAH. Consequently, from species to species, the minor CH–stretching region bands vary vastly more than predicted by the harmonic level analysis. This dramatic effect on the overall CH–stretching region can aid in the identification of specific species or sub–families of PAHs.

The average relative intensities ratios for the theoretical spectra to the experimental spectra for naphthalene, anthracene and tetracene are 0.34, 0.48, and 0.36 respectively. The theoretical spectra are normalized to the strongest bands, which for naphthalene is the band labeled 'O', for anthracene is the band labeled 'R', and for tetracene are the two nearly equal bands 'Y' and 'β'. This however leaves the remaining intensities under scaled. This is especially obvious for the second strongest band of naphthalene, 'R', and the second strongest band of anthracene, 'T'. If these strongest intensities are ignored and the spectra are instead normalized to the remaining bands the average ratio between theory to experiment jumps to 1.01, 0.95, and 0.93 for naphthalene, anthracene, and tetracene respectively. This leads us to believe that there may be either an issue with the double harmonic intensity calculations of the strongest CH–stretching fundamental bands, possibly due to the level of electronic structure theory used (as happens with the overestimation of the C–H stretching intensities for the B3LYP/4-31G case [86]) or the triple–combination–band resonances borrow significant intensity from the strongest bands. We are presently investigating this issue in more detail.

3.5.3 Astrophysical implications

Our study demonstrates that anharmonicity needs to be taken into account in order to have a more reliable understanding of astronomical IR PAH spectra. Current astronomical observations and modelling of the AIBs rely exclusively on the harmonic IR spectrum of PAHs, which fail to reproduce the spectra in a number of ways.

The shape and strength of all of the features falling in the C–H stretching region are controlled by resonances and anharmonicity, thus the harmonic approximation utterly fails here. Astronomical spectra of AIBs indeed show a series of secondary features, such as wings and broad plateaux close to the main 3.29 μm (3030 cm^{-1}) feature, which so far have not been adequately characterized[39]. Anharmonic studies of PAHs can help shed light on the the origin of these features and possibly their dependence on the structural properties of PAHs[22]. PAHs of varying shapes will be investigated in future work.

Current harmonic models do not predict any bands in the 5–5.5 μm region (2000–1820 cm^{-1}), although observations of the AIBs do see emission in this region[102]. The anharmonic calculations of this work have confirmed that these observed bands are indeed due to PAHs, specifically combination bands with their own relatively strong intrinsic intensities.

Astronomical emission models of PAHs rely on the so-called "infrared cascade"[39],

e.g. the energy of a photon is distributed amongst the harmonic IR active modes of the absorbing PAH. Since, in a real molecule, many more states are IR active due to anharmonicity, the energy distribution and therefore the resulting emission spectra of PAHs will lead to spectral complexity that may actually aid in species identification and understanding of astronomical PAHs. Inclusion of anharmonicity also allows for the inclusion of hot bands and overtones into models[85, 103, 104], and will be investigated in future work.

Lastly, anharmonic calculations eliminate the need for the typical frequency scaling factor[86] that is used to bring harmonic theoretical spectra into agreement with experimental matrix–isolation spectra. No frequency scaling factors or shifts are found in this work, line positions are accurately determined to within 10 cm^{-1}, with no bias towards either a red or blue shifts. Investigation into the possible causes of this error, i.e., the level of theory, is underway and will be reported in due course. Bearing this, anharmonic calculations do provide greater confidence in the theoretical spectra, especially when extrapolating to areas where experimental data is limited.

3.6 Conclusions

In this work we calculated the anharmonic IR spectrum of naphthalene, anthracene and tetracene, (the last two for the first time) and compare them with available gas–phase and MIS experiments, as well as our own low–temperature high–resolution gas–phase spectra in the CH–stretching region. It has been shown that there are clear differences between a harmonic IR spectrum and an anharmonic IR spectrum. Theoretical anharmonic spectra are needed in order to explain combination–bands, resonances in the C–H stretching region, as well as the frequency shifting factor normally seen in harmonic spectra simulation. Our anharmonic theoretical spectra are in excellent agreement with the experimental spectra.

All of the fundamental CH–stretching modes for each of the PAHs studied are in resonance with many combination–bands. This occurs because PAHs have a large number of CC–stretching modes around 1500 cm^{-1} that can enter into type–two Fermi resonances ($\nu_i \approx \nu_j + \nu_k$) with the CH–stretching modes around 3000 cm^{-1}. This type of resonance explains the asymmetric wings and overall shape observed in the CH region in low resolution experiments, and the large number of lines found in our high–resolution experiments. However, the comparison between predicted and experimentally observed spectra also indicates that there are still lines that cannot be accounted for. It is possible that this is due to potential interactions that were not accounted for such as combination–bands or higher order overtone states involving three or more vibrational quanta or modes. We can conclude that without the intensity borrowing between resonant states the number of computed features with significant intensity is unable to match the experiment. Sharing intensities through resonances produce spectra that better match the general shape and features in the CH stretch region when compared to harmonic treatments or VPT2 treatments that neglect intensity sharing and

polyad resonances[22].

The 1700–2500 cm^{-1} spectral region is also unaccounted for in the harmonic approximation, but shows up in experimental data. Experimental spectra show bands with noticeable intensity in this region, sometimes as strong as, or even greater than the surrounding fundamental bands. These bands are found to be combination–bands and can be predicted very well by the VPT2 anharmonic analysis both with respect to position and intensity. Since these bands are not involved in resonances, VPT2 reliably predicts these lines without the aid of polyad mixing.

In this work, deviations in band positions, and intensity problems in the CH–stretching region have been partially attributed to the level of electronic structure theory. Due to the size of the molecules studied in this work, current computational resources limit the level of theory that can be used. However, naphthalene QFF analysis is just barely feasible for the CCSD(T) approach with cc-pVTZ basis. . A detailed analysis into the effects of the level of electronic structure theory on anharmonic calculations of PAHs is currently underway using naphthalene as the test case.

The spectra comparison among the three PAHs studied in this work suggests that our anharmonic treatment may perform better as the size of the PAHs increases. Additional experimental and theoretical work on larger PAHs is currently underway using the same theoretical and experimental approaches as described in this work. Furthermore, it is hoped that better understanding of the effects that vibrational anharmonicities have on a typical PAH spectrum can possibly lead to more general predictions of the PAH family as a whole without the need for detailed anharmonic analyses on all PAH molecules.

Acknowledgments

The authors would like to thank the two anonymous reviewers for their helpful comments that improved the clarity of the manuscript. The spectroscopic study of interstellar PAHs at Leiden Observatory have been supported through the Advanced European Research Council Grant 246976, a Spinoza award, and through the Dutch Astrochemistry Network funded by the Netherlands Organization for Scientific Research, NWO. Computing time has been made available by NWO Exacte Wetenschappen (project MP–270–13 and MP–264–14) and calculations were performed at the LISA Linux cluster of the SurfSARA supercomputer center in Almere, The Netherlands. XH and TJL gratefully acknowledge support from the NASA 12–APRA12–0107 grant. XH acknowledges the support from NASA/SETI Co–op Agreement NNX12AG96A and NNX15AF45A. This material is based upon work supported by the National Aeronautics and Space Administration through the NASA Astrobiology Institute under Cooperative Agreement Notice NNH13ZDA017C issued through the Science Mission Directorate. AC acknowledges Fernando Clemente and Julien Bloino for insightful discussions.

Appendix

Mode	Freq	Symm	Description
ν_2	3184.55	b_{2u}	asym TS sym str (IP) ||a =s
ν_3	3172.85	b_{1u}	sym TS-LS asym str (IP) ||s =a
ν_6	3157.92	b_{2u}	asym TS-LS CH sym IP str ||a =s
ν_7	3155.20	b_{1u}	sym LS+TS asym str (IP) ||s =a
ν_9	1661.12	b_{3g}	sym 2-ring CH rock ||a =a
ν_{10}	1631.73	b_{1u}	sym CC and CH rock/wag (IP) ||s =a
ν_{12}	1542.43	b_{2u}	asym CC and CH wag, boating (IP) ||a =s
ν_{13}	1487.71	a_g	sym 2-ring CH sym wag ||s =s
ν_{14}	1485.75	b_{3g}	asym 2-ring CH rock ||a =a
ν_{15}	1415.55	b_{1u}	sym ring CH rotation (sym rock) (IP) ||s =a
ν_{16}	1393.46	a_g	center CC str ||s =s
ν_{17}	1386.34	b_{2u}	asym CC and CH wag, (IP) ||a =s
ν_{18}	1283.93	b_{1u}	sym LS rock (IP) ||s =a
ν_{20}	1227.77	b_{2u}	asym TS wag (IP) ||a =s
ν_{23}	1163.89	b_{2u}	asym CH wag (IP) ||a =s
ν_{24}	1147.15	b_{1u}	sym CH rock/wag (IP) ||s =a
ν_{26}	1030.13	b_{2u}	asym 2-ring breath (IP) ||a =s
ν_{27}	996.25	b_{2g}	sym TS asym OP bend ||s =a
ν_{28}	990.94	a_u	asym TS asym OP bend ||a =a
ν_{29}	979.34	b_{3u}	sym LS sym OP bend, ||s =s
ν_{32}	894.74	b_{2g}	sym CH asym OP bend ||s =a
ν_{33}	846.53	a_u	asym CH asym OP bend ||a =a
ν_{34}	804.60	b_{1u}	sym TS asym CC IP deform ||s =a
ν_{35}	797.02	b_{3u}	sym CH sym OP bend (CH inversion) ||s =s
ν_{36}	783.13	b_{2g}	asym LS sym OP bend ||s =a
ν_{38}	725.96	b_{1g}	asym CH sym OP bend (CH invers) ||a =s
ν_{40}	629.79	b_{2u}	2-ring asym str (IP) ||a =s
ν_{43}	482.17	b_{3u}	sym MR CH sym OP bend, fly ||s =a
ν_{46}	362.72	b_{1u}	2-ring ip bend ||s =a
ν_{47}	183.92	a_u	2-ring torsion OP ||a =a
ν_{48}	170.25	b_{3u}	2-ring OP bend ||s =s

Table 3.8 Mode descriptions and harmonic frequencies [cm^{-1}] of all IR active modes with double harmonic intensities > 0.05 km/mol and all modes that are involved in active combinations identified in this work for naphthalene.
OP – out of plane ; IP – in plane
LS – long side ; TS – terminal side (see Fig. 5.1)
MR – middle ring ; TR – terminal ring (see Fig. 5.1)
|| perpendicular to ring–ring–ring axis
= parallel to ring–ring–ring axis

Mode	Freq	Symm	Description
ν_2	3185.13	b_{2u}	asym TR CH sym str (IP) ||a =s
ν_3	3173.31	b_{1u}	sym TR asym CH str (IP) ||s =a
ν_6	3159.62	b_{2u}	asym (LS-TR + TS) CH IP sym str ||a =s
ν_7	3155.52	b_{1u}	sym LS asym str, TS asym str (IP) ||s =a
ν_{10}	3150.78	b_{1u}	MR CH asym str (IP) ||s =a
ν_{11}	1660.53	b_{1u}	sym 3-ring CC, CH rock/wag (IP) ||s =a
ν_{12}	1658.31	b_{3g}	sym 3-ring CH rock ||a =a
ν_{13}	1614.96	b_{3g}	asym 3-ring CC, CH rock/wag (IP) ||s =a
ν_{14}	1587.51	a_g	4-center-CC sym str, CH wag (IP) ||s =s
ν_{15}	1571.72	b_{2u}	asym 3-ring CC, CH wag (IP) ||a =s
ν_{17}	1480.78	b_{1u}	TS ring CH sym rock (rotation) (IP)||s =a
ν_{18}	1478.96	b_{2u}	asym TR CH wag (IP) ||a =s
ν_{19}	1422.09	a_g	4-center-CC asym str (IP) ||s =s
ν_{20}	1411.80	b_{3g}	asym TR CH rock (rotation) (IP) ||a =a
ν_{21}	1410.82	b_{2u}	MR asym CC + CH wag (IP) ||a =s
ν_{22}	1371.66	b_{2u}	sym LS wag (boating) (IP) ||a =s
ν_{23}	1333.61	b_{1u}	sym TR CH rock (IP) ||s =a
ν_{24}	1291.48	b_{3g}	MR CH rock (IP) ||a =a
ν_{25}	1287.35	b_{1u}	sym TS ring LS asym CH rock (IP) ||s =a
ν_{27}	1206.72	b_{3g}	sym LS rock (IP) ||a =a
ν_{28}	1186.78	a_g	sym TR CH asym wag (IP) ||a =a
ν_{29}	1185.52	b_{2u}	asym TS rock, MR CH rock (IP)
ν_{31}	1152.89	b_{2u}	3-ring sym CH wag (boating) (IP) ||a =s
ν_{34}	1020.99	b_{2u}	asym TR breath (IP) ||a =s
ν_{35}	991.76	b_{2g}	sym TR CH asym OP bend ||s =a
ν_{36}	991.45	a_u	asym TR CH asym OP bend ||a =a
ν_{37}	976.83	b_{3u}	sym LS bend - sym TS bend (OP) ||s =s
ν_{38}	971.95	b_{1g}	asym TR CH asym OP bend ||a =s
ν_{39}	926.06	b_{3g}	asym 3-ring deformation (IP) ||a =a
ν_{40}	916.28	b_{1u}	sym 3-ring distorsion (IP) ||s =a
ν_{41}	911.17	b_{2g}	MR CH - TR CH asym bend (OP) ||s =a
ν_{42}	898.87	b_{3u}	MR CH sym OP bend (inversion) ||s =s
ν_{43}	864.31	a_u	asym TR CH OP torsional bend ||a =a
ν_{44}	842.26	b_{2g}	MR CH - TR CH asym bend (OP) ||s =a
ν_{45}	817.11	b_{2u}	3-ring MR IP swing ||a =s
ν_{46}	781.16	b_{2g}	sym 3-ring LS asym OP bend ||s =a
ν_{47}	768.17	b_{1g}	asym TR CH sym OP bend ||a =s
ν_{49}	755.09	a_u	asym 3-ring OP bend ||a =a
ν_{50}	738.36	b_{3u}	sym TS sym OP bend (inversion) ||s =s
ν_{51}	657.68	b_{1u}	sym 3-ring wag (IP) ||s =a
ν_{53}	612.64	b_{2u}	asym TS ring str (IP) ||a =s
ν_{57}	480.17	b_{1g}	asym TR LS sym OP bend ||a =s
ν_{58}	473.60	b_{3u}	LS 3-ring inversion, fly (OP) ||s =s
ν_{59}	395.96	a_g	sym 3-ring stretch ||s =s
ν_{61}	384.15	b_{3u}	3-ring TR OP folding ||s =s
ν_{63}	234.35	b_{1u}	3-ring linear bend (IP) ||s =a
ν_{66}	89.25	b_{3u}	3-ring linear bend (OP) ||s =s

Table 3.9 Mode descriptions and harmonic frequencies [cm^{-1}] of all IR active modes with double harmonic intensities > 0.05 km/mol and all modes that are involved in active combinations identified in this work for anthracene.
OP – out of plane ; IP – in plane
LS – long side ; TS – terminal side (see Fig. 5.1)
MR – middle ring ; TR – terminal ring (see Fig. 5.1)
|| perpendicular to ring–ring–ring axis
= parallel to ring–ring–ring axis

Mode	Freq	Symm	Description
ν_2	3185.35	b_{2u}	asym TR CH sym str (IP) ||a =s
ν_3	3173.56	b_{1u}	sym TR CH asym str (IP) ||s =a
ν_6	3160.07	b_{2u}	asym TR CH sym str (IP) ||a =s
ν_7	3155.71	b_{1u}	sym LS asym str (IP) ||s =a
ν_{10}	3153.01	b_{1u}	sym MR CH sym str (IP) ||s =a
ν_{11}	3152.32	b_{2u}	asym MR CH sym str (IP) ||a =s
ν_{13}	1666.71	b_{1u}	sym 4-ring CH rock (IP) ||s =a
ν_{14}	1652.99	b_{3g}	asym TR CH wag/rock (IP) ||a =a
ν_{16}	1598.83	b_{1u}	sym 4-ring distorsion (IP) ||s =a
ν_{17}	1575.65	b_{2u}	asym 4-ring distorsion (IP) ||a =s
ν_{18}	1571.66	a_g	5-center-CC sym str, TS wag ||s =s
ν_{19}	1549.92	a_g	asym center CC str, CH rock/wag ||s =s
ν_{20}	1497.03	b_{2u}	asym TR CH wag (IP) ||a =s
ν_{21}	1476.24	a_g	sym TR CH sym wag (IP) ||s =s
ν_{22}	1474.48	b_{3g}	asym TR CH sym rock (IP) ||a =a
ν_{23}	1426.85	b_{2u}	asym 4-ring distorsion (IP) ||a =s
ν_{24}	1420.27	a_g	sym MR CH wag (IP) ||s =s
ν_{25}	1415.01	b_{1u}	sym TR rotation (IP) ||s =a
ν_{27}	1363.63	b_{2u}	sym LS wag (IP) boating mode ||a =s
ν_{29}	1311.03	b_{1u}	sym MR distorsion + CH rock (IP) ||s =a
ν_{30}	1310.82	b_{2u}	asym MR breath (IP) ||a =s
ν_{31}	1295.33	b_{1u}	sym MR CH rock (IP) ||s =a
ν_{34}	1218.47	b_{1u}	asym LS rock (IP) ||s =a
ν_{35}	1200.03	b_{3g}	sym LS asym rock (IP) ||a =a
ν_{36}	1185.82	b_{2u}	asym TR CH wag ||a =s
ν_{39}	1144.78	b_{1u}	sym TS rock (IP) ||s =a
ν_{40}	1140.55	b_{2u}	sym LS rock (IP) ||a =s
ν_{42}	1015.03	b_{2u}	asym TR CH wag (IP) ||a =s
ν_{43}	990.72	b_{2g}	sym TR CH asym OP bends ||s =a
ν_{44}	990.64	a_u	asym TR CH asym OP bends ||a =a
ν_{45}	976.59	b_{3u}	TR CH asym OP bend, fly ||s =s
ν_{46}	975.23	b_{1g}	asym TR CH asym OP bends ||a =s
ν_{47}	942.45	b_{1u}	4-ring distorsion (IP) ||s =a
ν_{48}	918.32	b_{3u}	sym MR CH sym OP bend ||s =s
ν_{49}	914.96	b_{2g}	sym MR CH asym OP bends ||s =a
ν_{51}	887.84	a_u	asym 2-ring 2-ring CH OP bend ||a =a
ν_{52}	865.37	b_{1g}	asym MR CH sym OP bends ||a =s
ν_{54}	851.11	b_{2g}	sym 4-ring CH asym OP bends ||s =a
ν_{55}	839.45	a_u	asym 4-ring CH asym OP bends ||a =a
ν_{57}	777.54	b_{2g}	sym 4-ring LS asym OP bends ||s =a
ν_{60}	755.83	b_{3u}	sym TR CH sym OP bend ||s =a
ν_{61}	754.29	b_{2u}	asym 4-ring breath (IP) ||a =s
ν_{62}	742.15	b_{1g}	asym TR CH sym OP bend ||a =s
ν_{63}	730.33	b_{2g}	asym 4-ring OP bend ||a =a
ν_{64}	638.61	b_{2u}	4-ring asym str (IP) ||a =s
ν_{66}	613.82	b_{1u}	4-ring distorsion (IP) ||s =a
ν_{68}	558.68	b_{2u}	4-ring asym str (IP) ||a =s
ν_{71}	478.92	b_{3u}	LS asym OP bend, fly ||s =s
ν_{73}	467.72	b_{3u}	LS sym OP bend ||s =s
ν_{74}	443.83	b_{1u}	sym ring-ring IP bending ||s =a
ν_{77}	314.06	a_u	asym 4-ring torsion ||a =a
ν_{79}	267.98	b_{3u}	4-ring waving (OP) ||s =s
ν_{81}	162.33	b_{1u}	4-ring linear bend (IP) ||s =a
ν_{84}	54.32	b_{3u}	4-ring linear bend (OP) ||s =s

Table 3.10 Mode descriptions and harmonic frequencies [cm^{-1}] of all IR active modes with double harmonic intensities > 0.05 km/mol and all modes that are involved in active combinations identified in this work for tetracene.
OP – out of plane ; IP – in plane
LS – long side ; TS – terminal side (see Fig. 5.1)
MR – middle ring ; TR – terminal ring (see Fig. 5.1)
|| perpendicular to ring–ring–ring axis
= parallel to ring–ring–ring axis

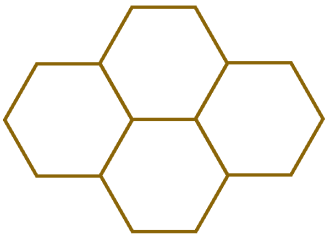

The anharmonic quartic force field infrared spectra of five non-linear Polycyclic Aromatic Hydrocarbons: benzanthracene, chrysene, phenanthrene, pyrene, and triphenylene

The study of interstellar polycyclic aromatic hydrocarbons (PAHs) relies heavily on theoretically predicted infrared (IR) spectra. Most earlier studies use scaled harmonic frequencies for band positions and the double harmonic approximation for intensities. However, recent high–resolution gas–phase experimental spectroscopic studies have shown that the harmonic approximation is not sufficient to reproduce experimental results. In our previous work we presented the anharmonic theoretical spectra of three linear PAHs, showing the importance of including anharmonicities into the theoretical calculations. In this paper, we continue this work by extending the study to include five non–linear PAHs (benz[a]anthracene, chrysene, phenanthrene, pyrene, and triphenylene), thereby allowing us to make a full assessment of how edge structure, symmetry and size influence the effects of anharmonicities. The theoretical anharmonic spectra are compared to spectra obtained under matrix isolation low–temperature conditions, low–resolution high–temperature gas–phase conditions, and high–resolution low–temperature gas–phase conditions. Overall, excellent agreement is observed between

the theoretical and experimental spectra although the experimental spectra show subtle but significant differences.

Cameron J. Mackie, Alessandra Candian, Xinchuan Huang, Elena Maltseva, Annemieke Petrignani, Jos Oomens, Andrew L. Mattioda, Wybren Jan Buma, Timothy J. Lee, Alexander G. G. M. Tielens
The Journal of Chemical Physics Volume 145, Issue 8, (2016)

4.1 Introduction

Polycyclic Aromatic Hydrocarbons (PAHs) are a family of molecules characterized by fused aromatic–benzenoid rings with the free carbon edges capped by hydrogens. These molecules are of great interest in a wide variety of scientific fields. From a material science standpoint they serve as models and precursors for various carbon–based nano–materials such as nanotubes, graphene, and fullerenes[5, 6, 7]. From an engineering standpoint they are a common, yet undesirable, by–product of combustion in engines and rockets[1, 2]. From a biological standpoint they are viewed as a common pollutant and are studied in the context of their carcinogenic properties[3].

PAHs are also of interest from the astrophysical standpoint. They are the most likely candidate for a set of infrared (IR) features known as the Aromatic Infrared Bands (AIBs)[26, 27] observed around a wide variety of astronomical objects. It has been estimated that up to 20% of the total carbon in the universe is locked up in PAHs[76]. Their importance has led experimentalists, theoreticians, and astronomers to work closely in order to characterize the IR emission of PAHs for use as a probe of the physical and chemical conditions in the astrophysical environments in which they are observed.

Experimental IR spectra have been reported for a wide variety of PAHs using various spectroscopic techniques. Due to the involatile nature of PAHs two dominant techniques are used to obtain the IR spectrum: high–temperature gas–phase spectroscopy, or low–temperature matrix–isolation spectroscopy[21, 77, 78, 79, 80, 81, 82, 83]. Attempts to extrapolate these experimental data to astrophysically relevant conditions are complicated by temperature effects in the former, and matrix–interaction effects in the latter. High–resolution low–temperature gas–phase spectra have been taken previously, but only for a handful of species and only in the C–H stretching region (2950–3150 cm^{-1}, 3μm)[22, 105].

The limited availability of PAH absorption spectra of the sizes and structures relevant to astrophysical environments has necessitated the development and use of computational quantum chemical techniques for PAHs. Databases of the IR spectra of astrophysically relevant PAHs have been compiled and are available online[33, 48]. Typically these theoretical IR spectra are constructed using the harmonic approximation within the Density Functional Theory (DFT) framework using B3LYP functionals with very small basis sets (e.g., 4–31G). This approach has been successful in roughly reproducing the overall IR features, but has compared poorly to high–resolution experiments[22]. Specifically the C–H stretching region and the pure combination band region (1700–2000 cm^{-1}) are incorrectly reproduced since mode couplings, resonances, and combination bands cannot be modelled at the harmonic level.

It has been shown in our previous work[22, 106] that an anharmonic theoretical approach is necessary to explain the experimental IR spectra of PAHs. While previous work concentrated on a set of three linear PAHs, this work expands to include a set of five non–linear PAHs which complete the series of PAHs containing up to four benzenoid rings. The reason for this choice is twofold; we want to show that the anharmonic treatment can be extended successfully to non-linear species, and at

the same time we want to understand how edge structure and symmetry influence the anharmonic spectrum. In fact, variations in the IR spectra of PAHs have been observed experimentally and have been attributed to various hydrogen–hydrogen interaction edge effects[107, 108], and to the variation in molecular symmetries from species to species. To study these edge and symmetry effects non–linear PAHs must be considered. This work aims to show that the anharmonic treatment can be extended to non–linear species: benz[a]anthracene ($C_{18}H_{12}$), chrysene ($C_{18}H_{12}$), phenanthrene ($C_{14}H_{10}$), pyrene ($C_{16}H_{10}$), and triphenylene ($C_{18}H_{12}$) (fig. 5.1). Moreover, we present low–temperature high–resolution gas–phase experimental IR absorption spectra of the five non–linear PAHs (first presented in the astrophysical companion paper[23]), as well as matrix–isolation spectra (MIS) which allows for direct comparisons with theory providing further validation for our approach. Although the theoretical spectra produced is in absorption at 0 K, understanding the fundamental nature of the anharmonicity of PAHs and the importance of resonances will allow us to better understand the emission features of astronomical PAHs.

4.2 Theory

The most commonly applied approximation in predicting the IR absorption characteristics of a molecule is the assumption of harmonic potentials. Given the equilibrium structure of a molecule, the nuclear potential can be approximated with just the second-order terms in a Taylor series expansion, referred to as the quadratic force constants. Solving for the eigenvectors and eigenvalues of this system of quadratic force constants leads to the normal mode atomic displacement descriptions and the excitation energies of each mode. The IR intensities of the modes are then calculated by what is called the double–harmonic approximation, which involves taking the derivative of the dipole of the molecule as it is displaced along the normal modes. The harmonic (and double-harmonic) approximation only allows the vibrational fundamentals to exhibit any IR intensity, and can greatly overestimate the energies of the fundamentals due to the neglect of anharmonicity.

In order to produce a more realistic spectrum, additional terms need to be included when producing the vibrational potential (and the dipole surface). This is accomplished through an anharmonic quartic force field (QFF) and consequential vibrational analysis. In this case, the nuclear potential is expanded to include up to quartic terms in the Taylor series expansion. Since the potential is no longer quadratic, an analytic solution for the modes and energies is no longer possible (as is possible for the harmonic case). As such, second–order vibrational perturbation theory (VPT2) is required to solve for the energies. The introduction of VPT2, however, leads to the possibility of singularities (near–zero terms in denominators if two states are very close in energy). The terms wherein singularities arise are removed from the VPT2 formula, and instead a matrix is constructed, including diagonal and coupling terms, that is then diagonalized. Four types of resonances are considered: Fermi one (a fundamental is approximately equal to an overtone),

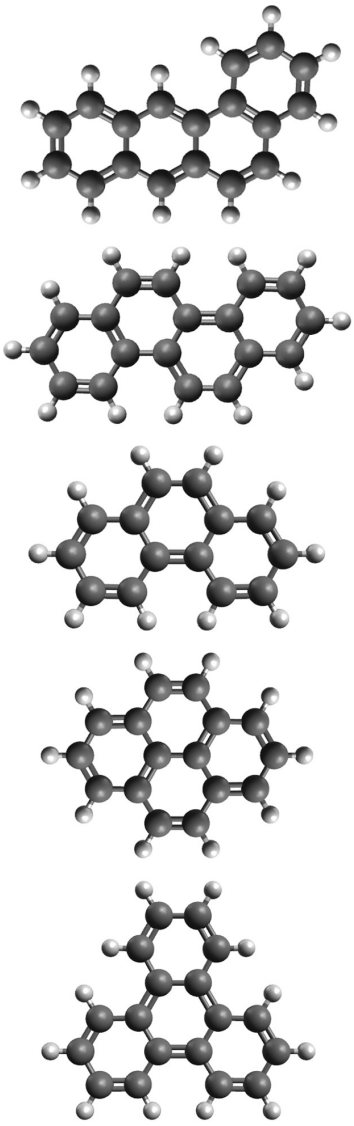

Figure 4.1 From top to bottom: benz[a]anthracene, chrysene, phenanthrene, pyrene, and triphenylene.

Fermi two (a fundamental is approximately equal to a combination band), Darling-Dennison (two overtones or two combination bands or a mixture of these two are approximately equal), and Coriolis (two fundamentals are approximately equal). The effect of a resonance is to push one member of the pair of states to a lower energy and the other to a higher energy. Intensity sharing across a resonance also occurs, which can result in bands that would normally be of zero or minimal intensity to gain significant intensity.

Additional complications arise when multiple modes or combination bands are in simultaneous resonances, respectively. These so–called *polyads*, need to be considered together through a resonance matrix (see Ref.56), and is the source of the vibrational Darling-Dennison and Coriolis resonances. The resulting eigenvectors (squared) and eigenvalues of the resonance matrix give the percent mixing of individual modes and combination bands involved in the polyad, and the new energies arising from the multiple interactions. The intensities can also be calculated individually through anharmonic means, as described in Ref. [91]. However, when there are resonances, the anharmonic IR intensities will also have resonant terms that need to be removed. In our previous work it was shown that double harmonic intensities distributed according to the eigenvectors of the polyad matrix accurately reproduce intensity patterns[106]. For a more detailed description of the theory involved in this work see ref. 106 and references therein.

4.3 Methods

4.3.1 Theoretical Methods

The quantum chemical calculations in this work were performed with Gaussian 09[51] and the VPT2 calculations were performed with SPECTRO[52]. Gaussian was used to compute the optimized geometry of the molecules, the harmonic intensities, the anharmonic intensities (no polyad mixings), and the quartic force fields (quadratic, cubic, and quartic force constants). A DFT framework, with the B971 functional[94] and a T2ZP basis[95] was used for the Gaussian calculations, as suggested in refs. 96, 97.

Gaussian09 is able to compute the VPT2 anharmonic spectrum of molecules, however, it was unable to reproduce accurately the C–H stretching region of PAHs due to the large number of simultaneous resonances occurring[22]. Therefore, the SPECTRO program was used to carry out the VPT2 calculations in order to handle these large resonant groups, or *polyads*.

The optimized geometry and the normal coordinate QFF of each molecule was taken from the Gaussian output and input into SPECTRO. Since the current version of SPECTRO cannot take normal coordinate QFFs as input, a linear transformation into Cartesian coordinates[98] was performed first.

SPECTRO determines what are considered to be resonant states, and therefore must be removed from the regular VPT2 treatment, through a set of thresholds. Two types of threshold are present: the maximum energy separation of the states considered Δ (denominator term), and the interaction strength of the states W (numerator term). In our previous work[106] it was found that the default values

used by SPECTRO to detect resonances ($\Delta = 200$ cm^{-1} and $W = 10$ cm^{-1}) were sufficient, i.e., the spectrum did not change significantly as these thresholds were further increased. After testing it was determined that the W threshold was allowing singularities (missed resonances) to enter into the VPT2 treatment causing significant changes to the resulting spectrum. As such, the W threshold was set to zero and resonances were detected purely on the energy separation of the states. A side effect of this however, is that it allows for states with incorrect symmetry to enter into resonance unnecessarily. A separate subroutine was therefore written to ensure symmetry constraints were obeyed. In passing by, we notice that if these symmetry constraints are broken, it will not cause changes to the computed spectrum, but it would increase significantly the number of resonant states and thus polyad sizes. This results in an unnecessary increase in computational time by adding many zero–valued entries to the resonance matrices.

The final QFF anharmonic spectra were constructed using the line positions from SPECTRO, the anharmonic intensities from Gaussian (for modes not in polyads), and the harmonic intensities from Gaussian distributed across the polyads (for modes in polyads), as described in Ref. [106].

Special theoretical consideration is necessary for triphenylene since it is a symmetric top with $\mathcal{D}_{3h}$ symmetry; additional discussion is given in the appendix.

4.3.2 Experimental Methods (MIS)

The MIS IR spectroscopic techniques employed for these samples have been described in detail elsewhere [78, 109, 110] and will only be briefly summarized here. All samples were isolated in an inert argon matrix prepared by vapor co–deposition of the PAH of interest with an over abundance of argon (Ar) onto a 15K CsI window suspended in a high–vacuum chamber (p $<10^{-8}$ Torr). The sample being investigated was vaporized from a heated Pyrex tube while the argon (Matheson prepurified, 99.998%) was admitted through an adjacent length of liquid nitrogen cooled copper tubing, to minimize water and other contaminates. The conditions were optimized to produce an Ar/PAH ratio in excess of ≈1000:1. An FTIR spectrum of the sample was recorded once a sufficient amount of neutral material was accumulated, as indicated by the strength of the weakest bands.

Samples of chrysene ($C_{18}H_{12}$, 98% purity), pyrene ($C_{16}H_{18}$, 99% purity), phenanthrene ($C_{14}H_{10}$, 98% purity), and triphenylene ($C_{18}H_{12}$, 98% nominal purity) were obtained from the Aldrich Chemical Company. Significant impurities were noticed, initially, in the samples of triphenylene. These less volatile impurities were removed by baking out the sample, under vacuum, just below the sublimation temperature of the sample. The benz[a]anthracene (1,2-benzanthracene) sample was obtained from Resolutions Systems, the U.S. supplier for Chiron Chemical Company and was 99% or greater purity. Deposition temperatures for the PAHs discussed here were phenanthrene, 13^{o}C (cooled); pyrene, 65^{o}C; benz[a]anthracene, 85^{o}C; chrysene, 95^{o}C; and triphenylene, 85^{o}C. The mid–IR spectra for chrysene, pyrene, phenanthrene, and triphenylene were recorded on a Nicolet Analytical Instruments, Model 740 FTIR spectrometer using an MCT–B detector/KBr beam splitter combination while the benz[a]anthracene data was

collected on a Bio–Rad/Digilab Excalibur FTS–4000 IR spectrometer using an MCT–B detector/KBR broadband beam splitter combination. All spectra were recorded as a co–addition of either 250 or 500 scans at a resolution of 0.5 cm^{-1}. For presentation purposes, the reported spectra have been baseline-corrected with several bands resulting from impurities (such as water and purge air) either subtracted or truncated using the Win–IR Pro 3.4 Software package.

4.3.3 Experimental Methods (High–resolution Gas–phase)

The experimental setup used to perform laser spectroscopy on a supersonic molecular jet has been described previously[99] as well. A given sample was kept at a temperature higher than its melting point to create enough vapor pressure for detection. Mixed with 2 bars of a carrier gas (argon), the sample was expanded into the vacuum through a pulsed valve (General Valve) with a typical opening time of 200 μs.

Detection of the molecules after the expansion was achieved through resonance enhanced multiphoton ionization followed by mass-selective ion detection. A dye laser (Sirah Cobra Stretch) was fixed on a specific electronic transition of the molecule under investigation (see ref. 23 for more details) while an ArF excimer laser beam (Neweks PSX-501) in temporal overlap with the dye laser was used to ionize the molecules from the electronically excited state.

To probe the ground state vibrational levels an IR laser beam with a line width of 0.07 cm^{-1} was introduced 200 ns before the excitation and ionization beams. The 3 μm pulse was a product of difference frequency mixing of the fundamental outputs of the dye laser (Sirah Precision Scan with LDS798 dye) and the Nd:YAG laser (Spectra Physics Lab 190) in a $LiNbO_3$ crystal. Resonant excitation of vibrational levels resulted in depletion of ground state population of the probed molecules and thus led to a dip in the ion signal.

4.4 Results

In the following we will compare the theoretical anharmonic spectra with experimental spectra obtained under three different experimental conditions. To allow for a proper comparison, we have convolved the theoretical stick spectra with Lorentzian profiles with appropriate full-width half-maximums (FWHM) (2 cm^{-1} for the MIS spectra , 18 cm^{-1} for the high–temperature gas–phase spectra and 2 cm^{-1} for the high-resolution low–temperature gas–phase data). Figures 4.7 and 4.12 show visual comparisons between the convolved theoretical spectrum and the MIS experiment, high–temperature experiment, and the high-resolution low–temperature gas–phase experiment for benz[a]anthracene. See the supplemental material for similar comparisons of each PAH.

These sets of convolved theoretical spectra are then used to assign the best match between experimental and theoretical bands based on position, intensities, and overall feature trends. The values given for the experimental and convolved theoretical band positions and intensities were determined by fitting Lorentzian profiles to the spectra using the software package Fityk[111]. Experimental bands

with relative peak intensities under 1% of the maximum intensity bands have been excluded.

For the high–temperature gas–phase spectra, as well as the MIS, line position and intensity comparisons between experiment and theory are given in the supplemental material. Similar spectral features (i.e., position, intensities, and profiles) between the five species are aligned across the rows of the tables. The MIS spectra are of high enough resolution to warrant direct comparison of the vibrational modes types. It is important to note that vibrational mode descriptions become vague when describing modes that are in resonance; as such the spectral bands are organized by their dominant resonant component. Two strong water bands at 1608 cm^{-1} and 1624 cm^{-1} are observed in the MIS spectra for each PAH (and have been truncated), as well as a continuum–like feature under these water bands for chrysene and phenanthrene. Seven MIS bands could not be assigned with theoretical bands.

Individual bands are not resolved in the C–H stretching region of the high–temperature and MIS experiments due to temperature effects for the former, and steric hindrance of the hydrogens for the latter. Therefore, analysis of the C–H stretching region is performed only for the high–resolution gas–phase spectra. A detailed line assignment and comparison between theory and the high–resolution experiment is given for benz[a]anthracene in table 4.7 and mode descriptions in table , similar comparisons are available for each of the molecules in the supplemental material. Since resonance mixing between modes is so strong in this region assignment of each band to a fundamental or combination band is impossible. Instead only the dominant resonant components (typically components that are over 10% mixed) and dominant intensity sources can be identified (note that these intensity sources are not necessarily the dominant resonant sources). Along with these identifications, an ID letter is given for each band which corresponds with the identification letters in the respective spectra shown.

4.5 Discussion

4.5.1 MIS

Excellent agreement between the MIS spectra and the convolved anharmonic spectra was achieved. See the supplemental material for figures of the theoretical spectra compared to experiment, as well as tables listing the band positions, relative intensities, and mode descriptions. Broadening of the C–H stretching modes due to solid state interactions between the PAH and the matrix prevents meaningful comparison in this region. Comparison between theory and experiment for the C–H modes is therefore reserved for the high–resolution gas–phase experiments.

The average absolute percent differences in line positions between the MIS spectra and the convolved theoretical spectra are given in table 4.3 for each molecule. Figure 5.5 shows a histogram of the percent differences between the line positions of the theory and MIS for all five species combined. This leads to a Gaussian distribution with the average deviation being 0.41% ±0.63%. Previous work [112] has shown that argon matrix interaction effects lead to an average deviation

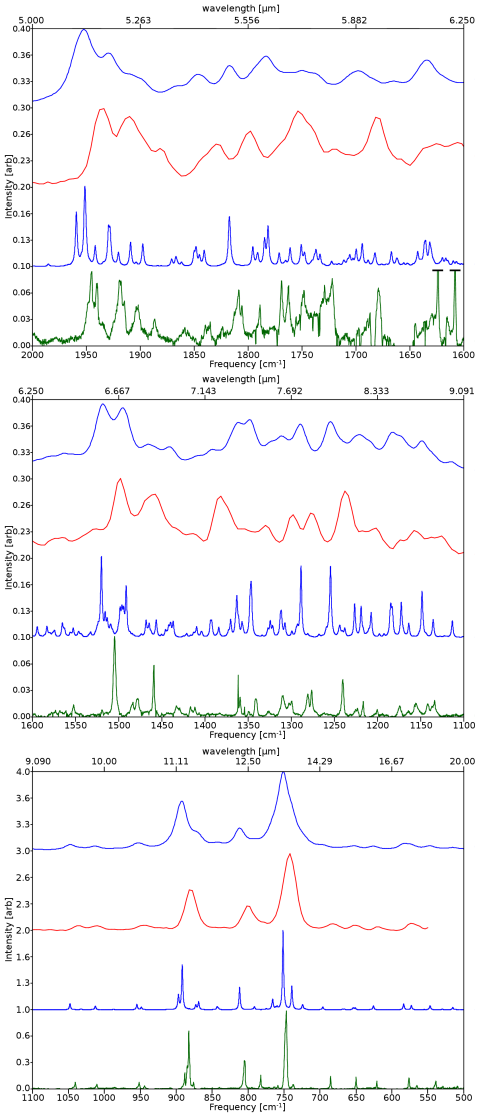

Figure 4.2 Comparison of the IR spectrum of benz[a]anthracene between the matrix–isolation experimental at 15 K (green, bottom spectrum of each panel), the theoretical anharmonic (this work) convolved with a FWHM of 2 cm^{-1} (blue, bottom middle spectrum of each panel), the gas–phase experimental at 300 K[21] (red, top middle spectrum of each panel), and the theoretical anharmonic (this work) convolved with a FWHM of 18 cm^{-1} (blue, top spectrum of each panel). Three spectral ranges are shown. Each range has its intensities normalized to the local maximum to enhance details. Water contaminant line intensities have been truncated.

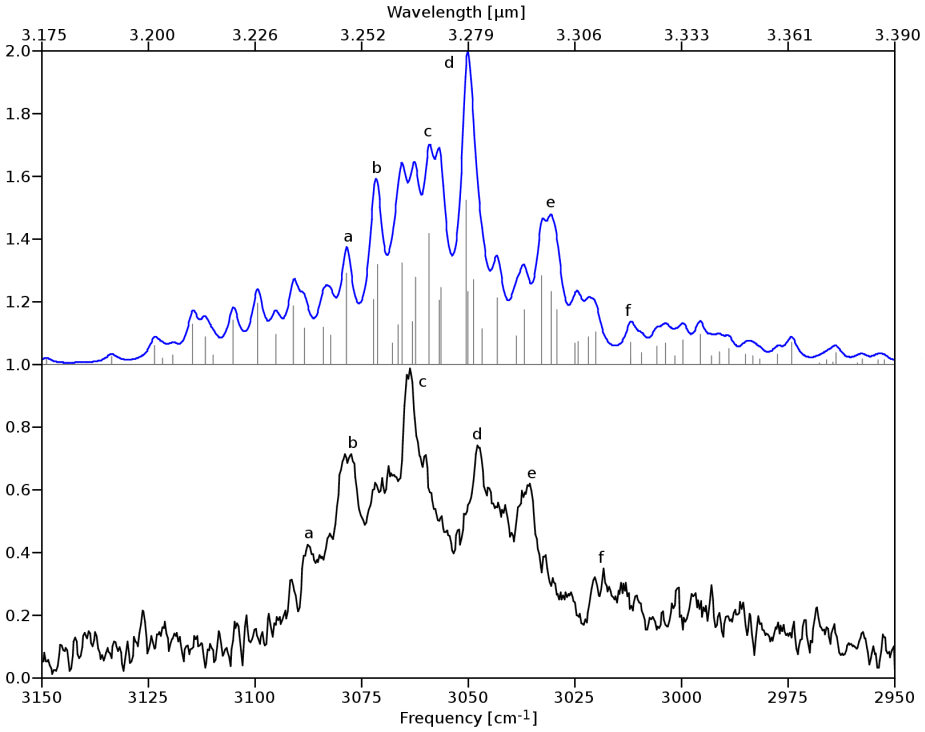

Figure 4.3 Anharmonic QFF IR spectrum of benz[a]anthracene (this work) compared to high–resolution gas–phase IR absorption spectra obtained in a molecular beam (this work).

ID	sym	exp[23]	rel. I[23]	anharm	rel. I	components	I source
a	a′	3087.8	0.37	3078.6	0.38	ν_2	ν_1
						ν_4	ν_2
						$\nu_{13} + \nu_{22}$	ν_3
						$\nu_{14} + \nu_{22}$	
b	a′	3079.0	0.69	3071.7	0.59	ν_1	ν_1
						ν_3	ν_2
						$\nu_{15} + \nu_{21}$	ν_3
c	a′	3063.8	1	3059.0	0.70	ν_2	ν_5
						ν_4	ν_2
						ν_5	
						ν_7	
						$\nu_{15} + \nu_{21}$	
						$\nu_{15} + \nu_{20}$	
						$\nu_{14} + \nu_{22}$	
d	a′	3047.8	0.73	3050.2	1	ν_5	ν_5
						$\nu_{14} + \nu_{24}$	
e	a′	3036.8	0.57	3030.7	0.48	$\nu_{13} + \nu_{24}$	ν_3
						$\nu_{17} + \nu_{20}$	ν_4
							ν_5
							ν_6
f	a′	3017.1	0.20	3012.0	0.14	$\nu_{17} + \nu_{21}$	ν_3
						$\nu_{14} + \nu_{25}$	ν_{12}
						$\nu_{15} + \nu_{24}$	

Table 4.1 Line positions [cm^{-1}], relative intensities, dominant resonant components, and origin of intensities for the bands of the benz[a]anthracene in the high–resolution gas–phase IR absorption spectra obtained in a molecular beam (this work) and the theoretical anharmonic spectrum (this work) as shown in figure 4.12.

Mode	Freq	Symm	Description
ν_1	3194.66	a′	bay symm CH stretch
ν_2	3185.43	a′	non-bay quartet symm CH stretch
ν_3	3183.64	a′	bay symm CH stretch
ν_4	3174.57	a′	bay asymm CH stretch
ν_5	3173.06	a′	non-bay quartet asymm CH stretch/duo CH stretch
ν_6	3172.62	a′	duo CH stretch/non-bay quartet asymm CH stretch/bay asymm CH stretch
ν_7	3166.93	a′	bay quartet CH stretch/bay asymm CH stretch
ν_{12}	3151.39	a′	non-bay singlet/non-bay duo asymm CH stretch
ν_{13}	1659.10	a′	“anthracene” edge CC stretch
ν_{14}	1651.83	a′	outer corner CC stretch
ν_{15}	1640.63	a′	“benzene” edge CC stretch
ν_{17}	1591.75	a′	ring fusing carbons CC stretch
ν_{20}	1508.64	a′	duo/non-bay quartet CH bend
ν_{21}	1482.50	a′	duo/bay quartet CH bend
ν_{22}	1467.65	a′	quartet/quartet CH bend
ν_{24}	1438.95	a′	duo CH bend
ν_{25}	1410.64	a′	singlet CH bend

Table 4.2 Mode descriptions and harmonic frequencies [cm^{-1}] of the IR active modes and modes involved in IR active combination bands/resonances identified in the CH–stretching region of benz[a]anthracene.

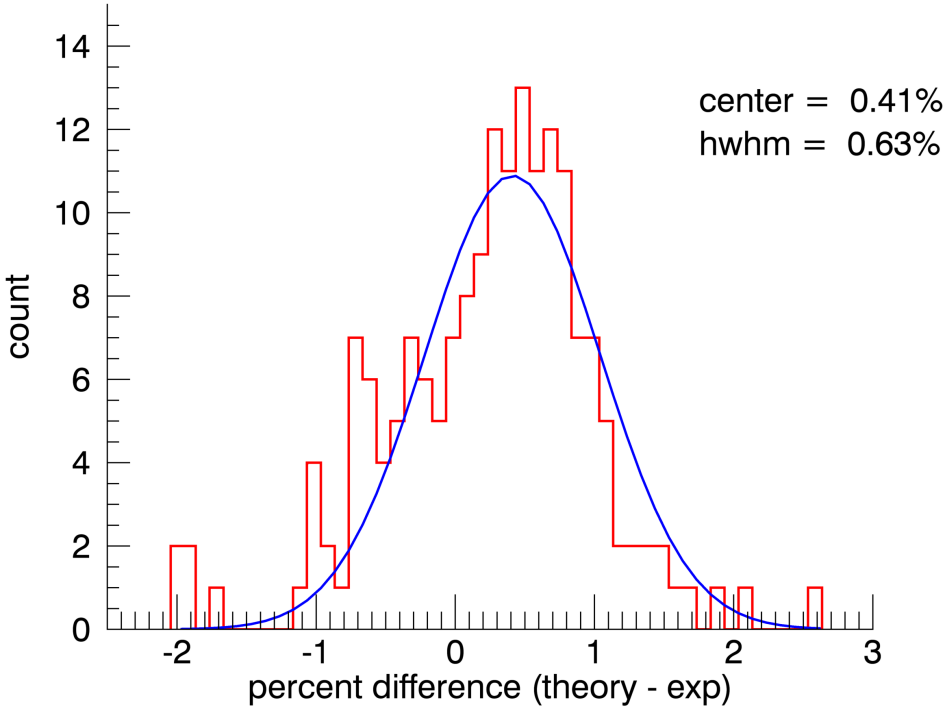

Figure 4.4 Histogram showing the percent differences between the line positions of the anharmonic theory (this work) and (from top to bottom) the MIS experiments for all five PAH species combined.

Molecule	MIS	I	NIST	I	C–H	I
benz[a]anthracene	0.67	66.5	1.02	38.3	0.19	21.7
chrysene	0.72	75.2	0.74	43.2	0.12	40.9
phenanthrene	0.47	53.9	0.55	68.5	0.21	39.7
pyrene	0.73	128	0.97	83.1	0.14	37.8
triphenylene	0.67	44.4	0.85	126	0.15	44.5

Table 4.3 Average absolute percent difference in line positions and relative intensities between the MIS, low–resolution high–temperature gas–phase (NIST), and the high–resolution low–temperature gas–phase (C–H) and the corresponding convolved theoretical anharmonic spectra of this work.

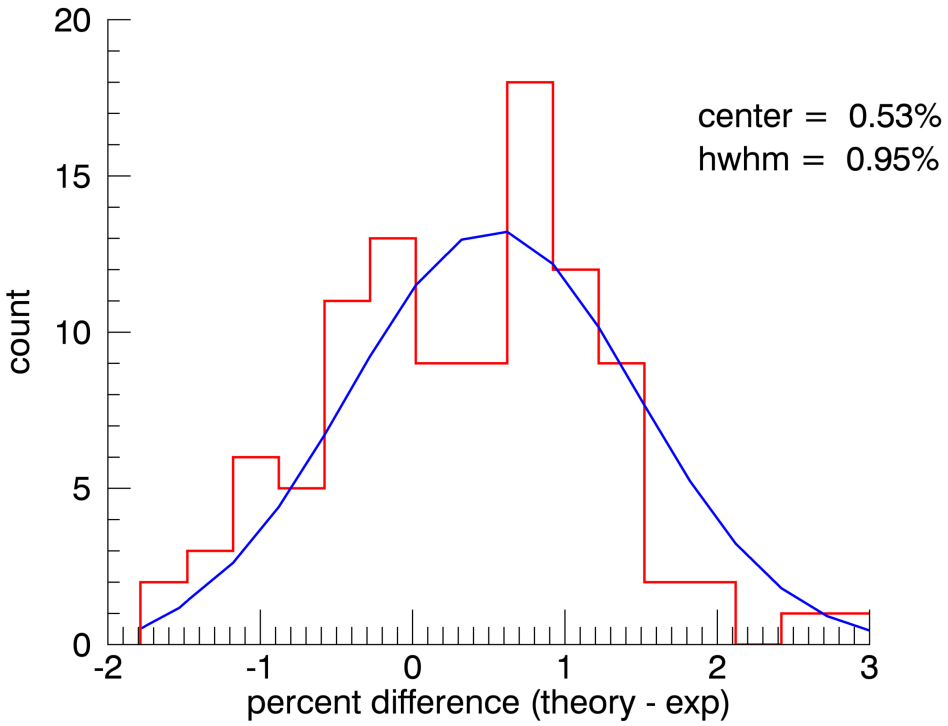

Figure 4.5 Histogram showing the percent differences between the line positions of the anharmonic theory (this work) and (from top to bottom) the NIST gas–phase experiments for all five PAH species combined.

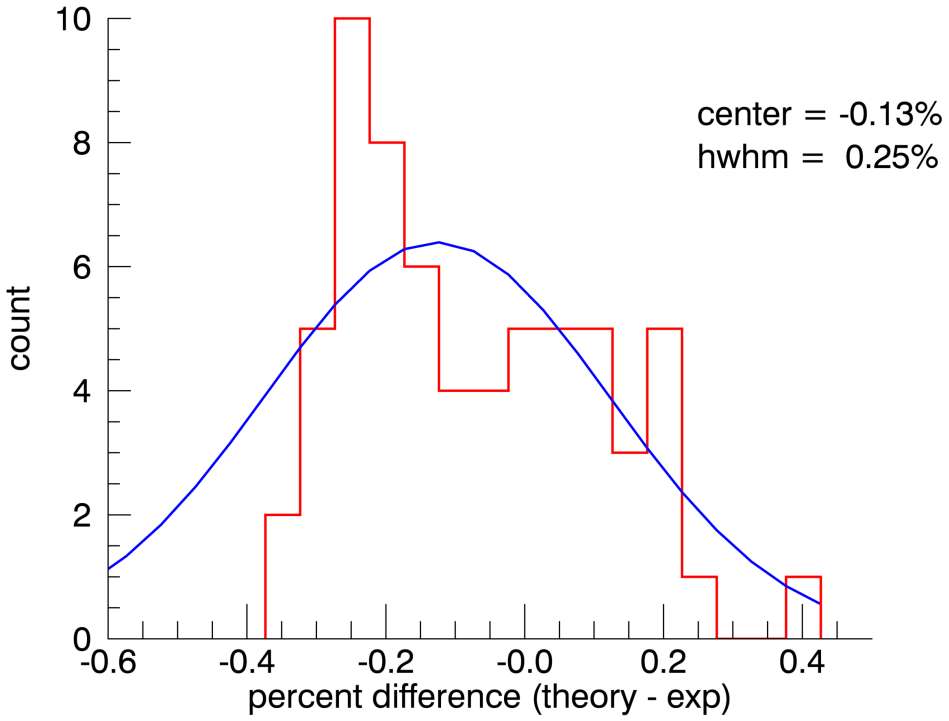

Figure 4.6 Histogram showing the percent differences between the line positions of the anharmonic theory (this work) and (from top to bottom) the low–temperature high–resolution gas–phase experiments for all five PAH species combined.

from the gas phase by 0.21% ±0.87%. The theoretical line positions in this work can therefore be determined accurately to within experimental limitations of MIS spectroscopy.

The average absolute percent differences in relative band intensities (relative to the peak intensity of the strongest out–of–plane C–H mode) between the MIS spectra and the convolved theoretical spectra are given in table 4.3 for each molecule. Matrix interaction effects on band intensities are not as well known as are line positions. However, since the largest deviations are seen for the weakest bands it is plausible that matrix effects are indeed occurring. Nevertheless, overall intensity features match well enough between theory and experiment that line assignment is generally unambiguous.

With the inclusion of anharmonicity the theoretical spectra now can reproduce the large number of combination bands with significant intensities that appear in the experimental spectra. From ~1200 – 1600 cm^{-1} there are a number of combination bands interspersed with the fundamental bands. These include in–plane ring deformations + in–plane ring deformations, out–of–plane C–H bends + out–of–plane drumheads, and out–of–plane C–H bends + out–of-plane C–C bends. The region from ~1600 – 2000 cm^{-1} is dominated by out–of–plane C–H bend + out–of–plane C–H bend combination bands; no fundamentals, and no other types of combination bands have appreciable intensity in this region.

4.5.2 High–temperature gas–phase

Excellent agreement between the low–resolution gas–phase spectra and the convolved anharmonic spectra was also achieved. See the supplemental material for figures of the theoretical spectra compared to experiment, as well as tables listing the band positions, and relative intensities.

The average absolute percent differences in line positions between the high–temperature gas–phase experimental spectra are given in table 4.3 for each molecule. Figure 4.5 shows a histogram of the percent differences between the line positions of the anharmonic theory and the high–temperature gas–phase for all five species combined. This leads to a Gaussian distribution with the average deviation being 0.53% ±0.95%. Using the temperature dependance linear fit equations of ref. 45 (using the pyrene and coronene data in this region) the expected average deviation due to temperature is calculated to be 0.52%. The theoretical line positions in this work can therefore be considered accurate to within temperature dependent shifts.

The average absolute percent differences in relative band intensities (relative to the peak intensity of the strongest out–of–plane C–H mode) between the high–temperature gas–phase experimental spectra and the convolved theoretical spectra is given in table 4.3 for each molecule. Temperature effects and line widths make intensity comparison unreliable. Nevertheless, as in the MIS case overall intensity features match well enough between theory and experiment that spectral feature assignment is unambiguous.

4.5.3 C–H stretching region (low–temperature gas–phase)

A high level of qualitative and quantitative agreement between theory and experiment was achieved for the low–temperature gas–phase experiments. See the supplemental material for figures of the theoretical spectra compared to experiment, as well as tables listing the band positions and assignments, relative intensities, and dominant resonances with mode descriptions.

The average absolute percent difference in line positions between the low–temperature high–resolution gas–phase experimental spectra in the C–H stretching region and the convolved theoretical spectra is given in table 4.3 for each molecule. Figure 5.4 shows a histogram of the percent differences between the line positions of the anharmonic theory and the high–resolution low–temperature gas–phase spectra for all five species combined. The number of bands observed for the five species in the C–H stretching region are limited, as such the statistics on this region are less rigorous. With this in consideration, this leads to a tentative Gaussian distribution with the average deviation being -0.13% ±0.25%. Agreement is best for the low–temperature high–resolution gas–phase data where physical perturbations are minimized.

The average absolute percent differences in relative band intensities (relative to the peak intensity of the strongest band in the C–H stretching region of each molecule) between the low–temperature high–resolution gas–phase experimental spectra and the convolved theoretical spectra is given in table 4.3 for each molecule. Again, agreement is best for the low–temperature high–resolution gas–phase data where physical perturbations are minimized.

This level of agreement in the C–H stretching region provides validation for the theoretical approach used in this work. It is possible that the remaining small deviations in line position and intensities between theory and experiment could be explained by the level of theory used. We therefore performed an MP2 with a cc-pVDZ basis set anharmonic analysis on naphthalene. After performing these calculations a slight improvement in some line positions was seen, but many experimental bands were still unexplained (possible triple combination bands[22]) or not improved at all. This leads to the conclusion that it may be more beneficial to include additional anharmonic terms (quintic, sextic, etc.), than to increase the level of theory. It should be noted that due to the size of PAHs, both raising the level of theory or including additional anharmonic terms is currently computationally not yet feasible.

The anharmonic analysis shows that resonances play a dominant role in describing the C–H stretching region of PAHs. Harmonic calculations predict only a handful of active modes in this region, while the experimental results show many. These additional modes were found to occur due to mainly type two Fermi resonances. It was also found that the strong resonances in this region *always* occur between one C–H stretching fundamental in resonance with an in–plane C–H bending mode in combination with an in–plane C–C stretching mode (see appendix for mode descriptions). Combinations between two in–plane C–H bends or two in–plane C–C stretches do not show strong coupling to the C–H stretching modes, even though the sum of their energies would put them in range to resonate in a

type two Fermi resonance.

4.5.4 Astrophysical implications

This study, in conjunction with our previous work[106] demonstrates the need for anharmonicities to be taken into account when studying astronomical IR PAH spectra. Again, we see how the current modelling of the AIBs can fall short due to the poor reliability of harmonic IR spectra.

The C–H stretching region is especially problematic as the shape and strength of the bands are controlled by resonances. This region can therefore only be understood properly by introducing anharmonicities to models and using an appropriate treatment of resonant states. This conclusion is even more important in the context of the upcoming launch of the James Webb Space Telescope, which will provide high–resolution spectra of this spectral region. Up until now harmonic IR models have sufficed due to the lack of high–resolution astronomical observations of this region, but it is clear that these will not suffice when high-resolution data will become available. This short-coming, in turn, will also be of major impact on the usefulness of astronomical models.

The pure combination band region is controlled by C–H out–of–plane + C–H out–of–plane combination bands. This region can also only be explained by introducing anharmonicities to models. These features have been observed in astronomical observations[102] and since this region is controlled by only C–H out–of–plane modes it may provide an additional means of characterizing the edge structure of astronomical PAHs. Investigations are currently underway.

Temperature effects, emission models, and PAH destruction models are also greatly affected by including anharmonicities. All of these properties are affected by the density of states of excited PAHs. Introducing anharmonicities dramatically changes the complexity of the available states. Investigations on these effects on the theoretical spectra are currently underway.

4.6 Conclusions

Five non–linear PAHs were considered in this work: benz[a]anthracene, chrysene, phenanthrene, pyrene, and triphenylene. All theoretical spectra show excellent agreement in band positions with the three types of experiments shown. The theoretical band positions have been shown to be in agreement with the MIS data to within an average of 0.41% with a standard deviation of 0.63%, with high–temperature gas–phase to within an average of 0.53% with a standard deviation of 0.95%, and with low–temperature gas–phase in the C–H stretching region to within an average of -0.13% with a standard deviation of 0.25%. The good comparison with the high–resolution, low–temperature gas–phase spectra is particularly gratifying as these spectra provide “ground truth”. Further, this is the region that is theoretically the most challenging due to the dominance of Fermi resonances, and hence we take it that this good comparison implies that in the absence of gas–phase data anharmonic calculations are the instrument of choice when analyzing astronomical observations.

Intensity comparison between the anharmonic IR spectra and experiments shows moderate agreement for the MIS and high-temperature gas-phase data. Temperature effects and matrix interaction effects could be responsible for the larger discrepancies in intensities. High–resolution data where these effects are absent show better agreement. This underlines the need for experimental low–temperature gas–phase spectra in the complete IR range. Triphenylene (see section 4.6) shows intensity problems, both due to a poorly estimated QFF and erroneously calculated anharmonic intensities.

The reduction of symmetry to handle a symmetric top molecule, such as triphenylene, with the anharmonic approach presented in this work has been shown to have limitations, but the results are surprisingly good in the C–H stretching region. Further investigation into other highly symmetric molecules as well as other techniques for dealing with symmetric tops are warranted. SPECTRO is able to handle symmetric top molecules, but there is a potential issue for non–degenerate, non–totally symmetric modes which must be handled carefully[113]. Symmetric top molecules are of special importance since many current astronomical models, both theoretical and experimental, use coronene ($\mathcal{D}_{6h}$ symmetry) as a typical PAH stand–in. Efforts are currently underway to apply the methods described in this work to coronene in order to better understand the issues that arise.

Compared to harmonic calculations (see ref. 23 for a comparison in the C–H stretching region) the anharmonic calculations provide a vast improvement. Harmonic frequencies are off by typically over 4%, whereas the anharmonic frequencies are off by less than 1%. This level of agreement eliminates the need for an empirical scaling factor to bring harmonic calculations in line with experiment. Harmonic calculations can also not explain the large number of bands seen in the C–H stretching region (type two Fermi resonances), or reproduce any of the large number of bands seen in the 1600–2000 cm^{-1} region (combination bands), while anharmonic calculations can. These conclusions are important as they imply that also for compounds for which it so far has not been possible to record experimental IR spectra it is possible to use theoretically predicted spectra as a reliable proxy. This, in turn, paves the way for a full in–silico screening of PAH models.

Patterns are beginning to arise with the anharmonic effects on the spectra of PAHs, especially in the resonance structure of the C–H stretching region and pure combination band region. *All* strong bands occurring in the C–H stretching region involve type two Fermi resonances ($\nu_a + \nu_b \approx \nu_c$) consisting of C–C stretching modes in combination with in–plane C–H bending modes resonating with in–plane C–H stretching fundamentals. Likewise, *all* strong bands occurring in the pure combination band region are combinations of two out–of–plane C–H bends. This, along with symmetry considerations, greatly simplifies the number of interacting modes to consider, and accounts for most of the anharmonic effects observed. This holds promise for generalizing anharmonic effects in order to avoid full anharmonic QFF analysis for many individual PAH species. However, a larger set of test cases, including larger PAHs sizes and various molecular symmetries, is necessary in order to further develop these generalizations and techniques. Efforts are currently underway. PAH derivatives (methylated, hydrogenated, dehydrogenated, nitrogen–substituted, cations, anions, etc.) are also of great interest to

astronomers. For that reason this work is also being extended into investigating anharmonic effects on these species.

Acknowledgments

The authors would like to thank the two anonymous reviewers for their helpful comments that improved the clarity of the manuscript. The spectroscopic study of interstellar PAHs at Leiden Observatory have been supported through the Advanced European Research Council Grant 246976, a Spinoza award, and through the Dutch Astrochemistry Network funded by the Netherlands Organization for Scientific Research, NWO. Computing time has been made available by NWO Exacte Wetenschappen (project MP–270–13 and MP–264) and calculations were performed at the LISA Linux cluster of the SurfSARA supercomputer center in Almere, The Netherlands. AC acknowledges NWO for a VENI grant (639.041.543). AP acknowledges NWO for a VIDI grant (723.014.007). XH and TJL gratefully acknowledge support from the NASA 12–APRA12–0107 grant. XH acknowledges the support from NASA/SETI Co–op Agreement NNX15AF45A. This material is based upon work supported by the National Aeronautics and Space Administration through the NASA Astrobiology Institute under Cooperative Agreement Notice NNH13ZDA017C issued through the Science Mission Directorate.

Appendix

Triphenylene

Triphenylene is a symmetric top, with $\mathcal{D}_{3h}$ symmetry. Gaussian09 cannot handle symmetric tops at the anharmonic level. Therefore, to circumvent this triphenylene was approximated as an asymmetric top by slightly perturbing the masses of two opposing carbon atoms of the central ring from 12 au to 12.01 au, consequently lowering the symmetry to C_{2v}.

By perturbing the masses slightly the symmetry of a molecule breaks, while preserving the symmetry of the potential energy surface as much as possible. Perturbing the masses resulted in the degenerate harmonic modes splitting by ~0.01%, leaving the potential with nearly the same symmetry at the harmonic level. The symmetry of the potential at the anharmonic level can be estimated by comparing the cubic force constants [114]. For degenerate modes of a symmetric top, the normal coordinate cubic force constants are related by

$$F_{aaa} = -F_{abb} \tag{4.1}$$

where a and b are components of a degenerate normal mode, and a is symmetric with respect to the operations of the point group while b is antisymmetric with respect to one operation.

For triphenylene the comparisons between the non–zero cubic force constants of the degenerate modes (14 pairs) shows a percent difference of 28% on average.

The sign of the cubic force constants are all found to be correct between pairs. This result shows that the symmetry of the QFF of triphenylene is more broken than ideal, most likely due to the level of theory used.

Performing the VPT2 anharmonic analysis with SPECTRO with this slightly broken symmetry QFF, it was found that there is moderate agreement in the 1600 – 2000 cm^{-1} region. Major deviations however, can be seen in between 1400 and 1550 cm^{-1} (see the supplemental material). The appearance of additional strong bands in this region (and a few minor bands in the 1600 – 2000 cm^{-1} region) are a result of the over–estimation of resonance strengths between modes caused by the breakdown of the QFF. For bands <1400 cm^{-1} major deviations are found with the anharmonic intensities reported by Gaussian09. Some anharmonic bands were found to have intensities two, or even sometimes three, orders of magnitude too high (not shown). For the <1400 cm^{-1} region we therefore reverted to using the harmonic intensities in our analysis. The extremely large intensities are likely due to "resonances" between modes that are actually different components of a degenerate vibration and are a byproduct of using an asymmetric top formulation for a symmetric top molecule.

The C–H stretching region, on the other hand, shows excellent agreement with experiment. This agreement is due to the fact that the parts of the QFF affecting resonances between C–H in–plane modes appear to largely unaffected by the symmetry lowering. Harmonic intensities are being utilized in this region for all molecules, so spurious anharmonic intensities are already excluded. The lowering of the symmetry of the molecule also led to changes in the symmetries of the individual bands, complicating assigning symmetries to individual bands, especially combination bands. Therefore, no symmetries are listed in the supplemental material.

4.7 Supplemental Material

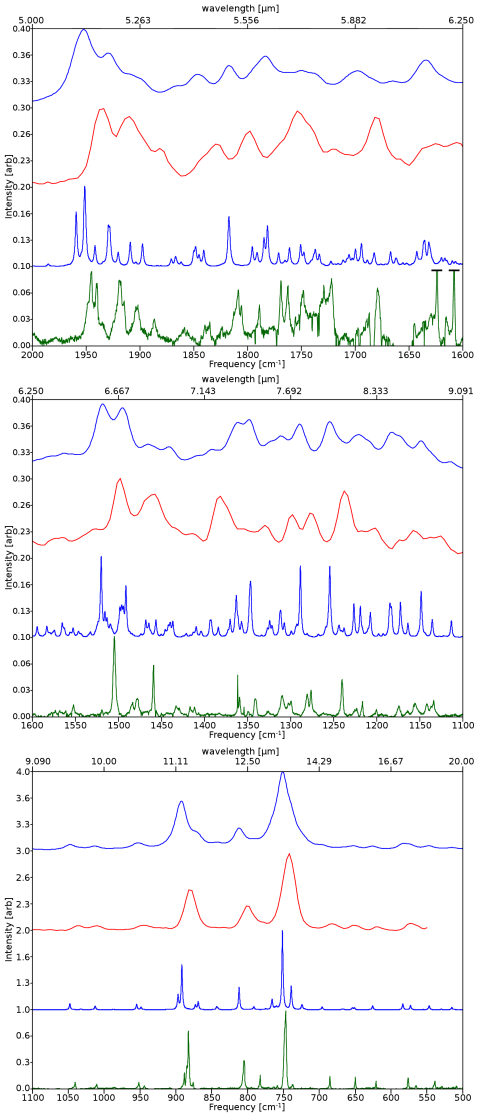

Figure 4.7 Comparison of the IR spectrum of benz[a]anthracene between the matrix–isolation experimental at 15 K (green, bottom spectrum of each panel), the theoretical anharmonic (this work) convolved with a FWHM of 2 cm^{-1} (blue, bottom middle spectrum of each panel), the gas–phase experimental at 300 K[21] (red, top middle spectrum of each panel), and the theoretical anharmonic (this work) convolved with a FWHM of 18 cm^{-1} (blue, top spectrum of each panel). Three spectral ranges are shown. Each range has its intensities normalized to the local maximum to enhance details. Water contaminant line intensities have been truncated.

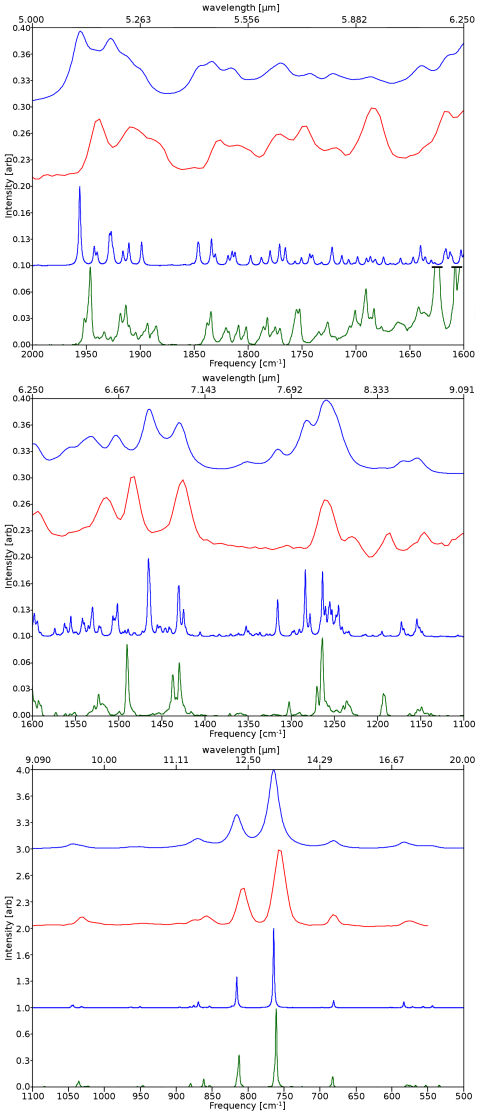

Figure 4.8 Comparison of the IR spectrum of chrysene between the matrix–isolation experimental at 15 K (green, bottom spectrum of each panel), the theoretical anharmonic (this work) convolved with a FWHM of 2 cm^{-1} (blue, bottom middle spectrum of each panel), the gas–phase experimental at 300 K[21] (red, top middle spectrum of each panel), and the theoretical anharmonic (this work) convolved with a FWHM of 18 cm^{-1} (blue, top spectrum of each panel). Three spectral ranges are shown. Each range has its intensities normalized to the local maximum to enhance details; see table 4.4 for true relative intensities. Water contaminant line intensities have been truncated.

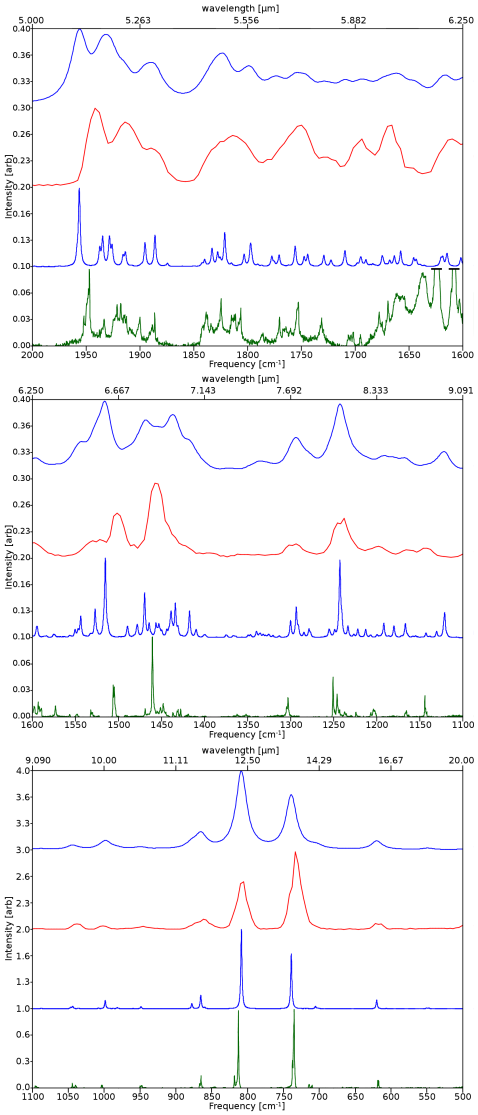

Figure 4.9 Comparison of the IR spectrum of phenanthrene between the matrix–isolation experimental at 15 K (green, bottom spectrum of each panel), the theoretical anharmonic (this work) convolved with a FWHM of 2 cm^{-1} (blue, bottom middle spectrum of each panel), the gas–phase experimental at 300 K[21] (red, top middle spectrum of each panel), and the theoretical anharmonic (this work) convolved with a FWHM of 18 cm^{-1} (blue, top spectrum of each panel). Three spectral ranges are shown. Each range has its intensities normalized to the local maximum to enhance details; see table 4.4 for true relative intensities. Water contaminant line intensities have been truncated.

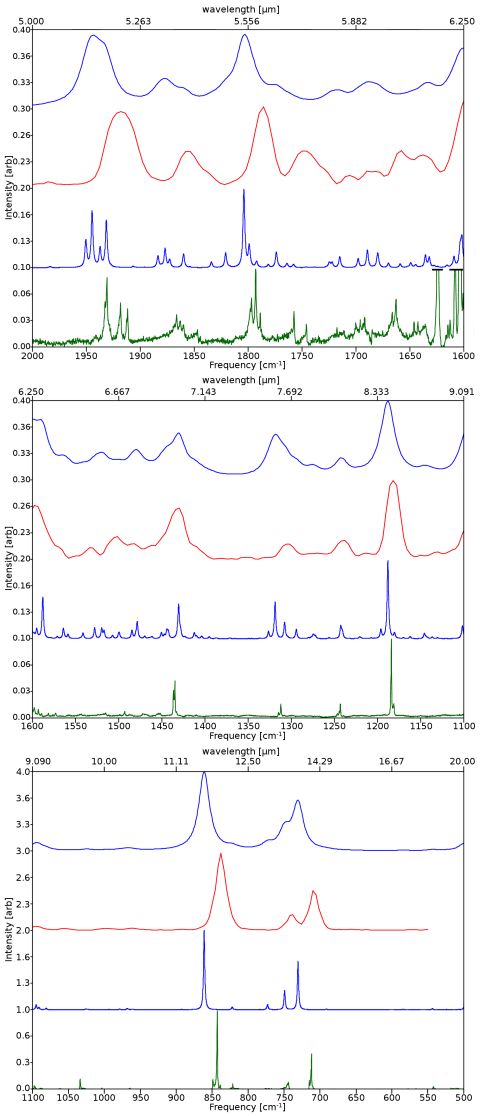

Figure 4.10 Comparison of the IR spectrum of pyrene between the matrix–isolation experimental at 15 K (green, bottom spectrum of each panel), the theoretical anharmonic (this work) convolved with a FWHM of 2 cm^{-1} (blue, bottom middle spectrum of each panel), the gas–phase experimental at 300 K[21] (red, top middle spectrum of each panel), and the theoretical anharmonic (this work) convolved with a FWHM of 18 cm^{-1} (blue, top spectrum of each panel). Three spectral ranges are shown. Each range has its intensities normalized to the local maximum to enhance details; see table 4.4 for true relative intensities. Water contaminant line intensities have been truncated.

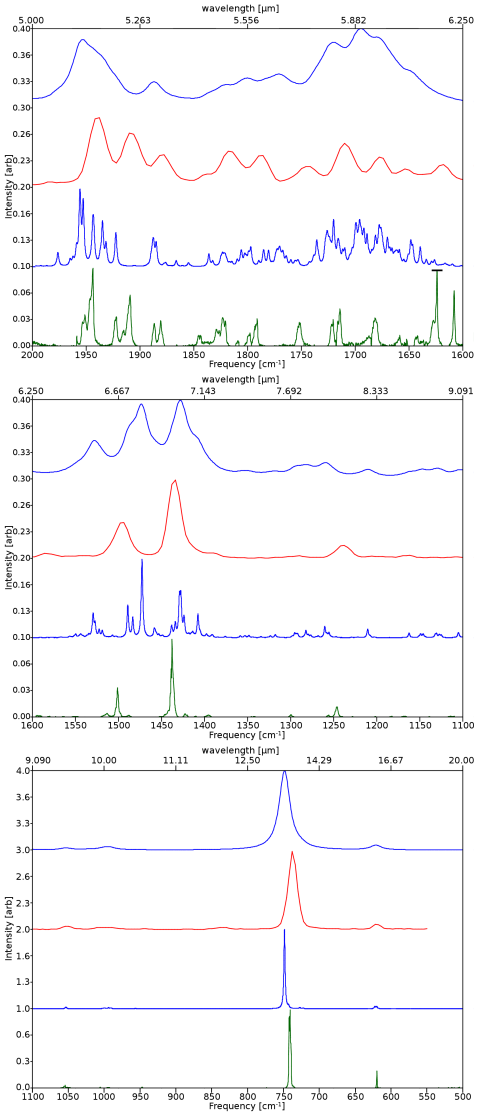

Figure 4.11 Comparison of the IR spectrum of triphenylene between the matrix–isolation experimental at 15 K (green, bottom spectrum of each panel), the theoretical anharmonic (this work) convolved with a FWHM of 2 cm^{-1} (blue, bottom middle spectrum of each panel), the gas–phase experimental at 300 K[21] (red, top middle spectrum of each panel), and the theoretical anharmonic (this work) convolved with a FWHM of 18 cm^{-1} (blue, top spectrum of each panel). Three spectral ranges are shown. Each range has its intensities normalized to the local maximum to enhance details; see table 4.4 for true relative intensities. Water contaminant line intensities have been truncated.

Table 4.4: MIS line positions [cm^{-1}] and relative intensities [arb], and corresponding theoretical line positions and relative intensities determined from the simulated spectrum (convolved with a FWHM of 2 cm^{-1} Fig. 4.7 – 4.10). Bands are arranged by vibrational mode description, determined from theoretical data. Similar spectral features between species are aligned across the rows.

Benz[a]anthracene				Chrysene				Phenanthrene				Pyrene				Triphenylene			
Matrix	I	Theory	I	Matrix	I	Theory	I	Matrix	I	Theory	I	Matrix	I	Theory	I	Matrix	I	Theory	I
ring stretch/deformations																			
				534.4	0.02	543.9	0.03												
576.6	0.14	583.9	0.08	567.4	0.02	571.7	0.01												
621.3	0.10	626.0	0.05	574.8	0.02	-	-	618.2	0.08	620.3	0.11					620.0	0.27	621.5	0.06
650.2	0.15	651.4	0.03																
				682.7	0.13	681.3	0.09												
								710.6	0.03	705.7	0.03								
758.8	0.04	759.9	0.05																
				853.7	0.02	854.1	0.02												
				880.4	0.05	875.9	0.03												
																993.4	0.01	994.2	0.01
								1003.3	0.04	998.7	0.10					1005.8	0.01	999.8	0.01
out–of–plane C–H bends																			
539.5	0.09	547.2	0.05																
565.6	0.04	573.1	0.05	553.2	0.02	556.8	0.02												
685.6	0.15	696.4	0.04																
737.7	0.05	739.5	0.30																
747.8	1	751.7	1	761.2	1	764.7	1	735.7	1	739.4	0.69	730.9	0.61	741.0	1	748.9	1		
782.8	0.15	791.5	0.04									744.1	0.09	749.6	0.24				
805.4	0.36	812.1	0.29	813.3	0.41	816.0	0.39	813.1	0.88	808.9	1	843.0	1	861.4	1				
882.7	0.79	891.9	0.57	862.1	0.09	869.5	0.08	865.4	0.12	865.6	0.17								
944.3	0.03	948.9	0.03	946.8	0.02	950.6	0.02	948.5	0.03	948.8	0.02	964.8	0.01	968.6	0.02	947.4	0.02	956.6	0.01
952.1	0.07	954.9	0.06	954.8	0.01	962.9	0.01												
out–of–plane C–C bends																			
				578.9	0.03	583.6	0.07												
												712.3	0.36						
in–plane C–C bends																			
												821.7	0.07	822.4	0.04				
in–plane C–H bends																			
1011.0	0.05	1012.7	0.05																
								1040.0	0.04	1036.6	0.01								
1040.8	0.08	1048.0	0.08									1033.9	0.12	-	-	1054.5	0.03	1053.5	0.02
												1088.4	0.01	1081.0	0.02				

Table 4.4 – continued from previous page

Benz[a]anthracene				Chrysene				Phenanthrene				Pyrene				Triphenylene			
Matrix	I	Theory	I	Matrix	I	Theory	I	Matrix	I	Theory	I	Matrix	I	Theory	I	Matrix	I	Theory	I
1134.9	0.03	1113.7	0.02																
1142.1	0.03	1135.7	0.03	1149.0	0.01	1154.7	0.02	1144.2	0.04	1121.4	0.02								
1155.5	0.03	1148.7	0.07	1153.4	0.01	1172.5	0.02												
1164.6	0.01	1172.7	0.05					1166.2	0.01	1167.0	0.02								
1174.6	0.02	1184.9	0.05																
1200.7	0.01	1207.6	0.04									1184.3	0.18	1188.3	0.14				
1276.5	0.06	1288.9	0.10					1250.9	0.11	1243.0	0.09					1246.7	0.04	1260.6	0.01
1310.0	0.05	1311.9	0.04																
1413.9	0.01	1409.9	0.02																
1459.6	0.13	1456.8	0.03																
in–plane C–C stretch																			
				1023.1	0.01	1032.2	0.02												
				1036.0	0.08	1043.5	0.05	1044.6	0.07	1046.8	0.02								
				1264.3	0.12	1283.9	0.06					1243.4	0.03	1242.9	0.02				
				1302.8	0.02	1315.8	0.04	1303.6	0.04	1293.7	0.03	1312.4	0.03	1319.0	0.06	1299.9	0.01	1294.2	0.01
1341.2	0.05	1346.7	0.08																
1360.7	0.04	1363.2	0.06																
				1416.2	0.01	1425.1	0.03	1431.5	0.02	1439.2	0.03					1422.9	0.01	1407.9	0.02
				1430.0	0.08	1430.4	0.05					1435.1	0.10	1430.7	0.06	1438.0	0.25	1428.5	0.04
				1437.7	0.06	1465.8	0.08												
1478.5	0.04	1491.5	0.06					1469.2	0.02	1478.3	0.02								
				1490.7	0.11	1501.4	0.03	1506.3	0.09	1515.5	0.09	1493.5	0.01	1478.8	0.03	1501.3	0.09	1472.9	0.06
1519.5	0.02	1516.0	0.04	1523.5	0.03	1539.9	0.01	1531.4	0.01	1544.1	0.02					1514.2	0.01	1489.4	0.03
				1551.3	0.01	1542.2	0.02												
				1590.1	0.01	1594.5	0.02					1604.4	0.08	1588.2	0.07				
ring stretch/deform + ring stretch/deform (combination bands)																			
												1097.3	0.03	1095.1	0.06				
1240.5	0.09	1254.7	0.10	1235.9	0.02	1245.4	0.03	1224.2	0.01	1213.2	0.01								
1326.4	0.01	1321.9	0.01																
								1427.9	0.02	1434.2	0.04					1396.2	0.01	1391.4	0.01
ring breathing																			
				1192.8	0.03	1195.1	0.01	1203.5	0.02	1192.0	0.02								
out–of–plane bend + drum head (combination bands)																			
1217.0	0.03	1226.7	0.05																
1224.7	0.02	1238.2	0.01																
				1240.4	0.01	1255.5	0.04												
				1246.8	0.01	1264.0	0.07												
1301.5	0.03	1307.6	0.02																
1505.0	0.20	1520.3	0.12																
out–of–plane C–H bend + out–of–plane C–C bend (combination bands)																			
1281.2	0.05	1299.6	0.10	1270.4	0.04	1278.5	0.02												

Table 4.4 – continued from previous page

Benz[a]anthracene				Chrysene				Phenanthrene				Pyrene				Triphenylene			
Matrix	I	Theory	I	Matrix	I	Theory	I	Matrix	I	Theory	I	Matrix	I	Theory	I	Matrix	I	Theory	I
								1436.7	0.01	1444.1	0.01								
1432.0	0.02	1437.1	0.02					1448.4	0.04	1453.4	0.02								
								1451.5	0.03	1456.7	0.02								
1484.4	0.03	1496.5	0.04									1452.3	0.01	1444.3	0.02	1488.2	0.01	1458.2	0.01
1552.5	0.02	1565.6	0.02																
out–of–plane C–H bend + out–of–plane C–H bend (combination bands)																			
																1627.2	0.01	1639.7	0.01
				1641.9	0.02	1640.3	0.02	1637.2	0.04	-	-								
								1660.6	0.02	-	-								
								1669.7	0.01	1663.8	0.01	1663.0	0.02	-	-				
1679.2	0.03	1667.4	0.02	1690.8	0.02	1686.9	0.01	1678.0	0.01	1675.0	0.01					1681.8	0.01	1676.9	0.02
				1701.0	0.01	1698.7	0.01												
1722.2	0.03	1733.5	0.01					1731.4	0.01	1729.4	0.01					1714.4	0.01	1720.3	0.02
1728.9	0.03	1737.3	0.02																
1747.4	0.02	1750.9	0.02																
				1755.5	0.01	1743.1	0.01	1753.8	0.01	1756.0	0.02					1752.1	0.01	1772.1	0.01
1763.1	0.03	1781.6	0.04									1757.5	0.01	1774.0	0.02				
1769.1	0.03	1785.1	0.03																
1789.1	0.02	1795.7	0.02	1782.5	0.01	1765.7	0.02					1793.2	0.03	1804.1	0.11	1792.2	0.01	1797.4	0.01
												1797.1	0.02	1799.2	0.03				
				1802.5	0.01	1787.7	0.01												
1809.5	0.02	1817.6	0.05	1809.6	0.01	1797.9	0.01	1812.7	0.01	1803.5	0.01								
				1820.7	0.01	1834.2	0.01	1825.4	0.01	1821.5	0.03					1823.2	0.01	1822.4	0.01
				1834.8	0.01	1846.3	0.02	1837.7	0.01	1833.2	0.02								
1837.9	0.01	1841.0	0.02																
1858.8	0.01	1867.2	0.01									1866.5	0.01	1860.0	0.02				
																1880.9	0.01	1885.1	0.01
1887.1	0.01	1897.8	0.02	1886.1	0.01	1898.9	0.02									1887.0	0.01	1888.0	0.01
1903.1	0.02	1909.2	0.02	1893.6	0.01	1910.8	0.02	1900.9	0.01	1895.5	0.02								
								1918.4	0.02	1928.6	0.03	1912.3	0.01	1931.7	0.07	1909.3	0.01	1922.6	0.01
1918.9	0.03	1929.5	0.04	1918.5	0.01	1927.6	0.03					1918.9	0.01	1937.4	0.03	1922.8	0.01	1935.1	0.02
1935.2	0.01	1942.0	0.02									1931.6	0.02	1944.9	0.08				
1940.1	0.04	1951.5	0.09																
1944.2	0.03	1959.5	0.06	1946.4	0.03	1956.3	0.06	1948.5	0.02	1956.6	0.07					1944.1	0.02	1952.9	0.02
																1951.4	0.01	1956.0	0.03
unidentified																			
												1003.8	0.01	-	-				
				1083.6	0.01	-	-												
								1095.4	0.03	-	-								
								1246.2	0.05	-	-								
																1256.4	0.01	-	-

Table 4.4 – continued from previous page

Benz[a]anthracene				Chrysene				Phenanthrene				Pyrene				Triphenylene			
Matrix	I	Theory	I	Matrix	I	Theory	I	Matrix	I	Theory	I	Matrix	I	Theory	I	Matrix	I	Theory	I
								1460.7	0.23	-	-								
								1573.4	0.03	-	-								
				1601.8	0.03	-	-												
water contamination																			
1608.3	0.07	-	-	1608.4	-	-	-	1608.3	0.19	-	-	1608.3	0.05	-	-	1608.4	0.01	-	-
1624.2	0.09	-	-	1624.1	-	-	-	1624.2	0.25	-	-	1624.2	0.11	-	-	1624.2	0.02	-	-

Benz[a]anthracene				Chrysene				Phenanthrene				Pyrene				Triphenylene			
Gas	I	Theory	I	Gas	I	Theory	I	Gas	I	Theory	I	Gas	I	Theory	I	Gas	I	Theory	I
570.9	0.09	582.5	0.10	574.2	0.08	583.6	0.09									620.1	0.07	621.5	0.06
619.2	0.05	624.6	0.05																
649.3	0.06	654.1	0.07					622.0	0.09	620.3	0.11								
685.3	0.07	699.2	0.08	682.0	0.18	681.3	0.11												
742.8	1	751.7	1	758.0	1	764.7	1	732.2	1	739.4	0.70	708.6	0.53	730.9	0.41	737.4	1	748.7	1
798.3	0.28	812.1	0.29									739.5	0.21	749.6	0.26				
879.9	0.54	892.8	0.62	806.0	0.51	816.1	0.43	808.0	0.66	808.9	1	838.1	1	861.3	1				
				858.0	0.16	870.6	0.13	862.8	0.13	865.6	0.23					835.6	0.02	-	-
940.0	0.06	952.4	0.10					945.7	0.03	949.2	0.04	964.8	0.01	967.0	0.04	944.6	0.01	956.4	0.01
1011.4	0.06	1013.4	0.06					1001.2	0.04	998.7	0.12	998.7	0.03	-	-	988.9	0.02	996.3	0.04
1036.9	0.06	1048.0	0.07	1030.0	0.14	1043.5	0.06	1038.3	0.08	1044.0	0.06	1054.2	0.03	-	-	1051.8	0.04	1053.1	0.02
								1090.7	0.01	1086.5	0.02	1095.3	0.05	1094.7	0.10				
1158.5	0.02	1148.7	0.09	1187.9	0.04	1195.9	0.02												
								1143.2	0.01	1133.2	0.03								
								1163.5	0.01	-	-								
1206.3	0.06	1225.5	0.07	1228.0	0.03	-	-	1200.9	0.02	1192.0	0.04								
1237.9	0.13	1255.1	0.12	1259.6	0.09	1258.7	0.16	1241.1	0.07	1243.0	0.12	1182.0	0.13	1188.3	0.14				
1275.9	0.09	1289.7	0.13									1241.3	0.02	1242.9	0.04	1239.0	0.03	1258.3	0.01
								1296.0	0.02	1293.7	0.06	1302.9	0.02	1318.7	0.08				
1327.5	0.05	1322.0	0.06																
1382.5	0.10	1364.2	0.11																
1417.4	0.05	1412.5	0.05																
1462.4	0.12	1463.9	0.06	1426.0	0.12	1430.2	0.11	1457.2	0.16	1469.1	0.10	1432.9	0.08	1430.7	0.08	1434.9	0.18	1425.9	0.08
												1483.0	0.02	-	-				
1498.5	0.12	1494.5	0.16	1482.0	0.11	1464.9	0.06	1500.7	0.09	1516.4	0.12	1504.0	0.04	1479.5	0.04	1496.5	0.08	1476.6	0.08
				1518.0	0.08	1503.4	0.09	1527.8	0.03	1545.6	0.06	1533.8	0.02	1520.0	0.05				
1571.8	0.04	1564.1	0.04																
1630.0	0.03	1621.5	0.05	1594.0	0.07	1599.2	0.07	1607.2	0.03	1617.1	0.03	1595.6	0.08	1595.8	0.11				
												1637.1	0.03	1634.6	0.04	1619.8	0.01	-	-
												1658.5	0.03	-	-				
1681.4	0.05	1697.0	0.06	1684.5	0.06	1686.9	0.03	1667.8	0.04	1659.5	0.04	1685.2	0.02	1688.7	0.04	1687.0	0.01	1687.2	0.09
								1696.5	0.03	1710.3	0.02	1707.2	0.01	1722.1	0.03	1709.5	0.02	-	-
1750.4	0.05	1784.9	0.07	1748.4	0.04	1741.0	0.02	1753.5	0.04	1748.7	0.04	1745.7	0.04	1774.1	0.04	1745.2	0.01	1723.9	0.04
1799.3	0.04	1817.8	0.06	1770.8	0.04	1769.9	0.05					1786.9	0.08	1803.2	0.14	1787.7	0.01	1772.3	0.02
1831.0	0.03	1843.2	0.04	1829.1	0.01	1845.5	0.03	1815.1	0.04	1823.7	0.06	1854.0	0.03	1877.2	0.05	1816.6	0.01	1805.4	0.02
1884.3	0.03	1907.6	0.05					1885.5	0.02	1887.6	0.05					1878.8	0.01	1886.2	0.02
1910.5	0.05	1928.5	0.06	1910.0	0.04	1927.8	0.07	1913.4	0.05	1932.0	0.08					1907.7	0.02	1936.1	0.04
1936.3	0.06	1952.1	0.12	1942.0	0.05	1956.8	0.07	1942.0	0.05	1957.1	0.05	1917.7	0.08	1943.1	0.13	1939.8	0.03	1954.8	0.06

Table 4.5 Gas phase[21] (300K) line positions [cm^{-1}] and relative intensities [arb], and corresponding theoretical line positions and intensities determined from the simulated spectrum (convolved with a FWHM of 18 cm^{-1}, Fig. 4.7 – 4.10). Similar spectral features between species are aligned across the rows.

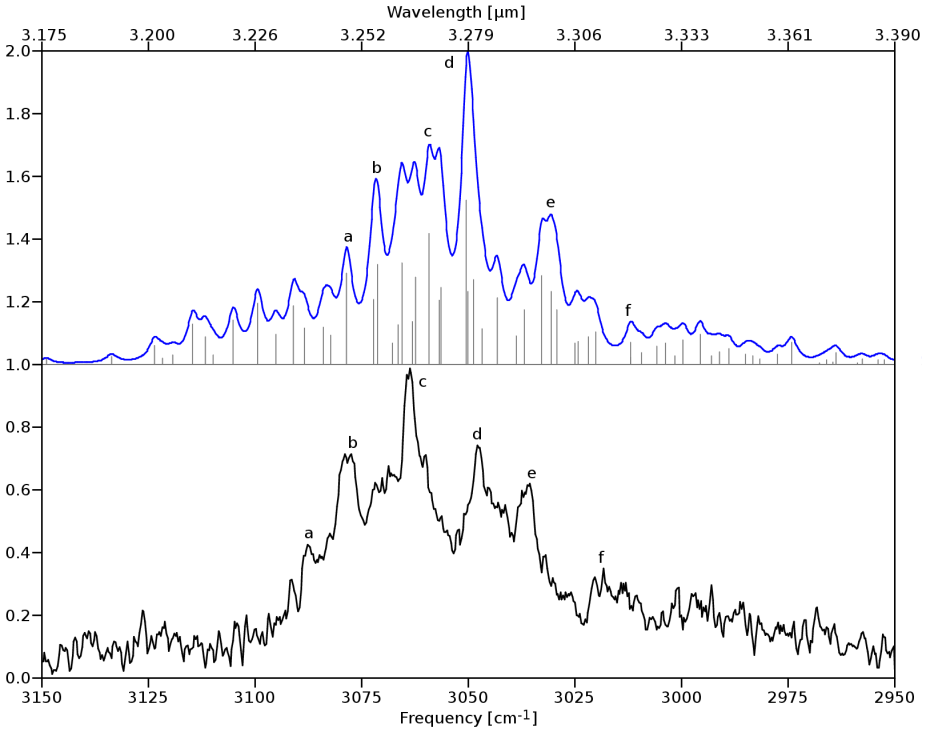

Figure 4.12 Anharmonic QFF IR spectrum of benz[a]anthracene (this work) compared to high–resolution gas–phase IR absorption spectra obtained in a molecular beam (this work).

Mode	Freq	Symm	Description
ν_1	3194.66	a′	bay symm CH stretch
ν_2	3185.43	a′	non-bay quartet symm CH stretch
ν_3	3183.64	a′	bay symm CH stretch
ν_4	3174.57	a′	bay asymm CH stretch
ν_5	3173.06	a′	non-bay quartet asymm CH stretch/duo CH stretch
ν_6	3172.62	a′	duo CH stretch/non-bay quartet asymm CH stretch/bay asymm CH stretch
ν_7	3166.93	a′	bay quartet CH stretch/bay asymm CH stretch
ν_{12}	3151.39	a′	non-bay singlet/non-bay duo asymm CH stretch
ν_{13}	1659.10	a′	“anthracene” edge CC stretch
ν_{14}	1651.83	a′	outer corner CC stretch
ν_{15}	1640.63	a′	“benzene” edge CC stretch
ν_{17}	1591.75	a′	ring fusing carbons CC stretch
ν_{20}	1508.64	a′	duo/non-bay quartet CH bend
ν_{21}	1482.50	a′	duo/bay quartet CH bend
ν_{22}	1467.65	a′	quartet/quartet CH bend
ν_{24}	1438.95	a′	duo CH bend
ν_{25}	1410.64	a′	singlet CH bend

Table 4.6 Mode descriptions and harmonic frequencies [cm^{-1}] of the IR active modes and modes involved in IR active combination bands/resonances identified in the CH–stretching region of benz[a]anthracene.

ID	sym	exp[23]	rel. I[23]	anharm	rel. I	components	I sources
a	a′	3087.8	0.37	3078.6	0.38	ν_2	ν_1
						ν_4	ν_2
						$\nu_{13} + \nu_{22}$	ν_3
						$\nu_{14} + \nu_{22}$	
b	a′	3079.0	0.69	3071.7	0.59	ν_1	ν_1
						ν_3	ν_2
						$\nu_{15} + \nu_{21}$	ν_3
c	a′	3063.8	1	3059.0	0.70	ν_2	ν_5
						ν_4	ν_2
						ν_5	
						ν_7	
						$\nu_{15} + \nu_{21}$	
						$\nu_{15} + \nu_{20}$	
						$\nu_{14} + \nu_{22}$	
d	a′	3047.8	0.73	3050.2	1	ν_5	ν_5
						$\nu_{14} + \nu_{24}$	
e	a′	3036.8	0.57	3030.7	0.48	$\nu_{13} + \nu_{24}$	ν_3
						$\nu_{17} + \nu_{20}$	ν_4
							ν_5
							ν_6
f	a′	3017.1	0.20	3012.0	0.14	$\nu_{17} + \nu_{21}$	ν_3
						$\nu_{14} + \nu_{25}$	ν_{12}
						$\nu_{15} + \nu_{24}$	

Table 4.7 Line positions [cm^{-1}], relative intensities, dominant resonant components, and origin of intensities for the bands of the benz[a]anthracene in the high–resolution gas–phase IR absorption spectra obtained in a molecular beam (this work) and the theoretical anharmonic spectrum (this work) as shown in figure 4.12.

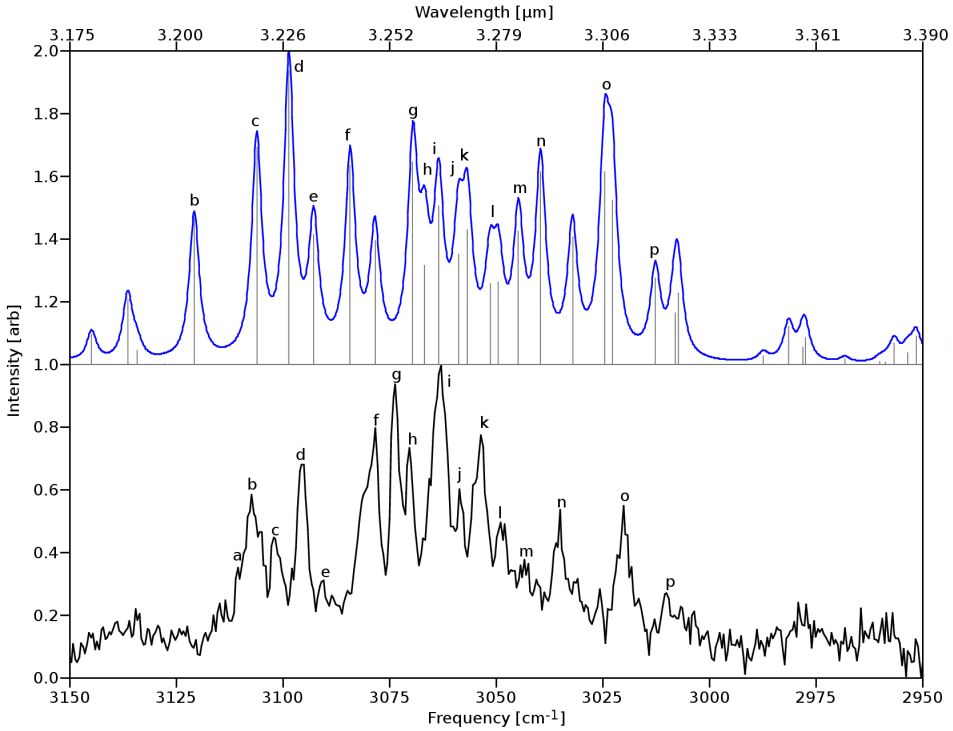

Figure 4.13 Anharmonic QFF IR spectrum of chrysene (this work) compared to high–resolution gas–phase IR absorption spectra obtained in a molecular beam (this work).

Mode	Freq	Symm	Description
ν_2	3207.21	b_u	bays symm CH stretch
ν_3	3191.81	b_u	bays asymm CH stretch
ν_6	3182.58	b_u	quartets asymm CH stretch
ν_7	3168.10	b_u	quartets asymm CH stretch
ν_{10}	3160.65	b_u	duos asymm CH stretch
ν_{11}	3156.72	b_u	non-bay edges asymm CH stretch
ν_{13}	1650.92	a_g	edge symm CC stretch
ν_{14}	1648.71	b_u	terminal rings CC stretch
ν_{15}	1638.32	a_g	edge asymm CC stretch
ν_{16}	1629.01	b_u	outer “naphthalene” edge symm CC stretch
ν_{17}	1599.42	a_g	ring fusing carbons CC stretch
ν_{18}	1553.44	a_g	duos/quartets asymm bay CH bend
ν_{19}	1549.78	b_u	terminal edge CC stretch
ν_{20}	1514.52	b_u	duos/quartets symm bay CH bend
ν_{21}	1480.80	a_g	duos/quartets symm bay CH bend
ν_{22}	1458.74	a_g	duos/quartets asymm bay CH bend
ν_{23}	1458.58	b_u	duos/quartets asymm bay CH bend
ν_{24}	1451.54	b_u	quartets asymm CH bend

Table 4.8 Mode descriptions and harmonic frequencies [cm^{-1}] of the IR active modes and modes involved in IR active combination bands/resonances identified in the CH–stretching region of chrysene.

ID	sym	exp[23]	rel. I[23]	anharm	rel. I	components	I sources
a	b_u	3110.7	0.29	-	-	-	
b	b_u	3107.4	0.54	3120.9	0.49	ν_2	ν_2
						$\nu_{16} + \nu_{18}$	
						$\nu_{13} + \nu_{20}$	
c	b_u	3102.3	0.40	3106.2	0.74	ν_2	ν_2
						$\nu_{13} + \nu_{20}$	
d	b_u	3095.7	0.65	3098.7	1	ν_6	ν_2
						$\nu_{15} + \nu_{20}$	ν_6
e	b_u	3091.0	0.23	3092.9	0.51	$\nu_{17} + \nu_{19}$	ν_2
							ν_3
							ν_7
f	b_u	3078.4	0.78	3084.3	0.70	$\nu_{14} + \nu_{21}$	ν_2
							ν_6
g	b_u	3073.8	0.93	3069.7	0.78	ν_6	ν_6
						$\nu_{14} + \nu_{21}$	
h	b_u	3070.5	0.71	3067.0	0.57	ν_{11}	ν_6
						$\nu_{13} + \nu_{23}$	ν_7
						$\nu_{14} + \nu_{22}$	
i	b_u	3063.0	1	3063.6	0.66	$\nu_{16} + \nu_{21}$	ν_6
							ν_7
j	b_u	3058.8	0.56	3058.7	0.59	$\nu_{15} + \nu_{23}$	ν_3, ν_7
k	b_u	3053.7	0.75	3057.0	0.63	ν_{10}	ν_7
						$\nu_{17} + \nu_{20}$	ν_{10}
						$\nu_{14} + \nu_{22}$	
	b_u					$\nu_{15} + \nu_{23}$	ν_7
l	b_u	3049.0	0.45	3050.6	0.44	$\nu_{14} + \nu_{22}$	ν_2
						$\nu_{13} + \nu_{23}$	
						$\nu_{18} + \nu_{19}$	
						$\nu_{17} + \nu_{20}$	
	b_u					$\nu_{17} + \nu_{20}$	ν_2
							ν_6
							ν_{10}
m	b_u	3043.5	0.32	3044.9	0.53	$\nu_{13} + \nu_{24}$	ν_2
							ν_6
n	b_u	3035.1	0.50	3039.7	0.69	ν_7	ν_7
						$\nu_{15} + \nu_{24}$	
o	b_u	3020.3	0.50	3024.4	0.86	ν_6	ν_6
						ν_{11}	
						$\nu_{18} + \nu_{20}$	
						$\nu_{15} + \nu_{24}$	
p	b_u	3010.1	0.20	3012.8	0.33	ν_{10}	ν_{10}
						ν_{11}	
						$\nu_{17} + \nu_{23}$	
						$\nu_{13} + \nu_{24}$	

Table 4.9 Line positions [cm^{-1}], relative intensities, dominant resonant components, and origin of intensities for the bands of the chrysene in the high–resolution gas–phase IR absorption spectra obtained in a molecular beam (this work) and the theoretical anharmonic spectrum (this work) as shown in figure 4.13.

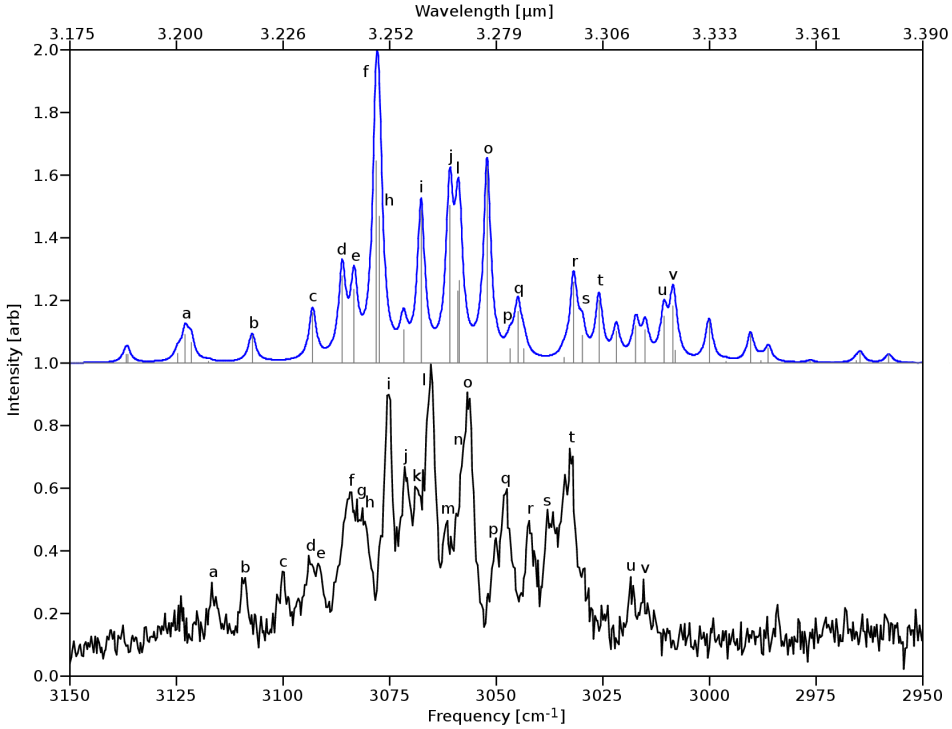

Figure 4.14 Anharmonic QFF IR spectrum of phenanthrene (this work) compared to high–resolution gas–phase IR absorption spectra obtained in a molecular beam (this work).

Mode	Freq	Symm	Description
ν_1	3199.53	a_1	bay symm CH stretch
ν_2	3189.22	b_2	quartets/bay asymm CH stretch
ν_4	3179.79	b_2	quartets/bay asymm CH stretch
ν_5	3172.54	a_1	duo symm CH stretch
ν_6	3168.11	a_1	quartets/duo symm CH stretch
ν_8	3157.11	b_2	quartets/duo asymm CH stretch
ν_9	3156.72	a_1	quartets (no bay) asymm stretch
ν_{11}	1651.44	a_1	corner edge CC stretch
ν_{12}	1646.57	b_2	terminal edge CC stretch
ν_{13}	1634.92	a_1	full edge CC stretch
ν_{14}	1601.29	b_2	ring fusing carbons CC stretch
ν_{15}	1556.72	a_1	quartets/asymm bay CH bend
ν_{16}	1529.25	b_2	quartets/duo/symm bay CH bend
ν_{17}	1486.53	b_2	quartets/duo/symm bay CH bend
ν_{18}	1466.74	a_1	quartets/duo/symm bay CH bend
ν_{19}	1446.12	a_1	quartets/asymm bay CH bend
ν_{20}	1442.79	b_2	duo/quartet (no bay) CH bend

Table 4.10 Mode descriptions and harmonic frequencies [cm^{-1}] of the IR active modes and modes involved in IR active combination bands/resonances identified in the CH–stretching region of phenanthrene.

ID	sym	exp[23]	rel. I[23]	anharm	rel. I	components	I sources
a	a_1	3116.6	0.24	3122.9	0.13	$\nu_{12}+\nu_{16}$	ν_1
						$\nu_{13}+\nu_{15}$	
	b_2					$\nu_{11}+\nu_{16}$	ν_4
b	b_2	3109.6	0.25	3107.4	0.10	$\nu_{13}+\nu_{16}$	ν_2
c	b_2	3100.0	0.28	3093.1	0.18	ν_2	ν_2
						ν_7	
						$\nu_{14}+\nu_{15}$	
d	a_1	3094.0	0.33	3086.2	0.33	ν_1	ν_1
						ν_3	
						$\nu_{12}+\nu_{17}$	
						$\nu_{12}+\nu_{16}$	
e	b_2	3091.8	0.30	3083.4	0.31	ν_4	ν_4
						$\nu_{11}+\nu_{17}$	
						$\nu_{13}+\nu_{16}$	
f	b_2	3084.3	0.55	3078.0	1	ν_2	ν_2
						ν_4	ν_4
						$\nu_{11}+\nu_{17}$	
g	-	3082.8	0.53	-	-	-	-
h	a_1	3081.5	0.50	3076.7	0.60	ν_1	ν_1
						ν_3	
						$2\nu_{15}$	
i	b_2	3075.4	0.89	3067.7	0.53	ν_2	ν_2
						$\nu_{13}+\nu_{17}$	ν_4
j	a_1	3071.6	0.64	3060.9	0.63	ν_5	ν_5
						$\nu_{14}+\nu_{16}$	
						$\nu_{11}+\nu_{18}$	
						$\nu_{11}+\nu_{19}$	
k	-	3069.0	0.57	-	-	-	-
l	b_2	3065.3	1	3059.0	0.59	ν_8	ν_4
						ν_4	ν_2
						$\nu_{13}+\nu_{17}$	
						$\nu_{12}+\nu_{18}$	
	a_1					ν_3	ν_6
						ν_6	
m	-	3061.8	0.05	-	-	-	-
n	-	3057.0	0.90	-	-	-	-
o	a_1	3056.4	0.88	3052.2	0.66	ν_5	ν_5
						ν_6	ν_6
						$\nu_{14}+\nu_{16}$	
p	b_2	3050.3	0.40	3046.8	0.12	ν_8	ν_8
						$\nu_{12}+\nu_{19}$	
q	a_1	3047.9	0.55	3045.0	0.21	ν_9	ν_9
						$\nu_{12}+\nu_{20}$	
r	a_1	3042.4	0.45	3031.9	0.30	ν_5	ν_5
						$2\nu_{15}$	
						$\nu_{11}+\nu_{18}$	
s	a_1	3037.6	0.47	3030.2	0.16	$2\nu_{15}$	ν_5
						$\nu_{14}+\nu_{17}$	
t	b_2	3032.8	0.68	3026.0	0.23	ν_4	ν_4
						$\nu_{12}+\nu_{18}$	
u	a_1	3018.6	0.26	3010.6	0.20	ν_6	ν_6
						$\nu_{14}+\nu_{17}$	
						$\nu_{13}+\nu_{19}$	
v	b_2	3015.5	0.25	3008.7	0.25	ν_4	ν_4
						ν_8	
						$\nu_{12}+\nu_{19}$	
						$\nu_{13}+\nu_{20}$	

Table 4.11 Line positions [cm^{-1}], relative intensities, dominant resonant components, and origin of intensities for the bands of the phenanthrene in the high–resolution gas–phase IR absorption spectra obtained in a molecular beam (this work) and the theoretical anharmonic spectrum (this work) as shown in figure 4.14.

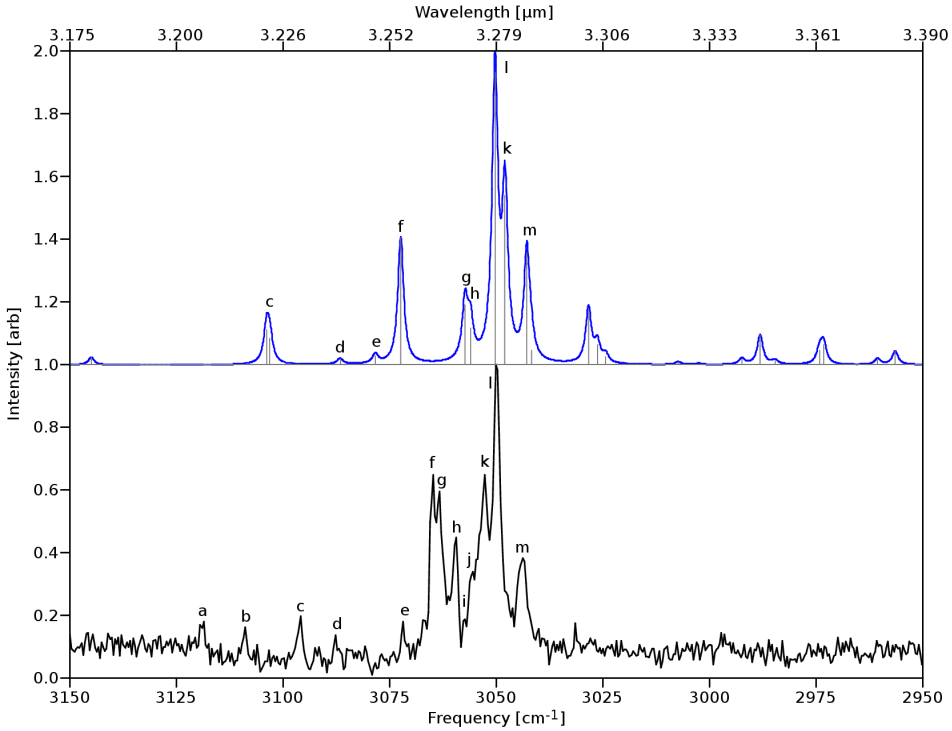

Figure 4.15 Anharmonic QFF IR spectrum of pyrene (this work) compared to high–resolution gas–phase IR absorption spectra obtained in a molecular beam (this work).

Mode	Freq	Symm	Description
ν_2	3181.48	b_{1u}	trios symm CH stretch
ν_4	3172.18	b_{2u}	duos symm CH stretch
ν_6	3164.47	b_{2u}	trios (no middle CH) asymm CH stretch
ν_{10}	3153.84	b_{1u}	duos assym CH stretch
ν_{11}	1660.92	a_g	middle “naphthalene” CC stretch
ν_{12}	1635.58	b_{2u}	edge asymm CC stretch
ν_{13}	1626.43	b_{1u}	terminal “benzene” symm CC stretch
ν_{14}	1618.23	b_{3g}	terminal “benzene” asymm CC stretch
ν_{16}	1528.64	b_{3g}	trios/duos symm CH bend
ν_{17}	1508.36	b_{2u}	trios/duos asymm CH bend
ν_{18}	1478.71	b_{1u}	duos symm CH bend
ν_{19}	1456.19	b_{1u}	trios/duos assym CH bend
ν_{20}	1453.29	b_{2u}	trios symm CH bend

Table 4.12 Mode descriptions and harmonic frequencies [cm^{-1}] of the IR active modes and modes involved in IR active combination bands/resonances identified in the CH–stretching region of pyrene.

ID	sym	exp[23]	rel. I[23]	anharm	rel. I	components	I sources
a	-	3118.7	0.12	-	-	-	-
b	-	3108.9	0.10	-	-	-	-
c	b_{1u}	3096.0	0.12	3103.7	0.17	$\nu_{12} + \nu_{16}$	ν_2
	b_{2u}					$\nu_{11} + \nu_{17}$	ν_4
d	b_{2u}	3087.8	0.08	3086.7	0.02	$\nu_{13} + \nu_{16}$	ν_6
e	b_{1u}	3071.9	0.11	3078.4	0.04	$\nu_{11} + \nu_{18}$	ν_2
							ν_{10}
f	b_{1u}	3064.9	0.59	3072.5	0.41	ν_2	ν_2
						$\nu_{14} + \nu_{17}$	
g	b_{2u}	3063.3	0.56	3057.3	0.24	ν_6	ν_4
						$\nu_{11} + \nu_{20}$	ν_6
h	b_{1u}	3059.5	0.39	3056.5	0.21	$\nu_{11} + \nu_{19}$	ν_2
i	-	3057.5	0.13	-	-	-	-
j	-	3055.6	0.29	-	-	-	-
k	b_{2u}	3052.9	0.60	3048.1	0.65	ν_4	ν_4
						ν_6	
l	b_{1u}	3049.8	1	3050.4	1	ν_2	ν_2
m	b_{2u}	3044.0	0.34	3042.9	0.40	ν_6	ν_4
						$\nu_{11} + \nu_{20}$	ν_6

Table 4.13 Line positions [cm^{-1}], relative intensities, dominant resonant components, and origin of intensities for the bands of the pyrene in the high–resolution gas–phase IR absorption spectra obtained in a molecular beam (this work) and the theoretical anharmonic spectrum (this work) as shown in figure 4.15.

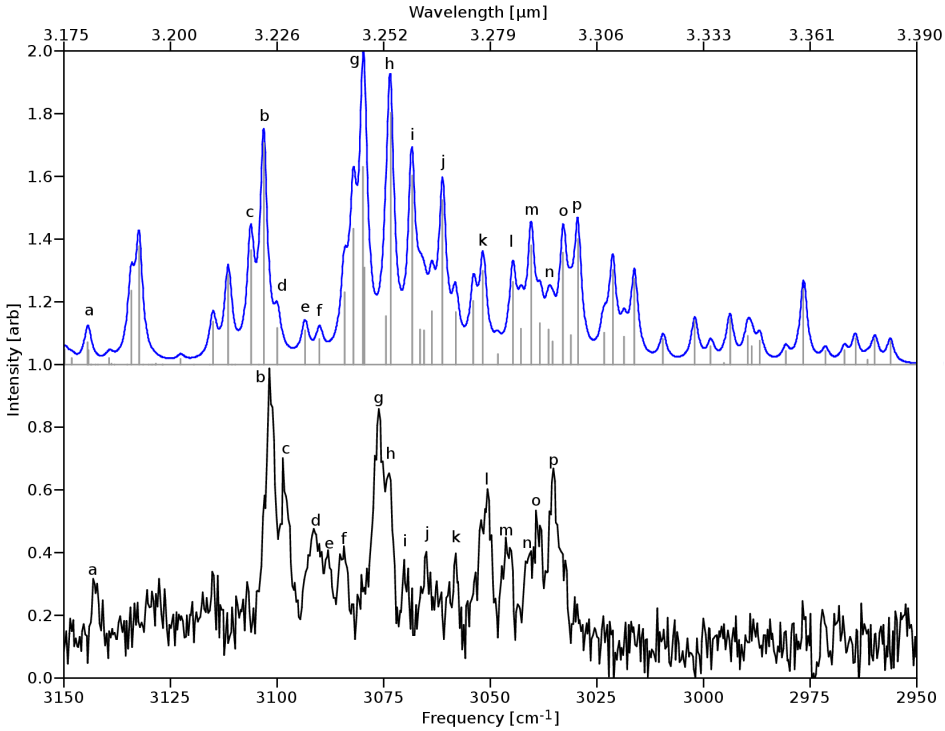

Figure 4.16 Anharmonic QFF IR spectrum of triphenylene (this work) compared to high–resolution gas–phase IR absorption spectra obtained in a molecular beam (this work).

Mode	Freq	Symm	Description
ν_1	3213.85		bay symm CH stretch
ν_2	3211.89	e	bay symm CH stretch
ν_3	3211.39	e	bay symm CH stretch
ν_4	3196.22	e	quartet/bay asymm CH stretch
ν_5	3195.83	e	quartet/bay asymm CH stretch
ν_6	3192.73		bay asymm CH stretch
ν_7	3181.62		quartet symm (no bay) CH stretch
ν_8	3178.58	e	quartet/bay asymm CH stretch
ν_9	3178.52	e	quartet/bay asymm CH stretch
ν_{12}	3164.34		quartet/bay asymm CH stretch
ν_{13}	1644.06		edge CC stretch
ν_{14}	1639.66	e	edge CC stretch
ν_{15}	1639.55	e	edge CC stretch
ν_{16}	1610.63	e	ring fusing carbons CC stretch
ν_{17}	1610.43	e	ring fusing carbons CC stretch
ν_{18}	1580.25		quartets/bay asymm CH bend
ν_{19}	1527.60	e	two symm bay/one asymm bay CH bend
ν_{20}	1526.99	e	one symm bay/two asymm bay CH bend
ν_{21}	1486.15		quartet (no bay) symm CH bend
ν_{22}	1474.23		three asymm bay CH bends
ν_{23}	1462.40	e	quartets/bay symm CH bend
ν_{24}	1462.17	e	quartets/bay symm CH bend

Table 4.14 Mode descriptions and harmonic frequencies [cm^{-1}] of the IR active modes and modes involved in IR active combination bands/resonances identified in the CH–stretching region of triphenylene. Due to the symmetry lowering of triphenylene the symmetries for each mode are not given. However, modes that are degenerate under $\mathcal{D}_{3h}$ symmetry are indicated by the symbol "e".

ID	exp[23]	rel. I[23]	anharm	rel. I	components	I sources
a	3143.2	0.20	3144.5	0.13	$2\nu_{16}$	ν_2
					$2\nu_{17}$	ν_8
					$\nu_{15} + \nu_{18}$	ν_9
b	3101.8	1	3103.2	0.77	$\nu_{15} + \nu_{20}$	ν_3
					ν_3	
c	3098.7	0.68	3106.3	0.40	ν_1 ν_5	ν_2
					$\nu_{13} + \nu_{20}$	ν_3
d	3091.5	0.43	3100.0	0.13	$\nu_{14} + \nu_{20}$	ν_2
						ν_9
e	3088.1	0.35	3093.5	0.12	$\nu_{17} + \nu_{20}$	ν_8
					$\nu_{16} + \nu_{20}$	ν_9
f	3084.3	0.36	3090.2	0.09	ν_7	ν_8
					$\nu_{16} + \nu_{20}$	ν_9
					$\nu_{17} + \nu_{20}$	
g	3076.2	0.85	3079.8	1	ν_5	ν_2
					$2\nu_{18}$	ν_8
					ν_7	ν_9
					ν_2	
					ν_9	
					ν_8	
					$\nu_{13} + \nu_{19}$	
h	3073.8	0.62	3073.7	0.96	ν_3	ν_3
					ν_6	
					ν_4	
					$\nu_{14} + \nu_{19}$	
i	3070.3	0.31	3068.5	0.64	ν_2	ν_2
					ν_5	
					ν_4	
					ν_1	
j	3065.0	0.34	3061.3	0.57	ν_9	ν_9
					$2\nu_{18}$	
k	3058.2	0.34	3051.8	0.33	$\nu_{18} + \nu_{20}$	ν_3
l	3050.8	0.57	3044.8	0.29	$\nu_{16} + \nu_{24}$	ν_2
					$\nu_{16} + \nu_{22}$	ν_9
					$\nu_{17} + \nu_{22}$	
m	3046.4	0.40	3040.5	0.41	ν_8	ν_8
					$\nu_{17} + \nu_{19}$	
					$\nu_{15} + \nu_{21}$	
n	3040.6	0.35	3036.1	0.17	ν_7	ν_9
					$2\nu_{20}$	
					$\nu_{14} + \nu_{16}$	
					$\nu_{16} + \nu_{22}$	
					$\nu_{14} + \nu_{21}$	
					$\nu_{13} + \nu_{23}$	
					$\nu_{17} + \nu_{21}$	
					$\nu_{16} + \nu_{24}$	
o	3039.4	0.50	3032.9	0.40	ν_9	ν_9
					$\nu_{16} + \nu_{21}$	
					$\nu_{13} + \nu_{23}$	
					$\nu_{16} + \nu_{19}$	
p	3035.3	0.64	3029.7	0.45	ν_8	ν_8
					ν_{12}	
					$\nu_{18} + \nu_{20}$	

Table 4.15 Line positions [cm^{-1}], relative intensities, dominant resonant components, and origin of intensities for the bands of the triphenylene in the high–resolution gas–phase IR absorption spectra obtained in a molecular beam (this work) and the theoretical anharmonic spectrum (this work) as shown in figure 4.16.

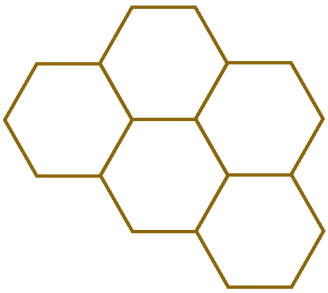

The anharmonic quartic force field infrared spectra of hydrogenated and methylated PAHs

Polycyclic aromatic hydrocarbons (PAHs) have been shown to be ubiquitous in a large variety of distinct astrophysical environments and are therefore of great interest to astronomers. The majority of these findings are based on theoretically predicted spectra, which make use of scaled DFT harmonic frequencies for band positions and the double harmonic approximation for intensities. However, these approximations have been shown to fail at predicting high–resolution gas–phase infrared spectra accurately, especially in the CH–stretching region (2950–3150 cm^{-1}, 3μm). This is particularly worrying for the subset of hydrogenated or methylated PAHs of which astronomers attribute the observed non–aromatic features which appear in the CH–stretching region of spectral observations of the interstellar medium (ISM). In our previous works, we presented the anharmonic theoretical spectra of three linear PAHs and five non–linear PAHs, demonstrating the importance of including anharmonicities into theoretical calculations. In this work we extend these techniques to two methylated PAHs (9–methylanthracene, and 9,10–dimethylanthracene) and four hydrogenated PAHs (9,10–dihydroanthracene, 9,10–dihydrophenanthrene, 1,2,3,4–tetrahydronaphthalene, and 1,2,3,6,7,8–hexahydropyrene) in order to better understand the aliphatic IR features of substituted PAHs. The theoretical spectra are compared with spectra obtained under matrix isolation low–temperature conditions for the full vibrational fundamental range and high–resolution, low–temperature gas-phase conditions for the CH–stretching region. Excellent agreement is observed between the theoretical and high–resolution ex-

perimental spectra with a deviation of 0.00% ±0.17%, and changes to the spectra of PAHs upon methylation and hydrogenated are tracked accurately and explained.

Cameron J. Mackie, Alessandra Candian, Xinchuan Huang, Elena Maltseva, Annemieke Petrignani, Jos Oomens, Wybren Jan Buma, Timothy J. Lee, Alexander G. G. M. Tielens
Physical Chemistry Chemical Physics Advance Article, (2018)

5.1 Introduction

Due to their remarkable stability, Polycyclic Aromatic Hydrocarbon (PAH) molecules are widespread in everyday life. They are a major component of soot, created during combustion processes[115] and their biological activity makes them pollutants of water and the atmosphere. In the terrestrial atmosphere, several reactions[116] lead to functionalised PAHs - PAHs with chemical side groups and/or heteroatom substitution. These functionalisations have an impact on the properties of the molecules, for example methylation can increase or decrease the carcinogenicity level of PAHs depending on the substitution position[117].

Functionalised PAHs are also of interest from a material science prospective. For example, hydrogenationation of PAHs change the local molecule hybridization from sp^2 to sp^3, and are therefore a model system for studies of hydrogenated graphene, which are promising successors of silicon in the electronic industry thanks to the tunability of the graphene band gap depending on the location of additional hydrogens[8].

Several studies indicate that PAHs are also of high importance in astrophysical environments. PAHs have been detected in interplanetary dust particles and meteorites[14, 118], and are most certainly the carriers of the Aromatic Infrared Bands (AIBs)[26, 27], a family of IR emission features spanning the 3-20 μm (3300-500 cm^{-1}) region, seen in a variety of astrophysical environments. In particular, hydrogenated and methylated PAHs are considered to be responsible for additional features at 3.40, 3.46, 3.51, 3.56 μm and 6.9 μm[37, 38, 39, 119, 120], which can be particularly strong in evolved stars[121]. Also, hydrogenated PAHs have gained interests as potential catalysts for H_2 formation in astrophysical regions dominated by visible-ultraviolet photons[122].

IR spectra of methylated and hydrogenated PAHs have been explored both experimentally[123, 124], mostly in a matrix-environment[125], and computationally using DFT and the double harmonic approximation [86]. For normal PAHs, previous experiments have shown that the theoretical double harmonic spectra compare poorly, especially in the 3.1-3.5 μm (3200-2900 cm^{-1})[22], and 5-6 μm (2000-1600 cm^{-1}) regions[106]. This is due to the inability of the harmonic approximation to account for combination bands, overtones, mode couplings and resonances.

In our previous work[22, 23, 106, 126] we showed that good agreement between theoretical and experimental spectra can be obtained when an anharmonic theoretical approach is used; specifically a second–order vibrational perturbation treatment, that accounts for large numbers of mutually resonating modes and combination bands. This work expands upon these studies in order to address the high–resolution spectra of hydrogenated and methylated PAHs. The anharmonic treatment is applied to six "decorated" PAH species: 9–methylanthracene, 9,10–dimethylanthracene, 9,10–dihydroanthracene, 9,10–dihydrophenanthrene, 1,2,3,4–tetrahydronaphthalene, and 1,2,3,6,7,8–hexahydropyrene (see figure 5.1). The goal is two–fold: to further expand and test the anharmonic methods outlined in our previous works to include hydrogenated and methylated species, and to explain how and why PAH spectra change with the introduction of aliphatic groups. A

robust theoretical understanding of the IR spectral features and the role of anharmonicities is key to analyzing and interpreting astronomical observations. Important particularly with the upcoming launch of the James Webb Space Telescope in 2018, as astronomers will get for the first time astronomical spectra at high spectral resolution and high sensitivity.

Of particular interest is the behavior of aliphatic vibrational modes in resonances with the CH–stretching region around 3 μm. For this we compare low–temperature high–resolution gas–phase IR absorption spectra of the six decorated species which allows direct comparisons to the theoretical methods, further validating our approach. Full peak analyses are given for the bands in the CH–stretching region. The remaining IR range is also compared to the available matrix isolation spectra (MIS) and high–temperature gas–phase spectra to confirm accuracy in the full IR range.

5.2 Theoretical Methods

The theoretical methods of this work follow similar techniques of our previous work[98, 106, 126]. The software package Gaussian09[51] is used to optimize the geometry of the molecules, as well as to calculate the quartic force fields (QFFs) and IR intensities. In order to handle the large number of mutually resonating modes (*polyads*[56]) we use a locally modified version of the SPECTRO[52] software package to perform a second order vibrational perturbation theory treatment (VPT2) after transforming the QFF constants from normal to Cartesian coordinates[98]. We use the resulting eigenvalues of the VPT2 polyad treatment for the final line positions and the square of the eigenvectors to distribute intensities over resonating modes (see ref. [106, 126] for more details).

Recently, problems with the stability of the quartic force field of PAHs using the B97-1 functional[94] and TZ2P basis set[95] combination has been discovered. Therefore, a switch has been made in this work to the B3LYP hybrid functional[127, 128], and the polarized double-ζ basis set N07D[129], a combination developed specifically for the anharmonic calculations of medium-size molecules in mind[50].

Known issues arise in the anharmonic analysis involving the low barrier "free–rotor" vibrational modes of methyl groups[130]. To circumvent this issue, cubic and quartic force constant terms involving the free–rotor modes were set to zero, essentially treating these vibrational modes at the harmonic level.

5.3 Results

Comparisons between the theoretical anharmonic spectra and experimental spectra obtained under the two experimental conditions were performed. To aid in the comparisons, the theoretical spectra have been convolved[131] with Lorentzian profiles to best match the experimental band–widths. Band assignments are made between theory and experiment based on position, intensity, and local trends of

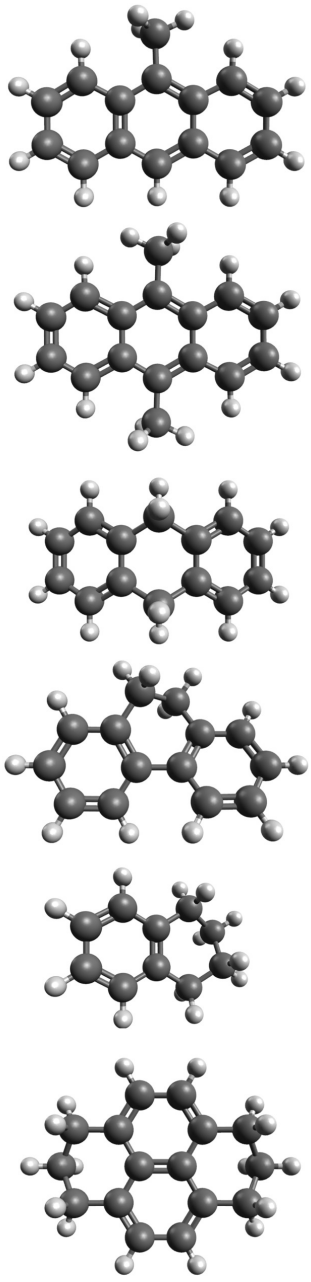

Figure 5.1 From top to bottom: 9–methylanthracene, 9,10–dimethylanthracene, 9,10–dihydroanthracene, 9,10–dihydrophenanthrene, 1,2,3,4–tetrahydronaphthalene, and 1,2,3,6,7,8–hexahydropyrene. Symmetries from top to bottom: C_s, C_{2h}, C_2, C_2, C_2, C_{2v}

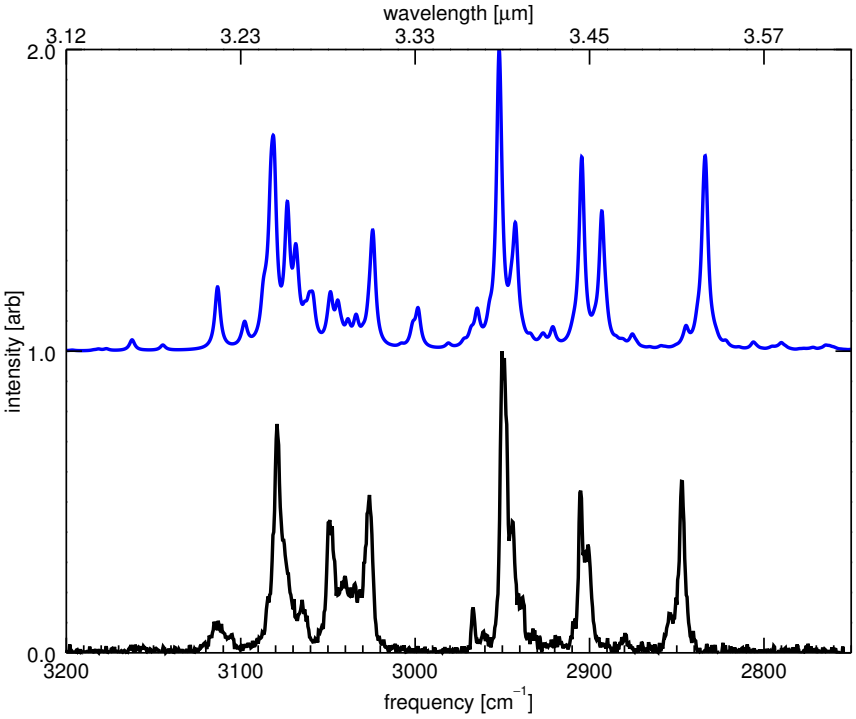

Figure 5.2 Theoretical anharmonic IR spectrum of this work of 9,10–dihydrophenanthrene compared with the high–resolution gas–phase IR absorption spectrum of this work.

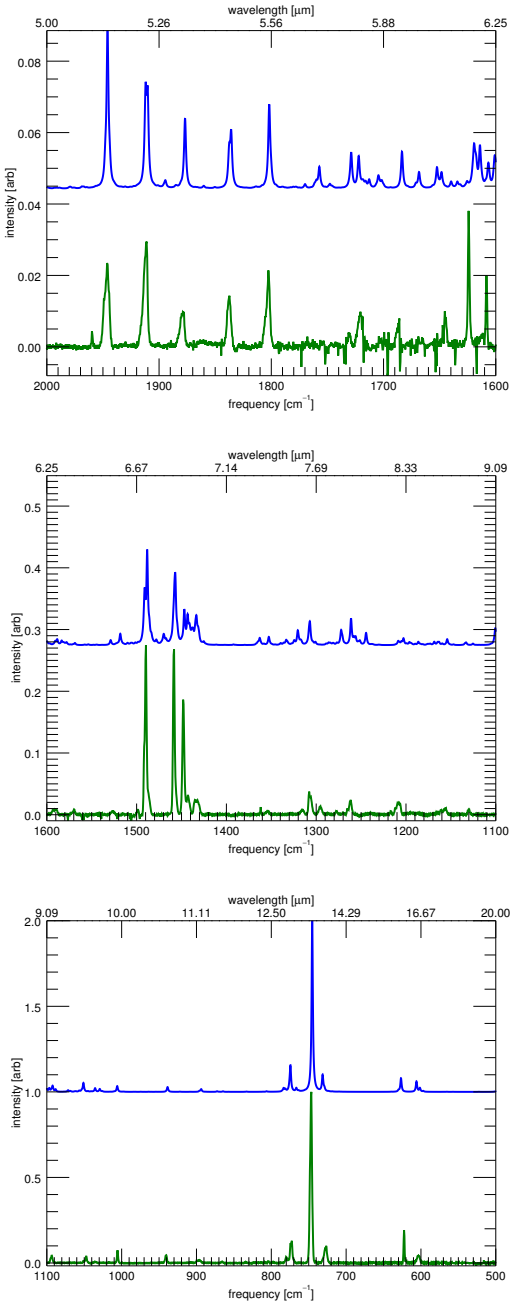

Figure 5.3 The matrix–isolation infrared spectrum[33, 78] of 9,10-dihydrophenanthrene (green, bottom of each panel) compared to the convolved (FWHM 2 cm^{-1}) theoretical anharmonic calculations of this work (blue, top each panel). Three spectral ranges are shown.

the convolved spectra. The values given for the experiment and theory are obtained through fitting Lorentzian profiles using the software package Fityk[111]. Vibrational mode descirptions were obtained through visualization of the atomic motions of each of the normal modes.

Figure 5.14 shows an example comparison between the convolved theoretical spectra (blue, HWHM = 1.6 cm^{-1}) and the high–resolution low–temperature gas–phase spectra (black), both normalized to their highest peak in this spectral range. See ESI for similar comparisons for the remaining molecules. Detailed band assignments are also given in the ESI for each PAH. Due to strong resonances in the CH–stretching region assignment to a single unique fundamental or combination bands is not possible; instead the dominant resonant components (typically over 10% contribution) are given. Intensity source is given as a separate column since a small resonance component (< 10%) can be the dominant source of intensity if the related fundamental is very intense (see Theory section of reference 106 for more details). Vibrational mode descriptions are also given for each PAH in corresponding tables (see ESI).

High–resolution low–temperature gas–phase experimental data does not exist for the full infrared range, so comparisons are performed between the anharmonic spectra and the available MIS[125, 132] spectra for the remaining IR range. Figure 5.15 shows an example comparison between the convolved theoretical spectra (blue, HWHM = 1 cm^{-1}) and the MIS spectra (green). See ESI for similar comparisons for the remaining molecules. Three ranges are shown for each molecule, 2000–1600 cm^{-1}, 1600–1100 cm^{-1}, and 1100–500 cm^{-1}. No significant features appear between 3000 and 2000 cm^{-1}. No data is available below 500 cm^{-1}. All intensities, both theoretical and experimental, are scaled to the their maximum intensity in the spectral range (2000–500 cm^{-1}). Assignments between the MIS data and the anharmonic data of this work is also presented in the ESI.

When changing from B97-1/TZ2P to B3LYP/N07D the improvement in agreement to between theory and experiment was found to be significant; from an error of 1% down to 0.1% (30 cm^{-1} to 3 cm^{-1} in the CH–stretching region). Further functional/basis set benchmark studies on the anharmonic spectra of PAHs is warranted and currently underway.

5.4 Discussion

5.4.1 Overall comparison to the low–temperature high–resolution gas–phase spectra

The low–temperature high–resolution gas–phase spectra and the corresponding convolved theoretical spectra (see ESI) show excellent agreement. Figure 5.4 shows a histogram of the percent differences between the theoretical and experimental line positions for the six PAHs combined. A fitted Gaussian gives an average deviation of 0.00% ± 0.17%. For *all* of the theoretical spectra in the CH–stretching region there appears to be a systematic shift of of the lowest energy aliphatic modes. This accounts for the secondary bump centered around -0.6% in the histogram of figure 5.4. The push to lower energies indicates an overcorrection of the anharmonic

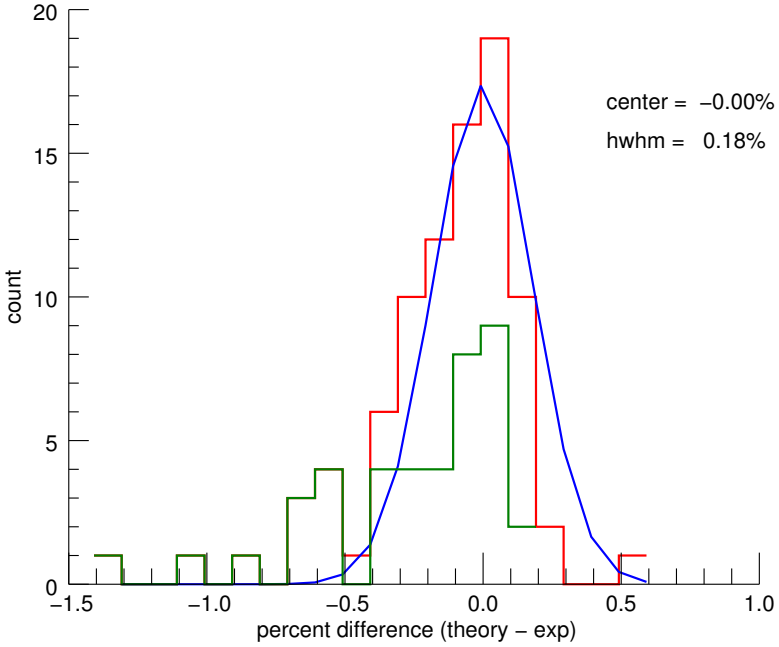

Figure 5.4 Histogram showing the percent differences between the line positions of the anharmonic theory (this work) and the low–temperature high–resolution gas–phase experiments for all six PAH species combined.

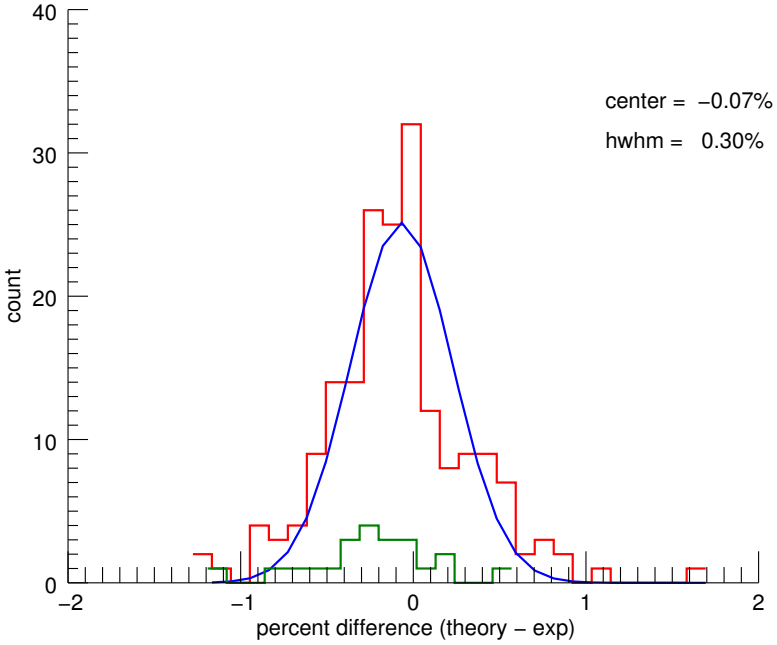

Figure 5.5 Histogram showing the percent differences between the line positions of the anharmonic theory (this work) and the MIS experiments for the five (no MIS data exists or 9,10–dimethylanthracene) PAH species combined.

effects. Whether this is due to the anharmonic correction of the bands, or due to the resonance terms themselves is not clear. The freezing of the methyl rotors could also be a factor, however the appearance of the same shift in the hydrogenated PAHs points away from this explanation. Future benchmark studies, including the decorated PAHs can address this minor issue.

Relative intensity agreement is moderate with an average deviation of -12% ± 50%. The major source of error in calculating the intensities of the CH–stretching region is the reliance on the distribution of harmonic intensities through the polyads rather than anharmonic intensities[106, 126]. Calculation and redistribution of "true" anharmonic intensities should improve the fits. The discrepancies between the theoretical and experimental intensities did not hamper reliable band identifications.

5.4.2 Overall comparison to MIS

The MIS spectra and the corresponding convolved theoretical spectra (see ESI) show good agreement. Figure 5.5 shows a histogram of the percent differences between the theoretical and experimental line positions for five of the PAHs combined (no MIS data exists for 9,10–dimethylanthracene). A fitted Gaussian gives an average deviation of -0.07% ± 0.30%. Previous work[112] has shown the unpredictable shifts due to matrix interactions to be 0.21% ± 0.63%. Therefore the theoretical spectra are accurate to within the limitations of MIS spectroscopy.

Relative intensity agreement is moderate with an average deviation of -18% ± 62%. It was possible to make use of anharmonic intensities in this region, however MIS experiments are notorious for affecting the intensities of bands. Therefore, confirmation of the reliability of the anharmonic intensity calculations needs to await high–resolution low–temperature gas–phase spectra in this region.

5.4.3 Anthracene series

Three anthracene–based PAHs have been considered: 9–methylanthracene; 9,10–dimethylanthracene; and 9,10–dihydroanthracene. Figure 5.6 shows the theoretical IR spectra of these three molecules in comparison with the theoretical spectrum of anthracene. Absolute intensities have been doubled, with the main peaks truncated, to show detail of the smaller peaks.

The most prominent change when moving from anthracene to the methylated and hydrogenated versions occurs in the CH–stretching region, with both methylated species bearing a strong resemblance to one another and to a lesser extent with the hydrogenated version. While anthracene shows one dominant peak, the decorated PAHs show five prominent features. These five features can be split into three regions based on the vibrational modes involved in the Fermi resonances:

1) Combinational aromatic states of CC–stretching modes paired with CH–in–plane–bending modes in Fermi resonances with aromatic CH–stretching modes. The behavior of this region is comparable to the "regular" CH–stretching region of a typical PAH. In anthracene this produces one main feature centered around 3055 cm^{-1}, while for the decorated anthracenes this feature is centered around 3085

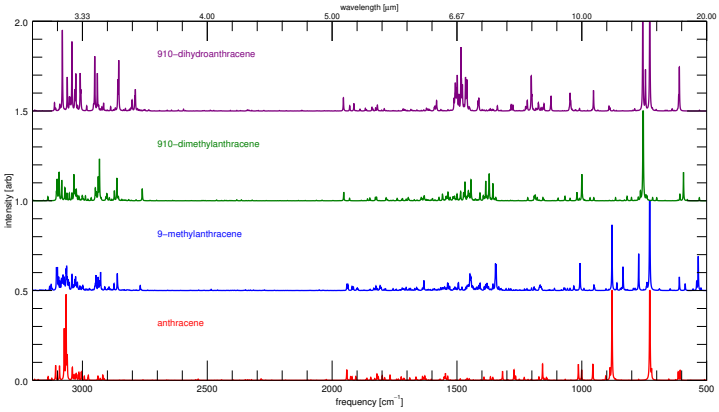

Figure 5.6 Comparison between anthracene–containing PAHs from the anharmonic theoretical spectra.

cm^{-1}. The push to higher energies is likely reflects steric interactions between the native anthracene hydrogens and the additional hydrogens. For the methylated anthracenes this region spans approximately 30 cm^{-1}, while the hydrogenated anthracene spans approximately 60 cm^{-1}. In regular anthracene this region spans the whole CH–stretching region (approximately 200 cm^{-1}).

2) Combinational aromatic/aliphatic states of CC–stretching modes paired with CH–in–plane–bending modes in Fermi resonances with aliphatic CH–stretching modes. For the methylated anthracenes this region is centered around 3055 cm^{-1} with a width of 30 cm^{-1} and is characterized by one dominant peak, while the hydrogenated anthracene is centered around 2960 cm^{-1} with a width of 160 cm^{-1} and is characterized by two dominant peaks.

3) Combinational aliphatic states of CH–in–plane–bending modes paired with CH–in–plane–bending modes in Fermi resonances with aliphatic CH–stretching modes. For the methylated anthracenes this region is centered around 2960 cm^{-1} with a width of 150 cm^{-1} and is characterized by two dominant peaks, while the hydrogenated anthracene is centered around 2849 cm^{-1} with a width of 50 cm^{-1} and is again characterized by two dominant peaks. The additional feature observed in the theoretical spectra of both methylated anthracenes around 2760 cm^{-1} are not observed in the experimental spectra.

One could argue that the region between 1000 and 600 cm^{-1} shows more variation between the anthracene–like species than the CH–stretching region around 3000 cm^{-1}. However, this is misleading. The differences are not directly due to methylation and hydrogenation, but rather indirectly due to the disruption of the types of CH bonds present in the molecule. As has been shown previously[30], the position of the bands in this region is sensitive to the the number of hydrogen atoms on a given aromatic ring involved in out–of–plane CH–bending modes.

For example, anthracene has two features in this region: one at 885 cm^{-1} from the out–of–plane CH–bendings of the hydrogens on the middle ring, or *solo* hydrogens (no adjacent hydrogens); and one at 730 cm^{-1} from the out–of–plane CH–bendings of the hydrogens on the terminal rings, or *quarto* hydrogens (four adjacent hydrogens). Similar characteristic features exist at distinct frequencies for other aromatic ring types; *duo* (two adjacent hydrogens) out–of–plane CH–bendings and *trio* (three adjacent hydrogens) out–of–plane CH–bendings. The intensity ratios of these bands have also been shown to correlate with the ratios of the edge structure of PAHs. Therefore, when moving from anthracene to 9–methylanthracene, the intensity of the solo CH–bending mode is observed to be reduced by a factor of two because one of the solo hydrogens has been replaced with the methyl group. This trend continues into 9,10–dimethylanthracene with the elimination of the solo CH–bending mode as both solo hydrogens have been replaced with methyl groups. Similarly, with 9,10–dihydroanthracene both solos are eliminated with the hydrogenation resulting in the loss of the solo CH–bending mode feature. Other subtle differences exist asl well. When moving from anthracene to 9–methylanthracene to 9,10–dimethylanthracene two sets of bands appear and disappear around 840 cm^{-1} and 775 cm^{-1}. These bands are again due to solo and quarto hydrogen bending modes. The appearance and disappearance of these bands is likely due to symmetry effects. These modes are weak or inactive in the higher symmetric anthracene, gain considerable intensity with the breaking of symmetry from the addition of one methyl group, and lose intensity again with the near symmetry restoration from the addition of the second methyl group. The splitting of the quarto feature of 9,10–dihydroanthracene is due to interference from the hydrogenated groups.

The final region that shows significant change in the methylated and hydrogenated versions of anthracene is from 1600 to 1300 cm^{-1}. Intensity in this region is doubled or even tripled compared to normal anthracene. This region is dominated by out–of–plane combination bands including CH–bends paired with CH–bends, CH–bends paired with CC–bends, and CC–bends paired with CC–bends. The enhancement of this region is likely due to the disruption of the planarity of the molecules, leading to stronger dipoles for the out–of–plane combination bands.

5.4.4 Hydrogenated series

Four hydrogenated PAHs have been considered: 9,10–dihydroanthracene; 9,10–dihydrophenanthrene; 1,2,3,4–tetrahydronaphthalene; and 1,2,3,6,7,8–hexahydropyrene. Figure 5.7 shows the theoretical IR spectra of these four molecules in comparison with their non–hydrogenated counterparts from our previous work[22, 106]. Absolute intensities have been doubled, with the main peaks truncated, to show detail of the smaller peaks. 9,10–dihydroanthracene is absent from figure 5.7, see figure 5.6 for its comparison.

As stated previously, the most dramatic change to the spectra occurs in the CH–stretching region of the PAHs upon hydrogenation. The features centered around 3080 cm^{-1} of all four hydrogenated PAHs behave similar to their normal PAH counterparts in that they are aromatic CH–stretching modes in resonance

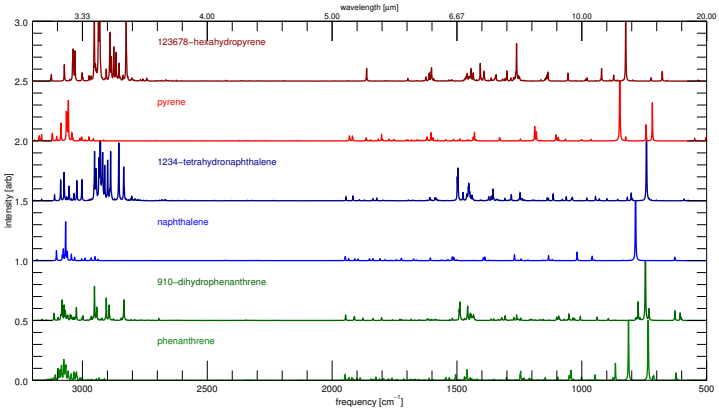

Figure 5.7 Comparison between normal and hydrogenated versions of PAHs from the anharmonic theoretical spectra.

with combination bands of CC–stretching with in–plane CH–bending modes. A spreading of intensity over a larger region is also observed in each of the hydro–PAHs when compared to their normal counterparts, especially for lower energy modes down to 3020 cm^{-1}. A break occurs before a sharp rise in aliphatic features beginning at 2950 cm^{-1} for all four hydro–PAHs. Three aliphatic regions then exist for each hydro–PAH: the features centered around 2950 cm^{-1} are due to in–plane CH–stretching modes of the aliphatic CH bonds that do not participate strongly in resonances; the features centered around 2900 cm^{-1} are due to out–of–plane CH–stretching modes of the aliphatic CH bonds in resonances; and the features centered near 2850 cm^{-1} are due to less sterically hindered out–of–plane CH–stretching modes of the aliphatic CH bonds in resonances. Notable changes can also be observed in the CH–stretching region as hydrogenation increases. In the slightly hydrogenated PAHs (9,10–dihydroanthracene and 9,10–dihydrophenanthrene) the aromatic region contains many closely spaced features, while the aliphatic region has fewer and more widely spaced features. In the highly hydrogenated PAHs (1,2,3,4–tetrahydronaphthalene and 1,2,3,6,7,8–hexahydropyrene) the opposite is true, the aliphatic region contains many closely spaced features, while the aromatic region has fewer and more widely spaced features. As shown in our previous work[106, 126], and confirmed here, the large number of closely spaced features in the CH–stretching region are due to strong Fermi resonances. As such there is not only the obvious loss of aromatic CH–stretching fundamentals and a gain in the aliphatic CH–stretching fundamentals as expected upon hydrogenation, but there is also a Fermi resonance shift from aromatic fundamentals and aromatic combination bands to between aliphatic fundamentals and aliphatic combination bands. This results in the forest of features moving from the aromatic region to the aliphatic region as observed in the highly

hydrogenated species.

As in the methyl–anthracene series significant changes occur in the 1000 and 600 cm^{-1} region. Again, these changes are not unique to hydrogenation, but rather reflect the loss of solo, duo, trio and quarto hydrogen edges. In 9,10–dihydroanthracene the solo CH–bending mode near 900 cm^{-1} is lost as both solo sites are hydrogenated. In 9,10–dihydrophenanthrene the duo CH–bending mode near 800 cm^{-1} is lost upon hydrogenation. In 1,2,3,4–tetrahydronaphthalene significant intensity is lost in the quarto CH–bending mode near 780 cm^{-1} as four out of eight quarto sites are hydrogenated, as well as a slight shift of the quarto bending mode to lower energy as the aromaticity is disrupted. In 1,2,3,6,7,8–hexahydropyrene the trio CH–bending modes near 780 cm^{-1} are lost as upon hydrogenation of the six trio hydrogens, as well as a slight shift of the duo bending mode to lower energy as the aromaticity is disrupted.

A significant increase in intensity is also observed in the bands near 1500 cm^{-1} for all of the hydrogenated PAHs. However, unlike the methylated species these features are more localized and are due to CH_2 bending modes of the hydrogenated sites.

5.4.5 Astrophysical implications

Determination of the carriers of the minor features observed at 3.40, 3.46, 3.51, and 3.56 μm (2941, 2890, 2849, and 2809 cm^{-1}) in the CH–stretching region of the AIBs is important to understanding the chemical populations in various physical environments. The lack of, or abundance of, these features in environments can point to chemical– or photo–processing of PAHs in space. It is generally believed that these bands are due to aliphatic substitutions to PAHs, either through hydrogenation or alkylation[37]. It has been shown previously[125] that the aliphatic groups of hydrogenated PAHs can indeed reproduce most of these features. Our work here confirms these findings. All four hydrogenated PAHs studied are able to contribute to the features observed at 3.40, 3.46, and 3.51 μm. For 9,10–dihydroanthracene and 9,10–dihydrophenanthrene the features are distinct and easily classified. The feature at 3.40 μm is due to in–plane CH–stretching modes of the hydrogenated sites with little contribution from resonances. The two features at 3.46, and 3.51 μm are due to out–of–plane CH–stretching modes of the hydrogenated sites in strong resonances with combination bands of paired CH–bending modes. The splitting of the out–of–plane CH–stretching modes into the two distinct features is due to the particular modes that are involved in the resonances. Moving up in the degree of hydrogenation with 1,2,3,4–tetrahydronaphthalene and 1,2,3,6,7,8–hexahydropyrene the previously distinct vibrational regions are now blurred into one. While both highly hydrogenated PAHs show many features centered near 3.40, 3.46, and 3.51 μm they are less separated in the spectra. This region is now dominated by Fermi resonances, resulting in many more aliphatic spectral features than seen for the dihydrogenated PAHs. This leads to the possibility that astronomical PAHs with only a few hydrogenated sites would show sharp distinct features around 3.40, 3.46, and 3.51 μm, while PAHs with a majority of hydrogenated sites would show wide blended features around 3.40, 3.46, and 3.51

μm. Although, the feature at 3.56 μm is unaccounted for in all of the theoretical spectra. The methylated PAHs 9–methylanthracene and 9,10–dimethylanthracene both show contributions to the 3.40, and 3.46 μm features. Here these features arise from the CH–stretching modes of the methyl groups in resonance with a wide variety of combination bands. This region is again dominated by Fermi resonances, spreading a large number of features over a wide range. No contributions to the 3.51, and 3.56 μm features are predicted for the two methylated PAHs.

The aromatic CH–stretching region is also affected by the inclusion of additional hydrogens or substitution of methyl groups. For the methylated PAHs the typical aromatic CH–stretching bands are pushed to higher energies (up as high as 3100 cm^{-1}), however they also now begin to resonate with lower energy combination bands involving methyl CH–bending modes (down to 3050 cm^{-1}) resulting in a wider, more even distribution of intensity over the aromatic region than a normal PAH. The aromatic CH–stretching region of the hydrogenated PAHs show similar behavior in that the intensity is distributed over a wider range than a normal PAH. However, there is no shift to higher energies, and the intensity is more concentrated in the lower energy aromatic modes and resonances. At higher temperatures, as lines broaden and blend, these behaviors will affect apparent line widths and positions.

It has also been proposed[125] that the feature at 6.9 μm (1450 cm^{-1}) is likely due to HCH–bending modes (or so–called *methylene scissoring* modes) of hydrogenated PAHs, and could be used as a tracer for hydrogenated PAHs in astronomical observations. The HCH–bending modes are indeed stronger around 6.9 μm, but regular in–plane CH–bending modes also gain significant intensity in this region. Complicating matters further, enhancements in intensities in this region are now also observed for the methylated PAHs. For the methylated PAHs this enhanced region extends from 6.9 μm down to 7.4 μm (1450 cm^{-1}) consisting of combination bands of both CC and CH out–of–plane bending modes.

5.5 Conclusions

This work presented the anharmonic spectrum of six CH–bond–containing PAHs: 9–methylanthracene, 9,10–dimethylanthracene, 9,10–dihydroanthracene, 9,10–dihydrophenanthrene, 1,2,3,4–tetrahydronaphthalene, and 1,2,3,6,7,8–hexahydropyrene. The choice of these PAHs was motivated largely by the need to describe accurately the CH–stretching region (3100 – 2800 cm^{-1}) to aid in the analysis of astronomical observations of the AIBs. Particularly, to explain the source of the 3.40, 3.46, 3.51, and 3.56 μm (2941, 2890, 2849, and 2809 cm^{-1}) IR features observed in a variety of astronomical objects. We have shown that hydrogenated PAHs can contribute to the 3.40, 3.46, and 3.51, μm features, and methylated PAHs to the 3.40, 3.46 μm features. No experimental bands were found to explain the 3.56 μm feature. In conjunction with the low–temperature high–resolution gas–phase spectra presented here, the vibrational sources of the dominant features in the CH–stretching region have been identified and characterized. As in our previous work[106, 126] Fermi resonances are shown to dominate the aromatic

CH–stretching region. Without proper treatment of resonances (i.e., polyad treatment) this region cannot be reproduced accurately. Fermi resonances are now shown to not affect only aromatic CH–stretching modes but also aliphatic CH–stretching modes. This results in many more strong aliphatic bands than would be predicted at the harmonic level. The CH–stretching region has been shown to be the most sensitive upon hydrogenation or methylation; with the gradual loss of aromatic features centered around 3050 cm^{-1} and the rise of the aliphatic features around 2900 cm^{-1}. Not only is there a loss in aromatic fundamental features, but the ability for the remaining aromatic fundamentals to engage in resonances is found to diminish as the molecule becomes more aliphatic. Conversely, as the aliphatic fundamental features become stronger their tendency to engage in strong resonances increases.

IR features have also been characterized in conjunction with MIS data for the range of 2000 through 500 cm^{-1}. The changes to the IR spectra of the hydrogenated and methylated PAHs in this region can be attributed mainly to changes in which IR modes are active (i.e., molecular symmetry considerations), or changes to the edge structure (i.e., solo, duo, trio, quarto out–of–plane CH–bending modes). These changes are not unique to hydrogenation or methylation of PAHs, but are seen across various PAH species and derivatives. The only significant changes that correlate with hydrogenation or methylation (save for the CH–stretching region discussed above) are the features between 1450 and 1350 cm^{-1}. The hydrogenated PAHs show a significant enhancement in intensity to the features near 1450 cm^{-1} compared to their non–hydrogenated counterparts. These features are confirmed as being due to CH_2 bending modes. The methylated PAHs also show enhanced features near 1450 cm^{-1}, but these are less localized and extend down to 1350 cm^{-1}. The features here consist of combination bands of both CC and CH out–of–plane bending modes.

Line position agreement between the anharmonic treatment of this work and the low–temperature high–resolution gas–phase is excellent, agreeing with an average deviation of 0.00% ± 0.17%. The MIS line positions agree with an average deviation of -0.07% ± 0.30%, well within expected experimental limitations. As stated previously, the improvement in accuracy compared to our previous work is due to the improved basis/functional combination (B3LYP/N07D) in the anharmonic approach. The issues observed in the previously recommended basis/functional for anharmonic calculations of PAHs (B97-1/TZ2P) lead to the call for a more in–depth benchmark study.

With the current anharmonic analysis of our collection of PAH families, the extensions into temperature dependent spectra, and full emission spectra are both feasible and currently underway.

Acknowledgements

The authors would like to thank Scott Sandford (NASA Ames) for providing the MIS data. The spectroscopic study of interstellar PAHs at Leiden Observatory have been supported through the Advanced European Research Council Grant

246976, a Spinoza award, and through the Dutch Astrochemistry Network funded by the Netherlands Organization for Scientific Research, NWO. We acknowledge the European Union (EU) and Horizon 2020 funding awarded under the Marie Sklodowska–Curie action to the EUROPAH consortium, grant number 722346. Calculations were carried out on the Dutch national e–infrastructure (Cartesius) with the support of SURF Cooperative, under NWO EW project SH-362-15. AC acknowledges NWO for a VENI grant (639.041.543). AP acknowledges NWO for a VIDI grant (723.014.007). XH and TJL gratefully acknowledge support from the NASA 12–APRA12–0107 grant. XH acknowledges the support from NASA/SETI Co–op Agreement NNX15AF45A. This material is based upon work supported by the National Aeronautics and Space Administration through the NASA Astrobiology Institute under Cooperative Agreement Notice NNH13ZDA017C issued through the Science Mission Directorate.

5.6 Supplemental Material

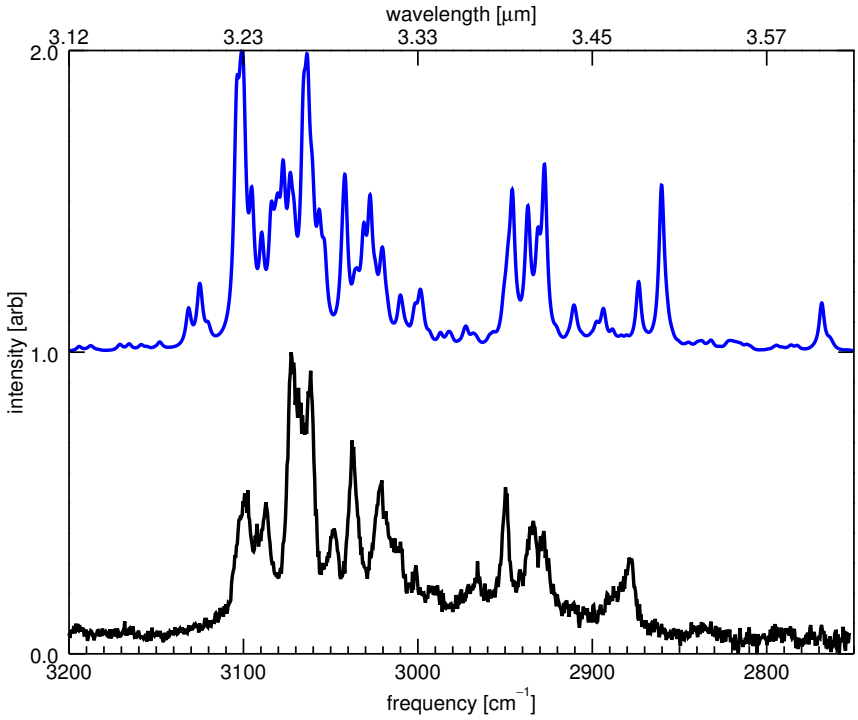

Figure 5.8 Theoretical anharmonic IR spectrum of this work of 9–methylanthracene compared with the high–resolution gas–phase IR absorption spectrum of this work.

exp[24]	rel I[24]	anharm	rel I	components	I source
3099.3	0.53	3100.0	0.58	ν_2, $\nu_{13}+\nu_{22}$, ν_4	ν_2, ν_4
		3101.6	0.42	$\nu_{16}+\nu_{17}$, ν_{13}	ν_3
3092.3	0.43	3089.5	0.40	$\nu_{14}+\nu_{19}$, $\nu_{15}+\nu_{18}$, $\nu_{14}+\nu_{21}$, ν_8	ν_4, ν_1
3087.1	0.50	3083.8	0.50	$\nu_{13}+\nu_{19}$, ν_3	ν_3, ν_1
3072.7	1	3077.3	0.64	$\nu_{13}+\nu_{22}$, $\nu_{14}+\nu_{21}$, ν_1	ν_1, ν_4
3068.5	0.88	3073.1	0.60	$\nu_{14}+\nu_{22}$, $\nu_{14}+\nu_{19}$, $\nu_{13}+\nu_{22}$, ν_4	ν_4
3061.5	0.94	3063.6	0.99	ν_4, $\nu_{14}+\nu_{22}$, ν_5	ν_4, ν_3, ν_5, ν_6
3048.0	0.41	3056.6	0.47	ν_5, $\nu_{14}+\nu_{22}$	ν_5
3037.8	0.70	3041.8	0.26	ν_9, $\nu_{15}+\nu_{19}$, $\nu_{13}+\nu_{23}$, ν_5	ν_5, ν_9
		3041.6	0.32	$\nu_{16}+\nu_{18}$, ν_6	ν_6, ν_4
3020.6	0.58	3027.4	0.52	ν_{10}, $\nu_{15}+\nu_{21}$, $\nu_{15}+\nu_{22}$	ν_{10}
3001.2	0.30	2998.6	0.21	$\nu_{16}+\nu_{22}$, $\nu_{13}+\nu_{26}$	ν_4, ν_3
2965.8	0.30	2972.5	0.09	$\nu_{15}+\nu_{24}$	ν_4, ν_3
2949.8	0.55	2945.9	0.54	ν_{11}, $\nu_{18}+\nu_{20}$	ν_{11}
2933.8	0.44	2936.9	0.49	$\nu_{18}+\nu_{22}$, ν_{12}	ν_{12}
2927.9	0.40	2927.4	0.62	$\nu_{19}+\nu_{19}$, ν_{12}, $\nu_{18}+\nu_{22}$	ν_{12}
2877.5	0.32	2860.3	0.55	$\nu_{20}+\nu_{20}$, ν_{12}	ν_{12}

Table 5.1 Line positions [cm^{-1}], relative intensities, resonance components, and intensity origins for the bands of 9–methylanthracene determined from the high–resolution gas–phase IR absorption spectra and the theoretical anharmonic spectrum of this work (figure 5.8).

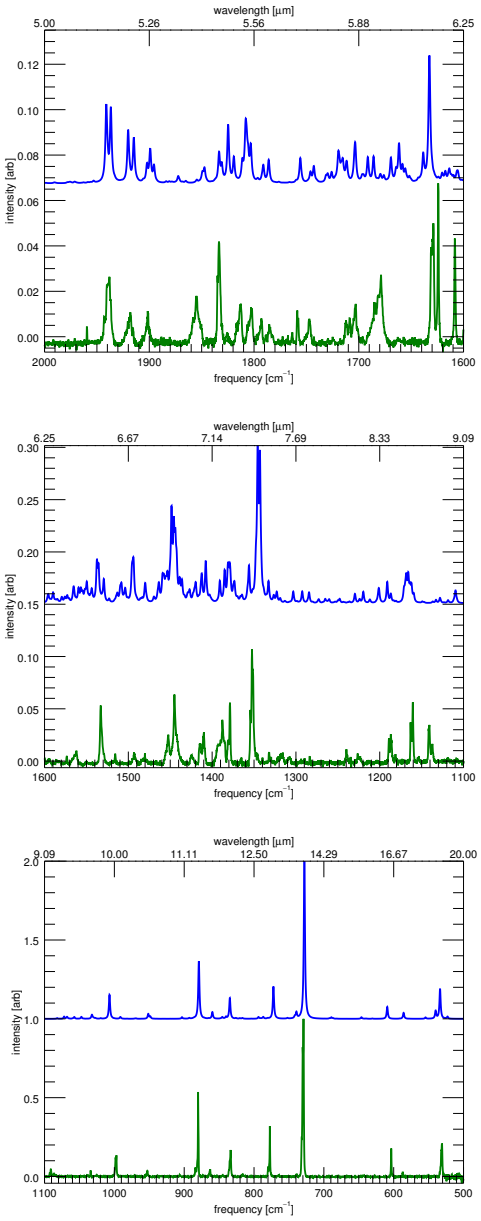

Figure 5.9 The matrix–isolation infrared spectrum[33, 78] of 9–methylanthracene (green, bottom of each panel) compared to the convolved (FWHM 2 cm^{-1}) theoretical anharmonic calculations of this work (blue, top each panel). Three spectral ranges are shown, with each range normalized to the local maximum to enhance details.

exp[33, 78]	rel I	anharm	rel I	mode
1939.1	0.030	1941.0	0.035	$\nu_{42} + \nu_{42}$
1918.8	0.012	1920.2	0.024	$\nu_{44} + \nu_{42}$
1901.5	0.011	1899.1	0.015	$\nu_{45} + \nu_{44}$
1855.0	0.018	1847.3	0.007	$\nu_{47} + \nu_{43}$
1833.4	0.045	1824.7	0.026	$\nu_{42} + \nu_{49}$
1825.7	0.004	1819.3	0.012	$\nu_{43} + \nu_{49}$
1813.5	0.016	1807.9	0.029	$\nu_{46} + \nu_{46}$
1802.4	0.015	1803.2	0.018	$\nu_{45} + \nu_{49}$
1793.3	0.009	1791.1	0.008	$\nu_{45} + \nu_{50}$
1784.9	0.006	1786.0	0.010	$\nu_{44} + \nu_{50}$
1758.4	0.013	1755.8	0.011	$\nu_{47} + \nu_{47}$
1747.2	0.010	1742.9	0.008	$\nu_{43} + \nu_{52}$
1711.9	0.006	1719.4	0.014	$\nu_{48} + \nu_{48}$
1709.8	0.008	1715.4	0.011	$\nu_{47} + \nu_{50}$
1703.3	0.016	1703.5	0.018	$\nu_{44} + \nu_{53}$
1682.7	0.018	1669.3	0.011	$\nu_{37} + \nu_{58}$
1678.8	0.017	1661.6	0.018	$\nu_{45} + \nu_{55}$
1629.7	0.053	1632.7	0.056	ν_{13}
1573.4	0.007	1572.9	0.008	$\nu_{28} + \nu_{70}$
1563.0	0.010	1565.2	0.016	ν_{16}
1532.6	0.052	1537.4	0.042	ν_{17}
1515.6	0.009	1508.3	0.020	$\nu_{51} + \nu_{56}$
1492.9	0.008	1494.0	0.044	ν_{18}
1480.9	0.004	1479.9	0.020	$\nu_{54} + \nu_{54}$
1452.7	0.024	1457.7	0.028	$\nu_{37} + \nu_{66}$
1444.5	0.053	1448.4	0.093	$\nu_{44} + \nu_{63}$
1424.3	0.007	1419.7	0.020	$\nu_{45} + \nu_{64}$
1414.3	0.020	1412.4	0.029	$\nu_{47} + \nu_{61}$
1410.1	0.029	1407.6	0.041	ν_{23}
1388.2	0.023	1390.8	0.022	ν_{24}
1387.6	0.020	1385.1	0.032	ν_{25}
1378.8	0.056	1380.9	0.039	$\nu_{49} + \nu_{61}$
1352.1	0.104	1345.6	0.151	ν_{27}
1332.0	0.011	1332.7	0.021	ν_{28}
1317.5	0.007	1322.9	0.011	$\nu_{54} + \nu_{59}$
1307.9	0.005	1303.2	0.011	$\nu_{52} + \nu_{61}$
1239.5	0.011	1229.6	0.009	ν_{31}
1225.1	0.006	1219.6	0.011	$\nu_{58} + \nu_{58}$
1189.1	0.022	1191.0	0.021	ν_{32}
1186.6	0.026	1186.8	0.009	ν_{33}
1162.9	0.036	1168.3	0.029	$\nu_{52} + \nu_{66}$
1160.6	0.057	1166.0	0.030	ν_{34}
1141.0	0.039	-	-	
1137.3	0.017	-	-	
1090.9	0.049	1109.5	0.012	$\nu_{60} + \nu_{60}$
1086.5	0.017	-	-	
1033.9	0.041	1032.1	0.027	ν_{38}
997.8	0.133	1007.0	0.153	ν_{41}
952.8	0.038	951.5	0.032	ν_{44}
880.0	0.507	879.1	0.363	ν_{47}
863.1	0.041	859.6	0.043	ν_{48}
833.9	0.156	834.6	0.133	ν_{50}
816.1	0.016	816.7	0.006	$\nu_{62} + \nu_{69}$
777.4	0.301	772.2	0.205	ν_{52}
729.7	1	727.9	1	ν_{55}
603.5	0.175	609.2	0.076	ν_{58}
587.0	0.030	585.8	0.038	ν_{59}
531.3	0.217	533.6	0.191	ν_{61}

Table 5.2 Line positions [cm^{-1}], relative intensities, and vibrational mode identifications for the bands of 9–methylanthracene determined from the matrix isolation spectra and the theoretical anharmonic spectrum of this work (figure 5.9).

mode	freq	symm	description
ν_1	3225.9	a′	hindered quarto CH stretch
ν_2	3219.1	a′	unhindered quarto CH stretch
ν_3	3202.1	a′	hindered quarto CH stretch
ν_4	3201.4	a′	unhindered quarto CH stretch
ν_5	3186.9	a′	hindered quarto CH stretch
ν_6	3186.3	a′	unhindered quarto CH stretch
ν_7	3176.8	a′	solo/quarto CH stretch
ν_9	3171.2	a′	solo CH stretch
ν_{10}	3165.6	a′	methyl CH stretch
ν_{11}	3083.7	a″	methyl CH stretch
ν_{12}	3038.6	a′	methyl CH stretch
ν_{13}	1670.9	a′	CC stretch
ν_{14}	1664.2	a′	CC stretch
ν_{15}	1621.0	a′	CC stretch
ν_{16}	1601.1	a′	CC stretch
ν_{17}	1570.8	a′	CC stretch/CH in-plane bend
ν_{18}	1528.1	a′	CH in-plane bend
ν_{19}	1496.6	a′	methyl HCH bend
ν_{20}	1489.7	a″	methyl HCH bend
ν_{21}	1481.9	a′	CH in-plane bend
ν_{22}	1478.0	a′	CH in-plane bend
ν_{23}	1445.3	a′	CC stretch
ν_{24}	1420.1	a′	CH in-plane bend
ν_{25}	1413.1	a′	CH in-plane bend
ν_{26}	1408.6	a′	CH in-plane bend
ν_{27}	1373.8	a′	CH in-plane bend
ν_{28}	1356.7	a′	CH in-plane bend
ν_{31}	1252.0	a′	CH in-plane bend
ν_{32}	1210.4	a′	CH in-plane bend
ν_{33}	1200.7	a′	CH in-plane bend
ν_{34}	1181.4	a′	CH in-plane bend
ν_{37}	1078.8	a′	CH in-plane bend (incl. methyl)
ν_{38}	1050.6	a′	methyl CC stretch
ν_{41}	1025.1	a′	CH in-plane bend (incl. methyl)
ν_{42}	991.2	a″	CH out-of-plane bend
ν_{43}	989.2	a″	CH out-of-plane bend
ν_{44}	971.3	a″	CH out-of-plane bend
ν_{45}	967.3	a″	CH out-of-plane bend
ν_{46}	914.0	a′	CC in-plane bend
ν_{47}	898.6	a″	CH out-of-plane bend
ν_{48}	870.0	a′	CC in-plane bend
ν_{49}	860.2	a″	CH out-of-plane bend
ν_{50}	849.1	a″	CH out-of-plane bend
ν_{51}	830.6	a′	ring breathe
ν_{52}	785.8	a″	CC out-of-plane bend
ν_{53}	765.8	a″	CH out-of-plane bend
ν_{54}	747.2	a″	CH out-of-plane bend
ν_{55}	741.0	a″	CH out-of-plane bend
ν_{56}	698.2	a′	CC in-plane bend
ν_{58}	616.0	a′	CC in-plane bend
ν_{59}	600.8	a″	CC out-of-plane bend
ν_{60}	559.5	a′	CC in-plane bend
ν_{61}	544.8	a″	CC out-of-plane bend
ν_{62}	528.7	a′	CC in-plane bend
ν_{63}	506.8	a″	CC out-of-plane bend
ν_{64}	483.1	a″	CC out-of-plane bend
ν_{66}	405.2	a″	CC out-of-plane bend
ν_{69}	299.5	a″	CC out-of-plane bend
ν_{70}	248.3	a′	body in-plane bend

Table 5.3 Harmonic mode descriptions and frequencies [cm^{-1}] of the IR active modes and modes involved in IR active combination bands for the identifications given in tables 5.1 and 5.2 of 9–methylanthracene.

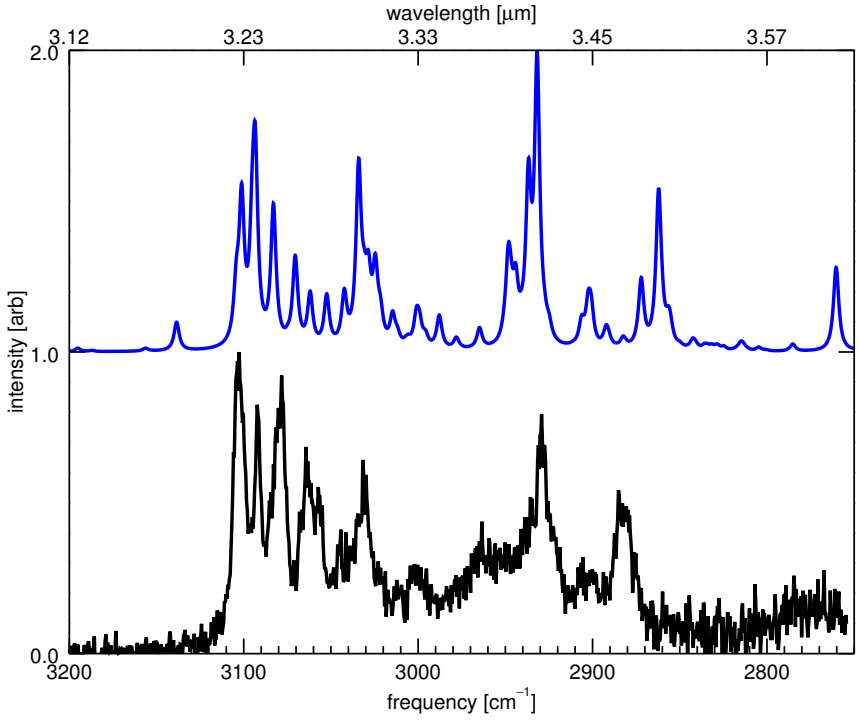

Figure 5.10 Theoretical anharmonic IR spectrum of this work of 9,10–dimethylanthracene compared with the high–resolution gas–phase IR absorption spectrum of this work.

exp[24]	rel I[24]	anharm	rel I	components	I source
3102.6	1	3101.2	0.55	ν_4, $\nu_{16}+\nu_{25}$, $\nu_{16}+\nu_{21}$	ν_4
3092.3	0.83	3093.7	0.77	ν_2, $\nu_{19}+\nu_{20}$	ν_2
3078.3	0.92	3083.0	0.49	$\nu_{16}+\nu_{21}$, ν_4, ν_2	ν_4, ν_2
3063.7	0.47	3070.5	0.32	$\nu_{16}+\nu_{26}$, $\nu_{16}+\nu_{21}$, ν_5	ν_5
3057.3	0.55	3052.4	0.19	$\nu_{16}+\nu_{26}$, $\nu_{19}+\nu_{20}$, ν_5	ν_5
3031.7	0.64	3034.1	0.64	ν_9, $\nu_{15}+\nu_{27}$, $\nu_{18}+\nu_{21}$	ν_9, ν_4
2963.5	0.44	2964.8	0.08	$\nu_{20}+\nu_{21}$	ν_{14}
2929.2	0.79	2932.8	1	ν_{14}, $\nu_{21}+\nu_{24}$	ν_{14}
2885.2	0.54	2862.1	0.54	$\nu_{22}+\nu_{23}$, ν_{14}, $\nu_{21}+\nu_{24}$	ν_{14}

Table 5.4 Line positions [cm^{-1}], relative intensities, resonance components, and intensity origins for the bands of 9,10–dimethylanthracene determined from the high–resolution gas–phase IR absorption spectra and the theoretical anharmonic spectrum of this work (figure 5.10).

mode	freq	symm	description
ν_2	3230.8	b	hindered quatro CH stretch
ν_4	3224.2	b	unhindered quatro CH stretch
ν_5	3196.9	b	CH stretch
ν_9	3168.7	b	methyl hindered CH stretch
ν_{14}	3038.3	b	methyl CH stretch
ν_{15}	1669.4	b	CC stretch
ν_{16}	1657.4	a	CC stretch
ν_{18}	1592.1	a	CC stretch
ν_{19}	1573.3	b	CC stretch
ν_{20}	1536.1	a	CH in-plane bend
ν_{21}	1507.1	b	methyl HCH bend
ν_{22}	1491.0	a	methyl HCH bend
ν_{23}	1490.8	a	methyl HCH bend
ν_{24}	1488.2	a	methyl HCH bend
ν_{25}	1482.5	b	CH in-plane bend
ν_{26}	1474.6	b	CH in-plane bend
ν_{27}	1450.5	a	CC stretch

Table 5.5 Harmonic mode descriptions and frequencies [cm^{-1}] of the IR active modes and modes involved in IR active combination bands for the identifications given in table 5.4 of 9,10–dimethylanthracene.

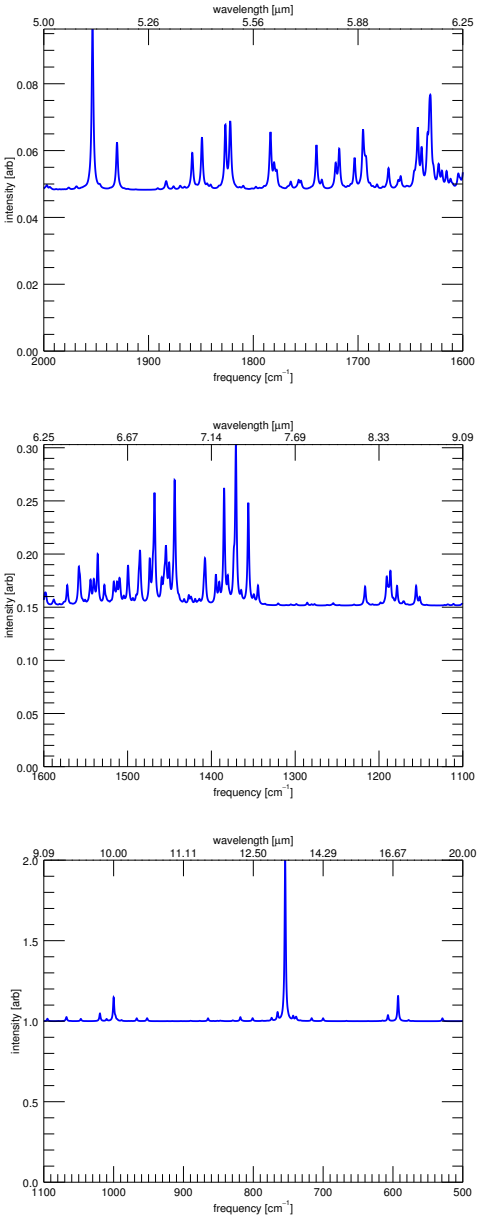

Figure 5.11 No matrix–isolation data is available for 9,10–dimethylanthracene. Therefore, only the convolved (FWHM 2 cm^{-1}) theoretical anharmonic calculations of this work (blue, top each panel). Three spectral ranges are shown, with each range normalized to the local maximum to enhance details.

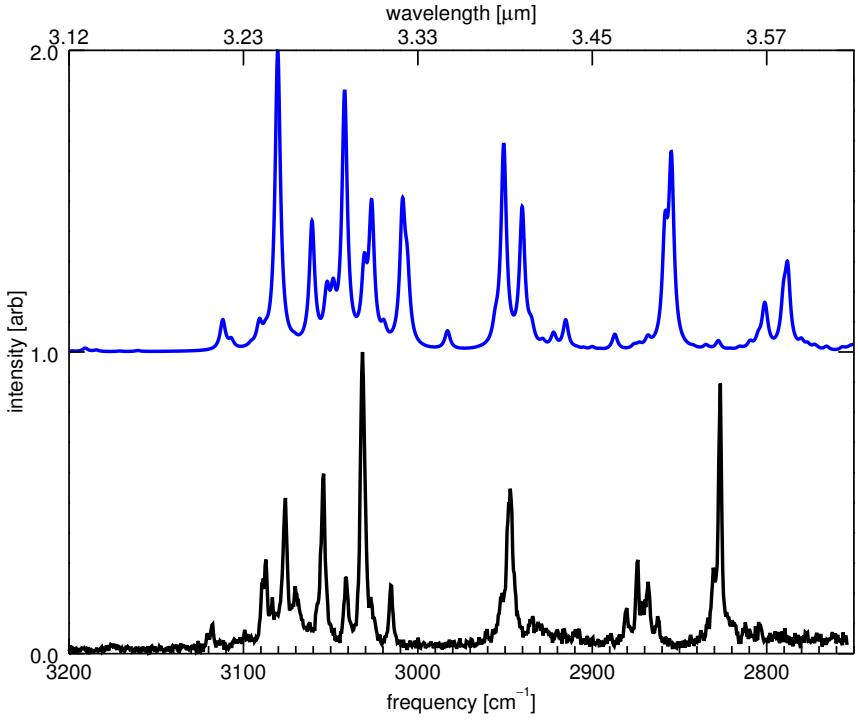

Figure 5.12 Theoretical anharmonic IR spectrum of this work of 9,10–dihydroanthracene compared with the high–resolution gas–phase IR absorption spectrum of this work.

exp[24]	rel I[24]	anharm	rel I	components	I source
3118.1	0.10	3111.8	0.11	$\nu_{13}+\nu_{17}$	ν_7
3087.1	0.31	3090.7	0.11	$\nu_{14}+\nu_{18}$	ν_7
3075.9	0.52	3080.3	1	ν_4, $\nu_{15}+\nu_{19}$, $\nu_{16}+\nu_{20}$	ν_4
3070.3	0.22	3060.7	0.43	$\nu_{16}+\nu_{18}$, ν_5, $\nu_{14}+\nu_{19}$	ν_5
3054.0	0.60	3042.0	0.87	ν_5, $\nu_{13}+\nu_{20}$, $\nu_{14}+\nu_{19}$	ν_5
3041.5	0.25	3030.6	0.33	$\nu_{13}+\nu_{21}$, ν_7, ν_3	ν_7
3031.7	1	3026.4	0.50	ν_8, ν_4, $\nu_{16}+\nu_{20}$	ν_4
3015.5	0.23	3008.7	0.51	ν_7, $\nu_{16}+\nu_{19}$, $\nu_{15}+\nu_{20}$	ν_7
2947.0	0.55	2950.8	0.69	ν_{10}, $\nu_{14}+\nu_{23}$	ν_{10}
2934.2	0.12	2940.2	0.48	ν_{10}, $\nu_{14}+\nu_{23}$, $\nu_{13}+\nu_{25}$	ν_{10}
2880.2	0.15	2887.1	0.06	$\nu_{13}+\nu_{26}$	ν_5
2873.8	0.31	2858.0	0.47	ν_{11}, $\nu_{21}+\nu_{22}$	ν_{11}, ν_{10}
2868.0	0.24	2854.7	0.66	ν_{12}, $\nu_{21}+\nu_{21}$	ν_{12}
2862.6	0.12				
2830.6	0.28	2801.1	0.16	$\nu_{15}+\nu_{29}$, $\nu_{19}+\nu_{24}$	ν_{12}
2826.6	0.90	2788.2	0.30	$\nu_{19}+\nu_{24}$, ν_{12}	ν_{12}

Table 5.6 Line positions [cm^{-1}], relative intensities, resonance components, and intensity origins for the bands of 9,10–dihydroanthracene determined from the high–resolution gas–phase IR absorption spectra and the theoretical anharmonic spectrum of this work (figure 5.12).

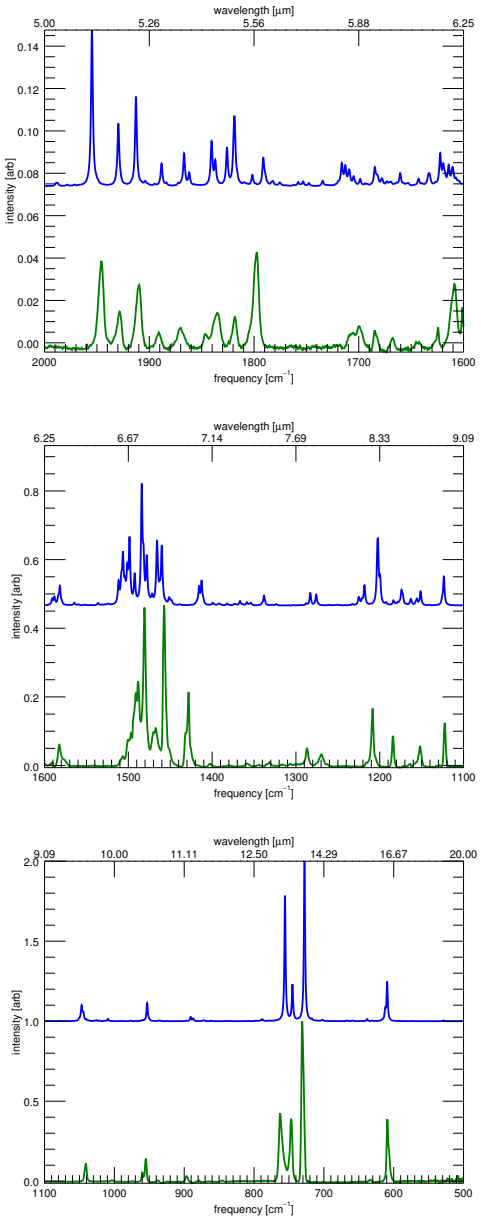

Figure 5.13 The matrix–isolation infrared spectrum[33, 78] of 9,10–dihydroanthracene (green, bottom of each panel) compared to the convolved (FWHM 2 cm^{-1}) theoretical anharmonic calculations of this work (blue, top each panel). Three spectral ranges are shown, with each range normalized to the local maximum to enhance details.

exp[33, 78]	rel I	anharm	rel I	mode
1946.1	0.040	1954.7	0.074	$\nu_{42} + \nu_{41}$
1928.8	0.016	1929.5	0.030	$\nu_{44} + \nu_{41}$
1910.3	0.030	1912.7	0.042	$\nu_{45} + \nu_{42}$
1891.1	0.007	1888.3	0.011	$\nu_{45} + \nu_{44}$
1870.0	0.009	1866.8	0.016	$\nu_{46} + \nu_{41}$
1846.0	0.006	1840.5	0.021	$\nu_{49} + \nu_{41}$
1835.7	0.017	1837.0	0.013	$\nu_{47} + \nu_{44}$
1818.6	0.014	1825.8	0.018	$\nu_{46} + \nu_{45}$
1798.1	0.044	1818.7	0.033	$\nu_{45} + \nu_{48}$
1702.1	0.009	1709.1	0.008	$\nu_{41} + \nu_{55}$
1684.1	0.008	1684.7	0.009	$\nu_{45} + \nu_{52}$
1667.9	0.005	1660.5	0.006	$\nu_{45} + \nu_{54}$
1643.5	0.003	1643.0	0.004	$\nu_{47} + \nu_{52}$
1582.5	0.055	1581.7	0.058	ν_{16}
1507.5	0.025	1511.6	0.074	$\nu_{41} + \nu_{60}$
1499.7	0.069	1506.4	0.158	$\nu_{48} + \nu_{57}$
1489.5	0.228	1498.6	0.201	$\nu_{49} + \nu_{57}$
1480.6	0.418	1484.0	0.356	ν_{18}
1468.9	0.100	1478.0	0.148	$\nu_{53} + \nu_{54}$
1457.3	0.424	1465.8	0.189	$\nu_{43} + \nu_{61}$
1428.8	0.167	1412.6	0.074	ν_{22}
1402.5	0.006	1399.3	0.009	$\nu_{47} + \nu_{61}$
1358.4	0.006	1366.7	0.014	$\nu_{55} + \nu_{57}$
1331.8	0.009	1338.1	0.029	ν_{23}
1286.7	0.048	1282.9	0.037	ν_{26}
1269.8	0.031	1275.8	0.033	ν_{27}
1208.6	0.125	1202.3	0.196	ν_{30}
1184.2	0.089	1174.0	0.046	ν_{33}
1152.0	0.053	1151.3	0.041	ν_{34}
1122.4	0.129	1123.5	0.084	ν_{37}
1041.1	0.110	1046.9	0.101	ν_{39}
959.7	0.050	959.8	0.008	$\nu_{58} + \nu_{66}$
955.0	0.145	953.1	0.115	ν_{44}
937.9	0.006	935.7	0.005	ν_{45}
896.6	0.035	890.8	0.028	ν_{46}
761.6	0.387	755.7	0.784	ν_{52}
747.0	0.382	745.0	0.231	ν_{53}
730.5	1	727.7	1	ν_{54}
633.6	0.011	638.1	0.013	ν_{57}
608.5	0.351	609.3	0.246	ν_{58}

Table 5.7 Line positions [cm^{-1}], relative intensities, and vibrational mode identifications for the bands of 9,10–dihydroanthracene determined from the matrix isolation spectra and the theoretical anharmonic spectrum of this work (figure 5.13).

mode	freq	symm	description
ν_3	3202.6	b_2	quatro CH stretch
ν_4	3202.4	a_2	quatro CH stretch
ν_5	3188.3	a_1	quatro CH stretch
ν_7	3169.1	b_2	quatro CH stretch
ν_8	3168.8	a_2	dihydro CH in-plane stretch
ν_{10}	3077.3	b_2	dihydro CH in-plane stretch
ν_{11}	2984.6	b_2	dihydro CH out-of-plane stretch
ν_{12}	2979.9	a_1	dihydro CH out-of-plane stretch
ν_{13}	1654.8	b_2	CC stretch
ν_{14}	1647.5	a_2	CC stretch
ν_{15}	1633.8	a_1	CC stretch
ν_{16}	1620.0	b_1	CC stretch
ν_{17}	1528.6	a_1	CH in-plane bend
ν_{18}	1514.8	b_1	CH in-plane bend
ν_{19}	1491.9	a_2	CH in-plane bend
ν_{20}	1483.4	b_2	CH in-plane bend
ν_{21}	1471.1	a_1	dihydro HCH bend
ν_{22}	1466.1	b_2	dihydro HCH bend
ν_{23}	1373.6	a_2	CH in-plane bend
ν_{24}	1367.2	b_1	CH in-plane bend
ν_{25}	1351.8	a_1	CC stretch
ν_{26}	1307.2	b_2	CH in-plane bend
ν_{27}	1304.8	b_1	CH in-plane bend
ν_{29}	1234.1	a_1	CH in-plane bend
ν_{30}	1229.5	b_1	CH in-plane bend
ν_{33}	1195.3	b_2	CC in-plane bend
ν_{34}	1184.2	b_1	CH in-plane bend
ν_{37}	1141.1	b_2	CH in-plane bend
ν_{39}	1062.0	b_1	CC in-plane bend
ν_{41}	988.4	b_2	CH out-of-plane bend
ν_{42}	988.3	a_2	CH out-of-plane bend
ν_{43}	975.1	b_2	dihydro out-of-plane twist
ν_{44}	972.5	a_1	CH out-of-plane bend
ν_{45}	951.9	b_1	CH out-of-plane bend
ν_{46}	911.3	a_1	dihydro out-of-plane twist
ν_{47}	896.2	b_2	CH out-of-plane bend
ν_{48}	877.6	a_2	CH out-of-plane bend
ν_{49}	870.0	a_2	CC in-plane bend
ν_{52}	769.0	a_1	CC in-plane bend
ν_{53}	756.9	b_1	CH out-of-plane bend
ν_{54}	739.1	a_1	ring breathe
ν_{55}	726.3	a_2	CC out-of-plane bend
ν_{57}	641.9	b_2	CC out-of-plane bend
ν_{58}	618.8	a_1	CC in-plane bend
ν_{60}	530.9	a_2	CC in-plane bend
ν_{61}	521.2	a_2	CC out-of-plane bend
ν_{66}	359.0	a_1	body drum

Table 5.8 Harmonic mode descriptions and frequencies [cm^{-1}] of the IR active modes and modes involved in IR active combination bands for the identifications given in tables 5.6 and 5.7 of 9,10–dihydroanthracene.

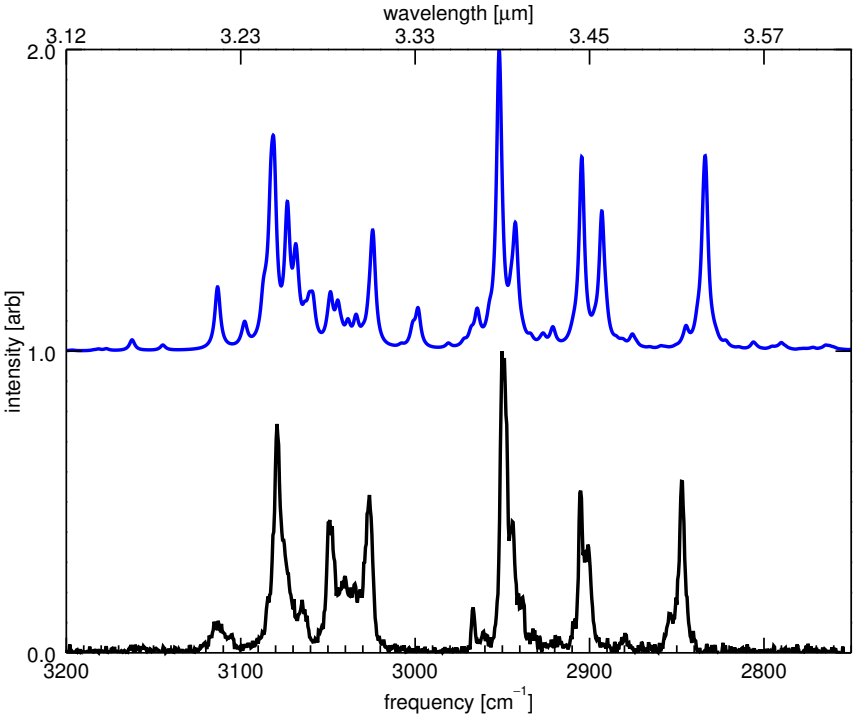

Figure 5.14 Theoretical anharmonic IR spectrum of this work of 9,10–dihydrophenanthrene compared with the high–resolution gas–phase IR absorption spectrum of this work.

exp[24]	rel I[24]	anharm	rel I	components	I source
3112.9	0.10	3113.0	0.11	$\nu_{13}+\nu_{18}$, $\nu_{14}+\nu_{17}$, ν_1	ν_1
		3113.6	0.10	$\nu_{13}+\nu_{17}$, $\nu_{14}+\nu_{18}$, ν_4	ν_4
3079.2	0.76	3081.4	0.72	ν_2, $\nu_{16}+\nu_{18}$, ν_4	ν_2, ν_4
3064.7	0.18	3059.2	0.20	$\nu_{16}+\nu_{17}$, ν_1	ν_1
3048.9	0.44	3048.5	0.20	$\nu_{16}+\nu_{18}$, ν_2	ν_2
3040.1	0.25	3044.4	0.17	$\nu_{14}+\nu_{19}$, $\nu_{14}+\nu_{22}$	ν_4, ν_2
3034.5	0.23	3033.9	0.12	$\nu_{15}+\nu_{19}$, $\nu_{14}+\nu_{21}$, $\nu_{16}+\nu_{21}$, ν_5	ν_5
3026.2	0.52	3024.0	0.22	ν_7, $\nu_{15}+\nu_{22}$, $\nu_{14}+\nu_{21}$	ν_7
		3024.6	0.18	ν_8, $\nu_{13}+\nu_{21}$, ν_4	ν_4, ν_8
2966.7	0.15	2964.4	0.14	$\nu_{13}+\nu_{23}$, $\nu_{18}+\nu_{18}$	ν_9
2950.2	1	2951.8	1	ν_9	ν_9
2944.3	0.44	2942.6	0.43	ν_{10}, $\nu_{13}+\nu_{24}$, $\nu_{14}+\nu_{23}$	ν_{10}
2938.3	0.18	2941.8	0.14	$\nu_{15}+\nu_{23}$, $\nu_{14}+\nu_{24}$	ν_9
2905.1	0.54	2904.5	0.64	ν_{11}, $\nu_{20}+\nu_{22}$, ν_{10}	ν_{11}, ν_{10}
2901.0	0.36	2893.0	0.46	$\nu_{20}+\nu_{20}$, ν_{12}, ν_9	ν_9, ν_{12}
2879.7	0.07	2875.4	0.06	$\nu_{22}+\nu_{22}$, $\nu_{20}+\nu_{20}$	ν_{12}
2854.5	0.13	2845.6	0.07	$\nu_{17}+\nu_{23}$	ν_{11}
2847.2	0.57	2833.7	0.65	ν_{11}, $\nu_{20}+\nu_{22}$, $\nu_{17}+\nu_{23}$	ν_{11}

Table 5.9 Line positions [cm^{-1}], relative intensities, resonance components, and intensity origins for the bands of 9,10–dihydrophenanthrene determined from the high–resolution gas–phase IR absorption spectra and the theoretical anharmonic spectrum of this work (figure 5.14).

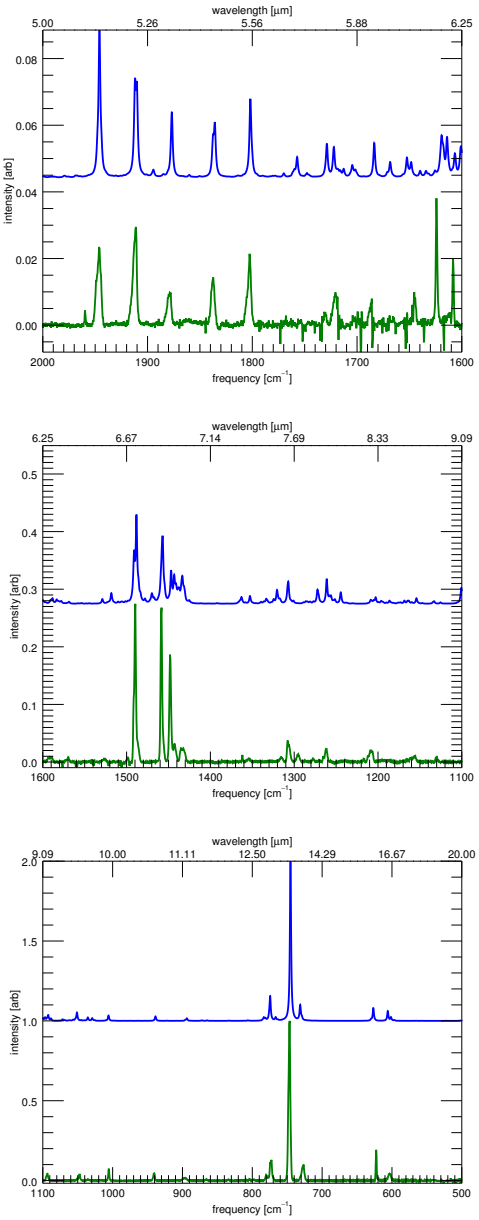

Figure 5.15 The matrix–isolation infrared spectrum[33, 78] of 9,10-dihydrophenanthrene (green, bottom of each panel) compared to the convolved (FWHM 2 cm^{-1}) theoretical anharmonic calculations of this work (blue, top each panel). Three spectral ranges are shown, with each range normalized to the local maximum to enhance details.

exp[33, 78]	rel I	anharm	rel I	mode
1946.6	0.022	1945.9	0.044	$\nu_{44} + \nu_{43}$
1912.1	0.029	1910.3	0.029	$\nu_{45} + \nu_{44}$
1879.4	0.010	1876.8	0.020	$\nu_{46} + \nu_{45}$
1837.7	0.015	1835.8	0.017	$\nu_{48} + \nu_{44}$
1802.9	0.019	1801.8	0.024	$\nu_{48} + \nu_{46}$
1730.5	0.004	1728.8	0.010	$\nu_{49} + \nu_{48}$
1721.0	0.010	1722.1	0.009	$\nu_{51} + \nu_{46}$
1687.4	0.006	1683.6	0.010	$\nu_{54} + \nu_{45}$
1645.1	0.008	1648.3	0.005	$\nu_{51} + \nu_{49}$
1593.0	0.007	1590.5	0.007	$\nu_{37} + \nu_{61}$
1589.6	0.008	1588.5	0.010	ν_{15}
1569.9	0.007	1568.7	0.004	ν_{16}
1489.9	0.253	1488.2	0.154	ν_{18}
1458.5	0.276	1457.1	0.118	ν_{19}
1448.0	0.190	1446.9	0.058	ν_{21}
1443.1	0.030	1443.2	0.050	ν_{20}
1433.3	0.025	1433.5	0.049	ν_{22}
1361.9	0.012	1362.9	0.012	$\nu_{49} + \nu_{61}$
1354.4	0.005	1352.8	0.014	ν_{23}
1315.6	0.008	1320.5	0.024	$\nu_{38} + \nu_{68}$
1306.9	0.034	1307.1	0.039	ν_{26}
1295.4	0.013	-		
1277.4	0.006	1272.2	0.025	$\nu_{52} + \nu_{61}$
1262.0	0.022	1261.2	0.043	ν_{29}
1239.5	0.002	1244.4	0.020	$\nu_{51} + \nu_{62}$
1216.8	0.006	1208.6	0.007	$\nu_{53} + \nu_{63}$
1208.5	0.020	1202.8	0.011	ν_{30}
1165.4	0.004	1168.5	0.006	ν_{34}
1161.0	0.007	1163.3	0.006	$\nu_{52} + \nu_{66}$
1156.4	0.010	1154.1	0.010	ν_{35}
1130.1	0.008	1133.1	0.005	ν_{36}
1093.7	0.042	1092.3	0.037	ν_{37}
1047.5	0.038	1051.1	0.053	ν_{39}
1005.5	0.075	1005.9	0.034	ν_{41}
940.7	0.049	938.7	0.028	ν_{46}
896.9	0.017	893.7	0.016	ν_{47}
779.7	0.032	783.5	0.024	ν_{51}
773.3	0.132	774.4	0.156	ν_{52}
746.9	1	745.3	1	ν_{53}
727.4	0.095	731.4	0.102	ν_{55}
622.5	0.203	626.7	0.080	ν_{57}
603.5	0.044	606.0	0.062	ν_{58}

Table 5.10 Line positions [cm^{-1}], relative intensities, and vibrational mode identifications for the bands of 9,10–dihydrophenanthrene determined from the matrix isolation spectra and the theoretical anharmonic spectrum of this work (figure 5.15).

mode	freq	symm	description
ν_1	3208.4	a	quatro CH stretch
ν_2	3204.5	b	quatro CH stretch
ν_4	3193.8	b	quatro CH stretch
ν_5	3184.3	a	quatro CH stretch
ν_8	3170.5	b	quatro CH stretch
ν_9	3078.5	b	dihydro CH in-plane stretch
ν_{10}	3078.1	a	dihydro CH in-plane stretch
ν_{11}	3013.2	b	dihydro CH out-of-plane stretch
ν_{12}	3003.4	a	dihydro CH out-of-plane stretch
ν_{13}	1652.2	b	CC stretch
ν_{14}	1643.8	a	CC stretch
ν_{15}	1628.2	b	CC stretch
ν_{16}	1607.2	a	CC stretch
ν_{17}	1525.5	a	CH in-plane bend
ν_{18}	1519.1	b	CH in-plane bend
ν_{19}	1486.2	b	CH in-plane bend
ν_{20}	1481.6	a	dihydro HCH bend
ν_{21}	1472.8	b	dihydro HCH bend
ν_{22}	1472.6	a	CH in-plane bend
ν_{23}	1380.9	b	dihydro CH in-plane bend
ν_{24}	1369.1	a	CH in-plane bend
ν_{26}	1339.0	a	dihydro CH in-plane bend
ν_{29}	1282.1	a	CH in-plane bend
ν_{30}	1224.5	a	CH in-plane bend
ν_{34}	1182.1	b	quatro CH in-plane bend
ν_{35}	1178.0	b	dihydro CH in-plane bend
ν_{36}	1149.5	b	CH in-plane bend
ν_{37}	1110.2	a	CC in-plane bend
ν_{38}	1071.8	a	CC in-plane bend
ν_{39}	1068.8	b	CC in-plane bend
ν_{41}	1020.3	b	CC in-plane bend
ν_{43}	989.9	b	dihydro CC in-plane stretch
ν_{44}	988.1	a	CH out-of-plane bend
ν_{45}	955.7	a	CH out-of-plane bend
ν_{46}	955.6	b	CH out-of-plane bend
ν_{47}	908.0	b	dihydro out-of-plane twist
ν_{48}	879.7	b	CH out-of-plane bend
ν_{49}	878.8	a	CH out-of-plane bend
ν_{51}	791.8	a	CH out-of-plane bend
ν_{52}	782.7	b	CH out-of-plane bend
ν_{53}	757.1	b	CH out-of-plane bend
ν_{54}	737.0	a	CH out-of-plane bend
ν_{55}	734.7	b	CC out-of-plane bend
ν_{57}	633.1	b	CC in-plane bend
ν_{58}	610.0	b	CC out-of-plane bend
ν_{61}	503.7	b	CC out-of-plane bend
ν_{62}	470.5	a	CC out-of-plane bend
ν_{63}	466.6	b	CC out-of-plane bend
ν_{66}	392.1	a	body in-plane stretch
ν_{68}	268.2	a	body twist

Table 5.11 Harmonic mode descriptions and frequencies [cm^{-1}] of the IR active modes and modes involved in IR active combination bands for the identifications given in tables 5.9 and 5.10 of 9,10–dihydrophenanthrene.

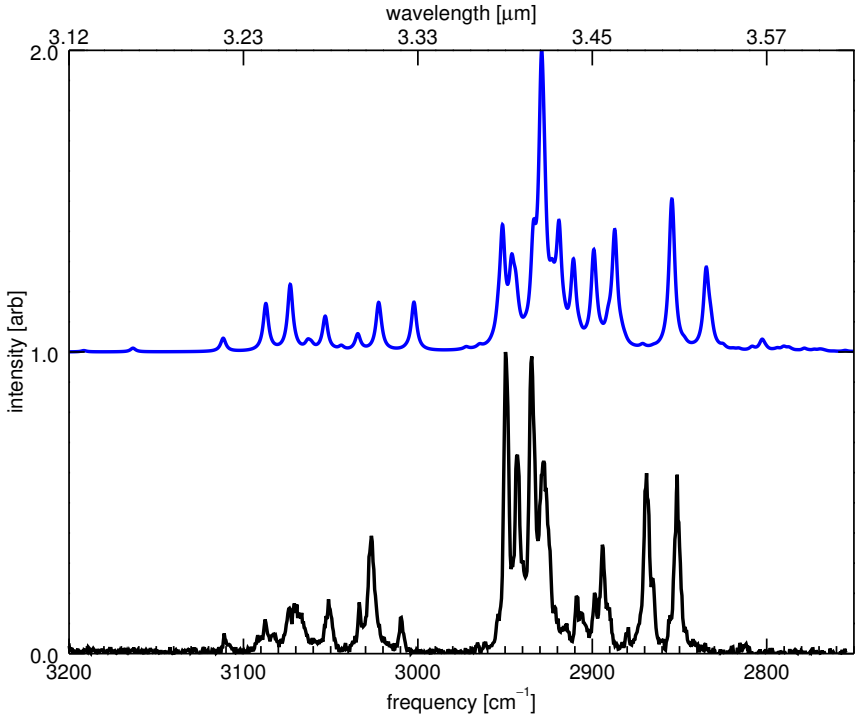

Figure 5.16 Theoretical anharmonic IR spectrum of this work of 1,2,3,4–tetrahydronaphthalene compared with the high–resolution gas–phase IR absorption spectrum of this work.

exp[24]	rel I[24]	anharm	rel I	components	I source
3111.0	0.07	3111.6	0.05	$\nu_{13}+\nu_{15}$, ν_4	ν_4
3087.6	0.10	3087.3	0.16	ν_1, $\nu_{14}+\nu_{15}$, $\nu_{13}+\nu_{18}$	ν_1
3082.5	0.07				
3073.6	0.15	3073.2	0.22	ν_2, $\nu_{14}+\nu_{18}$	ν_2
3070.8	0.17				
3051.2	0.18	3053.1	0.12	ν_3, ν_1, $\nu_{13}+\nu_{18}$	ν_1
3033.6	0.17	3034.4	0.06	ν_3, $\nu_{13}+\nu_{18}$, ν_1	ν_1
3026.6	0.39	3022.5	0.16	$\nu_{14}+\nu_{18}$, ν_4, ν_2	ν_4, ν_2
3009.5	0.12	3003.2	0.16	ν_4, $\nu_{14}+\nu_{18}$, ν_2	ν_4, ν_2
2949.8	1	2951.5	0.42	ν_6, $\nu_{16}+\nu_{16}$, $\nu_{17}+\nu_{17}$, ν_{10}	ν_6, ν_{10}
2942.9	0.66	2946.1	0.33	$\nu_{15}+\nu_{17}$, $\nu_{16}+\nu_{17}$, ν_9	ν_9, ν_8
2934.7	0.99	2929.0	1	ν_5	ν_5
2927.9	0.64	2919.1	0.44	$\nu_{16}+\nu_{16}$, ν_6	ν_6
2909.2	0.19	2910.8	0.31	$\nu_{17}+\nu_{17}$, ν_6, ν_{10}	ν_6, ν_{10}
2898.8	0.20	2899.1	0.34	$\nu_{16}+\nu_{19}$, ν_8	ν_8, ν_{12}
2894.2	0.36	2887.1	0.41	$\nu_{19}+\nu_{20}$, ν_{12}, ν_8, $\nu_{16}+\nu_{19}$	ν_{12}, ν_8
2879.3	0.09	2871.1	0.03	$\nu_{20}+\nu_{20}$, $\nu_{19}+\nu_{19}$	ν_{10}, ν_{11}
2868.9	0.60	2855.4	0.51	ν_{10}, $\nu_{17}+\nu_{17}$, $\nu_{16}+\nu_{20}$	ν_{10}
2851.3	0.60	2834.6	0.28	ν_{12}, $\nu_{19}+\nu_{20}$	ν_{12}

Table 5.12 Line positions [cm^{-1}], relative intensities, resonance components, and intensity origins for the bands of 1,2,3,4–tetrahydronaphthalene determined from the high–resolution gas–phase IR absorption spectra and the theoretical anharmonic spectrum of this work (figure 5.16).

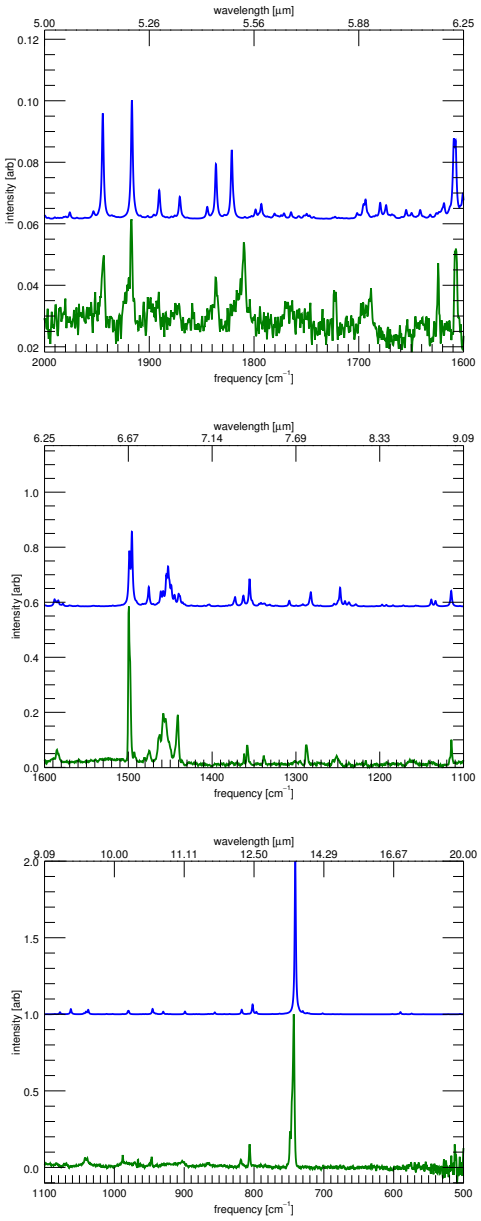

Figure 5.17 The matrix–isolation infrared spectrum[33, 78] of 1,2,3,4–tetrahydronaphthalene (green, bottom of each panel) compared to the convolved (FWHM 2 cm^{-1}) theoretical anharmonic calculations of this work (blue, top each panel). Three spectral ranges are shown, with each range normalized to the local maximum to enhance details.

exp[33, 78]	rel I	anharm	rel I	mode
1944.2	0.024	1944.4	0.034	$\nu_{39} + \nu_{39}$
1916.6	0.030	1916.6	0.039	$\nu_{40} + \nu_{39}$
1896.5	0.005	1890.5	0.009	$\nu_{40} + \nu_{40}$
1836.4	0.015	1837.4	0.011	$\nu_{27} + \nu_{30}$
1810.7	0.021	1821.3	0.023	$\nu_{40} + \nu_{43}$
1692.0	0.012	1693.5	0.006	$\nu_{43} + \nu_{45}$
1589.4	0.012	1588.0	0.026	ν_{14}
1585.2	0.043	1583.6	0.022	$\nu_{35} + \nu_{52}$
1498.9	0.624	1495.8	0.272	ν_{15}
1475.3	0.046	1475.6	0.071	$\nu_{39} + \nu_{52}$
1457.2	0.186	1452.6	0.146	ν_{17}
1441.4	0.196	1440.0	0.046	ν_{19}
1357.9	0.086	1355.3	0.100	ν_{21}
1338.1	0.036	1341.7	0.013	ν_{22}
1287.3	0.090	1282.3	0.052	ν_{26}
1251.9	0.034	1247.3	0.068	ν_{27}
1114.5	0.088	1114.7	0.057	ν_{34}
1040.1	0.048	1037.4	0.030	ν_{37}
988.0	0.063	979.7	0.023	ν_{38}
946.8	0.072	945.3	0.035	ν_{40}
860.7	0.019	856.2	0.013	ν_{44}
818.5	0.047	817.6	0.030	ν_{45}
806.3	0.174	802.1	0.065	ν_{46}
743.7	1	741.0	1	ν_{47}

Table 5.13 Line positions [cm^{-1}], relative intensities, and vibrational mode identifications for the bands of 1,2,3,4–tetrahydronaphthalene determined from the matrix isolation spectra and the theoretical anharmonic spectrum of this work (figure 5.17).

mode	freq	symm	description
ν_1	3200.2	a	quatro CH stretch
ν_2	3185.1	b	quatro CH stretch
ν_3	3165.7	a	quatro CH stretch
ν_4	3162.4	b	quatro CH stretch
ν_5	3073.0	b	dihydro CH stretch
ν_6	3070.0	a	dihydro CH stretch
ν_8	3057.9	b	dihydro CH stretch
ν_9	3025.4	b	dihydro CH stretch
ν_{10}	3020.3	a	dihydro CH stretch
ν_{11}	3006.9	a	dihydro CH stretch
ν_{12}	3006.4	b	dihydro CH stretch
ν_{13}	1649.3	b	aromatic CC stretch
ν_{14}	1622.1	a	aromatic CC stretch
ν_{15}	1525.4	a	aromatic CH in-plane bend
ν_{16}	1502.0	a	dihydro HCH bend
ν_{17}	1492.5	b	dihydro HCH bend
ν_{18}	1482.2	b	aromatic CH in-plane bend/dihydro HCH bend
ν_{19}	1478.8	b	aromatic CH in-plane bend/dihydro HCH bend
ν_{20}	1473.8	a	dihydro HCH bend
ν_{21}	1387.2	a	dihydro CH in-plane bend
ν_{22}	1373.8	a	dihydro CH in-plane bend
ν_{26}	1310.2	b	CH in-plane bend
ν_{27}	1272.9	a	dihydro CH in-plane bend
ν_{30}	1200.8	b	aromatic CC in-plane bend
ν_{34}	1134.3	b	quatro CH in-plane bend
ν_{35}	1100.5	a	alaphatic CC out-of-plane bend
ν_{37}	1056.1	a	ring breathe
ν_{38}	995.3	b	CC in-plane bend
ν_{39}	988.3	a	quatro CH out-of-plane bend
ν_{40}	961.5	b	quatro CH out-of-plane bend
ν_{43}	880.5	a	CH out-of-plane bend
ν_{44}	872.7	a	alaphatic CC in-plane stretch
ν_{45}	829.4	a	alaphatic CC out-of-plane bend
ν_{46}	811.9	b	CC in-plane bend
ν_{47}	753.6	b	quatro CH out-of-plane bend
ν_{52}	512.6	a	CH out-of-plane bend

Table 5.14 Harmonic mode descriptions and frequencies [cm^{-1}] of the IR active modes and modes involved in IR active combination bands for the identifications given in tables 5.12 and 5.13 of 1,2,3,4–tetrahydronaphthalene.

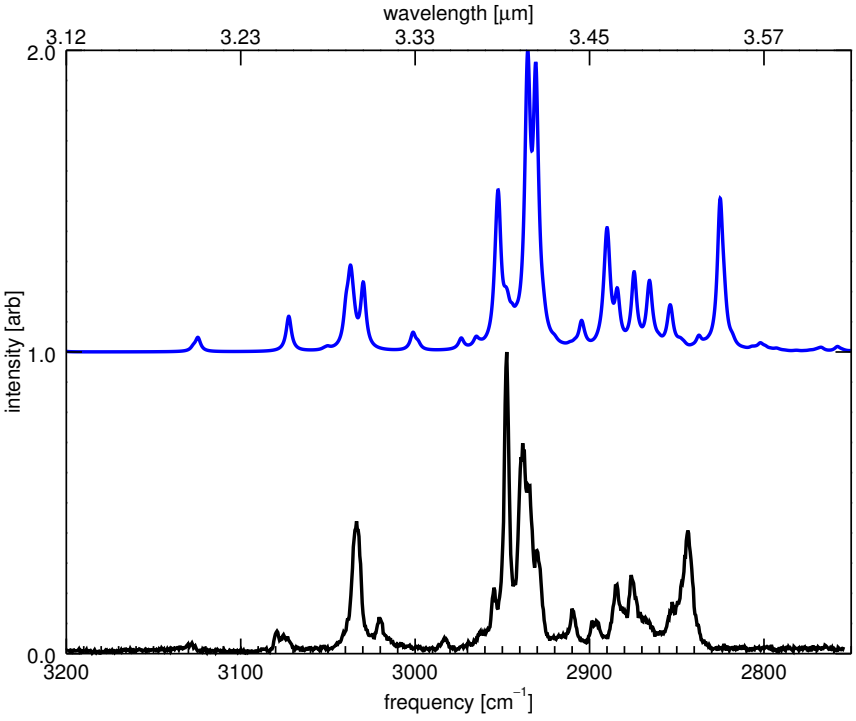

Figure 5.18 Theoretical anharmonic IR spectrum of this work of 1,2,3,6,7,8–hexahydropyrene compared with the high–resolution gas–phase IR absorption spectrum of this work.

exp[24]	rel I[24]	anharm	rel I	components	I source
3128.0	0.04	3124.6	0.05	$\nu_{17}+\nu_{29}$	ν_2
3079.2	0.07				
3075.5	0.06	3072.4	0.12	$\nu_{19}+\nu_{23}$, ν_2	ν_2
3033.6	0.44	3037.1	0.29	$\nu_{17}+\nu_{26}$, ν_2	ν_2
3020.6	0.12	3029.8	0.23	$\nu_{19}+\nu_{27}$, ν_2	ν_2
2982.3	0.05	3001.2	0.07	$\nu_{18}+\nu_{29}$	ν_2
2954.8	0.22				
2947.5	1	2952.4	0.54	$\nu_{21}+\nu_{22}$, ν_8, ν_{12}	ν_8, ν_{12}, ν_6
2938.3	0.70	2935.1	0.47	ν_9, $\nu_{19}+\nu_{33}$	ν_9
		2935.8	0.40	ν_8, ν_6	ν_8, ν_6
		2936.0	0.13	$\nu_{18}+\nu_{35}$, ν_7, $\nu_{19}+\nu_{32}$	ν_7, ν_5, ν_{11}
2934.7	0.56	2931.0	0.96	ν_5	ν_5, ν_{11}
2930.1	0.34	2930.7	-	ν_6	ν_6
2910.1	0.15	2904.6	0.10	$\nu_{21}+\nu_{24}$, $\nu_{21}+\nu_{22}$, $\nu_{22}+\nu_{25}$	ν_8
2896.0	0.10	2890.0	0.41	$\nu_{21}+\nu_{26}$, ν_9	ν_9
2884.3	0.20	2884.2	0.21	$\nu_{24}+\nu_{27}$, $\nu_{25}+\nu_{26}$, ν_{16}, ν_9	ν_9, ν_{16}
2876.1	0.26	2875.4	0.27	$\nu_{26}+\nu_{26}$, $\nu_{27}+\nu_{27}$, ν_{13}	ν_{13}
				$\nu_{26}+\nu_{27}$, ν_{14}	ν_{14}
2852.7	0.17	2853.8	0.16	$\nu_{22}+\nu_{29}$, $\nu_{20}+\nu_{34}$, ν_{11}	ν_{11}
2843.7	0.40	2825.1	0.51	ν_{14}, $\nu_{26}+\nu_{27}$	ν_{14}
				ν_{13}, $\nu_{18}+\nu_{42}$	ν_{13}

Table 5.15 Line positions [cm^{-1}], relative intensities, resonance components, and intensity origins for the bands of 1,2,3,6,7,8–hexahydropyrene determined from the high–resolution gas–phase IR absorption spectra and the theoretical anharmonic spectrum of this work (figure 5.18).

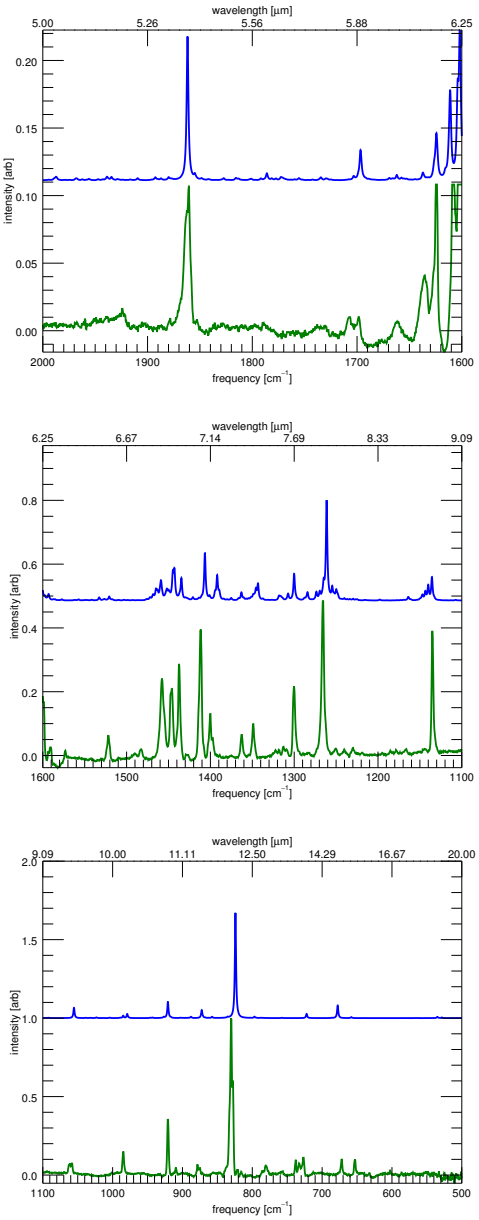

Figure 5.19 The matrix–isolation infrared spectrum[33, 78] of 1,2,3,6,7,8–hexahydropyrene (green, bottom of each panel) compared to the convolved (FWHM 2 cm^{-1}) theoretical anharmonic calculations of this work (blue, top each panel). Three spectral ranges are shown, with each range normalized to the local maximum to enhance details.

exp[33, 78]	rel I	anharm	rel I	mode
1862.1	0.110	1861.8	0.106	$\nu_{57} + \nu_{56}$
1706.4	0.018	1703.1	0.003	$\nu_{57} + \nu_{66}$
1698.2	0.015	1696.7	0.022	$\nu_{62} + \nu_{64}$
1660.7	0.019	1662.1	0.004	$\nu_{64} + \nu_{67}$
1636.0	0.060	1637.1	0.006	$\nu_{56} + \nu_{69}$
1521.8	0.078	1520.7	0.013	ν_{20}
1482.9	0.032	-		
1457.5	0.260	1459.0	0.064	ν_{22}
1446.4	0.249	1444.6	0.096	$\nu_{31} + \nu_{89}$
1437.3	0.310	1434.6	0.071	ν_{26}
1411.8	0.446	1406.6	0.150	ν_{29}
1399.9	0.123	1391.9	0.080	$\nu_{65} + \nu_{72}$
1362.7	0.076	1363.0	0.026	ν_{30}
1348.9	0.105	1345.6	0.054	ν_{32}
1322.2	0.015	1318.1	0.016	$\nu_{58} + \nu_{81}$
1311.6	0.024	1307.3	0.022	$\nu_{55} + \nu_{83}$
1300.1	0.246	1300.1	0.084	ν_{37}
1265.8	0.517	1261.3	0.315	ν_{38}
1250.9	0.020	1254.6	0.047	$\nu_{49} + \nu_{88}$
1240.3	0.015	1249.8	0.036	$\nu_{44} + \nu_{90}$
1229.9	0.021	-		
1135.0	0.419	1135.6	0.074	ν_{48}
1060.2	0.077	1055.4	0.066	ν_{52}
984.8	0.157	979.1	0.026	ν_{55}
920.8	0.406	920.9	0.103	ν_{58}
909.4	0.044	-		
877.0	0.052	872.4	0.051	ν_{61}
830.1	1	824.1	0.671	ν_{64}
780.5	0.058	-		
731.1	0.068	722.2	0.027	ν_{68}
672.1	0.104	677.7	0.080	ν_{70}
653.1	0.114	658.3	0.006	$\nu_{74} + \nu_{88}$

Table 5.16 Line positions [cm^{-1}], relative intensities, and vibrational mode identifications for the bands of 1,2,3,6,7,8–hexahydropyrene determined from the matrix isolation spectra and the theoretical anharmonic spectrum of this work (figure 5.19).

mode	freq	symm	description
ν_2	3177.8	b_1	duo CH stretch
ν_4	3161.5	b_2	duo CH stretch
ν_5	3077.5	a_1	dihydro CH stretch
ν_6	3077.3	b_2	dihydro CH stretch
ν_7	3068.3	b_2	dihydro CH stretch
ν_8	3067.9	b_2	dihydro CH stretch
ν_9	3065.9	b_1	dihydro CH stretch
ν_{11}	3032.8	a_1	dihydro CH stretch
ν_{12}	3032.7	b_2	dihydro CH stretch
ν_{13}	3000.9	a_1	dihydro CH stretch
ν_{14}	3000.8	b_2	dihydro CH stretch
ν_{16}	2998.9	b_1	dihydro CH stretch
ν_{17}	1644.0	a_2	aromatic CC stretch
ν_{18}	1643.7	a_1	aromatic CC stretch
ν_{19}	1638.8	b_2	aromatic CC stretch
ν_{20}	1557.9	b_1	aromatic CC stretch
ν_{21}	1496.4	a_1	dihydro HCH bend
ν_{22}	1496.3	b_2	dihydro HCH bend
ν_{23}	1495.6	a_2	CH in-plane bend
ν_{24}	1485.8	b_2	dihydro HCH bend
ν_{25}	1484.7	a_1	dihydro HCH bend
ν_{26}	1473.4	b_1	dihydro HCH bend
ν_{27}	1471.3	a_2	dihydro HCH bend
ν_{29}	1430.2	b_2	dihydro CH in-plane bend
ν_{30}	1392.4	b_1	duo CH in-plane bend
ν_{31}	1386.4	a_1	CC in-plane stretch
ν_{32}	1376.7	b_2	CH in-plane bend
ν_{33}	1372.3	a_2	dihydro CH in-plane bend
ν_{37}	1331.3	b_1	dihydro CH in-plane bend
ν_{38}	1288.2	b_2	CH in-plane bend
ν_{42}	1249.1	b_2	CH in-plane bend
ν_{44}	1195.4	b_1	dihydro CH in-plane bend
ν_{48}	1156.2	b_1	CH in-plane bend
ν_{49}	1150.0	a_2	CC in-plane bend
ν_{52}	1076.1	b_2	alaphatic CC out-of-plane bend
ν_{55}	995.4	b_2	alaphatic CC in-plane bend
ν_{56}	949.6	b_2	duo CH out-of-plane bend
ν_{57}	947.5	a_2	duo CH out-of-plane bend
ν_{58}	935.4	b_1	CC in-plane bend
ν_{61}	886.6	a_1	dihydro CH out-of-plane bend
ν_{62}	883.4	b_1	CH out-of-plane bend
ν_{64}	841.0	a_1	dihydro CH out-of-plane bend
ν_{65}	832.3	b_2	CC in-plane bend
ν_{66}	812.4	b_1	CH out-of-plane bend
ν_{67}	808.5	b_2	CC out-of-plane bend
ν_{68}	730.6	b_2	CC in-plane bend
ν_{69}	714.5	a_2	CC in-plane bend
ν_{70}	686.4	a_1	CC out-of-plane bend
ν_{72}	586.4	a_1	body breathe
ν_{74}	543.3	b_1	CC in-plane bend
ν_{81}	399.7	a_1	body stretch
ν_{83}	332.9	a_2	CC out-of-plane bend
ν_{88}	131.2	b_1	body twist
ν_{89}	97.7	a_1	out-of plane body bend
ν_{90}	86.9	a_2	body twist

Table 5.17 Harmonic mode descriptions and frequencies [cm^{-1}] of the IR active modes and modes involved in IR active combination bands for the identifications given in tables 5.15 and 5.16 of 1,2,3,6,7,8–hexahydropyrene.

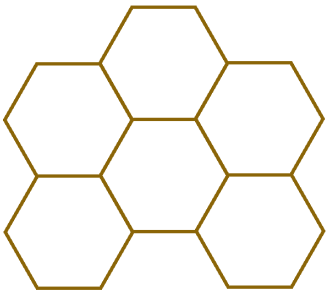

Accounting for large numbers of resonances in temperature dependent infrared spectra

A Wang–Landau statistical approach, making use of anharmonic quartic force fields, has been shown to reproduce temperature shifts and broadenings in the theoretical infrared spectra of small molecules. However, in order to reproduce the low–temperature gas–phase experimental infrared spectra of large molecules, it is crucial to account for a large number of resonances. A second order vibrational treatment, again making use of anharmonic quartic force fields, can account for these resonances through a polyad approach. Therefore, accurate reproduction of high–temperature gas–phase infrared spectrum of large molecules requires the combination of these two approaches. This work harmonizes these two distinct anharmonic effects into one theoretical treatment.

Cameron J. Mackie, Alessandra Candian, Xinchuan Huang, Timothy J. Lee, Alexander G. G. M. Tielens

Submitted, (2018)

6.1 Introduction

As computational power increases and theoretical methods improve, the calculation of highly accurate ab–initio molecular properties is being extended into the domain of larger molecules. Previously, due to computational limitations these larger molecules have been largely overlooked, but can ironically show a greater need for improved theoretical treatments. For example, the inclusion of anharmonicities through a quartic force field (QFF) potential energy surface (PES) has been shown to alter dramatically the resulting theoretical infrared (IR) spectra of polycyclic aromatic hydrocarbons (>20 atoms)[22, 23, 24, 106, 126, 133]. These changes to the spectra have been attributed large numbers of resonances that occur between the ever increasing number of normal modes. These large groups of resonances, so–called *polyads*, are handled sufficiently using a modified second order perturbation theory (VPT2) method akin to degenerate perturbation theory[49, 56].

Other effects attributed to anharmonicities are also known. Band shifts and broadenings are directly related to the temperature of the species due to anharmonic mode interactions. Again, the use of a QFF as the PES allows for accurate reproduction of these effects. Quantum statistical methods, such as a Wang–Landau approach have been shown to reproduce the high–temperature spectrum of small to medium sized molecules[134].

In order to reproduce the high–temperature spectrum of medium to large molecules, the VPT2 and Wang-Landau approaches need to be applied simultaneously. The same anharmonic PES of a molecule can be used to account for both of these effects in a simple manner. This work combines these anharmonic phenomenon (polyads and temperature) into one harmonized theoretical approach.

6.2 Theory

6.2.1 Polyads

In a VPT2 treatment, the anharmonic transition energies between neighboring vibrational levels ($n_k \rightarrow n_k$+1) is written as

$$\Delta E_k(n) = \omega_k + 2\chi_{kk} + \frac{1}{2}\sum_{i\neq k}\chi_{ik} + 2\chi_{kk}n_k + \sum_{i\neq k}\chi_{ik}n_i \tag{6.1}$$

where ω_k is the harmonic frequency of the k^{th} fundamental mode, n_k and n_l are the number of quanta in the respective k and l fundamental modes, and χ_{kl} are the anharmonic constants joining the k and l fundamentals.

The anharmonic constants are calculated in the VPT2 treatment using the calculated QFF of the molecule (see reference 88). During the calculation of these anharmonic constants there exists terms that are inversely proportional to the sums and differences of the harmonic frequencies (see equations A1 and A2 of reference 56). This opens up the possibility for mathematical singularities to occur when these sums and differences are equal (or nearly equal) resulting in divisions by zeros. These singularities are referred to as *resonances*. Four types of resonances

are possible within a VPT2 perturbation treatment: 1) Fermi 1; a fundamental band is approximately equal to two times another, 2) Fermi 2; a fundamental is approximately equal to the sum of two others, 3) Coriolis; two fundamentals are approximately equal, 4) Darling-Dennison; two first overtones are approximately equal. When a resonance occurs, the offending terms must be removed from the regular VPT2 treatment and instead treated in a degenerate VPT2 treatment. A two-by-two matrix is constructed with the diagonals consisting of the *deperturbed* transition energies (equation 7.6), and the off–diagonals with the appropriate coupling terms (Fermi 1, Fermi 2, etc.) (see reference 49). Once solved, this matrix provides the corrected band positions as the eigenvalues, and the degree of mixing between the modes as the square of the eigenvectors. In a physical sense, the offending modes push each other apart slightly in energy, and one mode can borrow intensity from the other. The degree of mode mixing is used to estimate this redistribution of intensity between the resonating modes[106].

Complications arise when modes are in simultaneous resonances with other modes. Treating each resonance individually leads to erroneous results. Instead the group of resonances need to be treated together in what is known as a *polyad*. The polyad resonance matrix is constructed in a similar manner, however additional "2-2" interactions need to be included to account for interactions between combination bands (see reference 49). Again, these matrices are diagonalized, giving the final band positions and intensities (see ref. 106, 126 for more details).

6.2.2 Temperature spectra

The temperature dependent IR spectra of a molecule can be produced in one of two ways. Either a full "exact" method or a Monte–Carlo "sampling" method. In the exact method, thermal populations of the lower levels are calculated at a specific temperature, then band energies and intensities are calculated for every possible transition between the sufficiently populated upper and lower states (see 85 for more details). In the sampling method, a biased sampling known as the Wang–Landau method[135, 136] is performed over vibrational energy space. The use of this method for PAHs was pioneered by Basire et al and applied to a variety of applications[134, 137, 138, 139]. The incorporation of polyads into this biased sampling method is straightforward and will be explained below.

The sampling method begins with calculating the vibrational density of states (DoS) through a random walk over internal vibrational energies, given for an asymmetric top as

$$\begin{aligned} E(\{n\}) = &\sum_{i=1}^{m} h\omega_i \left(n_i + \frac{1}{2}\right) \\ &+ \sum_{1 \le i \le j} \chi_{ij} \left(n_i + \frac{1}{2}\right)\left(n_i + \frac{1}{2}\right) \end{aligned} \tag{6.2}$$

The Wang–Landau method is a biased sampling method in which each time an energy bin is visited it is penalized slightly against further visits, forcing the walk to visit each energy bin a roughly equal amount of times (see 134, 140 for a full

description). This penalization factor converges to the DoS over enough iterations of the walk. Once complete, a second Wang–Landau walk is performed (using the previously calculated DoS to again bias the walk), however during this run the spectrum at each given step is recorded resulting in an absorption spectrum at each energy bin visited given by

$$\mathcal{S}(\nu, E) = \sum_k (n_k + 1)\sigma^k_{0\to1}\delta[h\nu - \Delta E^{(k)}] \tag{6.3}$$

With $\sigma^{(k)}_{0\to1}$ being the absorption cross section of mode k. For combination bands, the corresponding anharmonic cross sections are used with n_k taken to be the lower of the quanta of the two modes. $\Delta E^{(k)}$ becomes the asymmetric top term for the combination band (sum of the individual $\Delta E^{(k)}$'s).

Once complete, the energy dependent spectra are normalized by the number of visits to each energy bin. This results in the microcanonical absorption spectra of the molecule as a function of internal energy I(ν,E).

Transforming from an energy dependent spectrum to a temperature dependent spectrum is then simply a Laplace transformation

$$I(\nu, T) = \frac{1}{Z(T)} \int_{E_{min}}^{E_{max}} I(\nu, E)\Omega(E)e^{(-E/k_BT)}dE \tag{6.4}$$

With Z being the partition function

$$Z(T) = \int \Omega(E)e^{(-E/k_BT)}dE \tag{6.5}$$

The advantage of the sampling method over the exact method is that once the DoS and $I(\nu, E)$ are calculated then producing the spectrum at any desired temperature can be performed in a matter of seconds. In contrast, the exact method needs to be started from scratch for each desired temperature. Additionally, as long as enough steps are performed and the bin sizes are small enough, the sampling method rapidly converges to the exact method. More importantly, it can be seen easily where polyads readily fit into the Wang–Landau sampling method.

6.3 Temperature polyads

Incorporating polyads into the Wang–Landau method is straightforward. At each iteration of the second Wang–Landau walk used to construct $I(\nu, E)$, a polyad matrix is constructed as in a regular anharmonic treatment, except the diagonal terms are replaced by the new transition energies given by equation 7.6. The off–diagonal coupling terms of the polyad matrix are left unchanged in the VPT2 treatment, as they do not depend on the vibrational energy levels occupied, but only on the change in number of quanta in a given mode (equations 4-7 in reference 49 (here $\Delta(n_k)$ is always 1). Therefore, the polyad matrices only need to be constructed once, and at each iteration only the diagonal terms need to be replaced and the new matrix diagonalized. As before, the eigenvalues of the new polyad matrix gives the transition energies of the vibrationally excited states (i.e., a new set of Δ

$E^{(k)}(\{n\})$, and the squared eigenvalues give the intensity sharing percentages over the resonating modes (i.e., a new set of $\sigma^{(k)}_{0\rightarrow 1}$). It is possible, but not necessary to perform these polyad corrections within the Wang–Landau walk used to construct the DoS, but as resolution of the bin sizes is low (typically 25cm^{-1}) the corrections are insignificant. All other steps during the Wang–Landau creation of the temperature dependent spectrum remain the same as references 134, 140.

6.4 Methods

To demonstrate the of inclusion of polyads into a temperature dependent spectrum of a medium sized molecule, phenanthrene ($C_{14}H_{10}$) was chosen as a test case. A non–temperature dependent and temperature dependent (1000 K) spectrum were produced, each including and excluding polyads. Additionally, tetracene ($C_{18}H_{12}$) was chosen to demonstrate the changes that can occur in resonances as temperature is increased (from 100 K – 700 K).

The methods for producing the anharmonic IR spectra follow our previous work [106, 126, 133]. The software package Gaussian09[51] is used to optimize the geometry, calculate the QFFs, and produce the ground state IR intensities. Density functional theory is used (DFT) using the B3LYP functional[127] and N07D basis[129]. For the VPT2 treatment, and to produce the initial polyad matrices, a locally modified version of the SPECTRO software package[52] was used after transforming the QFF produced by Gaussian from normal to Cartesian coordinates[98].

The parameters used for the Wang–Landau walks were comparable to the values given in reference 134. For the initial Wang–Landau walk the vibrational quanta number probability increase/decrease parameter was set to 5%. The DoS energy bins were set to 25 cm^{-1}. The energy range of the walk was 0 – 15 eV (0 – 120983 cm^{-1}). Twenty iterations of decreasing penalization factors (f) were run, with each iteration consisting of $1{\times}10^7$ steps. For the second Wang–Landau walk, which was used to produce the energy dependent spectrum, the spectral bin size was set to 0.1 cm^{-1}. The second walk was performed until each energy bin was visited 2,500 times.

6.5 Results

Figure 6.1 shows the theoretical spectrum of phenanthrene computed at 0 K with and without including polyads compared to a high–resolution low–temperature gas–phase experimental spectrum[23]. As can be seen, additional bands are present due to intensity borrowing, as well as shifts in band positions, both occurring due to resonances and the inclusion of polyads in the calculations. Many features are absent and shifted incorrectly when polyads are ignored, and as a result the match to the experimental spectrum is quite poor. In contrast, the polyad results give very satisfactory comparisons to experimental data (see references 22, 23, 24 for more comparisons). Figure 6.2 shows the comparison of the theoretical spectrum at 1000 K computed with and without polyads. Significant differences can still

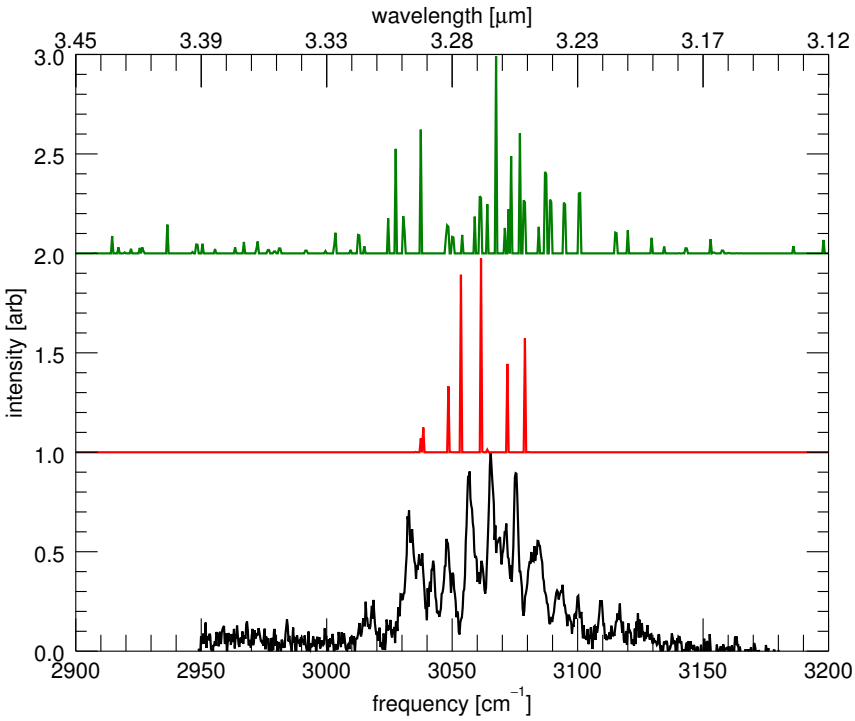

Figure 6.1 Comparison of the 0 K theoretical spectrum of phenanthrene including polyads (green), and excluding polyads (red), compared to a high–resolution low–temperature gas–phase experimental spectrum[23].

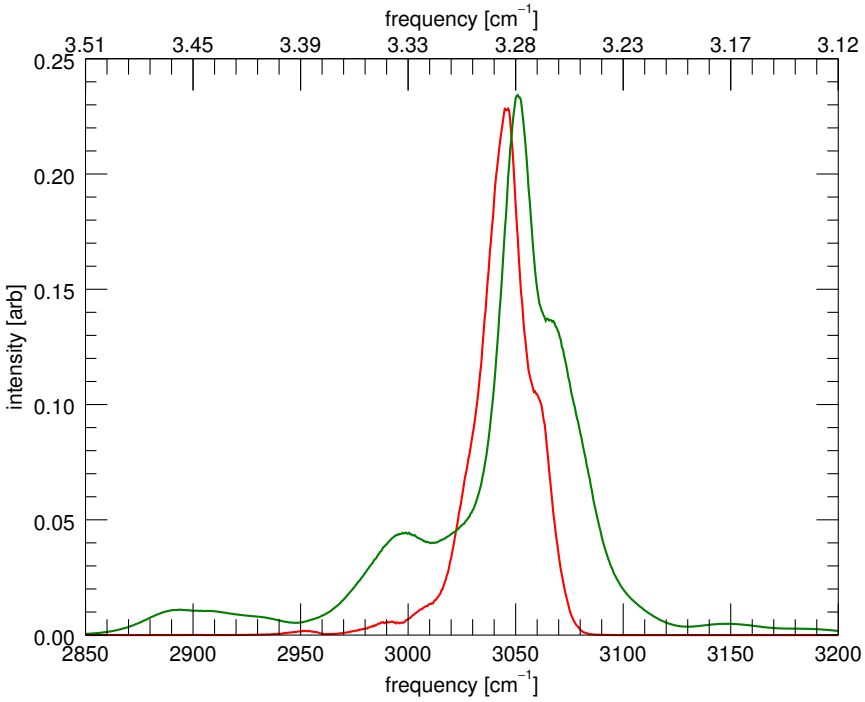

Figure 6.2 Comparison of theoretical spectrum of phenanthrene at 1000 K including polyads (green), and excluding polyads (red).

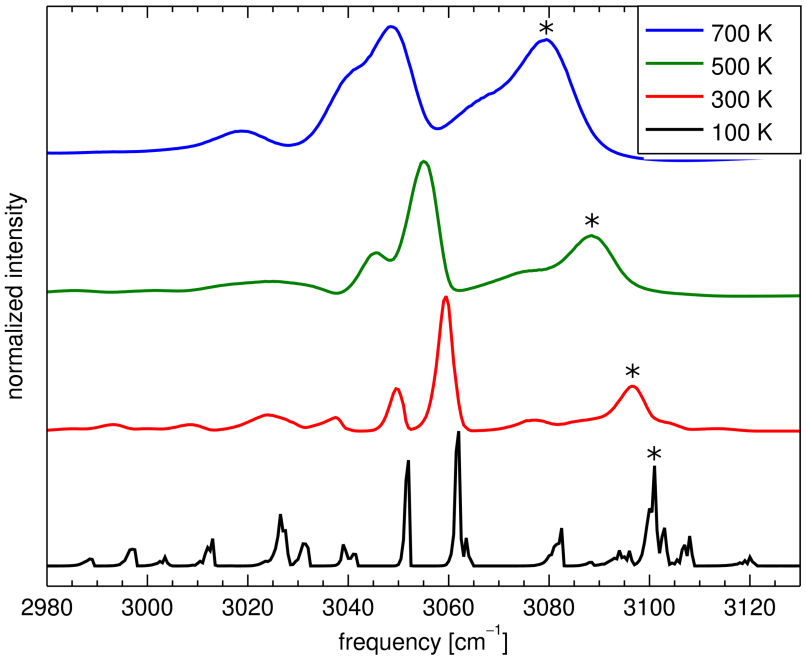

Figure 6.3 The theoretical infrared spectrum of tetracene showing an increase in relative intensity of a combination band (marked with a "*") as the internal temperature is increased.

be observed even in this highly broadened spectrum. Besides frequency shifts, the effects of intensity borrowing can also be observed, especially for the feature at 3000 cm^{-1}. The minor features arising from intensity borrowing are also still visible, now as an extended pseudo–continuum under the main spectral features. There is also an overall shift and broadening of the main spectral features when moving from the non–polyad to the polyad spectrum.

The anharmonic constants and quantum occupations of the CH–stretching modes, and the combination bands which resonate with them, were found to differ enough that it was possible for the combination bands to "catch–up" to the position of the CH–stretching modes. In other words, the resonance between a particular combination band and a fundamental can wax or wane as thermal population of vibrational levels increases. Since the strength of the interactions between resonating modes depends on the energy separation of the modes, as the combination bands catch–up they begin to borrow more intensity from the fundamentals. This has the effect of a gradual increase in intensity of the combination bands as the internal energy of the molecules is increased. For example, this effect was found to be very strong for a particular combination band in tetracene. The combination band was observed to gain significant intensity up to an internal energy of approximately 2.5 eV before decreasing again at higher energies. Figure 6.3 shows the effect this has on the temperature dependent spectrum. It can be seen that the combination band marked with a "*" initially drops in intensity (due to thermal broadening), but then grows again at higher temperatures compared to the two strongest fundamentals.

The methods described in this work have also been applied successfully to a larger set of PAHs (including hydrogenated, methylated, nitrogen–substituted, and cationic PAHs), which are the topics of future work. Similar behavior is found.

6.6 Conclusions

Incorporating resonances and polyads into a Wang–Landau statistical approach to temperature dependent spectra is straight forward. As shown previously[22, 23, 24, 106, 126, 133], the change in the IR spectrum of molecules where resonances play an important role is significant at low temperatures. The same holds true for high temperatures. Changes in both band positions and widths, as well as the appearance of additional features is observed even in the unresolved spectrum at high temperatures. The predicted temperature effects on an IR spectrum can be significantly underestimated when polyads are neglected. Additionally, resonances may wax and wane as the temperature increases, which can dramatically alter the measured spectra at specific internal energies or temperatures. The low effort and high impact of including polyads into the Wang–Landau approach warrants their inclusion in all temperature calculations of large molecules.

Acknowledgments

Spectroscopic studies of interstellar PAHs at Leiden Observatory are supported through a Spinoza award, and through the Dutch Astrochemistry Network funded by the Netherlands Organization for Scientific Research, NWO. We acknowledge the European Union (EU) and Horizon 2020 funding awarded under the Marie Sklodowska–Curie action to the EUROPAH consortium, grant number 722346. Calculations were carried out on the Dutch national e–infrastructure (Cartesius) with the support of SURF Cooperative, under NWO EW project SH-362-15. TC sincerely thanks the support from Swedish Research Council (grant No. 2015-06501). AC acknowledges NWO for a VENI grant (639.041.543). XH and TJL gratefully acknowledge support from the NASA 12–APRA12–0107 grant. XH acknowledges the support from NASA/SETI Co–op Agreement NNX15AF45A. This material is based upon work supported by the National Aeronautics and Space Administration through the NASA Astrobiology Institute under Cooperative Agreement Notice NNH13ZDA017C issued through the Science Mission Directorate.

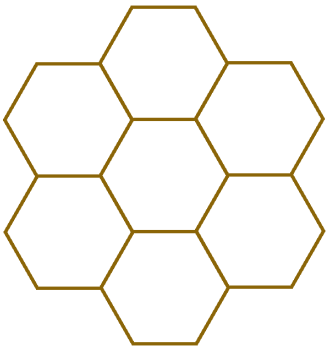

Fully anharmonic infrared cascade spectrum of polycyclic aromatic hydrocarbons

The infrared (IR) emission of polycyclic aromatic hydrocarbons (PAHs) permeates our universe; astronomers have detected the infrared signature of PAHs around every interstellar object with sufficient energy to excite them. The IR emission of interstellar PAHs differs from their emission seen under conditions on Earth, as they emit through a collisionless cascade down through their excited vibrational states from high internal energies. The difficulty in reproducing interstellar conditions in the laboratory results in a reliance on theoretical techniques. However, the size and complexity of PAHs requires careful consideration when producing the theoretical spectra. In this work we outline the theoretical methods necessary to lead to a fully theoretical IR cascade spectra of PAHs including: an anharmonic second order vibrational perturbation theory (VPT2) treatment; the inclusion of Fermi resonances through polyads; and the calculation of anharmonic temperature band shifts and broadenings (including resonances) through a Wang–Landau approach. We also suggest a simplified scheme to calculate vibrational emission spectra that retains the essential characteristics of the full IR cascade treatment and can directly transform low temperature absorption spectra in IR cascade spectra. Additionally we show that past astronomical models were in error in assuming a 15 cm^{-1} correction was needed to account for anharmonic emission effects.

Cameron J. Mackie, Alessandra Candian, Xinchuan Huang, Timothy J. Lee, Alexander G. G. M. Tielens
Submitted, (2018)

7.1 Introduction

Polycyclic aromatic hydrocarbons (PAHs) are a family of molecules characterized by containing multiple fuzed benzenoid rings with the free edges capped with hydrogen. Their size, complexity, stability, and universal abundance make their study appealing to vastly different areas of research: from biology for their carcinogenic properties[3], to material science for their desirable structural properties[5, 6, 7], to engineering for their role in the undesirable combustion byproducts of engines and rockets[2]. Perhaps the most surprising field to study PAHs is astronomy. The infrared (IR) signatures of aromatic carbon–containing molecules have been observed in all interstellar objects with sufficient ultra–violet (UV) radiation to excite them; from reflection nebulae, to photo–dissociation regions, to emissions from distant galaxies as a whole[76]. These so–called "aromatic infrared bands" (AIBs) are generally attributed to PAHs and PAH derivatives[26, 27]. The interstellar PAHs absorb UV photons from a source (i.e., a parent star) becoming electronically excited, then quickly (hundreds of femtoseconds) return to their electronic ground state through emission-less internal conversion into highly excited vibrational states. They then relax radiatively through gradual (˜seconds) emission of IR photons from their excited vibrational states producing what is known as an *IR cascade spectrum*[39, 104].

Producing experimental IR cascade spectra under astrophysically relevant conditions (i.e., an extreme vacuum with zero collisions) is extremely difficult with current technolgies. Therefore, extrapolations from available data must be made. Experimental high–resolution, low–temperature, gas–phase emission spectra would be ideal. However, experiments have been limited largely to either high–temperature gas–phase absorption spectra[21, 82, 83], or low–temperature matrix–isolation spectra[77, 78, 79, 80, 109, 110]. The usefulness of these experiments in modeling IR cascade spectra are complicated by temperature and pressure effects in the former, and unpredictable matrix interaction effects in the later. Recently, high–resolution, low–temperature, gas–phase *absorption* spectra have been produced for a handful of small PAH species in the CH–stretching IR region[22, 23, 24].

Due to the large variety and size of PAHs, most theoretical calculations to date have been performed using low levels of theory, typically scaled density functional theory (DFT) calculations at the double harmonic level, using the B3LYP functional[127] and 4-31G[141] basis set. Databases of the theoretical calculations of PAHs have been compiled[33, 48] and are used by astronomers in modeling PAH IR cascade emission. These databases have been vital to understanding the variation in the PAH emission observed both between different interstellar environments, and spatially within a given interstellar object. These variations can be used to track properties such as size, structure, temperature, and charge balance[18, 25, 30].

Although successful in many ways, detailed comparison between theory and experiments have revealed that that these double harmonic calculations cannot model accurately the PAH emission at high resolution, especially in the CH–stretching region centered around 3.3 μm[22, 23, 24]. While this has not hindered observations of PAHs using current telescopes, it is bound to become a glaring issue with the

upcoming launch of the James Webb Space Telescope, which will give an unprecedented combination of spectral and spatial resolution in the infrared region. Recent work has shown[106, 126, 133] that in order to overcome these deficiencies an anharmonic approach is necessary. The anharmonic approach is not only better in predicting the vibrational fundamental band positions and intensities themselves, but also allows for the calculation of combination bands, overtones, and hot–bands. Additionally, anharmonic calculations can account for mixing between modes in *Fermi resonances*, which are vitally important for reproducing the 3.3 μm region accurately.

These anharmonic calculations also allow for an ab–initio approach for generating internal energy/temperature dependent spectra. Two main methods have been put forward: a direct approach – whereby the thermal population of each vibrational state is calculated, then transition energies and intensities are calculated for every possible transition between populated states[85]; and a statistical approach – whereby a biased Monte Carlo walk, known as the Wang–Landau method[135, 136], is used to construct the density of states (DoS) and the energy dependent spectra. These methods then produce temperature dependent spectra through a Laplace transformation[134]. This latter approach has been shown to be quite efficient since the time consuming DoS and energy spectrum calculations need to be performed only once for each molecule, then any desired temperature spectrum can be generated in a matter of seconds using the Laplace transformation. The latter method has also been shown to be advantageous in that incorporating the important Fermi resonances into the spectrum is a straight forward exercise[142].

The collision–free cascade emission process of PAHs needs to be considered when modelling the IR spectrum of interstellar PAHs. As stated previously, the PAHs absorb UV photons, interconvert electronically into the ground electronic state with excited vibrational states, then emit IR photons slowly as they cool. Attempts have been made to replicate these conditions in the laboratory[40, 41, 42] with some success. Theoretical modelling of the IR cascade emission has also been preformed, typically using DFT calculations at the double harmonic level[43, 44], and to a lesser extent at the anharmonic level[138, 139]. However, a sufficient treatment of Fermi resonances in a full anharmonic cascade model has never been taken into account previously, leading to spectra that could not be fully trusted, especially in the troublesome 3.3 μm region. Additionally, due to the limited datasets and number of species analyzed, these previous studies have given rise to approximated methods whose validity has to be assessed, as will be explained below.

With the proper incorporation of anharmonicities, resonances, and internal energy/temperature dependence (including the incorporation of polyads), the ingredients are present for a full theoretical anharmonic IR cascade spectra of PAHs. In this work, these calculations are performed for a small subset of astrophysically relevant species, including regular, hydrogenated, and methylated PAHs, as well as cationic species (see supporting material for all results). This work also shows that the Wang–Landau approach can reach the same accuracy of more "exact" techniques like the direct counting methods at a fraction of the computational

cost. The indivual theories underlying each theoretical step used towards the full cascade model are outlined in section 7.2. Details of the application of these methods are given in section 7.3. The results are give in section 7.4 as well as in the supporting material**??**. Discussion and conclusions follow.

7.2 Theory

7.2.1 Anharmonicity

In the double harmonic approximation the vibrational potential of a molecule in its stationary point geometry is given by

$$V = \frac{1}{2} \sum_{i=1}^{3N} \sum_{j=1}^{i} F_{ij} X_i X_j \tag{7.1}$$

where V is the total vibrational potential, $F_{ij} = \frac{\partial V}{\partial X_i \partial X_j}$ are the quadratic force constants between atoms i and j, and X_i and X_j are the Cartesian coordinates of atom i and j relative to the stationary point geometry.

The quadratic force constants are computed through ab–initio analytical second derivative techniques. Once computed these quadratic force constants are used to construct a Hessian matrix, which upon diagonalization yields the individual vibrational band energies (harmonic frequencies) as the eigenvalues, and the individual vibrational mode displacement descriptions or "normal modes" as the eigenvectors. This method results in 3N-6 normal modes for non–linear molecules and 3N-5 normal modes for linear molecules (where N is the number of atoms). The harmonic intensities of the vibrational modes are calculated using the double harmonic approximation, whereby a matrix is constructed and solved using the derivatives of the dipole moment as the molecule is displaced along its normal modes. In this approximation the intensities of the overtones, combinations bands, and hot bands are exactly zero. Additionally, interactions between modes such as couplings and resonances cannot be taken into account. This results in a spectrum that needs to be scaled in frequency, and a spectrum that miss a large number of features. In addition this, in order to include temperature effects such as band broadenings and shifts empirically derived expressions need to be applied[43, 45].

To account for these short comings, a more accurate approach is necessary. Ideally, the exact potential could be written as an infinite order Taylor series. The harmonic equation above would represent the first order terms of such an expansion. Subsequent higher order terms would include cubic, quartic, pentic, hextic, etc. force constants (derivative terms). However, to sufficiently account for combination bands, overtones, hot–bands, couplings, resonances, and temperature effects it is enough to include the first three non–zero terms of the expansion,

leading to the so–called anharmonic quartic force field (QFF)

$$\begin{aligned} V = & \frac{1}{2}\sum_{i=1}^{3N}\sum_{j=1}^{i}\left(\frac{\partial^2 V}{\partial X_i \partial X_j}\right)_{V_0} X_i X_j \\ & + \frac{1}{6}\sum_{i=1}^{3N}\sum_{j=1}^{i}\sum_{k=1}^{j}\left(\frac{\partial^3 V}{\partial X_i \partial X_j \partial X_k}\right)_{V_0} X_i X_j X_k \\ & + \frac{1}{24}\sum_{i=1}^{3N}\sum_{j=1}^{i}\sum_{k=1}^{j}\sum_{l=1}^{k}\left(\frac{\partial^4 V}{\partial X_i \partial X_j \partial X_k \partial X_l}\right)_{V_0} X_i X_j X_k X_l \end{aligned} \tag{7.2}$$

A simple Hessian can no longer be constructed to solve this potential since it is now non–linear. Instead, the harmonic solution is calculated as usual, then the cubic and quartic force constants are used to perturb the harmonic solution in a second order perturbation theory treatment (VPT2) (see Ref. [87] for a full description). With the total vibrational energy of the perturbed molecule given by

$$\begin{aligned} E(v) = & \sum_k \omega_k \left(n_k + \frac{1}{2}\right) + \sum_{k\le l} \chi_{kl}\left(n_k + \frac{1}{2}\right) \\ & \times \left(n_l + \frac{1}{2}\right) \end{aligned} \tag{7.3}$$

where ω_k is the harmonic frequency of the k^{th} fundamental, n_k are the number of quanta in the k^{th} fundamental vibrational mode, and χ_{kl} are the corresponding anharmonic constants, with the anharmonic constants being calculated from the cubic and quartic force constants (see 88). Combination bands are given as the sum of the perturbed fundamentals, and the hot–bands and overtones are determined by increasing the number of quanta in the relevant vibrational modes. Equation 7.3 shows that the vibrational band positions are no longer independent, but now depend on the excitement of the other vibrational modes. This gives rise to temperature dependent shifts and broadenings, which will be expanded upon below.

Intensities can also be calculated at the anharmonic level for fundamentals, overtones, and combination bands. See Ref. 91 for the complete set of equations.

Figure 7.1 shows the effect that including anharmonicities into the potential energy surface has on the infrared spectrum of a PAH. A comparison is made between the unshifted harmonic, full anharmonic, and high–resolution low–temperature gas–phase experimental[24] infrared spectrum of the 3.3 μm CH–stretching region of 9-methylanthracene. This region is particularly sensitive to anharmonic effects.

7.2.2 Resonances and polyads

In an anharmonic treatment the vibrational modes are no longer independent from one another, and so they can interact through *resonances*. A resonance occurs when the energy of the normal modes or the sum of modes are close to one

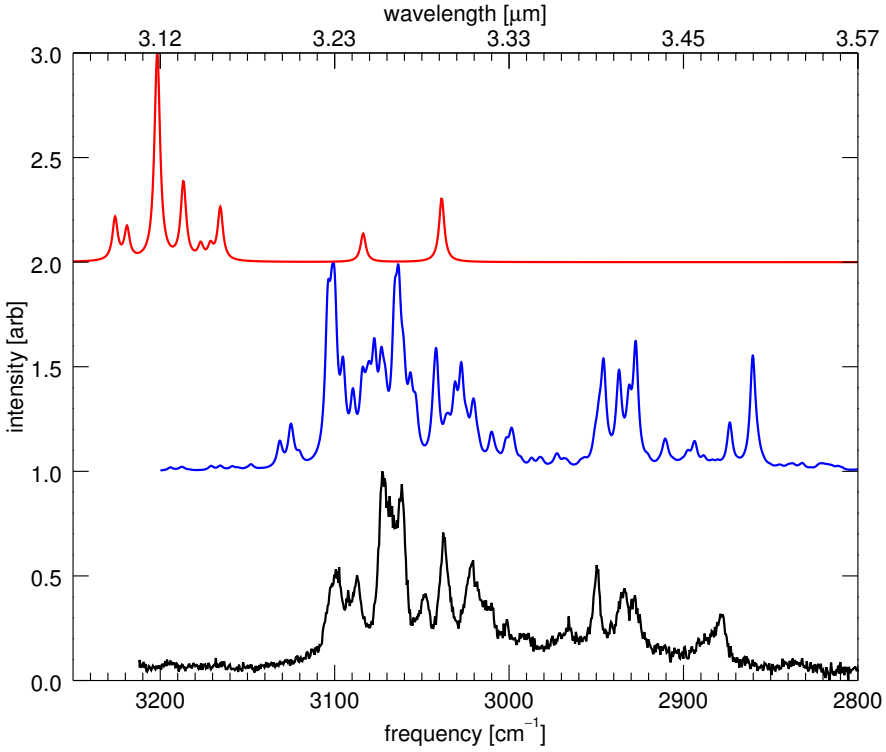

Figure 7.1 The change in the theoretical infrared spectrum of 9-methylanthracene when moving from a harmonic (red) to anharmonic (blue) treatment compared to high–resolution low–temperature gas–phase experimental[24] spectrum (black).

another in energy. Mathematically speaking, a resonance occurs in the context of a VPT2 treatment when the denominator of a term in the anharmonic constant calculation approaches zero causing the offending term to increase dramatically in value. These singularities or resonances have to be removed from the VPT2 treatment and handled separately in a method akin to second order degenerate perturbation theory (see reference 49 and references therein). In a typical VPT2 treatment four main types of resonance occur: Coriolis, when two fundamental vibrational modes are approximately equal to one another; Darling–Dennison, when two vibrational first overtones are approximately equal to one another; type one Fermi, when one fundamental vibrational mode is approximately equal to a first overtone; and type two Fermi, when one fundamental vibrational mode is equal to the sum of two vibrational modes. The result of a resonance on a spectrum is that the vibrational modes involved tend to push one another apart in frequency (compared to their non–resonant frequencies) and their intensities can be redistributed between them.

Complicating matters further is that any given vibrational state can be involved in many different resonances simultaneously. It is not sufficient to handle each resonance individually, instead these groups of mutually resonating modes or *polyads* need to be handled variationally through the construction of a resonance matrix. The diagonal terms of this matrix are the perturbed states as given in equation 7.3 (with the resonant terms already removed from the anharmonic constants) and the off diagonal terms are the coupling constants (see reference 56 for more details). Diagonalization of this matrix gives the new line positions as the eigenvalues, and the strengths of the state mixings as the square of the eigenvectors. These state mixing terms can be used to determine the redistribution of intensities between resonating modes[106]. This treatment was applied to a series of PAHs in our previous works[106, 126, 133] and was shown to be crucial in reproducing the CH–stretching region due to the large number of type two Fermi resonances.

Figure 7.2 shows the effect of performing a polyad resonance treatment on the 0 Kelvin anharmonic infrared spectrum of a 9-methylanthracene. A comparison is made between the convolved (HWHM = 1.8 cm^{-1}) anharmonic spectrum with the polyads suppressed, with the polyads included (the same as figure 7.1), and the high–resolution low–temperature gas–phase experimental[24] infrared spectrum of the 3.3 μm CH–stretching region.

7.2.3 Temperature dependent spectra

Detailed models describing the temperature effects on IR spectra of PAHs have been pioneered by references 85, 134, 137, 138, 140. Here, we summarize their approach for completeneness. The first step in producing a temperature dependent spectrum is to calculate the vibrational DoS (Ω). As the number of atoms in a molecule increases, the number of possible states falling in a given energy range grows extremely fast, especially at high internal energies. For this reason exact counting of the density of states becomes impossible. Therefore, Monte Carlo type samplings are used instead, with the preferred method for calculating the DoS being the Wang–Landau method[135, 136]. Producing temperature–dependent

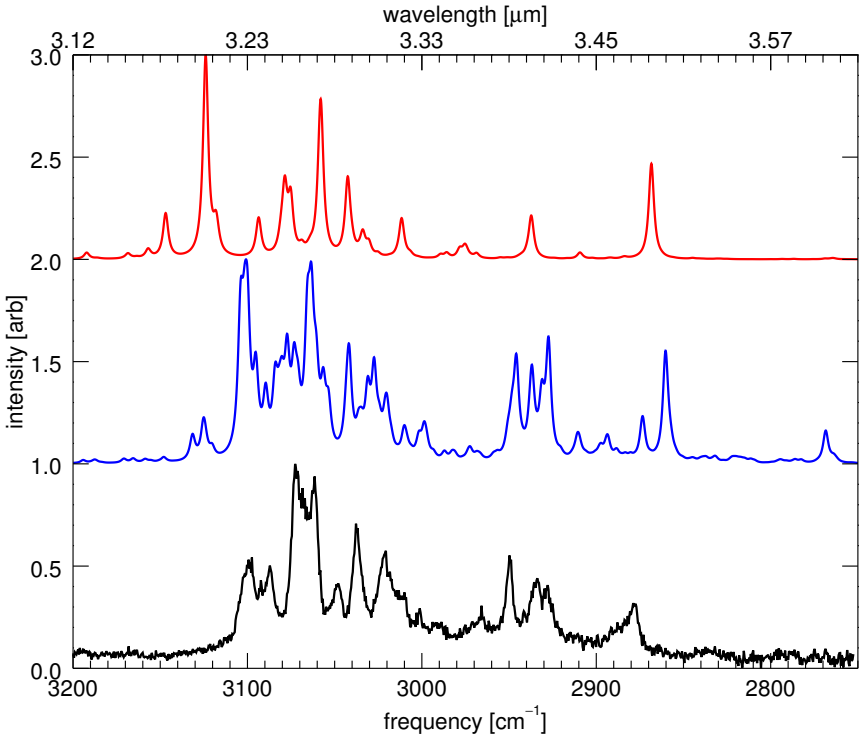

Figure 7.2 The change in the 0 K theoretical infrared spectrum of 9-methylanthracene when moving from a non–polyad treatment (red) to a polyad treatment (blue) compared to high–resolution low–temperature gas–phase experimental[24] spectrum (black).

spectra from a QFF using a Wang–Landau style walk has been shown previously to work successfully for PAHs[134, 137], therefore similar methods have been adopted in this work.

The aim of a Wang–Landau walk is to visit all predefined energy bins (δE) equally in an efficient manner. This is accomplished by biasing the walk to prefer states that have been visited less than the energy bin of the current state. Initially, Ω is set to 1 for the whole energy range of interest ($[E_{min},E_{max}]$). The set of vibrational quantum numbers {n} is initially set to a random state inside the energy range. At each step there is a probability that any of the vibrational quantum numbers can either increase or decrease by one quanta, or remain the same. The value of this probability is chosen to be large enough so that the walk covers the whole energy range in a reasonable amount of steps, but also small enough as to not jump outside of the energy range constantly. Typical values for this probability range from 4–23%. After the set of new quantum numbers, $\{n\}_{new}$, are generated the probability (P) that this state is accepted into the accumulation of Ω is given by

$$P(\{n\}_{current} \rightarrow \{n\}_{new}) = min[1, \frac{\Omega(E_{current})}{\Omega(E_{new})}] \tag{7.4}$$

If the new state is accepted then $\Omega(E_{new})$ is updated by adding a quantity f, where f is a modification factor set to some initial quantity greater than zero (typically the mathematical constant e). Since Ω can become quite large, the value $\ln(\Omega)$ is generally stored instead. A histogram of number of times a energy bin is visited is also accumulated to test for equal sampling (flatness) of the walk. After sufficient flatness is achieved, the value of f is updated by taking its square root, H is reset, and the walk is continued again until the flatness is once again achieved. This process of updating f and re–running the walk ensures quick and accurate convergence towards the true DoS. Typically, f is updated and the walk re–run on the order of 20 times, depending on the desired accuracy of the density of state calculation.

Once Ω is calculated, the next step is to produce the absorption spectrum of the molecule. A separate Wang–Landau walk over the same internal energy range is performed. With the acceptance criteria of a state (P) now being based on the completed Ω(E) values.

At each step of this second walk an accumulated absorption spectrum $\mathcal{S}$ at internal vibrational energy E is updated according to

$$\mathcal{S}(\nu, E) = \sum_k (n_k + 1)\sigma_{0\rightarrow 1}^{(k)} \delta[h\nu - \Delta E^{(k)}] \tag{7.5}$$

with $\sigma_{0\rightarrow 1}^{(k)}$ being the absorption cross section of mode k or combination band at the vibrational ground state. For combination bands n_k is taken to be the smaller of the two vibrational quantum numbers of the two bands involved.

The energy difference at the anharmonic level for a given vibrational transition

of mode k ($n_k \rightarrow n_k + 1$) is then given by

$$\Delta E^{(k)}(\{n\}) = \omega_k + 2\chi_{kk} + \frac{1}{2}\sum_{i\neq k}\chi_{ik} + 2\chi_{kk}n_k + \sum_{i\neq k}\chi_{ik}n_i \tag{7.6}$$

Once the walk is complete, the states are then normalized by the number of entries in the histogram giving the microcanonical absorption intensity I(ν,E).

The conversion from an energy dependent spectrum to a temperature dependent spectrum at any temperature T is then given by a Laplace transformation

$$I(\nu, T) = \frac{1}{Z(T)}\int_{E_{min}}^{E_{max}} I(\nu, E)\Omega(E)e^{(-E/k_BT)}dE \tag{7.7}$$

With Z being the partition function

$$Z(T) = \int \Omega(E)e^{(-E/k_BT)}dE \tag{7.8}$$

The maximum and minimum reliable T values are determined by the energy range of Ω. $\Omega(E)e^{(-E/k_BT)}$ at a given T should die off rapidly at E_{min} and E_{max} to ensure the integral over E_{min} to E_{max} is close to the true integral over an infinite energy range.

Figure 7.3 shows the effect of incorporating anharmonic temperature effects into the theoretical spectrum using the Wang–Landau approach. The strongest IR band of 9-methylanthracene is shown at three temperatures: 100 K, 500 K, and 1000 K. Notice the shift in band position and asymmetric broadening of the profile.

7.2.4 Polyads and temperature dependence

The incorporation of polyads into a Wang–Landau treatment of the IR energy/temperature dependent spectrum is straight forward and is outlined in reference 142. In brief, at each iteration of the Wang–Landau absorption spectrum walk a resonance matrix is constructed using the ground state resonance matrix with the diagonal terms updated by the new deperturbed transition energies given by equation 7.6, or in the case of combination bands and overtones the sum of the transition energies of the modes involved. The off–diagonal coupling terms of the resonance matrix are left unchanged as they do not depend on the vibrational energy levels occupied, but only the change in the occupation of vibrational levels of the transitions ($\Delta(n_k)$ is always 1). Once modified, the eigenvalues of the altered resonance matrix give the new transition energies of the vibrationally excited states (i.e., a new set of $\Delta E^{(k)}(\{n\})$, and the squared eigenvalues give the intensity sharing percentages over the resonating modes (i.e., a new set of $\sigma^{(k)}_{0\rightarrow 1}$). All other steps during the Wang–Landau creation of the temperature dependent spectrum remain the same[134].

Figure 7.4 shows the effect of incorporating polyads into the Wang–Landau calculations of the temperature dependent spectrum. The two spectra are of the theoretical calculations of 9-methylanthracene at 1000 Kelvin. The top spectrum (red) is the temperature spectrum with polyads suppressed, the bottom spectrum

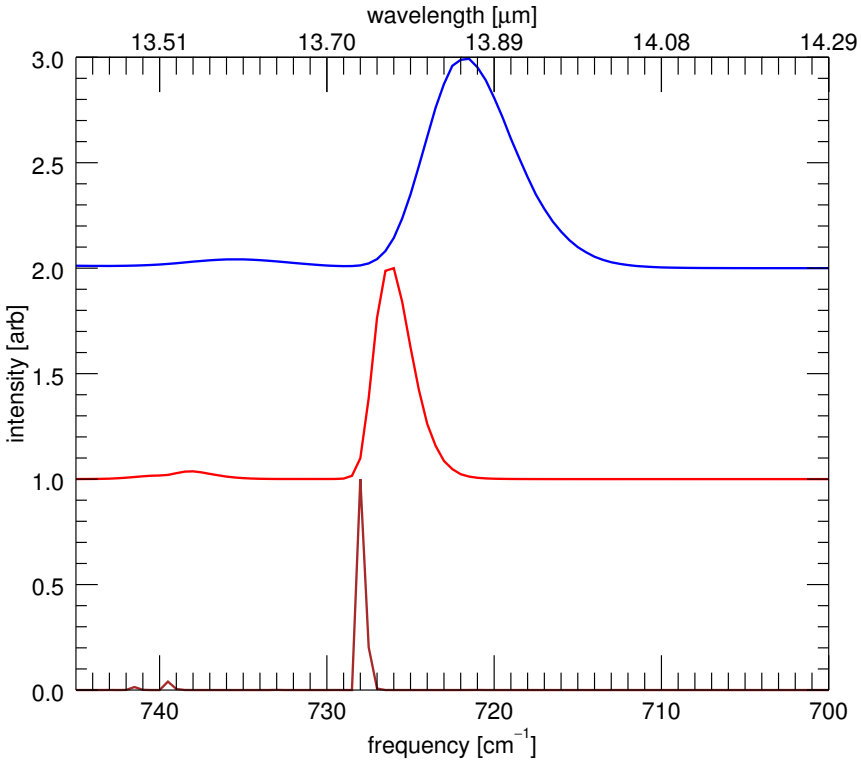

Figure 7.3 Temperature effects on the position and profile of the CH out–of–plane bending mode of the anharmonic theoretical IR spectrum of 9-methylanthracene at 100 K (brown, bottom panel), 500 K (red, middle panel), 1000 K (blue, top panel).

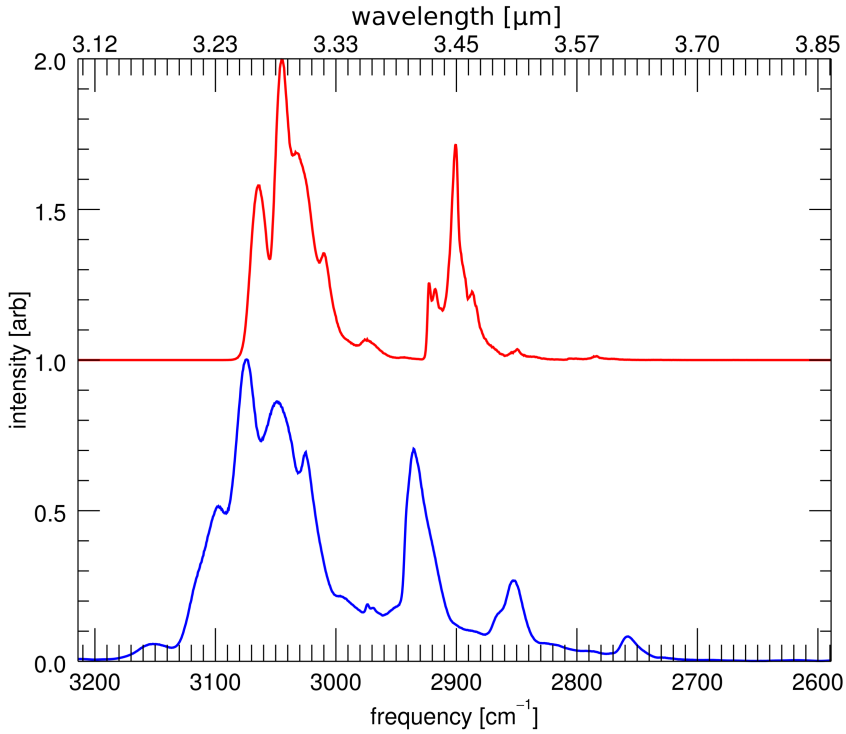

Figure 7.4 The effect of including polyads (blue, bottom panel) and excluding polyads (red, top panel) from the anharmonic temperature dependent calculations of 9–methylanthracene using the Wang–Landau approach.

(blue) is the temperature spectrum with polyads included. Even with the line blending which occurs at high temperatures, significant issues with the polyad suppressed spectrum can still be seen. Discrepancies in band positions and widths, and the loss of features are all present when polyads are excluded.

7.2.5 PAH IR cascade spectra

Interstellar PAHs are electronically excited by UV photons originating from stellar sources, then converts quickly to their ground electronic state through emissionless internal conversion to highly excited vibrational states. PAHs then slowly emit this vibrational energy as IR radiation. When a PAH emits an IR photon, its internal energy is decreased by the energy of said photon. This decrease in internal energy affects the energy at which the next IR photons emit (see equation 7.6). In the interstellar medium this process is stochastic, in that the PAHs have time to cool fully to the vibrational ground states in between UV photon absorption events,

and collisionless, in that the only way to shed energy is through the emission of IR photons.

Modelling this process is straight forward[43]. The probability of a PAH absorbing a stellar UV photon is proportional to the product of the blackbody spectrum of a star of a given temperature and the UV absorption cross section of the PAH. The total internal vibrational energy E_{tot} of the PAH is then equal to the energy of the absorbed UV photon. The probability of emitting an IR photon (E_{IR}) at a given internal energy (E_{tot}) is proportional to its rate, which in turn is proportional to the energy dependent spectrum at E_{tot}. For the cascade model, an IR photon is randomly selected based on this probability. At each step of a cascade, a spectral histogram is updated at E_{IR}. The new total internal energy is then updated: $E_{tot_{new}} = E_{tot} - E_{IR}$ leading to a new set of probabilities of IR emission. This cascade process is repeated until the PAH has fully cooled to its vibrational ground state. At this point a new UV photon is absorbed and the full cascade is repeated again. This process continues until the desired resolution is achieved.

Figure 7.5 shows a full anharmonic cascade spectrum of 9–methylanthracene pumped by an 18000 Kelvin blackbody source (simulating an OB type star). Most notable are the long red wings compared to a strictly temperature dependent spectrum as shown in Figure 7.4.

7.3 Implementation

7.3.1 Quartic force fields

The QFFs of the PAHs in this work were calculated using Gaussian 09[51] within the DFT framework, using the B3LYP functional[127] and the N07D basis set[129]. A tight convergence criterion was used for the geometry optimization and a very fine grid (Int=200974) was used for numerical integrations.

7.3.2 VPT2

The VPT2 treatment was handled by a locally modified version of SPECTRO[52], after conversion of the QFF produced by Gaussian09 from normal coordinates to Cartesian coordinates[98]. SPECTRO has the flexibility to handle large polyads as described in section 7.3.3. Additionally, the SPECTRO output of the resonant matrices were necessary for the energy/temperature incorporation as described in section 7.2.4.

7.3.3 Polyads

The cut–off for considering states to be in resonance is controlled by two parameters in SPECTRO, the minimum interaction strength between the two bands (W), and the difference in energy between the two bands (Δ). It was found[126] that the default value of W (10 cm^{-1}) missed important resonances, so this value was dropped to 0 cm^{-1}. With this value set to zero, the polyads were no longer

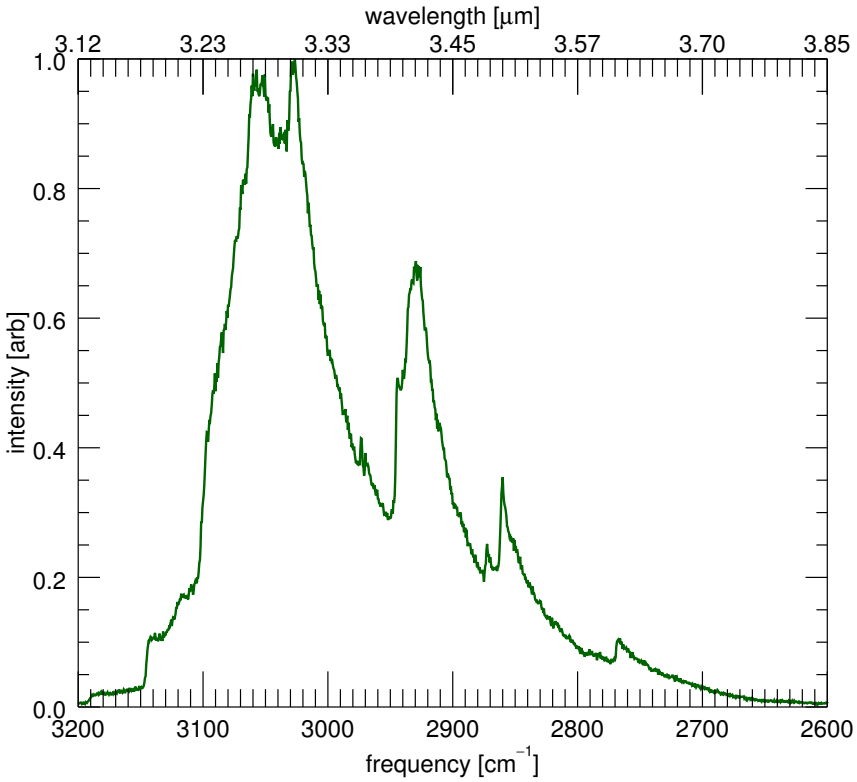

Figure 7.5 Fully anharmonic simulated cascade spectrum of the CH–stretching region of 9–methylanthracene.

atomically separated by irreducible representations, therefore to reduce computational cost they were separated outside of SPECTRO. The default value of Δ (200 cm^{-1}) has been shown to reproduce the CH–stretching region of PAHs accurately[126, 133]. However, polyad sizes can grow quite large with this cut–off, especially when the molecule has a low symmetry. For example, the three IR active polyads of benz[a]anthracene ($C_{18}H_{12}$, C_s symmetry) contain 117, 675, and 204 states respectively. This occurs because of *resonance chaining*, where a series of modes resonate with their neighbors who in turn resonate with their neighbors etc., leading to a polyad where the highest energy mode and the lowest energy mode could end up with a Δ that is over 1500 cm⁻1. While diagonalizing these large polyad matrices are not a problem when obtaining a zero Kelvin vibrational spectra, they pose a significant issue when calculating an energy/temperature dependent spectra as they have to be rediagonalized with each iteration of the Wang–Landau walk. To resolve this, two separate Δ values were set: for modes > 2000 cm^{-1} Δ = 200 cm^{-1}, and for modes < 2000 cm^{-1} Δ = 25 cm^{-1}. It was found that the CH–stretching region (above 3000 cm^{-1}) is extremely sensitive to the lowering of Δ due to strong Fermi resonances and was thus left alone. Fortunately, a natural large break occurs between the CH–stretching vibrational mode energies and all other vibration modes (below 2000 cm^{-1}) so no resonance chaining occurs to the lower modes here. The vibrational modes below 2000 cm^{-1} were found to only weakly interact through Fermi resonances, so lowering Δ down to 25 cm^{-1} showed little effect on the resulting spectra, but reduced the polyad sizes dramatically.

7.3.4 Wang–Landau

For all Wang–Landau calculations the vibrational quantum number probability increase/decrease parameter was set to 5%. For the density of states calculation the energy bins were set to 25 cm^{-1}. The energy range over which the walks took place was 0–15 eV (0–120,983cm^{-1}). Twenty Wang–Landau iterations of decreasing f were run for each molecule, with each iteration consisting of 1×10^7 steps. For the majority of the energy dependent spectra the accumulated absorption spectrum bins were set to 0.1 cm^{-1}. For the high–resolution energy dependent spectra used in figures 7.6 and 7.7, the spectrum bins were set to 0.005 cm^{-1}. The walks to calculate I(ν,E) were carried out until all of the energy bins (of the total internal vibrational energy) were visited an average of 2,500 times.

7.3.5 Cascade spectra

A total of twenty PAHs were subjected to the simulated cascade method described in this work; Seven neutral PAHs and their cationic counterparts: naphthalene, anthracene, tetracene, phenanthrene, chrysene, pyrene, and benz[a]anthracene; and six aliphatic containing PAHs: 9–methylanthracene, 9,10–dimethylanthracene, 9,10–dihydroanthracene, 9,10–dihydrophenanthrene, 1,2,3,4–tetrahydronaphthalene, and 1,2,3,6,7,8–hexahydropyrene. These molecules were chosen based on previous confirmation of their anharmonic infrared spectra compared with matrix–isolation data, NIST database gas–phase data, as well as high–resolution, mass–selected,

low–temperature, gas–phase spectra in our previous work[106, 126, 133]. Four separate simulations were run for each molecule with varying excitation photon energies: 3, 6, 9, and 12 eV. The cascade spectrum of each PAH was simulated using 1×10^7 UV photons, resulting in approximately 1×10^9 emitted IR photons per simulation.

7.4 Results

In order to test the reliability of the Wang–Landau method, Figure 7.6 shows a comparison of the ν_{46} vibrational band of naphthalene between the Wang–Landau approach, the high–resolution experimental data of reference 85, and the direct counting method as described in reference 85. The Wang–Landau method is able to reproduce the spectrum as well as the direct counting method. Differences in band positions between the Wang–Landau and the direct counting method are mainly due to differences in the DFT functional used. Attempts to use the QFF from their online supporting material were made. However, as confirmed by the original authors of reference 85, their QFF was corrected post–calculation and differs from the online version. Therefore, an *exact* one to one comparison between the Wang–Landau and direct counting method was not possible here.

The features in the unconvolved spectrum of Figure 7.6 (blue) are individual peaks (not noise), and each feature can be individually assigned with careful book-keeping during the energy dependent spectrum generation step. Figure 7.7 shows an example of a series of zoomed in panels to show the level of detail that can be achieved even with the random walk. Unlike the direct counting method, no prior cutoff of states to visit (i.e., sufficient thermal population) must be specified. Therefore, the detail becomes limited by the number of Wang–Landau steps taken, and the bin size set, for the energy dependent spectrum generation.

Peak positions of cascade features compared to "0 Kelvin" theoretical anharmonic spectra are found to be equal. While large shifts in peak positions are expected for high temperature/highly excited molecules (equation 7.6), the nature of the IR cascade process leads to features that are not shifted. While the high internal–energy emissions of IR photons are indeed shifted in position, the emission probability is also broadened. This results in the lowering of probability of emitting an IR photon at its "peak" position when compared to lower internal–energy emission, as shown in Figure 7.8. This results in the piling up of IR photons at relatively the same position during lower internal–energy emissions, while the high internal–energy IR photons are spread over a larger area. An increase in initial UV photon energy therefore results *only* in the growth of a low–energy wing, with no change in the position of the peak intensity. The only shifts seen in the resulting spectra are due to secondary effects as described below. No growth is seen in the high–energy wings, leaving an unchanging steep wall on the high–energy side of the majority of features.

Shifts of the features *appear* to occur, however these "pseudoshifts" are not due to the typical temperature related shifts per se, but are instead due to the cascade process as a whole. The dominant type of pseudoshift occurs when separate IR

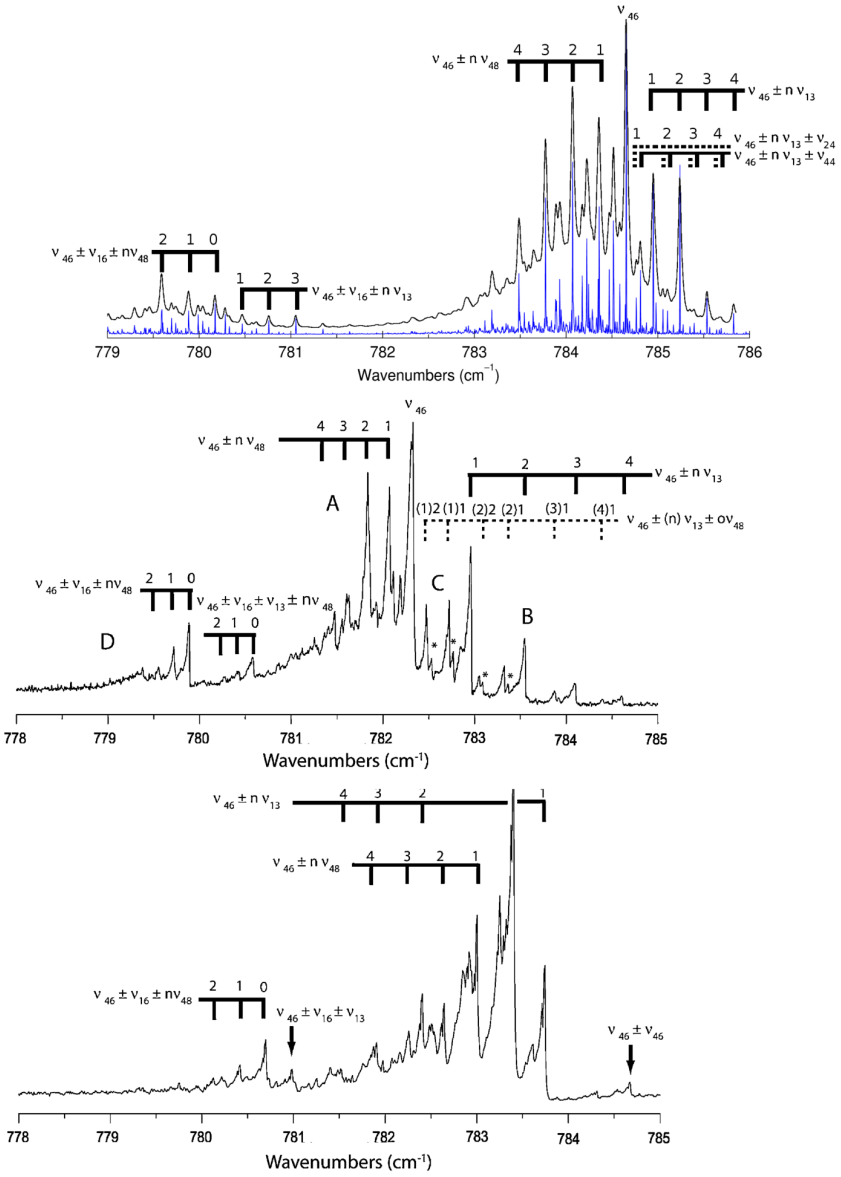

Figure 7.6 Comparison of high–resolution experimental data of thermally excited naphthalene (300 K)[85] (middle panel) to the "direct" theoretical approach[85] (bottom panel) to the Wang–Landau method of this work (top panel, blue, with convolved spectrum in black). Figure has been partially adopted from reference 85.

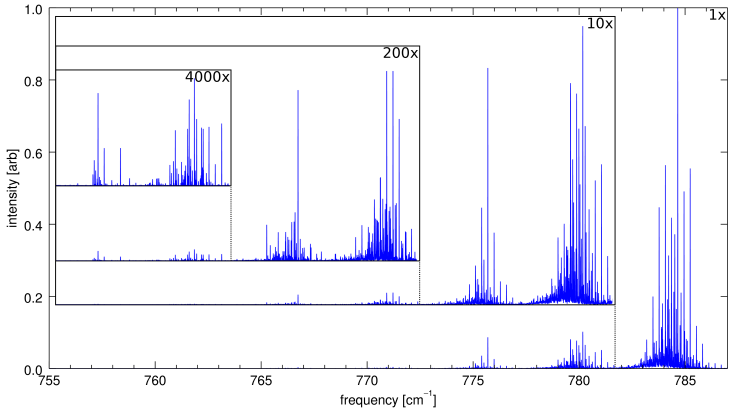

Figure 7.7 A sampling of the series hot–band features of the ν_{46} band of naphthalene at 300 K simulated using the Wang–Landau method for producing a temperature dependent spectrum. Total magnification is given for each portion of the spectrum.

modes are closely spaced. As the initial exciting UV photon energy is increased, more IR photons are released in an ever growing low–energy IR wing. This lowers the relative peak intensity of all of the cascade features, however, if two or more features are closely spaced then the low–energy IR wing of one feature can slip under the peak of its neighbor, which in turn inhibits the degradation of the neighboring feature. This can cause the lower energy feature to become more intense than the previously stronger higher energy feature (as shown in the top right panel of Figure 7.9). Even very weak neighboring features can cause the appearance of a shift. The amount of shifting produced by this phenomenon depends on the initial band spacing, and has been observed to occur for bands separated by up to 20 cm^{-1} for cascades starting at high energies. Once the lower intensity neighbor overtakes the initially intense band the "shifting" stops abruptly.

A similar type of pseudoshift was found to occur from a feature's own hot–band. If a hot–band is intense enough at very low internal energies (< 1 eV) it can also sit upon the cascade wing of its fundamental. If initial absorbed UV photon energy is high enough, the hot–band can overtake the intensity of the fundamental resulting in the appearance of a shift in position (as shown in the bottom right panel of Figure 7.9). Again, the degree of the apparent shift is dependent on the initial band, hot–band spacing and the shifting stops when the hot–band finally overtakes the fundamental in intensity.

A less common pseudoshift occurs in a "leveling–off" manner. If excitation is high enough a low–energy wing can appear to flatten out, starting at the 0 Kelvin position and continuing down the wing as the initial UV energy is increased (as shown in the bottom left panel of Figure 7.9). This is a consequence of the

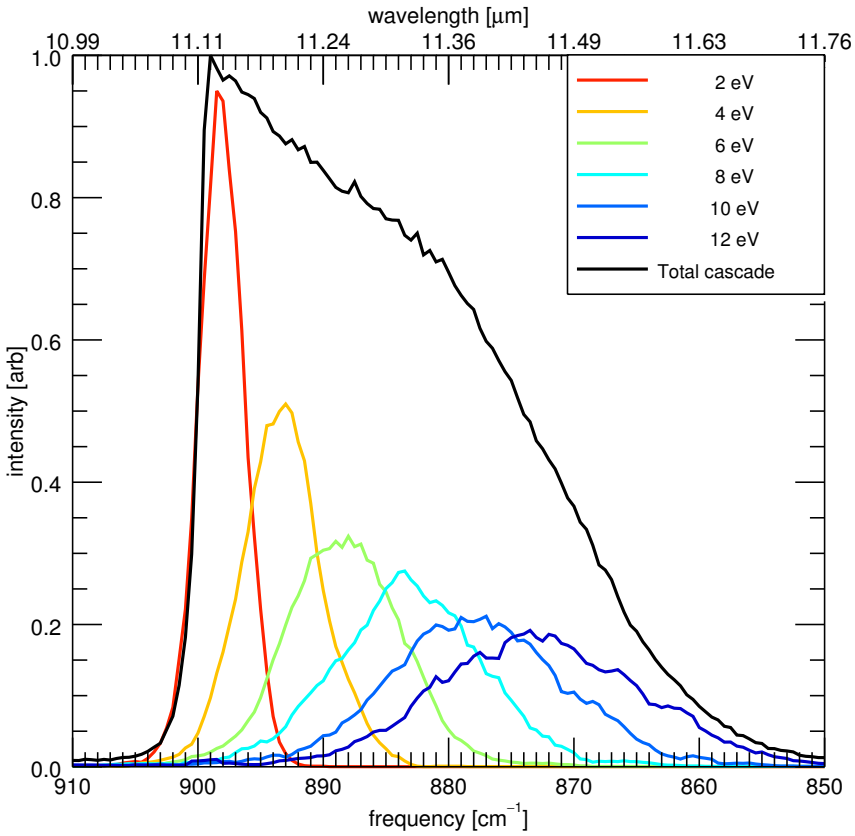

Figure 7.8 The distribution of IR photon emission probabilities at various internal energies along the cascade of a C–H out–of–plane bending mode of tetracene (colors), with the resulting IR cascade spectrum (black).

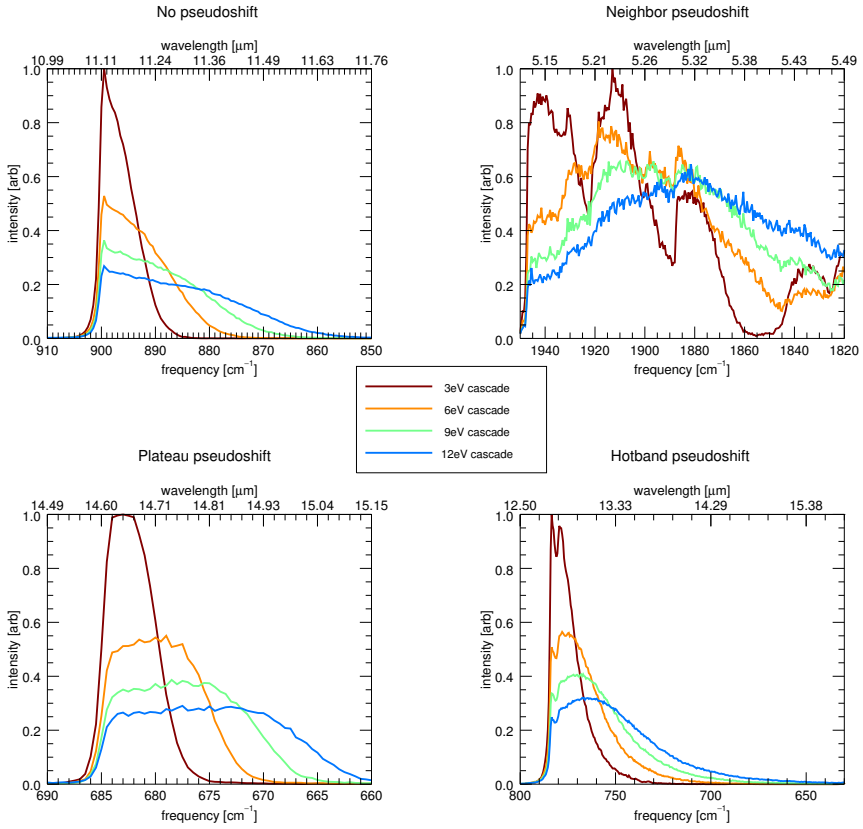

Figure 7.9 Examples of the three types of pseudoshifts seen in the theoretical IR cascade spectra. Clockwise from top left: tetracene, phenanthrene, chrysene, and naphthalene.

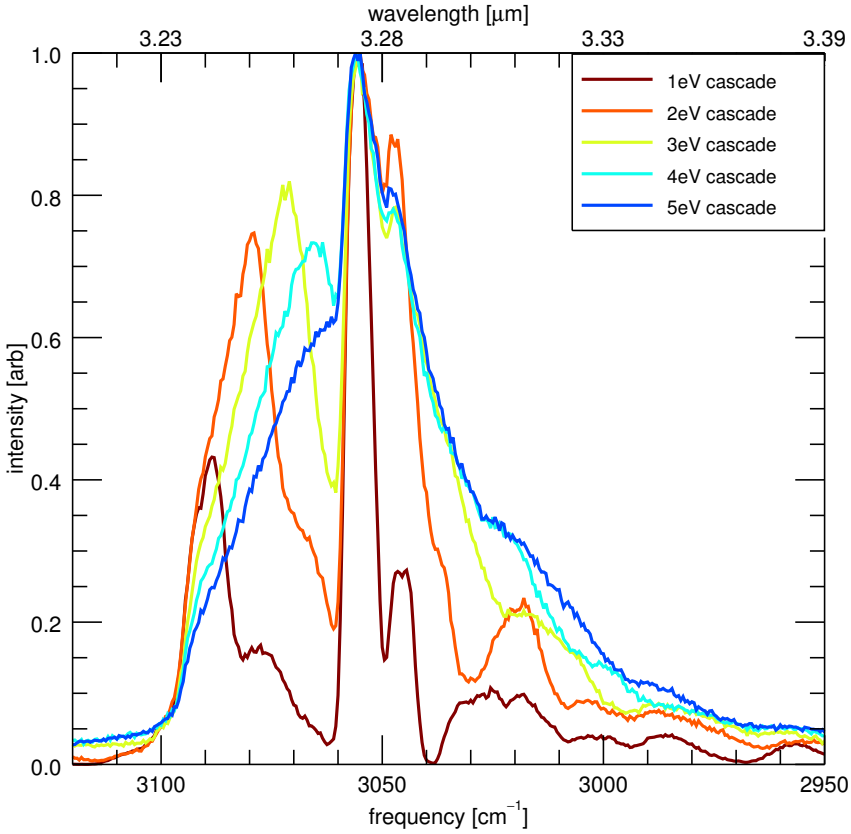

Figure 7.10 The IR cascade spectrum of the CH–stretching region of tetracene.

statistics of emission at various energies of the cascade, if the overlap of the shifted and broadened features during the cascade is just right, a plateau can be achieved.

Although the vast majority of cascade features do not appear to move with excitation energies, in rare cases the growth of a high energy wing and shift in feature position can occur in the CH–stretching region for combination bands that are of higher frequency than the fundamentals. This occurs due to Fermi resonances. The magnitude of interaction between resonating modes has been shown to change at different internal energies in the CH–stretching region of some PAHs[142]. Differences in the anharmonic constants and quantum occupation numbers, fundamental bands and combination bands shift at different rates leading to resonances that wax and wane as the states move closer and further apart in energy. This results in more intensity being borrowed by the combination bands at particular internal energies. Although minor in most cases, tetracene shows this effect quite strongly (figure 7.10). The feature at 3100 cm^{-1} can be seen to grow and then shrink relative the the strongest band as the cascade starting energy is increased, while the other main features show the typical stationary behavior.

7.5 Conclusions

As shown throughout the theoretical section of this work and in previous studies, careful anharmonic treatment is necessary to reproduce experimental results for PAHs: The inclusion of anharmonicities accounts for the large shifts seen in harmonic fundamental band positions; Fermi resonances dominate the CH–stretching region and account for the large number of bands observed; anharmonic temperature affects account for band shifts and broadenings (and need to be included in the polyad treatments), with the Wang–Landau approach being preferred due to its efficiency, and ease of incorporation of resonances.

It was previously believed that a PAH IR absorption spectrum greatly differs from an IR cascade emission spectrum. Previous cascade emission models[143] of PAHs applied a 15 cm^{-1} shift indiscriminantly to all absorption spectra in order to account for the anharmonic emission processes. As this study shows, the experimental shifts observed are due to the pseudoshifts described above rather than anharmonic temperature shifts. One main conclusion from this study is that, in general, it will be quite straightforward to transform measured or calculated PAH absorption spectra into cascade spectra relevant for astrophysics as frequency shifts are not relevant.

While this work shows the complexity necessary to reproduce the temperature/energy dependent spectra of PAHs, this work also suggests that this complexity may be unnecessary for the cascade spectra. The stability of the peak positions of the cascade spectra enables the use of 0 Kelvin theoretical spectra, or low–temperature gas–phase *absorption* experimental spectra to determine the peak positions (or high energy wall) of IR emission cascade spectra. Previous work has suggested this was not possible[41]. This knowledge can be used to both simplify and improve greatly the current astronomical PAH IR cascade spectra models[33]. To this end, further research into the "growth" rate of the cascade

wings as function of initial cascade energy is currently underway.

Acknowledgments

The spectroscopic study of interstellar PAHs at Leiden Observatory have been supported through a Spinoza award, and through the Dutch Astrochemistry Network funded by the Netherlands Organization for Scientific Research, NWO. We acknowledge the European Union (EU) and Horizon 2020 funding awarded under the Marie Sklodowska–Curie action to the EUROPAH consortium, grant number 722346. Calculations were carried out on the Dutch national e–infrastructure (Cartesius) with the support of SURF Cooperative, under NWO EW project SH-362-15. TC sincerely thanks the support from Swedish Research Council (grant No. 2015-06501). AC acknowledges NWO for a VENI grant (639.041.543). XH and TJL gratefully acknowledge support from the NASA 12–APRA12–0107 grant. XH acknowledges the support from NASA/SETI Co–op Agreement NNX15AF45A. This material is based upon work supported by the National Aeronautics and Space Administration through the NASA Astrobiology Institute under Cooperative Agreement Notice NNH13ZDA017C issued through the Science Mission Directorate.

References

References

[1] H. Richter and J. Howard, Prog. Energy Combust. Sci. **26**, 565 (2000).
[2] A. M. Mastral and M. S. Callén, Environ. Sci. Technol **34**, 3051 (2000).
[3] IRAC, Monogr. Eval. Carcinog. Risk Chem. Hum **100**, 111 (2012).
[4] K. M.G., S. C.P., P. P., and F. J.S., Impact of Processing on Food Safety. Advances in Experimental Medicine and Biology, volume 459, Springer, Boston, MA, 1999.
[5] H. Lai, M. Lin, M. Yang, and A. Li, Mater. Sci. Eng.: C **16**, 23 (2001).
[6] J. Berashevich and T. Chakraborty, J. Phys. Chem. C **115**, 24666 (2011).
[7] X. Wan, K. Chen, D. Liu, J. Chen, Q. Miao, and J. Xu, Chem. Mater **24**, 3906 (2012).
[8] D. C. Elias, R. R. Nair, T. M. G. Mohiuddin, S. V. Morozov, P. Blake, M. P. Halsall, A. C. Ferrari, D. W. Boukhvalov, M. I. Katsnelson, A. K. Geim, and K. S. Novoselov, Science **323**, 610 (2009).
[9] D. M. Hudgins, C. W. Bauschlicher Jr, and L. Allamandola, The Astrophysical Journal **632**, 316 (2005).
[10] V. Mennella, L. Hornekær, J. Thrower, and M. Accolla, The Astrophysical Journal Letters **745**, L2 (2011).
[11] C. J. Mackie, E. Peeters, C. W. Bauschlicher Jr, and J. Cami, Astrophys. J **799**, 131 (2015).
[12] H. Andrews, A. Candian, and A. Tielens, Astronomy & Astrophysics **595**, A23 (2016).

[13] M. P. Bernstein, J. P. Dworkin, S. A. Sandford, G. W. Cooper, and L. J. Allamandola, Nature **416**, 401 (2002).
[14] F. L. Plows, J. E. Elsila, R. N. Zare, and P. R. Buseck, Geochim. Cosmochim. Ac **67**, 1429 (2003).
[15] E. Micelotta, A. Jones, and A. Tielens, Astronomy & Astrophysics **526**, A52 (2011).
[16] T. Geballe, A. Tielens, L. Allamandola, A. Moorhouse, and P. Brand, The Astrophysical Journal **341**, 278 (1989).
[17] V. Le Page, T. P. Snow, and V. M. Bierbaum, The Astrophysical Journal **584**, 316 (2003).
[18] L. Verstraete, A. Léger, L. d'Hendecourt, D. Defourneau, and O. Dutuit, Astronomy and Astrophysics **237**, 436 (1990).
[19] Z. Martins, O. Botta, M. L. Fogel, M. A. Sephton, D. P. Glavin, J. S. Watson, J. P. Dworkin, A. W. Schwartz, and P. Ehrenfreund, Earth and planetary science Letters **270**, 130 (2008).
[20] P. P. Bera, T. Stein, M. Head-Gordon, and T. J. Lee, Astrobiology **17**, 771 (2017).
[21] d. NIST Mass Spec Data Center, S.E. Stein, Eds. P.J. Linstrom and W.G. Mallard, National Institute of Standards and Technology, Gaithersburg MD (2015).
[22] E. Maltseva, A. Petrignani, A. Candian, C. J. Mackie, X. Huang, T. J. Lee, A. G. G. M. Tielens, J. Oomens, and W. J. Buma, Astrophys. J **814**, 23 (2015).
[23] E. Maltseva, A. Petrignani, A. Candian, C. J. Mackie, X. Huang, T. J. Lee, A. G. Tielens, J. Oomens, and W. J. Buma, Astrophys. J **831**, 58 (2016).
[24] E. Maltseva, A. Petrignani, A. Candian, C. J. Mackie, X. Huang, T. J. Lee, A. G. Tielens, J. Oomens, and W. J. Buma, Astron. Astrophys., Accepted (2018).
[25] A. Ricca, C. W. Bauschlicher Jr, C. Boersma, A. G. Tielens, and L. J. Allamandola, The Astrophysical Journal **754**, 75 (2012).
[26] A. Leger and J. L. Puget, Astron. Astrophys. **137**, L5 (1984).
[27] L. J. Allamandola, A. G. G. M. Tielens, and J. R. Barker, Astrophys. J **290**, L25 (1985).
[28] A. Léger, L. Verstraete, L. d'Hendecourt, D. Défourneau, O. Dutuit, W. Schmidt, and J. Lauer, The PAH hypothesis and the extinction curve, in Symposium-International Astronomical Union, volume 135, pp. 173–180, Cambridge University Press, 1989.
[29] T. N. Tingle, C. H. Becker, and R. Malhotra, Meteoritics & Planetary Science **26**, 117 (1991).
[30] S. Hony, C. Van Kerckhoven, E. Peeters, A. Tielens, D. Hudgins, and L. Allamandola, Astron. Astrophys. **370**, 1030 (2001).
[31] E. Peeters, S. Hony, C. Van Kerckhoven, A. Tielens, L. Allamandola, D. Hudgins, and C. Bauschlicher, Astronomy & Astrophysics **390**, 1089 (2002).
[32] B. Van Diedenhoven, E. Peeters, C. Van Kerckhoven, S. Hony,

D. Hudgins, L. Allamandola, and A. Tielens, The Astrophysical Journal **611**, 928 (2004).
[33] C. Boersma, C. W. Bauschlicher, Jr., A. Ricca, A. L. Mattioda, J. Cami, E. Peeters, F. Sánchez de Armas, G. Puerta Saborido, D. M. Hudgins, and L. J. Allamandola, Astrophys. J **211**, 8 (2014).
[34] B. P. Abbott, R. Abbott, T. Abbott, M. Abernathy, F. Acernese, K. Ackley, C. Adams, T. Adams, P. Addesso, R. Adhikari, et al., Physical review letters **116**, 061102 (2016).
[35] G. Birkhoff and J. Von Neumann, Annals of mathematics , 823 (1936).
[36] L. Allamandola, D. Hudgins, and S. Sandford, The Astrophysical Journal Letters **511**, L115 (1999).
[37] D. Wagner, H. Kim, and R. Saykally, Astrophys. J **545**, 854 (2000).
[38] C. Joblin, A. G. G. M. Tielens, L. J. Allamandola, and T. R. Geballe, Astrophys. J **458**, 610 (1996).
[39] L. J. Allamandola, A. G. G. M. Tielens, and J. R. Barker, Astrophys. J. Suppl. S **71**, 733 (1989).
[40] I. Cherchneff and J. R. Barker, The Astrophysical Journal **341**, L21 (1989).
[41] J. Brenner and J. R. Barker, The Astrophysical Journal **388**, L39 (1992).
[42] H.-S. Kim, D. Wagner, and R. Saykally, Physical review letters **86**, 5691 (2001).
[43] D. Cook and R. Saykally, The Astrophysical Journal **493**, 793 (1998).
[44] C. Pech, C. Joblin, and P. Boissel, Astronomy & Astrophysics **388**, 639 (2002).
[45] C. Joblin, P. Boissel, A. Leger, L. d'Hendecourt, and D. Defourneau, Astron. Astrophys. **299**, 835 (1995).
[46] P. W. Atkins and R. S. Friedman, Molecular quantum mechanics, Oxford university press, 2011.
[47] C. Pasquini, Journal of the Brazilian Chemical Society **14**, 198 (2003).
[48] G. Malloci, C. Joblin, and G. Mulas, Chem. Phys **332**, 353 (2007).
[49] K. K. Lehmann, Mol. Phys **66**, 1129 (1989).
[50] V. Barone, M. Biczysko, and J. Bloino, Phys. Chem. Chem. Phys **16**, 1759 (2014).
[51] M. J. Frisch, G. W. Trucks, H. B. Schlegel, G. E. Scuseria, M. A. Robb, J. R. Cheeseman, G. Scalmani, V. Barone, B. Mennucci, G. A. Petersson, H. Nakatsuji, M. Caricato, X. Li, H. P. Hratchian, A. F. Izmaylov, J. Bloino, G. Zheng, J. L. Sonnenberg, M. Hada, M. Ehara, K. Toyota, R. Fukuda, J. Hasegawa, M. Ishida, T. Nakajima, Y. Honda, O. Kitao, H. Nakai, T. Vreven, J. A. Montgomery, Jr., J. E. Peralta, F. Ogliaro, M. Bearpark, J. J. Heyd, E. Brothers, K. N. Kudin, V. N. Staroverov, R. Kobayashi, J. Normand, K. Raghavachari, A. Rendell, J. C. Burant, S. S. Iyengar, J. Tomasi, M. Cossi, N. Rega, J. M. Millam, M. Klene, J. E. Knox, J. B. Cross, V. Bakken, C. Adamo, J. Jaramillo, R. Gomperts, R. E. Stratmann, O. Yazyev, A. J. Austin, R. Cammi, C. Pomelli,

J. W. Ochterski, R. L. Martin, K. Morokuma, V. G. Zakrzewski, G. A. Voth, P. Salvador, J. J. Dannenberg, S. Dapprich, A. D. Daniels, Ã. Farkas, J. B. Foresman, J. V. Ortiz, J. Cioslowski, and D. J. Fox, (2009), Gaussian Inc. Wallingford CT 2009.

[52] J. F. Gaw, A. Willets, W. H. Green, and N. C. Handy, Advances in Molecular Vibrations and Collision Dynamics, JAI Press, Inc.: Greenwich, Connecticut, 1991.

[53] W. Thiel, Mol. Phys **68**, 427 (1989).

[54] T. J. Lee and G. E. Scuseria, J. Chem. Phys **93**, 489 (1990).

[55] T. J. Lee, J. M. L. Martin, and P. R. Taylor, J. Chem. Phys **102**, 254 (1995).

[56] J. M. Martin, T. J. Lee, P. R. Taylor, and J.-P. François, J. Chem. Phys **103**, 2589 (1995).

[57] X. Huang and T. J. Lee, J. Chem. Phys **129** (2008).

[58] X. Huang, P. R. Taylor, and T. J. Lee, J. Phys. Chem. A **115**, 5005 (2011), PMID: 21510653.

[59] A. T. Wong and G. B. Bacskay, Molecular Physics **79**, 819 (1993).

[60] W. D. Allen and A. G. Császár, J. Chem. Phys **98**, 2983 (1993).

[61] A. T. Wong and G. B. Bacskay, Chem. Phys. Lett **207**, 360 (1993).

[62] I. Mills, K. N. Rao, and C. W. Mathews, Academic Press, New York , 115 (1972).

[63] M. Aliev, J. Watson, and K. N. Rao, KN Rao (Academic, New York, 1985) **3**, l (1985).

[64] G. Fogarasi, P. Pulay, and b. J. Durig, Elsevier, Amsterdam **14**, 125 (1985).

[65] A. Hoy, I. Mills, and G. Strey, Mol. Phys **24**, 1265 (1972).

[66] S. Carter, J. M. Bowman, and N. C. Handy, Theor. Chem. Acc **100**, 191 (1998).

[67] J. M. Bowman, S. Carter, and X. Huang, Int. Rev. Phys. Chem **22**, 533 (2003).

[68] D. W. Schwenke, J. Phys. Chem **100**, 2867 (1996).

[69] C. E. Dateo, T. J. Lee, and D. W. Schwenke, J. Chem. Phys **101**, 5853 (1994).

[70] R. C. Fortenberry, X. Huang, A. Yachmenev, W. Thiel, and T. J. Lee, Chem. Phys. Lett **574**, 1 (2013).

[71] W. Schneider and W. Thiel, Chem. Phys. Lett **157**, 367 (1989).

[72] E. B. Wilson, J. C. Decius, and P. C. Cross, McGraw-Hill **305**, 616 (1955).

[73] M. Rey, A. V. Nikitin, and V. G. Tyuterev, J. Chem. Phys **141** (2014).

[74] J. Ochterski, Vibrational Analysis in Gaussian (1999).

[75] X. Huang and T. J. Lee, Astrophys. J **736**, 33 (2011).

[76] A. G. G. M. Tielens, Annu. Rev. Astron. Astrophys. **46**, 289 (2008).

[77] D. M. Hudgins, S. A. Sandford, and L. J. Allamandola, Infrared Spectroscopy of Matrix Isolated PAHs, in The First Symposium on the Infrared Cirrus and Diffuse Interstellar Clouds, edited by R. M. Cutri and

W. B. Latter, volume 58 of Astronomical Society of the Pacific Conference Series, p. 283, 1994.
[78] D. M. Hudgins and S. A. Sandford, J. Phys. Chem. A **102**, 329 (1998).
[79] D. M. Hudgins and L. J. Allamandola, J. Phys. Chem. A **101**, 3472 (1997).
[80] D. M. Hudgins and S. A. Sandford, J. Phys. Chem. A **102**, 344 (1998).
[81] A. L. Mattioda, C. W. Bauschlicher, J. D. Bregman, D. M. Hudgins, L. J. Allamandola, and A. Ricca, Spectrochim. Acta, Part A **130**, 639 (2014).
[82] E. Cané, A. Miani, P. Palmieri, R. Tarroni, and A. Trombetti, Spectrochim. Acta, Part A **53**, 1839 (1997).
[83] E. Cané, A. Miani, P. Palmieri, R. Tarroni, and A. Trombetti, J. Chem. Phys **106**, 9004 (1997).
[84] C. Joblin, L. D'Hendecourt, A. Leger, and D. Defourneau, Astron. Astrophys. **281**, 923 (1994).
[85] O. Pirali, M. Vervloet, G. Mulas, G. Malloci, and C. Joblin, Phys. Chem. Chem. Phys **11**, 3443 (2009).
[86] S. R. Langhoff, J. Phys. Chem **100**, 2819 (1996).
[87] A. G. Csaszar, Wiley Interdiscip. Rev: Comput. Mol. Sci **2**, 273 (2012).
[88] R. Burcl, N. C. Handy, and S. Carter, Spectrochim. Acta, Part A **59**, 1881 (2003).
[89] K. Yagi, S. Hirata, and K. Hirao, Phys. Chem. Chem. Phys **10**, 1781 (2008).
[90] K. Yagi and H. Otaki, J. Chem. Phys **140**, 084113 (2014).
[91] J. Bloino and V. Barone, J. Chem. Phys **136**, (2012).
[92] A. Willetts, N. C. Handy, W. H. Green, and D. Jayatilaka, J. Chem. Phys **94**, 5608 (1990).
[93] J. Vázquez and J. F. Stanton, Mol. Phys **105**, 101 (2007).
[94] F. A. Hamprecht, A. J. Cohen, D. J. Tozer, and N. C. Handy, J. Chem. Phys **109**, 6264 (1998).
[95] T. Dunning et al., J. Chem. Phys **55**, 716 (1971).
[96] E. Cané, A. Miani, and A. Trombetti, J. Phys. Chem. A **111**, 8218 (2007), PMID: 17672437.
[97] A. D. Boese and J. M. L. Martin, J. Phys. Chem. A **108**, 3085 (2004).
[98] C. J. Mackie, A. Candian, X. Huang, T. J. Lee, and A. G. G. M. Tielens, J. Chem. Phys **142**, 244107 (2015).
[99] S. Smolarek, A. Vdovin, A. Rijs, C. A. van Walree, M. Z. Zgierski, and W. J. Buma, J. Phys. Chem. A **115**, 9399 (2011), PMID: 21332230.
[100] C. W. Young, R. B. DuVall, and N. Wright, Anal. Chem. **23**, 709 (1951).
[101] G. Socrates, Infrared and Raman characteristic group frequencies: tables and charts, John Wiley & Sons, 2004.
[102] C. Boersma, A. L. Mattioda, C. W. B. Jr, E. Peeters, A. G. G. M. Tielens, and L. J. Allamandola, Astrophys. J **690**, 1208 (2009).
[103] C. Pech, C. Joblin, and P. Boissel, Astron. Astrophys. **388**, 639 (2002).
[104] J. R. Barker, L. J. Allamandola, and A. G. G. M. Tielens, Astro-

phys. J **315**, L61 (1987).
[105] A. J. Huneycutt, R. N. Casaes, B. J. McCall, C.-Y. Chung, Y.-P. Lee, and R. J. Saykally, ChemPhysChem **5**, 321 (2004).
[106] C. J. Mackie, A. Candian, X. Huang, E. Maltseva, A. Petrignani, J. Oomens, W. J. Buma, T. J. Lee, and A. G. G. M. Tielens, J. Chem. Phys **143**, 224314 (2015).
[107] C. W. Bauschlicher, Jr., E. Peeters, and L. J. Allamandola, Astrophys. J **697**, 311 (2009).
[108] A. Candian, T. H. Kerr, I.-O. Song, J. McCombie, and P. J. Sarre, Mon. Not. R. Astron. Soc **426**, 389 (2012).
[109] A. Mattioda, D. Hudgins, C. B. Jr., and L. Allamandola, Adv. Space Res. **36**, 156 (2005), Space Life Sciences: Astrobiology: Steps toward Origin of Life and Titan before Cassini.
[110] A. Mattioda, D. Hudgins, C. B. Jr, M. Rosi, , and L. Allamandola, J. Phys. Chem. A **107**, 1486 (2003).
[111] M. Wojdyr, J. Appl. Crystallogr. **43**, 1126 (2010).
[112] M. E. Jacox, Chem. Soc. Rev **31**, 108 (2002).
[113] T. J. Lee, A. Willetts, J. F. Gaw, and N. C. Handy, J. Chem. Phys **90**, 4330 (1989).
[114] A. P. Rendell, T. J. Lee, and P. R. Taylor, J. Chem. Phys **92**, 7050 (1990).
[115] A. L. C. Lima, J. W. Farrington, and C. M. Reddy, Environ. Forensics **6**, 109 (2005).
[116] D. Vione, S. Barra, G. de Gennaro, M. de Rienzo, S. Gilardoni, M. G. Perrone, and L. Pozzoli, Ann. Chim-Rome **94**, 257 (2004).
[117] S. Hecht, S. Amin, A. Melikian, E. La Voie, D. Hoffmann, and R. Harvey, Polycyclic Hydrocarbons and Carcinogenesis, in ACS Monograph No. 283, pp. 85–106, American Chemical Society Washington, DC, 1985.
[118] I. Allamandola, S. Sandford, and B. Wopenka, Science **237**, 56 (1987).
[119] A. Moorhouse, T. R. Geballe, L. J. Allamandola, A. G. G. M. Tielens, and P. W. J. L. Brand, Spatial variations of the 3 μm emission features within nebulae., in Interstellar Dust, edited by L. J. Allamandola and A. G. G. M. Tielens, volume 135 of IAU Symposium, p. 107, 1989.
[120] K. V. Bruce J. Hrivnak and S. Kwok, Astrophys. J **535**, 275 (2000).
[121] T. R. Geballe and W. E. C. J. van der Veen, Astron. Astrophys. **235**, L9 (1990).
[122] E. Rauls and L. H. r, Astrophys. J **679**, 531 (2008).
[123] J. Semmler, P. W. Yang, and G. E. Crawford, Vib. Spec. **2**, 189 (1991).
[124] M. Steglich, C. Jäger, F. Huisken, M. Friedrich, W. Plass, H.-J. Räder, K. Müllen, and T. Henning, Astrophys. J. Suppl. S **208**, 26 (2013).
[125] S. A. Sandford, M. P. Bernstein, and C. K. Materese, Astrophys.

J. Suppl. S **205**, 8 (2013).
[126] C. J. Mackie, A. Candian, X. Huang, E. Maltseva, A. Petrignani, J. Oomens, A. L. Mattioda, W. J. Buma, T. J. Lee, and A. G. Tielens, J. Chem. Phys **145**, 084313 (2016).
[127] A. D. Becke, J. Chem. Phys **98**, 5648 (1993).
[128] C. Lee, W. Yang, and R. G. Parr, Phys. Rev. B **37**, 785 (1988).
[129] V. Barone, P. Cimino, and E. Stendardo, J. Chem. Theory Comput **4**, 751 (2008).
[130] J. Bloino, M. Biczysko, and V. Barone, J. Chem. Theory Comput **8**, 1015 (2012).
[131] A.-R. Allouche, J. Comput. Chem **32**, 174 (2011).
[132] S. R. Langhoff, C. W. Bauschlicher, D. M. Hudgins, S. A. Sandford, and L. J. Allamandola, J. Phys. Chem. A **102**, 1632 (1998).
[133] C. J. Mackie, A. Candian, X. Huang, E. Maltseva, A. Petrignani, J. Oomens, W. J. Buma, T. J. Lee, and A. G. G. M. Tielens, Phys. Chem. Chem. Phys., Advance Article (2018).
[134] M. Basire, P. Parneix, F. Calvo, T. Pino, and P. Bréchignac, The Journal of Physical Chemistry A **113**, 6947 (2009).
[135] F. Wang and D. Landau, Physical review letters **86**, 2050 (2001).
[136] D. Landau, S.-H. Tsai, and M. Exler, American Journal of Physics **72**, 1294 (2004).
[137] F. Calvo, M. Basire, and P. Parneix, The Journal of Physical Chemistry A **115**, 8845 (2011).
[138] C. Joblin, A. Tielens, M. Basire, P. Parneix, T. Pino, P. Bréchignac, and F. Calvo, European Astronomical Society Publications Series **46**, 95 (2011).
[139] P. Parneix, M. Basire, and F. Calvo, Computational and Theoretical Chemistry **990**, 112 (2012), Chemical reactivity, from accurate theories to simple models, in honor of Professor Jean-Claude Rayez.
[140] M. Basire, P. Parneix, and F. Calvo, Quantum anharmonic densities of states using the Wang–Landau method, 2008.
[141] W. J. Hehre, R. Ditchfield, and J. A. Pople, The Journal of Chemical Physics **56**, 2257 (1972).
[142] C. J. Mackie, T. Chen, A. Candian, X. Huang, T. J. Lee, and A. G. G. M. Tielens, Submitted (2018).
[143] C. W. Bauschlicher Jr, E. Peeters, and L. J. Allamandola, The Astrophysical Journal **678**, 316 (2008).
[144] P. Castellanos, J. Bouwman, A. Candian, C. J. Mackie, H. A. Galue, D. Paardekooper, A. Petrignani, J. Oomens, H. Linnartz, and A. G. G. M. Tielens, Submitted (2018).
[145] A. Candian and C. J. Mackie, Int. J. Quantum Chem **117**, 146 (2017).
[146] L. S. Rothman, I. E. Gordon, Y. Babikov, A. Barbe, D. C. Benner, P. F. Bernath, M. Birk, L. Bizzocchi, V. Boudon, C. J. Mackie, et al., J. Quant. Spectrosc. Radiat. Transfer **130**, 4 (2013).

Nederlandse samenvatting

Dutch summary goes here.

Publications

1. C. J. Mackie, T. Chen, A. Candian, X. Huang, T. J. Lee, and A. G. G. M. Tielens, Submitted (2018)
2. P. Castellanos, J. Bouwman, A. Candian, C. J. Mackie, H. A. Galue, D. Paardekooper, A. Petrignani, J. Oomens, H. Linnartz, and A. G. G. M. Tielens, Submitted (2018)
3. C. J. Mackie, T. Chen, A. Candian, X. Huang, T. J. Lee, and A. G. G. M. Tielens, Submitted (2018)
4. C. J. Mackie, A. Candian, X. Huang, E. Maltseva, A. Petrignani, J. Oomens, W. J. Buma, T. J. Lee, and A. G. G. M. Tielens, Phys. Chem. Chem. Phys., Advance Article (2018)
5. E. Maltseva, A. Petrignani, A. Candian, C. J. Mackie, X. Huang, T. J. Lee, A. G. Tielens, J. Oomens, and W. J. Buma, Astron. Astrophys., Accepted (2018)
6. A. Candian and C. J. Mackie, Int. J. Quantum Chem **117**, 146 (2017)
7. C. J. Mackie, A. Candian, X. Huang, E. Maltseva, A. Petrignani, J. Oomens, A. L. Mattioda, W. J. Buma, T. J. Lee, and A. G. Tielens, J. Chem. Phys **145**, 084313 (2016)
8. E. Maltseva, A. Petrignani, A. Candian, C. J. Mackie, X. Huang, T. J. Lee, A. G. Tielens, J. Oomens, and W. J. Buma, Astrophys. J **831**, 58 (2016)
9. C. J. Mackie, A. Candian, X. Huang, E. Maltseva, A. Petrignani, J. Oomens, W. J. Buma, T. J. Lee, and A. G. G. M. Tielens, J. Chem. Phys **143**, 224314 (2015)

10. E. Maltseva, A. Petrignani, A. Candian, C. J. Mackie, X. Huang, T. J. Lee, A. G. G. M. Tielens, J. Oomens, and W. J. Buma, Astrophys. J **814**, 23 (2015)

11. C. J. Mackie, A. Candian, X. Huang, T. J. Lee, and A. G. G. M. Tielens, J. Chem. Phys **142**, 244107 (2015)

12. C. J. Mackie, E. Peeters, C. W. Bauschlicher Jr, and J. Cami, Astrophys. J **799**, 131 (2015)

13. L. S. Rothman, I. E. Gordon, Y. Babikov, A. Barbe, D. C. Benner, P. F. Bernath, M. Birk, L. Bizzocchi, V. Boudon, C. J. Mackie, et al., J. Quant. Spectrosc. Radiat. Transfer **130**, 4 (2013)

Curriculum Vitae

Acknowledgements